UNIVERSIDAD COMPLUTENSE DE MADRID
FACULTAD DE CIENCIAS QUÍMICAS

TESIS DOCTORAL

Propiedades físico-químicas de polímeros conjugados nanoestructurados y sus aplicaciones en células solares orgánicas

Physicochemical properties of nanoestructured conjugated polymers and their applicactions in organic photovoltaics

MEMORIA PARA OPTAR AL GRADO DE DOCTOR

PRESENTADA POR

Álvaro Rodríguez Rodríguez

Directores

Mari Cruz García Gutiérrez
Esther Rebollar González
Tiberio Ezquerra Sanz

Madrid, 2018

UNIVERSIDAD COMPLUTENSE DE MADRID

FACULTAD DE CIENCIAS QUÍMICAS

Tesis doctoral

Propiedades físico-químicas de polímeros conjugados nanoestructurados y sus aplicaciones en células solares orgánicas

Physicochemical properties of nanostructured conjugated polymers and their applications in organic photovoltaics

Memoria para optar al título de Doctor

Presentada por Álvaro Rodríguez Rodríguez

Directores: Mari Cruz García Gutiérrez (IEM-CSIC)

Esther Rebollar González (IQFR-CSIC)

Tiberio Ezquerra Sanz (IEM-CSIC)

Madrid, 2017

Table of Contents

Agradecimientos

Esta Tesis doctoral ha sido realizada en el Instituto de Estructura de la Materia (CSIC) con la subvención del programa de ayudas para contratos predoctorales para la formación de doctores (BES-2013-062620) del MINECO.

En primer lugar me gustaría agradecer a mis directores de Tesis, la Dra. Mari Cruz García Gutiérrez, la Dra. Esther Rebollar González y el Prof. Tiberio Ezquerra Sanz por su constante entrega, ayuda, apoyo e implicación. En definitiva, gracias por hacer todo posible para que esta Tesis salga adelante. Agradezco y valoro enormemente la oportunidad que he tenido de aprender de tres personas que han sabido transmitirme desde el primer día su gusto por la ciencia.

He tenido la suerte de formar parte del fantástico grupo *Softmatpol* del Instituto de Estructura de la Materia del CSIC y me gustaría agradecer a cada uno sus miembros toda la ayuda recibida durante estos años: Aurora, Amelia, Daniel, José Carlos, Alex, Dani, Nacho, Michela, Jaime, Marga, Jing y Edgar. Con ese equipo es difícil que las cosas salgan mal.

Me gustaría agradecer también a la gente del Instituto de Estructura de la Materia, en especial a José Vicente, de quien he recibido un vital asesoramiento durante las medidas de espectroscopia Raman y a Guillermo por su apoyo y disponibilidad en todos los asuntos relacionados con el Instituto.

Al grupo *Lanamap* del Instituto de Química Física Rocasolano: Marta, Rebeca, Mohamed, Mikel, Nacho, Rene, por la ayuda y paciencia recibida durante los experimentos en el laboratorio de láser.

Durante mi doctorado he tenido la gran oportunidad de realizar estancias en el extranjero en otros grupos de investigación. Gracias al Prof. Peter Müller-Buschbaum de la Universidad Técnica de Munich, Alemania y al Dr. Cheng Wang del Lawrence Berkeley National Laboratory (LBNL) así como a la gente de sus respectivos grupos de investigación por acogerme en sus laboratorios y por la enseñanza recibida durante esos meses.

Además, quería agradecer a mis padres y a mi familia por todo el apoyo y cariño que he recibido ante cualquier decisión, siempre con una sonrisa.

Abstract

The discovery of semiconducting polymers opened the way for the development of the organic electronics with the emergence of new applications such as Organic Light-Emitting Diodes (OLEDs), Organic Field-Effect Transistors (OFETs), Organic Photovoltaics (OPVs), sensors for gases and biosensors among others. Moreover, the high demand of making smaller electronic devices has allowed the development of sophisticated nanostructuring methods such as soft lithography, nanoimprinting lithography and electron-beam lithography which can achieve sub-100 nm patterns.

In recent years, patterning methods have been successfully employed to improve the efficiency of Organic Solar Cells (OSC). A typical organic solar cell consists of a donor material, which is usually a semiconducting polymer blended with an acceptor material such as fullerene derivatives. However, efficiency of OSC is still very low in comparison with conventional silicon-based solar cells. One of the reasons is due to the very short diffusion length of the excitons, in the order of tens of nm, which is much shorter than the distance between donor-acceptor materials in a standard organic solar cell and thus facilitates the charge recombination. Moreover, lithography methods have been used to generate patterned surfaces limiting the distance between the donor and the acceptor materials as well as for improving the light absorption since they may act as light trapping systems.

Nanostructuring by laser techniques can be considered as an alternative approach to the conventional patterning methods based on optical lithography. In particular, the direct laser illumination of a material surface can lead to the formation of the so-called Laser-Induced Periodic Surface Structures (LIPSS). LIPSS in the form of ripples develop on the material surface as a result of irradiation with a linearly polarized laser beam in such a way that the interference between the incoming and the surface scattered waves causes a heterogeneous intensity distribution, which together with a feedback mechanism, results in the enhancement of the modulation intensity. The period of the ripples depends basically on the laser wavelength. LIPSS have been observed on thin polymer films by varying both pulse duration ranging from nano- to femtoseconds and laser wavelengths from the IR to the UV spectral regions.

This Thesis work evaluates the possibility of fabricating LIPSS on conjugated polymers and the incorporation of such nanostructured films in photovoltaics. In particular the main general objectives of this Thesis work are the following:

- To investigate the physical properties of semiconducting polymers under confinement.
- Fabrication and characterization of Laser-Induced Periodic Surface Structures (LIPSS).
- Applicability of nanostructured semiconducting polymers in organic photovoltaics.

This Thesis is divided into 6 chapters. In Chapter 1 general aspects of polymer materials and in particular of conjugated polymers are included, as well as the basis of the fabrication of LIPSS. Finally general aspects of organic solar cells are also included in this chapter. In Chapter 2 the materials studied in this Thesis, the methods used for the preparation of samples and the experimental techniques used for characterizing, nanostructuring and the study of properties are presented. In Chapter 3 the investigation of confinement and phase separation in thin films of immiscible blends of conjugated polymers and the influence in their electrical properties at nanometer scale are presented. Chapter 4 reports the results obtained on the preparation and characterization of LIPSS in conjugated polymers. Optimal conditions for LIPSS formation are given in this chapter for the different conjugated polymers and blends. In addition, the preparation of LIPSS in a polymer/fullerene blend and the study of the phase separation by Resonant Soft X-ray Scattering (RSoXS) are described in this chapter. The results obtained from the *in situ* monitoring by Grazing Incidence Small Angle X-ray Scattering (GISAXS) of the LIPSS formation are also shown and discussed. In Chapter 5 the incorporation of LIPSS in the active layer of solar cells devices is presented. Finally, in Chapter 6, the conclusions are pointed out.

The main conclusions of this work are that LIPSS can be formed on conjugated polymers and their blends with other conjugated polymers or with fullerene derivatives. The dimensions of the obtained nanostructures can be controlled by changing the laser parameters of irradiation and the results obtained shown that there is a weak impact on the chemical stability of the nanostructured polymer material. Furthermore, by irradiation in vacuum, the effects are negligible. The characterization of the electrical properties of the substrates with LIPSS shows that they exhibit a heterogeneous

conductivity alternating conductive and non-conductive regions. Finally, LIPSS have been successfully incorporated in active layers of organic solar cells, which suggest that LIPSS could be a compatible technology with organic photovoltaic devices.

Resumen

El descubrimiento de los polímeros semiconductores en el año 1977 ha dado lugar al desarrollo de la electrónica basada en materiales orgánicos con la eclosión de nuevas aplicaciones como los diodos emisores de luz (OLEDs), los transistores orgánicos de efecto de campo (OFETs), las células solares orgánicas (OPVs), los sensores de gases o biosensores entre otras. Por otra parte, la alta demanda por la continua miniaturización de los dispositivos electrónicos ha permitido el desarrollo de métodos de nanoestructuración sofisticados tales como la litografía blanda, litografía por nano impresión y litografía por haz de electrones con los cuales se pueden alcanzar impresiones con patrones de menos de 100 nm.

En los últimos años, los métodos de estructurado han sido empleados con éxito para mejorar la eficiencia de células solares orgánicas. Una capa activa típica está formada por un material dador de electrones, el cual suele ser un polímero semiconductor mezclado con un material aceptor de electrones, como por ejemplo los derivados de fulerenos. Sin embargo, la eficiencia de las células orgánicas es todavía muy baja en comparación con las celdas solares de silicio, en parte debido a la corta distancia de difusión de los excitones, que es mucho más pequeña que la distancia entre dador y el aceptor en una célula solar estándar. Esto facilita la recombinación de los excitones limitando la transferencia de carga desde el dador al aceptor. Por lo tanto, los métodos litográficos han sido aplicados para generar superficies nanoestructuradas en las cuales es posible disminuir la distancia entre el dador y el aceptor. Además, se han utilizado para mejorar la absorción de luz ya que al tener dimensiones de la longitud de onda de la luz interfieren con ésta de manera que permiten disminuir la cantidad de luz reflejada.

La nanoestructuración mediante técnicas láser puede considerarse una alternativa a los métodos de nanoestructuración convencionales basados en litografía óptica. La irradiación directa con un láser sobre la superficie de un material puede dar lugar a la formación de estructuras periódicas superficiales inducidas por láser *(Laser-Induced Periodic Surface Structures, LIPSS*). Las LIPSS en forma de pequeñas ondulaciones se desarrollan en la superficie de un material como resultado de la irradiación con un haz láser linealmente polarizado de tal manera que la interferencia entre la onda incidente y la reflejada en la superficie provoca una distribución de intensidades heterogénea que junto a un mecanismo de retroalimentación resulta en el aumento de la intensidad de

modulación. La periodicidad de las estructuras básicamente depende de la longitud de onda de irradiación. Hasta la fecha se han observado LIPSS sobre películas delgadas de polímero variando tanto la duración del pulso láser, desde nano- a femtosegundos como la longitud de onda del láser desde el IR al UV.

En esta Tesis, se ha investigado la posibilidad de fabricar LIPSS en películas delgadas de polímeros conjugados y la incorporación de las películas nanoestructuradas en células solares orgánicas. En particular, los objetivos principales de esta Tesis son:

- Investigar las propiedades físicas de polímeros semiconductores en condiciones de confinamiento.
- Fabricación y caracterización de estructuras superficiales periódicas inducidas por láser (LIPSS).
- Aplicabilidad de polímeros semiconductores nanoestructurados en particular en celdas solares fotovoltaicas.

La Tesis está dividida en 6 capítulos. En el primero de ellos se introducen brevemente aspectos generales de los materiales poliméricos y de los polímeros conjugados en particular, así como los fundamentos de la fabricación de estructuras superficiales periódicas inducidas por láser. Finalmente en este capítulo se presentan aspectos generales de las celdas solares orgánicas. En el Capítulo 2 se describen los materiales utilizados en esta Tesis, así como los métodos usados para la preparación de muestras y las técnicas experimentales utilizadas para la caracterización, nanoestructuración y estudio de propiedades. En el Capítulo 3 se presenta el estudio del confinamiento y separación de fase en películas delgadas de mezclas inmiscibles de polímeros conjugados, así como su influencia en las propiedades eléctricas a escala nanoscópica. A continuación, el Capítulo 4 contiene los principales resultados obtenidos sobre la preparación y caracterización físico-química de las LIPSS en los polímeros descritos en el Capítulo 2. Las condiciones óptimas para la fabricación de LIPSS tanto en polímeros como en mezclas polímero/polímero y polímero/fulerenos están recogidas en este capítulo. Al final del mismo se muestran y discuten los resultados obtenidos sobre la monitorización de la formación de LIPSS *in situ* mediante la técnica de dispersión de rayos-X a ángulos pequeños en geometría de incidencia rasante (*Grazing Incidence Small Angle X-ray Scattering*, GISAXS) utilizando radiación sincrotrón. En el Capítulo 5 se recogen los principales resultados sobre la fabricación de células solares

orgánicas implementando la tecnología LIPSS en la capa activa. Finalmente, en el Capítulo 6 se recogen las conclusiones derivadas de este trabajo de Tesis doctoral.

Las principales conclusiones de esta Tesis son que se ha conseguido fabricar LIPSS en polímeros conjugados y sus mezclas con otros polímeros conjugados y con derivados de fulerenos. Las dimensiones de las películas nanoestructuradas obtenidas pueden ser controladas cambiando los parámetros de irradiación del láser y los resultados muestran que la irradiación afecta levemente en la estabilidad química del material nanoestructurado. Asimismo, irradiando en vacío los efectos son casi insignificantes. La caracterización de las propiedades eléctricas de las muestras con LIPSS demuestra que exhiben una conductividad eléctrica heterogénea que alterna regiones conductoras y no conductoras. Finalmente, se han incorporado las LIPSS a capas activas en células solares orgánicas, lo que sugiere que LIPSS podría ser una tecnología compatible con la fabricación de dispositivos fotovoltaicos orgánicos.

List of symbols and abbreviations

α_i	Incident angle in an X-ray experiment
α	Exit angle
α_{crit}	Critical angle
$\boldsymbol{\alpha}$	Mass absorption coefficient
β	Imaginary part of the refraction index
δ	Real part of the refraction index
ε	Molar absorption coefficient
ε_r	Dielectric constant
ε_0	Vacuum permittivity
θ	Laser incidence angle
2θ	Scattering angle
λ	Wavelength
μ	Charge mobility
μ_0	The zero-field mobility
$\boldsymbol{\mu}$	Linear absorption coefficient
ρ	Mass density
ϕ	Relative fraction of crystalline phase
ω	Out of plane scattering angle
A	Absorbance
A_a	Area of crystalline contribution
A_c	Area of amorphous contribution
b	Path length
$\boldsymbol{c}$	Concentration

c	Speed of light
d_{hkl}	Interplanar distance
E	Electric field intensity
E_0	Field coefficient
E	Energy
E_g	Energy gap
e^-	Electron
h	Planck's constant
h^+	Hole
I	Transmitted radiation
I	Current intensity
I_0	Incident radiation
I_{mp}	Intensity at maximum point
I_{sc}	Short circuit current
J	Current density
$\vec{k}_i$	Incident wave vector
$\vec{k}_f$	Scattered wave vector
L	Period of the ripples
M_i	Molar mass
M_n	Number average molecular weight
M_w	Weight average molecular weight
N_i	Number of molecules
n	Refraction index
P_{max}	Largest power output
P_{in}	Incident light power density

$\vec{q}$	Scattering vector
R_a	Average roughness
t	Thickness
T	Transmittance
T_g	Glass transition temperature
T_m	Melting point
T_I	Isotropization temperature
V	Applied voltage
V_{mp}	Voltage at maximum point
V_{oc}	Open circuit voltage
W_i	Mass of molecules
X_i	Composition
Z	Depth of the ripples
AAO	Anodic Aluminum Oxide
AEY	Auger Electron Yield
AFM	Atomic Force Microscopy
BHJ	Bulk Heterojunction
C-AFM	Conductive-Atomic Force Microscopy
CB	Chlorobenzene
CCD	Charge-Coupled Device
FF	Fill Factor
GISAXS	Grazing Incidence Small Angle X-ray Scattering
GIWAXS	Grazing Incidence Wide Angle X-ray Scattering
GIXS	Grazing Incidence X-ray Scattering
HOMO	Highest Occupied Molecular Orbital

IR	Infrared
ITO	Indium Tin Oxide
ICT	Intramolecular Charge Transference
LED	Light-Emitting Diode
LINAC	Linear particle accelerator
LIPSS	Laser-Induced Periodic Surface Structures
LUMO	Lowest Unoccupied Molecular Orbital
NEXAFS	Near Edge X-ray Absorption Fine Structure
NIL	Nanoimprint Lithography
NIR	Near-infrared
OD	Optical Density
OFET	Organic Field-Effect Transistor
OLED	Organic Light-Emitting Diode
OPVs	Organic Photovoltaics
OSC	Organic Solar Cell
P3HT	Poly(3-hexylthiophene-2,5-diyl)
PCE	Power Conversion Efficiency
$PC_{71}BM$	Phenyl-C71-butyric-acid-methyl-ester
PCDTBT	Poly[N-9'-heptadecanyl-2,7-carbazole-alt-5,5-(4',7'-di-2-thienyl-2',1',3'-benzothiadiazole)]
PEDOT:PSS	Poly(3,4-ethylenedioxythiophene) polystyrene sulfonate
PDI	Polydispersity Index
PSC	Polymer Solar Cell
RSoXS	Resonant Soft X-Ray Scattering

RR-P3HT	Regioregular P3HT
SAXS	Small Angle X-ray Scattering
SCLC	Space-Charge Limited Current
SERS	Surface-Enhanced Raman Scattering
STM	Scanning Tunneling Microscopy
STXM	Scanning Transmission X-ray Microscopy
SVD	Single Value Decomposition
TEM	Transmission Electron Microscopy
TEY	Total Electron Yield
UV	Ultraviolet
UV-vis	Ultraviolet-visible
WAXS	Wide Angle X-ray Scattering

Prologue

Human civilization can be considered to be supported by several pillars which include: education, communication information, energy and materials. Materials represent one of the most important preconditions of the quality of life of human society. Indeed, historians use some typical materials for the characterization of the technological level distinguishing the stone age, followed by the periods of bronze and iron.[1] There is no doubt that part of the new materials of the future will be either nanostructured or multicomponent or both.

One possible application of nanotechnology is based on exploiting the properties of materials associated with their inherent nanostructure. Since the second half of the 20th century, polymers have become the primary material of mankind thus becoming an important support of our everyday life. By definition, a polymer is a very big molecule that contains more than 1000 atoms (up to millions). They are mainly based on the chemistry of carbon although there are many inorganic polymers, too. Synthetic polymers complement natural ones such as wood, cellulose, wool, leather, or natural rubber that have been used by man from the very beginning of civilization. Along the twentieth century synthetic polymers have made continuously their way to the top. The production of polymers increases every year and will continue to do so. From the markets point of view, polymers can be divided into two broad groups: commodities and specialty polymers. Commodity polymers are produced from a few simple starting compounds. They are very inexpensive and are used in large amounts. Most widespread are polyethylene, polypropylene, poly(vinyl chloride), polystyrene and poly(ethylene terephthalate). These five materials cost less than 1 €/kg and cover more than 80% of the world production of polymers. In contrast, specialty polymers are made from many different compounds. They are more costly, but can be tailored for nearly every use. Consequently, they are employed in traditional applications as well as in high technology and are often at the base for the continuous progress in air, space, computer and medical technology. Though prices for specialty polymers are usually still low to moderate (below 10 €/kg), certain specialties can be more expensive than gold or diamonds. In addition, the combination of polymer and non-polymer material to give rise to a new hybrid and composite materials is of great interest because the resulting systems may show highly improved properties over the starting materials.[2]

Polymeric materials, including polymers and composites, are an essential part of the technological revolution of the information age through their multiple applications ranging from lithographic masks to electronic connections and packaging. Among commodity polymers, semicrystalline ones (polyethylene, polypropylene and poly(ethylene terephthalate)) represent approximately two thirds of the annual production of synthetic polymers and their preparation has experienced a remarkable progress with the advent of new techniques of synthesis.

Due to the great length of the molecules of a polymer, the intrinsic structure of crystallizable polymers is semicrystalline, alternating regions including crystalline and amorphous phases of thicknesses in the range of nanometers.[3] The great versatility in the mechanical properties of semicrystalline polymers stems from the fact that the crystalline phase can provide the system with a high resistance to fracture (strength) while the amorphous one can provide a high capacity for mechanical energy absorption before fracture (toughness).

Although semicrystalline polymers are inherently nanostructured materials, the control over the nanostructure is very limited. One possibility to control the nanostructuring in the bulk is to introduce into the polymer matrix nanoadditives with defined aspect ratio. Carbon nanotubes (CNT) tend to induce fibre-like structures in the polymer matrix because their surfaces force the polymer chains to adopt a conformation that controls the orientation of crystals.[2]

An additional complication occurs when a polymer is subjected to some form of confinement in the nanometer range aiming to develop a nanomaterial. This happens, for example, in the preparation of thin polymer films (nanofilms) inducing a confinement of the polymer in two dimensions (2D).[4] Another example is the preparation of polymer nanotubes, nanogrooves or nanocylinders induced by confinement in one dimension (1D) using inorganic templates,[5, 6] nanoimprinting[7] or by laser irradiation.[8] The nanoconfinement can produce large effects on both the structure and the dynamics of the material and it even may affect any phase transitions or physical processes.[5] It is important to emphasize that this phenomenon is ubiquitous and has significant implications in fields as diverse as the transportation of fluids in porous media, the mobility of the substance in cell membranes and micro-lubrication among others. Also, the understanding of confinement effects is crucial, not only in the development of nanostructured materials for specific applications such as

Soft-lithography[9] but also to contribute to the understanding of the physical basis of Nanotechnology.

The ability to fabricate structures from the micro- to the nanoscale with high precision in a wide variety of materials is of paramount importance for the advancement of micro- and nanotechnology and nanoscience. Several alternative approaches towards nanostructure fabrication have been exploited in the past 15 years. These techniques include microcontact printing (or soft lithography),[9] nanoimprint lithography,[7, 10] scanning-probe-based techniques (e.g., atomic force microscope lithography),[11] templating by nanoporous alumina membranes[12] and Laser-Induced Periodic Surface Structures (LIPSS)[8, 13] among others.

Within this context, the main general objectives of this thesis work are the following:

• To investigate the physical properties of semiconducting polymers under confinement.

• Fabrication and characterization of Laser-Induced Periodic Surface Structures (LIPSS).

• Applicability of nanostructured semiconducting polymers in organic photovoltaics.

References

(1) Raab, M.; Kotek, J. *Polimeri* **2005**, *26 (4)*, 172-175.

(2) Thostenson, E.T.; Li, C.; Chou, T.-W. *Composites Science and Technology* **2005**, *65 (3–4)*, 491-516.

(3) Strobl, G.R., The Physics of Polymers: Concepts for Understanding Their Structures and Behavior, *Springer-Verlag Berlin Heidelberg* (2007).

(4) Rueda, D.R.; Nogales, A.; Hernández, J.J.; García-Gutiérrez, M.-C.; Ezquerra, T.A.; Roth, S.V.; Zolotukhin, M.G.; Serna, R. *Langmuir* **2007**, *23 (25)*, 12677-12681.

(5) Steinhart, M.; Göring, P.; Dernaika, H.; Prabhukaran, M.; Gösele, U.; Hempel, E.; Thurn-Albrecht, T. *Physical Review Letters* **2006**, *97 (2)*, 027801.

(6) Garcia-Gutierrez, M.-C.; Linares, A.; Martin-Fabiani, I.; Hernandez, J.J.; Soccio, M.; Rueda, D.R.; Ezquerra, T.A.; Reynolds, M. *Nanoscale* **2013**, *5 (13)*, 6006-6012.

(7) Schift, H. *Journal of Vacuum Science & Technology B: Microelectronics and Nanometer Structures Processing, Measurement, and Phenomena* **2008**, *26 (2)*, 458-480.

(8) Rebollar, E.; Castillejo, M.; Ezquerra, T.A. *European Polymer Journal* **2015**, *73*, 162-174.

(9) Xia, Y.; Whitesides, G.M. *Annual Review of Materials Science* **1998**, *28*, 153-184.

(10) Rueda, D.R.; Martin-Fabiani, I.; Soccio, M.; Alayo, N.; Perez-Murano, F.; Rebollar, E.; Garcia-Gutierrez, M.C.; Castillejo, M.; Ezquerra, T.A. *Journal of Applied Crystallography* **2012**, *45 (5)*, 1038-1045.

(11) Fernández-Regúlez, M.; Evangelio, L.; Lorenzoni, M.; Fraxedas, J.; Pérez-Murano, F. *ACS Applied Materials & Interfaces* **2014**, *6 (23)*, 21596-21602.

(12) Martín, J.; Vázquez, M.; Hernández-Vélez, M.; Mijangos, C. *Nanotechnology* **2008**, *19 (17)*, 175304.

(13) Martin-Fabiani, I.; Rebollar, E.; Perez, S.; Rueda, D.R.; Garcia-Gutierrez, M.C.; Szymczyk, A.; Roslaniec, Z.; Castillejo, M.; Ezquerra, T.A. *Langmuir* **2012**, *28 (20)*, 7938-7945.

Chapter 1. Introduction

1.1. General concepts of polymer materials

Polymers are macromolecules built up by a large number of molecular units (monomers) that are linked together by covalent bonds. Usually they represent organic compounds, containing carbon atoms together with hydrogen, nitrogen, oxygen, sulfur, etc. Macromolecules are generally obtained by a polymerization process starting from reactive low molar mass compounds. The number of repeating units is defined by the degree of polymerization.[1, 2] Rather than leading to polymers with a single degree of polymerization, reactions usually result in a mixture of macromolecules with different molecular weight. Therefore, for a full characterization, the molecular weight distribution function has to be determined. In this context, the molecular weight is commonly expressed as a number average (M_n) or weight average (M_w) molecular weight defined by:[3]

$$M_n = \frac{\sum N_i M_i}{\sum N_i} \quad ; \quad M_w = \frac{\sum N_i {M_i}^2}{\sum N_i M_i} = \frac{\sum W_i M_i}{\sum W_i} \tag{1.1}$$

Where N_i is the number of molecules of molar mass M_i and W_i is the mass of the molecules of molar mass M_i. In order to measure the size distribution of the polymer chains a polydispersity index (PDI) is defined as:

$$PDI = \frac{M_w}{M_n} \tag{1.2}$$

Therefore, when $M_w = M_n$ a monodisperse polymer is obtained in which all the polymer chains have the same size.

Polymers typically consist of one type of repeating unit (A). In this case they are referred as homopolymers. However, polymer chains can be synthesized combining different monomers (A, B...). In this case large variations in the chemical structure may be achieved giving rise to copolymers. According to the relative position of the different monomers, the copolymers can be classified into random copolymers, alternating copolymers and block copolymers.

From the structural point of view, polymers are divided into three classes: amorphous,[4] liquid crystalline,[5] and semicrystalline polymers.[1-3, 6] Amorphous polymers have neither positional order nor orientational order, like a liquid or a glass. Their physical properties are defined by the glass transition temperature (T_g). Above this temperature, which is specific for each polymer, polymer chains have enough mobility to reorganize. Semicrystalline polymers, consisting of a composite of small crystals with long range positional order in a matrix of amorphous phase, present in addition to the T_g a temperature characteristic of the crystalline phase which is known as melting temperature (T_m).[6] In fact, they can crystallize in a temperature window between the T_g and the T_m. For liquid crystalline polymers there is an additional characteristic thermal transition, characterized by the isotropization temperature T_i, which marks the order-disorder transition of the liquid crystalline phase.[5] Liquid crystalline polymers are characterized by phases in which molecules are arranged with a degree of order intermediate between the complete disorder of a liquid and the three-dimensional order of a crystal.

Semicrystalline polymers have a hierarchical structure, with different structures on different length scales as illustrated in Figure 1.1. The basic unit of most polymer crystals is the chain-folded lamella with a typical thickness of about 10 nm. Lamellae are separated by amorphous regions (Figure 1.1.b). Individual polymer chains may be involved in more than one lamella as well as the amorphous regions in between. The chain-folded lamellae are themselves organized in larger scale structures with different morphologies, which may be several micrometers in size (Figure 1.1.a).

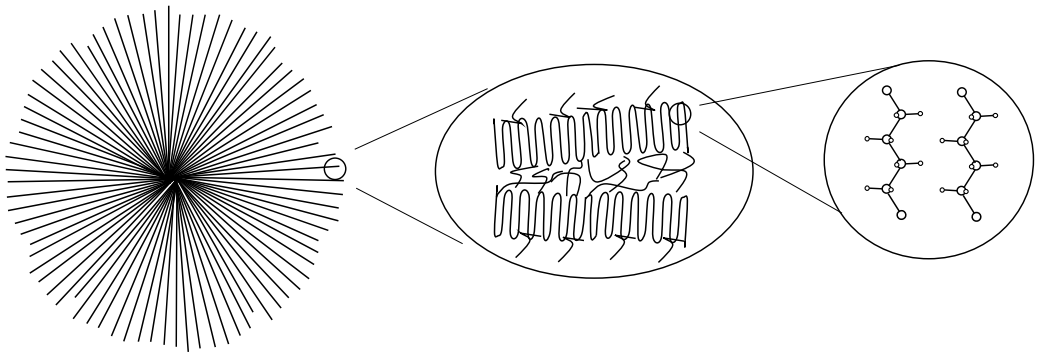

(a) Microscopic scale **(b) Mesoscopic scale** **(c) Atomic scale**

Figure 1.1. Morphological hierarchy exhibited by semicrystalline polymers. (a) spherulites, (b) lamellar crystals, (c) crystalline unit cell. Adapted from reference [7].

1.2. Conjugated polymers

Since the middle part of the last century polymers became commodities. In comparison to other materials, synthetic commodity polymers have been extensively exploited partially due to their low cost, easy manipulation and possibility of tuning their physical properties, mechanical as well as thermal, by controlling their chemical composition. In general, commodity polymers are electrical insulators and some of them transparent to visible light with absorption bands in the ultraviolet (UV) region. However, in 1977 it was discovered[8, 9] a new class of polymers with unexpected electrical conductivity.[10] These polymers have the characteristic of being formed by the alternation of single and double bonds giving rise to a π-conjugated backbone along the polymer chain. As an example of conjugated polymers, polyacetylene and polythiophene are shown in Figure 1.2.

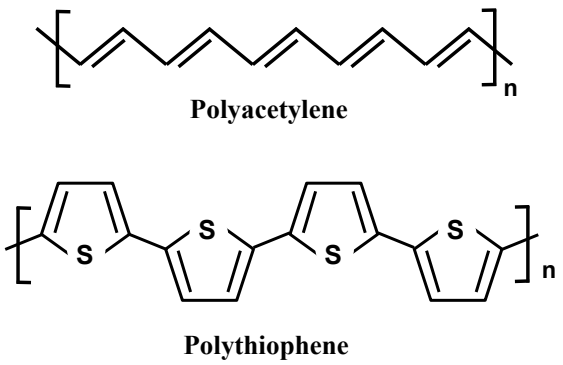

Figure 1.2. Chemical representation of common conjugated polymers. The alternation of simple and double bonds gives rise to a conjugated polymer backbone.

This discovery paved the way for a new class of polymers referred to as special or advanced polymers.[11] Initially conjugated polymers like those shown in Figure 1.2 were insoluble and they degraded before melting, therefore they were difficult to be processed. However chemical modification of conjugated main-chain polymer was developed adding, for example, alkyl side chains. This led to a new generation of processable conjugated polymers.[12-16]

In a conjugated polymer, carbon atoms are linked each other by C sp_2 hybrids. Perpendicular to the C-C σ-bond, an atomic p_z orbital with one electron contributes to the π-bond and thus electrons are delocalized along the carbon backbone (Figure 1.3).

This property is the reason why conjugated polymers can be electrical semiconductors and belong to a new class of materials with a delocalized π-electron system which are known in general as organic semiconductors.[17]

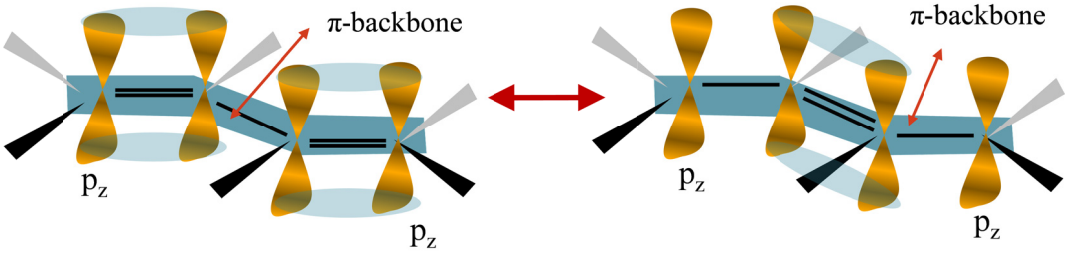

Figure 1.3. Schematic representation of delocalized electrons along the π orbitals resulting in a π-conjugated backbone and enabling proper charge transport.

The molecular orbitals diagram of a conjugated polymer is shown Figure 1.4. Similar to conventional inorganic semiconductors, in organic semiconductors, π orbitals can be visualized as narrow energy bands with a gap of energy (E_g) defined by the difference between the Highest Occupied Molecular Orbital (HOMO) and Lowest Unoccupied Molecular Orbital (LUMO) bands[18] of the polymer. Band gaps with different values can be tuned by using the wide possibilities of the organic chemistry synthesis.[19, 20] In contrast to electrically insulating polymers, semiconducting polymers typically have a strong optical absorption in the visible range. This fact makes semiconducting polymers to be potential candidates to be used for organic photovoltaics.[21, 22]

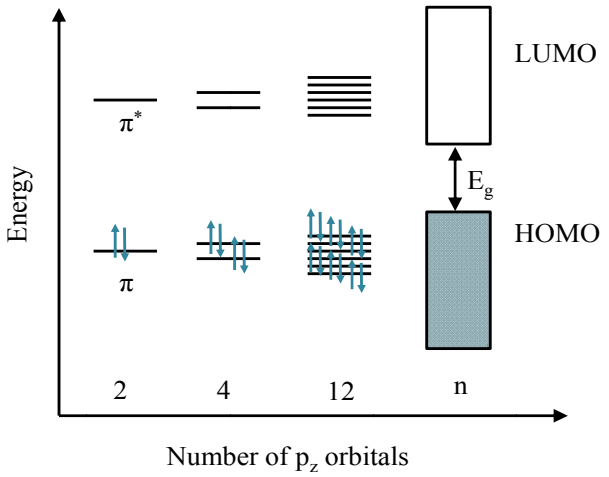

Figure 1.4. Electronic structure of a conjugated chain depending on the amount of p_z orbitals. Blue arrows represent electrons occupying the energy bands. The band gap (E_g) is given by the difference between the HOMO and LUMO.[23]

In general, polymer semiconductors have a low charge carrier concentration in the conduction band associated to the LUMO level. This fact implies a low electrical conductivity. Nevertheless, it is possible to increase the charge carrier concentration by the incorporation of impurities in a doping process which resembles that used for traditional inorganic semiconductors.[24] Essentially, there are two possibilities for doping a conjugated polymer[25, 26] as schematized in Figure 1.5 and consisting of:

(a) N-type doping: this is a process in which a reducing agent donates electrons to the LUMO of the polymer and thus a polymer with high concentration of electrons as charge carriers is obtained.

(b) P-type doping: This occurs when removing electrons from the HOMO of the conjugated polymer by some oxidizing agent[26] such as iodine (I_2) or perchloric acid ($HClO_4$), leaving the respective holes in the HOMO level. In this type of materials, holes are the majority charge carriers.

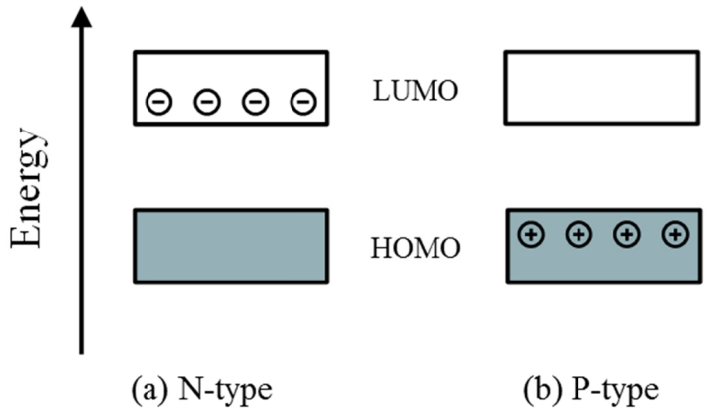

Figure 1.5: Schematic representation of molecular doping in organic semiconductors.

In brief, n-type doping generates an electron-rich polymer material and a p-type process produces electron-poor polymer one. Since a conjugated polymer is intrinsically an electron rich material it is more common and easy to obtain p-type doped polymers. Ambipolar charge has been reported for some organic semiconductors[27, 28] and can be obtained when both electrons and holes are mobile.

Conjugated polymers may exhibit ordered phases because of its ability to form packing ordered structures in the three spatial directions due to the π-π stacking interaction. In these materials, electrical conductivity depends closely on the disorder as well as on the

conjugation length of the polymer chains. Larger conjugation lengths give rise to materials with better electronic transport properties.[18, 29]

Since 1977 a great variety of conjugated polymers have been synthesized.[30, 31] Among them poly(3-hexylthiophene-2,5-diyl) (P3HT) has emerged as one of the most interesting due to its application in Organic Light Emitting Diodes (OLEDs)[32] and in Organic Photovoltaics (OPV)[33] among others.[34]

P3HT is a semicrystalline conjugated polymer with significant electrical conductivity which can be easily processed as thin films, with thicknesses below 100 nm, by spin-coating on different substrates.[29] In this case, P3HT crystals self-organize with the lateral chain direction (100) perpendicular to the substrate (edge-on) or parallel to the substrate (face-on) as it is represented in Figure 1.6. P3HT chains are also able to interact to each other by π-π interactions forming fibrillar structures which give rise to anisotropic electrical properties.[10, 35]

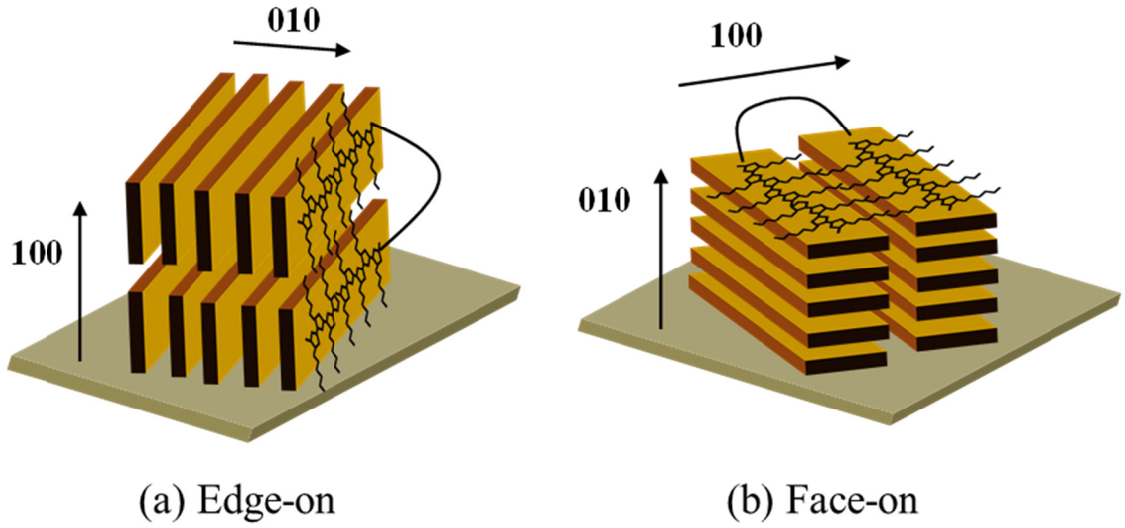

Figure 1.6. Possible structural organization of the polymer chains in P3HT: (a) edge-on and (b) face-on. Adapted from reference [35].

Due to the special properties of some polymer semiconductor materials such as the good processability from solution, the moderate production cost and the flexibility among others, many applications have been exploited in order to obtain efficient organic devices: Organic Solar Cells (OSC) , organic transistors, OLED'S, etc .[36, 37]

1.3. Organic Solar Cells (OSC)

An organic solar cell is based on the energy generation by means of the charge transfer between an electron donor and acceptor materials when illuminated by sunlight. Usually a conjugated polymer (e.g. P3HT) acts as an electron donor when blending with an acceptor compound such as fullerene derivatives.[21, 38] In the case of using other polymer as acceptor material they are known as all-Polymer Solar Cells (PSC).[21] In OSC, the energy generation occurs in four steps as described in Figure 1.7.[39] The first step is the light absorption by the donor material, typically a polymer semiconductor. When a photon interacts with the polymer, an electron is excited from the HOMO to the LUMO of the polymer leaving a hole in the HOMO. This electron-hole pair is called exciton.[40] These excitons diffuse to the donor-acceptor interface (step 2) and they are separated into positive and negative charge carriers (step 3). Afterwards, positive charge carriers (holes) move through the donor to the anode and negative charge carriers (electrons) through the acceptor material to the cathode (step 4).

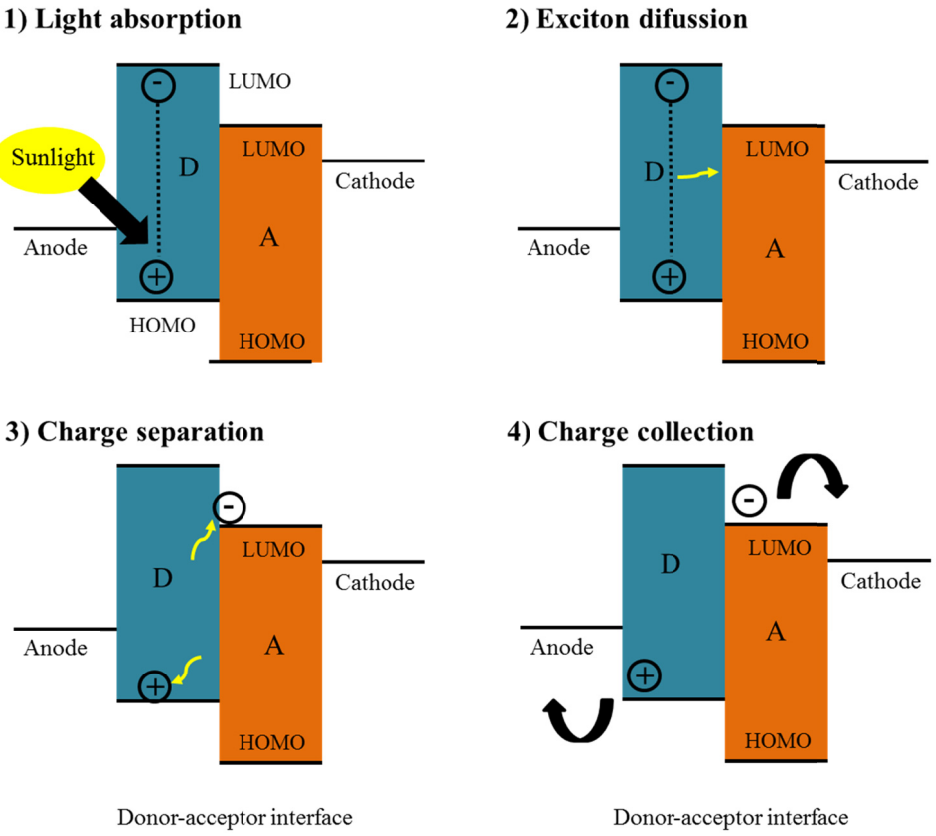

Figure 1.7. Operating principle of organic solar cells with the active layer formed by a donor (D) material and an acceptor (A) one.

Additionally, it is worth noting that work functions of the metal electrodes must be close in energy to the bands of the donor and acceptor materials for an effective charge current injection. The work function is the energy required to remove an electron from the highest energy filled level of a metal.[41] Therefore, anode will collect holes from the HOMO of the donor while electrons from the LUMO of the acceptor are collected by the cathode.[42-44]

The typical current-voltage characteristics of a solar cell in the dark and under illumination are shown in Figure 1.8. While in the dark there is almost no current flowing, when illuminating the solar cell generates photocurrent.

The power-conversion efficiency (PCE) can be obtained from the product of voltage (V_{mp}) and intensity (I_{mp}) at the maximum power point divided by the incident light power density (P_{in}).[21, 45]

$$PCE = \frac{I_{\mathrm{mp}} V_{\mathrm{mp}}}{P_{\mathrm{in}}} \tag{1.3}$$

The incident light intensity is standardized at 1000 W/m^2 with a spectral intensity distribution matching that of the sun on the earth's surface at an incident angle of 48.2°, which is called the AM 1.5 spectrum.[45, 46]

However, usually PCE is expressed in terms of the open circuit voltage (V_{oc}), the short circuit current (I_{sc}) and the fill factor (FF) since these four magnitudes are the more relevant to characterize a solar cell. FF is the product of I_{mp} and V_{mp} divided by V_{oc} and I_{sc}. Therefore the equation 1.3 can be rewritten as:

$$PCE = \frac{I_{sc}\, V_{oc}\, FF}{P_{\mathrm{in}}} \tag{1.4}$$

Generally, V_{oc} of a metal-insulator-metal device is determined by the difference in work functions of the two metal contacts.[47] In organic solar cells, V_{oc} is found to be linearly dependent on the HOMO level of the donor and LUMO level of the acceptor.[48 21] The FF is essentially a measurement of quality of the solar cell and it is often represented as a percentage and PCE is an indication of the device performance.

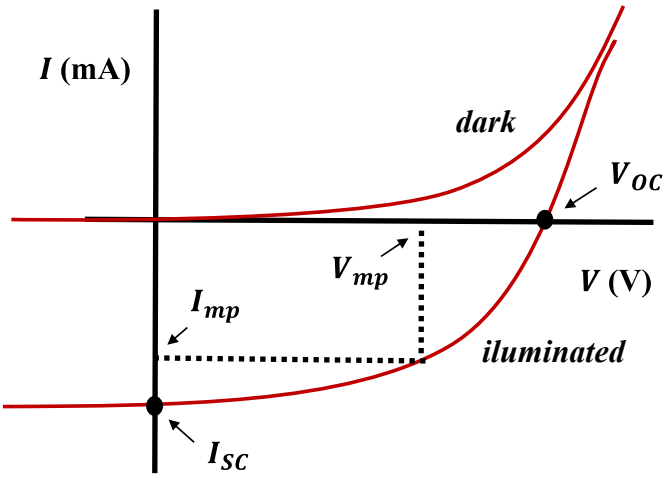

Figure 1.8. Current-voltage (*I-V*) curves of an organic solar cell. The characteristic intersections with the abscissa and ordinate are V_{oc} and I_{sc} respectively. PCE can be determined by the product of voltage (V_{mp}) and intensity (I_{mp}) at the maximum power point.

1.4. Nanostructured organic solar cells

The simplest solar cell consists in a bilayer architecture in which the acceptor material is deposited on top of the donor layer between two electrodes (Figure 1.9.a). However, this geometry gives rise to poor efficiency devices with a very low V_{oc} due to the large interface distance between donor and acceptor materials which facilitates the charge recombination.[49] In recent years, organic solar cells have experienced an important improvement of the performance of devices by the development of bulk heterojunction (BHJ) solar cells (Figure 1.9.b).[44, 50, 51] This morphology can be achieved from blends of donor and acceptor materials when they phase separate. In BHJ solar cells the distance between interfaces of both materials is still much larger than the exciton diffusion length which is reported to be on the order of 10 nm, in addition isolated islands of one of the components act as traps during charge separation.[18, 21] Theoretically, an ideal geometry to obtain high efficiency devices is to fabricate an interdigitated active layer of donor and acceptor materials by means of nanostructuring techniques such as Nanoimprint Lithography (NIL) or template methods[52-55] (Figure 1.9.c). In particular, nano imprinted solar cells have been reported to improve the efficiency.[53] Authors attributed this enhancement to the improved electrical conductivity of the polymer induced by the chain orientation and morphology produced during the fabrication and resulting in a positive effect on the device performance. Furthermore, nanostructured devices have also exhibited a better light absorption and charge collection in devices with patterned electrodes.[56, 57]

Figure 1.9. Common architectures for organic solar cells: (a) bilayer morphology, (b) bulk heterojunction and (c) ideal nanostructured morphology.[39, 43]

In addition to conventional nanostructuring methods, in the last years the number of laser patterning techniques in polymers is experiencing an important growth. Recently, polymers have been nanostructured by using laser methods such as laser interference with two and three laser beams,[58] nanostructuring with optical near fields,[59] and by spontaneous formation of Laser-Induced Periodic Surface Structures (LIPSS).[60, 61] However, it is an open question how laser irradiation affects the structural and optical properties of conjugated polymers.

1.5. Laser-Induced Period Surface Structures (LIPSS)

LIPSS formation is a non-ablative method and it was first observed by Birnbaum on the surface of several semiconductor materials after irradiation with a ruby laser.[62] By this process typically ripples are formed in the surface of a material (Figure 1.10.a) by irradiation with a linearly polarized laser beam, while dots are formed when irradiation is carried out with a circularly polarized laser beam (Figure 1.10.b).[63]

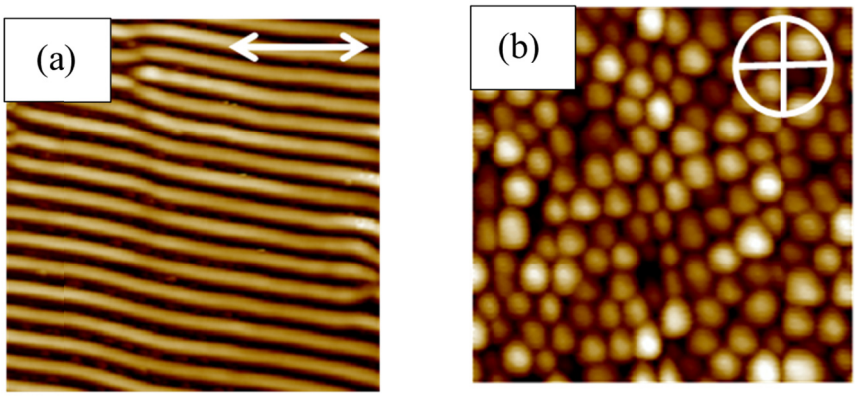

Figure 1.10. AFM height images (4 x 4 μm^2) of a poly(ethylene terephthalate) film irradiated at 266 nm with 1200 pulses and with laser beams of different polarization: (a) linear (↔) and (b) circular (⊕) .

LIPSS originate from the interference of the incident and reflected/refracted laser light with the scattered light near the sample surface. The interference between the different waves leads to an inhomogeneous energy input which, together with positive feedback mechanisms, can cause surface instabilities.[64] LIPSS have been reported on the surface of a wide variety of materials such as metals, semiconductors and dielectrics[65-67] with lasers of different pulse duration from nanosecond to femtosecond,[68] and different wavelengths from the ultraviolet (UV) to the infrared (IR).[69] In the case of polymers, several studies have shown that irradiation by a linearly polarized laser beam induces self-organized ripple structure formation within a narrow fluence range, well below the ablation threshold.[60] A scheme of a LIPSS experiment is shown in Figure 1.11.

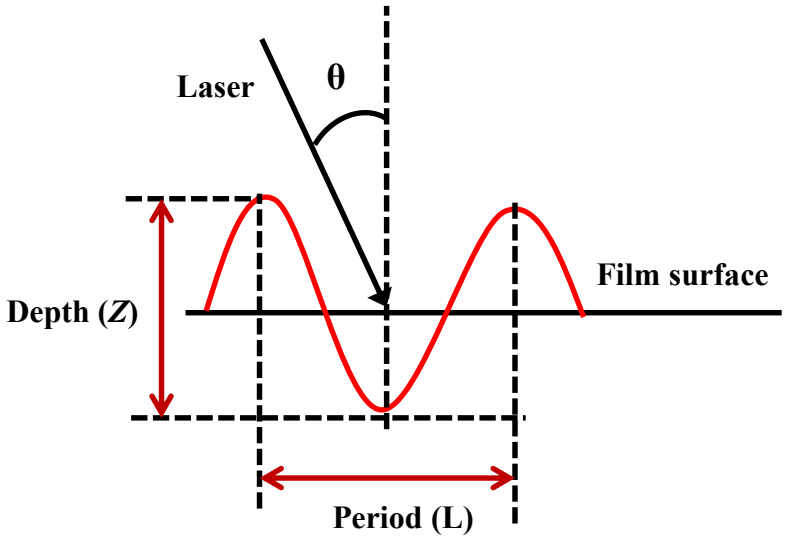

Figure 1.11. Characteristic parameters of a LIPSS experiment in polymers.

The period of the ripples L can be described by the expression:[70]

$$L = \frac{\lambda}{n - \sin\theta} \tag{1.5}$$

where λ is the laser wavelength, n the effective refractive index of the material and θ the angle of incidence of the laser beam with the normal to the sample surface. In the case of polymers, LIPSS appear parallel to the laser polarization and the obtained depth depends on the laser processing conditions. To fabricate LIPSS in polymers some conditions must be fulfilled: a high absorption coefficient at the irradiation wavelength and a roughness of a few nanometers. In addition, the polymer chains should have enough mobility to be able to reorganize and form LIPSS. When the laser light reaches

the sample, the surface is heated. The required temperature to obtain LIPSS is above the T_g in the case of amorphous polymers and above the T_m in the case of semicrystalline polymers.

Until now, LIPSS have been fabricated successfully in some model polymers, mainly amorphous, as a patterning method and implemented in some applications such as cell culture[71, 72] and Surface-Enhanced Raman Spectroscopy (SERS) sensors.[73] A further step would be to fabricate LIPSS in conjugated polymers and the subsequent application in organic optoelectronic devices that is the main purpose of this thesis.

1.6. Thesis Outline

This thesis is divided into 6 chapters. In Chapter 1 general aspects of polymer materials are included and in particular of conjugated polymers, as well as the basis of the fabrication of laser-induced periodic surface structures. Finally general aspects of organic solar cells are also explained in this chapter. In Chapter 2 the materials studied in this thesis, the methods used for the preparation of samples and the experimental techniques used for characterizing, nanostructuring and the study of properties are presented. In Chapter 3 the investigation of confinement and phase separation in thin films of immiscible blends of conjugated polymers and the influence in their electrical properties at nanometer scale are shown. Chapter 4 reports the results obtained on the preparation and characterization of LIPSS in conjugated polymers. Optimal conditions for LIPSS formation are given in this chapter for the different conjugated polymers and blends. In addition, the preparation of LIPSS in a polymer/fullerene blend and the study of the phase separation by resonant soft X-ray scattering are described in this chapter. Finally, the results obtained from the *in situ* monitoring by grazing incidence small angle X-ray scattering of the LIPSS formation are also shown and discussed. In Chapter 5 the incorporation of LIPSS in the active layer of solar cells devices is presented. Finally the main conclusions derived from this thesis are summarized in Chapter 6.

References

(1) Gedde, U.W., Polymer Physics, *Springer Netherlands* (1999).

(2) Strobl, G.R., The Physics of Polymers: Concepts for Understanding Their Structures and Behavior, *Springer-Verlag Berlin Heidelberg* (2007).

(3) Fried, J.R., Polymer Science and Technology in Introduction to Polymer Science, *Prentice Hall* (2014).

(4) Donth, E.-J., Relaxation and thermodynamics of polymers: Glass transition, *Akademie Verlag Berlin* (1992).

(5) Ciferri, A., Liquid crystallinity in polymers : principles and fundamental properties, *VCH Publishers* (1991).

(6) Boyd, R.H.; Phillips, P.J., The Science of Polymer Molecules, *Cambridge Solid State Science Series* (1996).

(7) Watts, B.; Swaraj, S.; Nordlund, D.; Lüning, J.; Ade, H. *The Journal of Chemical Physics* **2011**, *134 (2)*, 024702.

(8) Shirakawa, H.; Louis, E.J.; MacDiarmid, A.G.; Chiang, C.K.; Heeger, A.J. *Journal of the Chemical Society, Chemical Communications* **1977**, *16*, 578-580.

(9) Chiang, C.K.; Fincher, C.R.; Park, Y.W.; Heeger, A.J.; Shirakawa, H.; Louis, E.J.; Gau, S.C.; MacDiarmid, A.G. *Physical Review Letters* **1977**, *39 (17)*, 1098-1101.

(10) Patil, A.O.; Heeger, A.J.; Wudl, F. *Chemical Reviews* **1988**, *88 (1)*, 183-200.

(11) Laschewsky, A. *http://www.chem.uni-potsdam.de/apc/polymer.html*.

(12) Rühe, J.; Ezquerra, T.A.; Wegner, G. *Synthetic Metals* **1989**, *28 (1)*, 177-181.

(13) Rehahn, M.; Schlüter, A.-D.; Wegner, G.; Feast, W.J. *Polymer* **1989**, *30 (6)*, 1054-1059.

(14) Bolognesi, A.; Porzio, W.; Provasoli, F.; Ezquerra, T. *Die Makromolekulare Chemie* **1993**, *194 (3)*, 817-827.

(15) Ezquerra, T.A.; Sánchez-Cuesta, M.; Ungar, G.; Feijoo, J.L.; López-Cabarcos, E. *Journal of Polymer Science Part B: Polymer Physics* **1998**, *36 (1)*, 49-54.

(16) Winokur, M.J.; Spiegel, D.; Kim, Y.; Hotta, S.; Heeger, A.J. *Synthetic Metals* **1989**, *28 (1)*, 419-426.

(17) Facchetti, A. *Chemistry of Materials* **2011**, *23 (3)*, 733-758.

(18) Heeger, A.J. *Chemical Society Reviews* **2010**, *39 (7)*, 2354-2371.

(19) Fei, Z.; Boufflet, P.; Wood, S.; Wade, J.; Moriarty, J.; Gann, E.; Ratcliff, E.L.; McNeill, C.R.; Sirringhaus, H.; Kim, J.-S.; Heeney, M. *Journal of the American Chemical Society* **2015**, *137 (21)*, 6866-6879.

(20) Li, L.; Collard, D.M. *Macromolecules* **2005**, *38 (2)*, 372-378.

(21) Günes, S.; Neugebauer, H.; Sariciftci, N.S. *Chemical Reviews* **2007**, *107 (4)*, 1324-1338.

(22) Winder, C.; Sariciftci, N.S. *Journal of Materials Chemistry* **2004**, *14 (7)*, 1077-1086.

(23) Salaneck, W.R.; Seki, K.; Kahn, A.; Pireaux, J.-J., Conjugated Polymer And Molecular Interfaces: Science And Technology For Photonic And Optoelectronic Application, *M. Dekker New York* (2002).

(24) Kittel, C., Introduction to Solid State Physics, 8th Edition, *Wiley* (2004).

(25) Kumar, D.; Sharma, R.C. *European Polymer Journal* **1998**, *34 (8)*, 1053-1060.

(26) MacDiarmid, A.G.; Mammone, R.J.; Kaner, R.B.; Porter, S.J.; Pethig, R.; Heeger, A.J.; Rosseinsky, D.R. *Philosophical Transactions of the Royal Society of London. Series A, Mathematical and Physical Sciences* **1985**, *314 (1528)*, 3-15.

(27) Zaumseil, J.; Sirringhaus, H. *Chemical Reviews* **2007**, *107 (4)*, 1296-1323.

(28) Kim, B.-G.; Ma, X.; Chen, C.; Ie, Y.; Coir, E.W.; Hashemi, H.; Aso, Y.; Green, P.F.; Kieffer, J.; Kim, J. *Advanced Functional Materials* **2013**, *23 (4)*, 439-445.

(29) Sirringhaus, H.; Brown, P.J.; Friend, R.H.; Nielsen, M.M.; Bechgaard, K.; Langeveld-Voss, B.M.W.; Spiering, A.J.H.; Janssen, R.A.J.; Meijer, E.W.; Herwig, P.; de Leeuw, D.M. *Nature* **1999**, *401 (6754)*, 685-688.

(30) Dhanabalan, A.; van Duren, J.K.J.; van Hal, P.A.; van Dongen, J.L.J.; Janssen, R.A.J. *Advanced Functional Materials* **2001**, *11 (4)*, 255-262.

(31) Feast, W.J.; Tsibouklis, J.; Pouwer, K.L.; Groenendaal, L.; Meijer, E.W. *Polymer* **1996**, *37 (22)*, 5017-5047.

(32) Grimsdale, A.C.; Leok Chan, K.; Martin, R.E.; Jokisz, P.G.; Holmes, A.B. *Chemical Reviews* **2009**, *109 (3)*, 897-1091.

(33) Cheng, Y.-J.; Yang, S.-H.; Hsu, C.-S. *Chemical Reviews* **2009**, *109 (11)*, 5868-5923.

(34) Ludwigs, S., P3HT Revisited – From Molecular Scale to Solar Cell Devices, *Springer-Verlag Berlin Heidelberg* (2014).

(35) Gargi, D.; Kline, R.J.; DeLongchamp, D.M.; Fischer, D.A.; Toney, M.F.; O'Connor, B.T. *The Journal of Physical Chemistry C* **2013**, *117 (34)*, 17421-17428.

(36) Murat, A.; Tolga, K.; Sarac, A.S. *Current Physical Chemistry* **2012**, *2 (3)*, 224-240.

(37) Li, Y., Conducting Polymers in Organic Optoelectronic Materials *Springer International Publishing Switzerland* (2015).

(38) Chandrasekhar, P., Conducting Polymers, Fundamentals and Applications: A Practical Approach, *Springer US* (1999).

(39) Scharber, M.C.; Sariciftci, N.S. *Progress in Polymer Science* **2013**, *38 (12)*, 1929-1940.

(40) Hill, I.G.; Kahn, A.; Soos, Z.G.; Pascal, J.R.A. *Chemical Physics Letters* **2000**, *327 (3–4)*, 181-188.

(41) Rebollar, E.; Perez, S.; Hernandez, J.J.; Martin-Fabiani, I.; Rueda, D.R.; Ezquerra, T.A.; Castillejo, M. *Langmuir* **2011**, *27 (9)*, 5596-5606.

(42) García-Valverde, R.; Cherni, J.A.; Urbina, A. *Progress in Photovoltaics: Research and Applications* **2010**, *18 (7)*, 535-558.
(43) Mayer, A.C.; Scully, S.R.; Hardin, B.E.; Rowell, M.W.; McGehee, M.D. *Materials Today* **2007**, *10 (11)*, 28-33.
(44) Steim, R.; Kogler, F.R.; Brabec, C.J. *Journal of Materials Chemistry* **2010**, *20 (13)*, 2499-2512.
(45) Hoppe, H.; Sariciftci, N.S. *Journal of Materials Research* **2004**, *19 (7)*, 1924-1945.
(46) Rostalski, J.; Meissner, D. *Solar Energy Materials and Solar Cells* **2000**, *61 (1)*, 87-95.
(47) Parker, I.D. *Journal of Applied Physics* **1994**, *75 (3)*, 1656-1666.
(48) Brabec, C.J.; Cravino, A.; Meissner, D.; Sariciftci, N.S.; Fromherz, T.; Rispens, M.T.; Sanchez, L.; Hummelen, J.C. *Advanced Functional Materials* **2001**, *11 (5)*, 374-380.
(49) Tada, A.; Geng, Y.; Wei, Q.; Hashimoto, K.; Tajima, K. *Nature Materials* **2011**, *10 (6)*, 450-455.
(50) Treat, N.D.; Shuttle, C.G.; Toney, M.F.; Hawker, C.J.; Chabinyc, M.L. *Journal of Materials Chemistry* **2011**, *21 (39)*, 15224-15231.
(51) Wang, M.; Wudl, F. *Journal of Materials Chemistry* **2012**, *22 (46)*, 24297-24314.
(52) Aryal, M.; Buyukserin, F.; Mielczarek, K.; Zhao, X.M.; Gao, J.M.; Zakhidov, A.; Hu, W. *Journal of Vacuum Science & Technology B* **2008**, *26 (6)*, 2562-2566
(53) Aryal, M.; Trivedi, K.; Hu, W. *ACS Nano* **2009**, *3 (10)*, 3085-3090.
(54) Hu, J.; Shirai, Y.; Han, L.; Wakayama, Y. *Nanoscale Research Letters* **2012**, *7 (1)*, 469.
(55) Tumbleston, J.R.; Gadisa, A.; Liu, Y.; Collins, B.A.; Samulski, E.T.; Lopez, R.; Ade, H. *ACS Applied Materials & Interfaces* **2013**, *5 (16)*, 8225-8230.
(56) Yang, Y.; Mielczarek, K.; Aryal, M.; Zakhidov, A.; Hu, W. *ACS Nano* **2012**, *6 (4)*, 2877–2892.
(57) Yang, Y.; Mielczarek, K.; Aryal, M.; Zakhidov, A.; Hu, W. *Nanoscale* **2014**, *6 (13)*, 7576-7584.
(58) Martín-Fabiani, I.; Riedel, S.; Rueda, D.R.; Siegel, J.; Boneberg, J.; Ezquerra, T.A.; Nogales, A. *Langmuir* **2014**, *30 (29)*, 8973-8979.
(59) Martín-Fabiani, I.; Siegel, J.; Riedel, S.; Boneberg, J.; Ezquerra, T.A.; Nogales, A. *ACS Applied Materials & Interfaces* **2013**, *5 (21)*, 11402-11408.
(60) Rebollar, E.; Pérez, S.; Hernández, J.J.; Martín-Fabiani, I.; Rueda, D.R.; Ezquerra, T.A.; Castillejo, M. *Langmuir* **2011**, *27 (9)*, 5596-5606.
(61) Martin-Fabiani, I.; Rebollar, E.; Perez, S.; Rueda, D.R.; Garcia-Gutierrez, M.C.; Szymczyk, A.; Roslaniec, Z.; Castillejo, M.; Ezquerra, T.A. *Langmuir* **2012**, *28 (20)*, 7938-7945.
(62) Birnbaum, M. *Journal of Applied Physics* **1965**, *36 (11)*, 3688-3689.
(63) Rebollar, E.; Hernández, M.; Sanz, M.; Pérez, S.; Ezquerra, T.A.; Castillejo, M. *Journal of Applied Polymer Science* **2015**, *132 (45)*, 42770.

(64) Rebollar, E.; Castillejo, M.; Ezquerra, T.A. *European Polymer Journal* **2015**, *73*, 162-174.
(65) Reif, J.; Varlamova, O.; Ratzke, M.; Schade, M.; Leipner, H.S.; Arguirov, T. *Applied Physics A* **2010**, *101 (2)*, 361-365.
(66) Sanz, M.; Rebollar, E.; Ganeev, R.A.; Castillejo, M. *Applied Surface Science* **2013**, *278*, 325-329.
(67) Csete, M.; Hild, S.; Plettl, A.; Ziemann, P.; Bor, Z.; Marti, O. *Thin Solid Films* **2004**, *453–454*, 114-120.
(68) Rebollar, E.; Vazquez de Aldana, J.R.; Martin-Fabiani, I.; Hernandez, M.; Rueda, D.R.; Ezquerra, T.A.; Domingo, C.; Moreno, P.; Castillejo, M. *Physical Chemistry Chemical Physics* **2013**, *15 (27)*, 11287-11298.
(69) Rebollar, E.; Aldana, J.R.V.d.; Pérez-Hernández, J.A.; Ezquerra, T.A.; Moreno, P.; Castillejo, M. *Applied Physics Letters* **2012**, *100 (4)*, 041106.
(70) Sipe, J.E.; Young, J.F.; Preston, J.S.; van Driel, H.M. *Physical Review B* **1983**, *27 (2)*, 1141-1154.
(71) Rebollar, E.; Frischauf, I.; Olbrich, M.; Peterbauer, T.; Hering, S.; Preiner, J.; Hinterdorfer, P.; Romanin, C.; Heitz, J. *Biomaterials* **2008**, *29 (12)*, 1796-1806.
(72) Rebollar, E.; Perez, S.; Hernandez, M.; Domingo, C.; Martin, M.; Ezquerra, T.A.; Garcia-Ruiz, J.P.; Castillejo, M. *Physical Chemistry Chemical Physics* **2014**, *16 (33)*, 17551-17559.
(73) Rebollar, E.; Sanz, M.; Perez, S.; Hernandez, M.; Martin-Fabiani, I.; Rueda, D.R.; Ezquerra, T.A.; Domingo, C.; Castillejo, M. *Physical Chemistry Chemical Physics* **2012**, *14 (45)*, 15699-15705.

Chapter 2. Materials and Methods

2.1. Materials

2.1.1. Poly(3-hexylthiophene-2,5-diyl) (P3HT)

P3HT is a conjugated semiconducting polymer (p-type) which is soluble up to concentrations as high as 50 g/L in chlorinated solvents such as chloroform, chlorobenzene, dichlorobenzene and trichlorobenzene.[1, 2] The presence of lateral chains makes the polymer melt processable and also regioselective[3] (Figure 2.1).

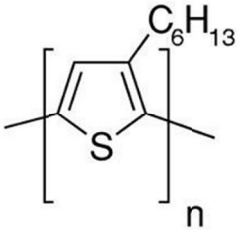

Figure 2.1. Chemical structure of P3HT.

P3HT has a T_g of about 10-12 ºC, a phase transition corresponding to the side chains melting at about 60 ºC and a T_m of about 230 ºC, as determined by calorimetry.[4-6] Electrical properties of P3HT depend strongly on the ordering of the polymer chains. Regioregular P3HT (RR-P3HT) gives rise to semicrystalline phases with ordered chains, longer conjugation length and higher crystallinity. P3HT presents a high hole mobility as a result of the low HOMO and LUMO energy levels. In this thesis, P3HT has been purchased from Ossila with the following characteristics: M_w= 34100 g/mol, M_n= 19500 g/mol, PDI = 1.7, regioregularity = 94.7%.

2.1.2. Poly[N-9'-heptadecanyl-2,7-carbazole-alt-5,5-(4',7'-di-2-thienyl-2',1',3'-benzothiadiazole)] (PCDTBT)

PCDTBT is a semiconducting polymer mainly amorphous under most of processing conditions and it has ambipolar electronic properties. As it is shown in Figure 2.2, chemical structure of PCDTBT is composed by the alternation of a carbazole derivative which is a donor unit (electron-rich) and benzothiadiazole unit which is an electron acceptor (electron-deficient).[7] PCDTBT was developed as donor material for organic photovoltaics to produce better efficiencies and lifetimes.[8] The key properties of PCDTBT result from the lower HOMO/LUMO levels which lead to advantages over

standard organic photovoltaic materials of increased open circuit voltage, longer wavelength absorption and improved stability under ambient conditions.[8] PCDTBT has a T_g of about 130 ºC and melts into a liquid crystalline state at around 268 °C and upon subsequent cooling can eventually recrystallize at around 259 °C.[9, 10]

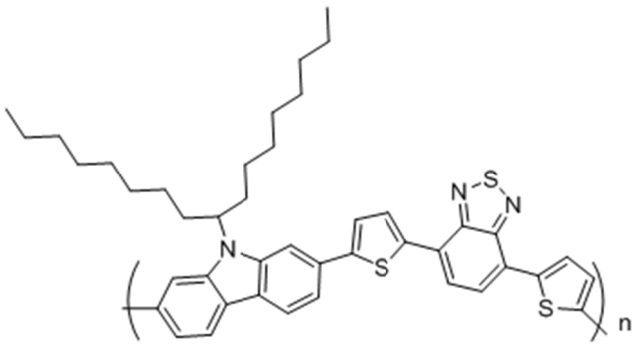

Figure 2.2. Chemical structure of PCDTBT.

In this thesis, PCDTBT has been purchased from Ossila with the following characteristics: M_w= 35400 g/mol, M_n=14750 g/mol, PDI = 2.4.

2.1.3. Poly(3,4-ethylenedioxythiophene) polystyrene sulfonate (PEDOT:PSS)

PEDOT:PSS is a polyelectrolyte consisting of a mixture of two ionomers (Figure 2.3). This polymer is transparent to visible light and conducting when prepared as a thin film. Due to its unique combination of conductivity, transparency, ductility, and ease of processing, PEDOT:PSS has become a benchmark material in thin-film electronic fabrication.[11] This polymer can be used as an interfacial layer for hole transport in organic light emitting diodes, organic photovoltaics, and perovskite photovoltaics.[12]

In this thesis, PEDOT:PSS has been purchased from Ossila with the following characteristics: Heraeus Clevios PH1000 PEDOT:PSS.

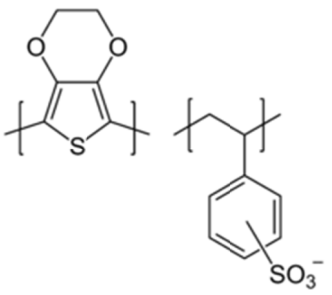

Figure 2.3. Chemical structure of PEDOT:PSS.

2.1.4. Phenyl-C71-butyric acid methyl ester ($PC_{71}BM$)

Fullerene derivatives like $PC_{71}BM$ (Figure 2.4) are n-type organic semiconductors commonly used as electron accepting material in organic photovoltaic devices.[13, 14] Its good solubility enables one to dissolve it in common solvents used to dissolve donor polymers.

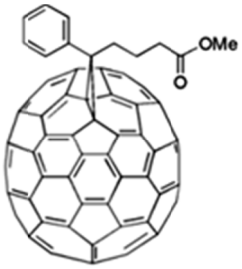

Figure 2.4. Chemical structure of $PC_{71}BM$.

In this thesis, $PC_{71}BM$ with a molecular weight of 1031 g/mol has been purchased from Ossila with purity higher than 99%.

2.2. Experimental Methods

2.2.1. Thin film preparation by spin-coating

Spin-coating method is a relatively simple, fast and low cost way to prepare thin films.[15, 16] This method, as schematically described in Figure 2.5, can be divided in three stages. First of all, a fixed amount of polymer solution is dropped on a substrate placed in the center of a rotating metallic horizontal plate by using a pipette. Immediately, the substrate is accelerated to the desired rotation rate. During this fast rotation the solvent is evaporated and a thin film remains on the substrate. Thicknesses obtained basically depend on the solution concentration and the rotation rate.

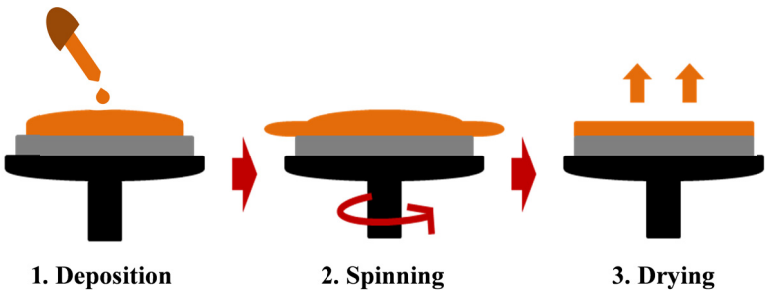

Figure 2.5. Scheme of the spin-coating technique for thin polymer film preparation.

2.2.2. Nanostructuring with Laser-Induced Periodic Surface Structures (LIPSS)

Laser irradiation was carried out under ambient air conditions at normal incidence with a linearly polarized laser beam of a Q-switched Nd:YAG laser (Lotis TII LS-2131M, pulse duration of 8 ns full width half-maximun). Two wavelengths have been employed by using the second (532 nm) and fourth harmonic (266 nm) of the laser. The repetition rate can be changed from 1 to 10 Hz. In a typical LIPSS experiment as presented in Figure 2.6 the beam is directed to the sample using a dichroic mirror and the laser energy is tuned using a variable attenuator. The irradiation fluences were determined by measuring the laser energy in front of the sample with a joulemeter (Gentec-E, QE25SP-H-MB-D0) and considering 5 mm as the diameter of the laser spot.

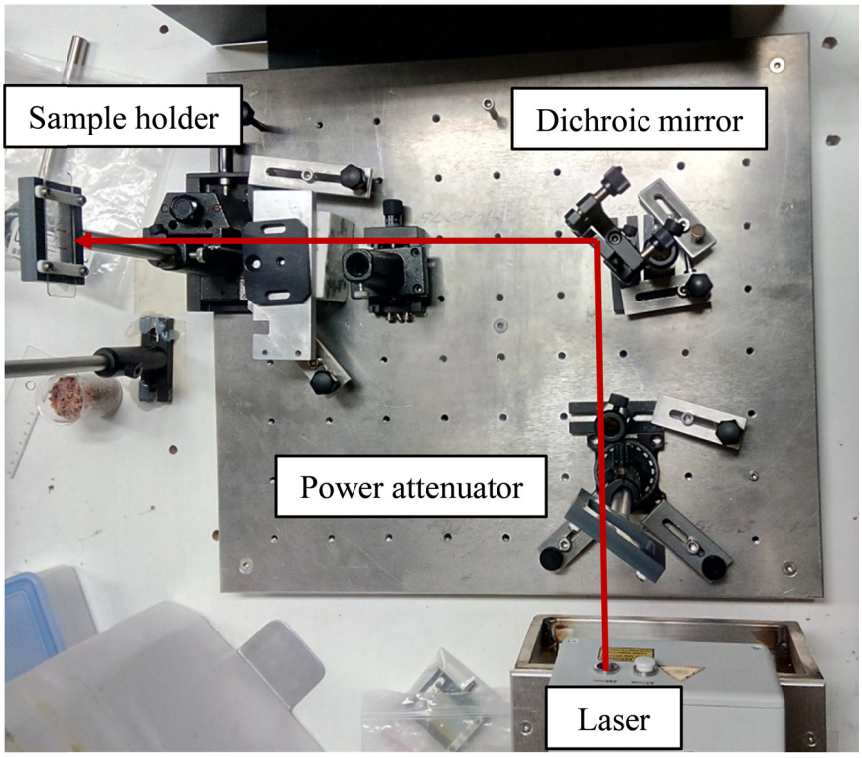

Figure 2.6. Scheme of a LIPSS experiment.

2.2.3. Atomic Force Microscopy

Atomic Force Microscopy (AFM) is a technique based on the interaction between a tip and the surface of one material.[17] In 1986, Binnig, Quale and Geber adapted the conventional Scanning Tunneling Microscope (STM) -which is limited to measure

conductive samples- to study non-conducting samples. This discovery, together with the already known STM has contributed to the development of the Nanotechnology.[18] It allows obtaining at nanometric scale the surface topography of all types of samples: metals, semiconductors as well as insulators.

As represented in Figure 2.7, the AFM uses a cantilever with a nanometric tip attached at the end to scan the surface of the sample. The sample is mounted on a piezoelectric scanner, which allows a precise scanning of the sample.[17]

When an AFM is operating, the interaction forces between the tip and the surface causes the cantilever deflection. There are mainly three methods for establishing the forces between a tip and a sample: contact, non-contact and tapping modes.[17, 19]

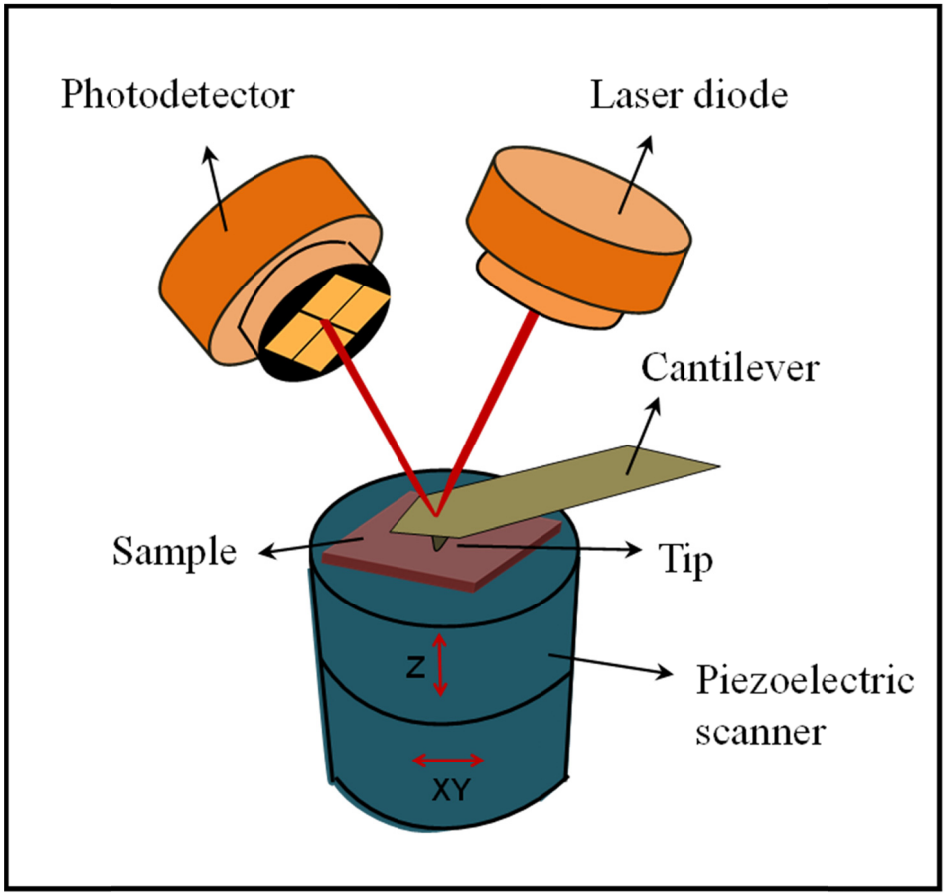

Figure 2.7. Scheme of an Atomic Force Microscopy (AFM) setup

2.2.3.1. Contact mode

The AFM tip makes physical contact with the sample using a cantilever with a low spring constant. When the tip scans the sample, the repulsive force causes the cantilever

deflection. This deflection depends on the surface topography of the sample. Contact mode is typically used for investigating hard samples, such as metals. The cantilevers are usually made of silicon (Si) or silicon nitride (Si_3N_4), with typical resonant frequencies of 50 kHz and force constants below 1 N/m.

2.2.3.2. Non-contact mode

In non-contact mode, attractive Van der Waals forces acting between the tip and the sample are detected, and topographic images are constructed by scanning the sample with the tip above the surface. The attractive forces from the sample are substantially weaker than the forces used by contact mode.

2.2.3.3. Tapping mode

In tapping mode, the cantilever is oscillating at a constant frequency which is called resonance frequency. The oscillation amplitude is measured as a root mean square value of the deflection signal. The feedback system is set to detect the perturbation of the oscillation amplitude caused by the intermittent contact with the surface.[19] The tapping mode is more sensitive to the interaction of the tip with the surface since when the vibrating tip reaches the surface, the involved forces are not only repulsive, but also adhesive and capillary among others. So the interaction between the tip and the sample surface produces changes in the frequency as well as in the phase. This mode of operation is referred to as phase contrast imaging mode and it works simultaneously to the topography imaging.

The state of the art of AFM techniques has driven to the development of some extensions of AFM to get information about a large amount of physical properties, such as nanomechanical, nanoelectrical, ferroelectrics and dielectrics.[19]

In this thesis, atomic force microscopy measurements were carried out under ambient conditions using a commercial scanning probe microscope (MultiMode 8 equipped with the Nanoscope V controller, Bruker). The topography AFM images were collected in tapping mode using silicon probes (NSG30 probes by NT-MDT). Roughness, thicknesses, heights and periods of the nanostructures were measured in three different zones of the sample and analyzed by Nanoscope Analysis 1.50 software (Bruker).

2.2.4. Conductive Atomic Force Microscopy

Conductive Atomic Force Microscopy (C-AFM) is a technique that uses a conducting AFM tip to measure local current images in contact mode. Typical C-AFM setup as shown in Figure 2.8 requires a direct electric contact between the sample and the tip to ensure a correct measurement of the current and to characterize conductivity variations in conducting materials.[20] The potential of this technique is to measure and map current in the 2 pA to 1 μA range while simultaneously collecting topographic information.

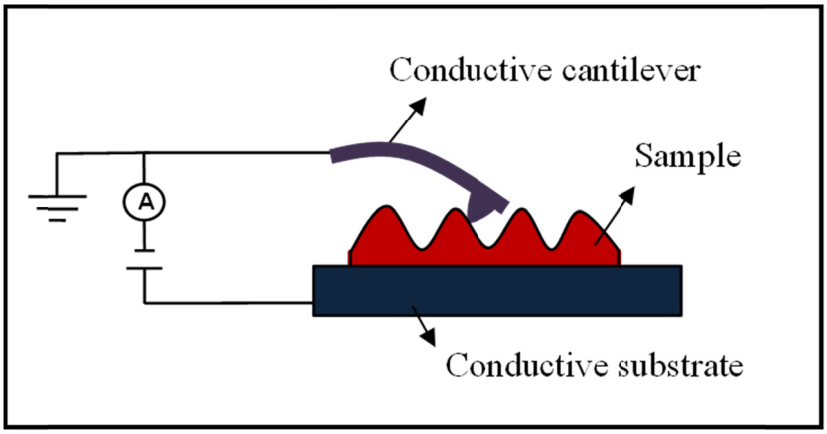

Figure 2.8. Conductive AFM setup.

Basically, C-AFM instrumentation is the same than conventional AFM but it needs to be equipped with a specific module in order to apply a voltage between the tip and the substrate. Moreover, the current is detected using a current-to-voltage preamplifier.[21] The applied voltage is in the range from -10 V to 10 V.

In this thesis, the C-AFM measurements were carried out using the same microscope mentioned above equipped with a C-AFM module. The microscope was used in contact mode, keeping a constant deflection of 0.3 V to avoid sample damage. To ensure electrical contact, the samples were glued to the conducting substrate by epoxy resin (Chemtronics, CW 2400). Silicon (Si) probes coated with a conductive Pt-Ir layer and a low spring constant, k = 0.2 N/m, (SCM-PIC by Bruker) were used to characterize the electrical properties of different semiconducting materials. The bias was applied to the conducting substrate, and the current was measured by a preamplifier.[20]

2.2.5. UV-visible absorption spectroscopy

When the light passes through a material, the amount of light absorbed is the difference between the incident radiation (I_0) and the transmitted one (I). The amount of light absorbed is expressed as either transmittance (T) or absorbance (A) and it is defined as follows:

$$T = I/I_0 \tag{2.1}$$

$$A = -\log T \tag{2.2}$$

The amount of light absorbed is proportional to the concentration of absorbing species by means of the Lambert Beer law: [22]

$$A = -\log(I/I_0) = \varepsilon b \boldsymbol{c} \tag{2.3}$$

where ε is the molar absorption coefficient, b is the path length of the beam through the material and $\boldsymbol{c}$ the concentration of absorbing species.
For solid materials such as thin films, the Lambert- Beer law takes the form:

$$A = -\log(I/I_0) = \boldsymbol{\alpha}\rho t = \boldsymbol{\mu} t \tag{2.4}$$

being $\boldsymbol{\alpha}$ the mass absorption coefficient which is characteristic of each material and depends on the light wavelength, ρ the mass density and t is the thickness of the sample. Mass absorption coefficient can be calculated knowing the thickness and density of the material. By multiplying the mass absorption density by the mass density it is possible to obtain the linear absorption coefficient ($\boldsymbol{\mu}$) which is often reported.

Ultraviolet-visible (UV-vis) absorption spectroscopy characterizes transitions between electronic energy levels. Since the energy levels of matter are quantized, only light with the precise amount of energy can be absorbed producing transitions from fundamental level to excited states. In the practice, UV-vis spectroscopy is an easy way to analyze the absorbing species of unknown samples.[23]

UV-vis spectroscopy has been used for characterizing conjugated polymers because LIPSS fabrication requires a strong absorption at the laser irradiation wavelength and therefore a previous knowledge of the absorption coefficient of the pristine materials at each wavelength is necessary.

In this Thesis, a UV-Vis-NIR spectrophotometer (UV-3600 Shimadzu), which is a double beam instrument, interfaced to a personal computer loaded with the UV-Probe software was used. A baseline was taken by using an empty substrate as reference. In order to avoid the substrate absorption in the UV range, thin polymer films were spin-coated onto quartz substrates. All measurements were carried out from 200 nm to 800 nm.

2.2.6. Raman spectroscopy

Raman spectroscopy is a chemical sensitive technique based on the inelastic scattering of a photon by molecules, providing information about molecular vibration modes[24] and can be a complementary technique to IR spectroscopy. One disadvantage of the Raman spectroscopy is that the Raman scattering is very weak and thus it was required to wait for the development of laser sources in the 1960s to fabricate simplified Raman spectroscopy instruments and to boost the sensitivity of the technique. Some advantages such as the easy sample preparation and high sensitivity make Raman spectroscopy a powerful technique to characterize chemical compounds. The Raman effect can be enhanced when using excitation wavelengths in which the material has a strong absorption. This effect is known as resonance Raman effect and gives rise to a more intense Raman spectrum of the absorbing species present in the sample.[25]

In this thesis, Raman spectroscopy was accomplished by using a Renishaw Raman InVia Reflex Spectrophotometer, equipped with a Leica Microscope and an electrically refrigerated CCD camera, with excitation lines at 442 nm (HeCd laser), 532 nm (Nd:YAG laser), and 785 nm (diode laser). The spectra were acquired with a spectral resolution of 2 cm^{-1} using a 50× objective providing a spot with a diameter of about 1 μm on the samples. Laser power conditions were those that ensured the integrity of the material.

2.2.7. Synchrotron Radiation

2.2.7.1. General concepts of X-rays

X-rays are electromagnetic radiation with a wavelength, λ, in the range from 0.01 nm to 25 nm. When X-rays interact with matter two main processes may occur: absorption and scattering. In the case of ordered matter it acts as a diffraction lattice when interacting

with X-rays.[26] In Figure 2.9 a scheme of a standard scattering experiment in transmission geometry is shown.

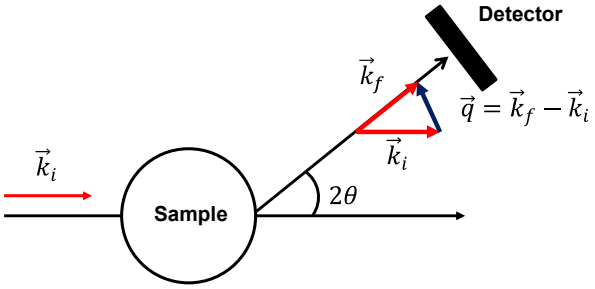

Figure 2.9. Scheme of an X-ray scattering experiment in transmission geometry.

In an X-ray scattering experiment, the scattering vector $\vec{q}$ is defined as:

$$\vec{q} = \vec{k}_f - \vec{k}_i \tag{2.5}$$

Where $\vec{k}_i$ and $\vec{k}_f$ represent the incident and scattered wave vectors respectively. In the case of elastic scattering, the modulus of the incident and scattered wave vectors do not change and are defined by equation 2.6.

$$\left|\vec{k}_f\right| = \left|\vec{k}_i\right| = \frac{2\pi}{\lambda} \tag{2.6}$$

According to the Bragg's law (Figure 2.10), the interplanar distance, d, and the scattering angle 2θ are related by:

$$n\lambda = 2d \sin\theta \tag{2.7}$$

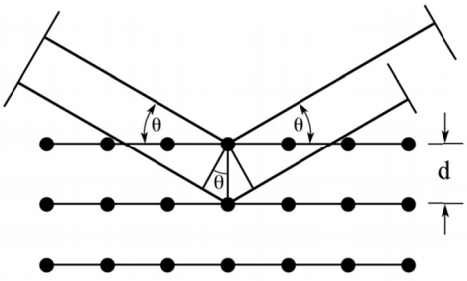

Figure 2.10. Geometry of the Bragg's law.

In addition, the module of the scattering vector, q, can be defined by:

$$q = \frac{4\pi}{\lambda}\sin\theta \tag{2.8}$$

The module of the scattering vector can be also related to the distances between planes, d_{hkl} :

$$q = \frac{2\pi}{d_{hkl}} \tag{2.9}$$

One essential condition to develop a constructive interference is that the scattering vector $\vec{q}$ coincides with some reciprocal space vector ($\vec{a}^*, \vec{b}^*\ \vec{c}^*$) as follows:

$$\vec{q} = h\vec{a}^* + k\vec{b}^* + l\vec{c}^* \tag{2.10}$$

When a plane family satisfies the Laue condition (Equation 2.10), it produces a coherent scattering of the radiation with an angle which will be inversely proportional to the interplanar distances and directly proportional to the wavelength. As a consequence, at a given wavelength the regularly ordered motifs separated by bigger distances will scatter at lower angles. Therefore, by varying the experimental conditions (sample-detector distance as shown in Figure 2.11) it is possible to achieve information about different angles (2θ), and therefore about the structure at different length scales.

Due to the hierarchical nature of the polymer materials, X-rays scattering experiments are ideal for their characterization at different structural levels. Collecting the scattered intensity at wide angles, typically ($2\theta > 1^{o}$) provides information about the internal structure of the crystalline domains. This experiment is known as Wide Angle X-ray Scattering (WAXS). On the other hand, the scattered intensity at small angles typically ($2\theta < 0.3^{o}$), collected by the detector situated far away from the sample position allows accessing to larger correlation distances. With this set-up the experiment is known as Small Angle X-ray Scattering (SAXS).

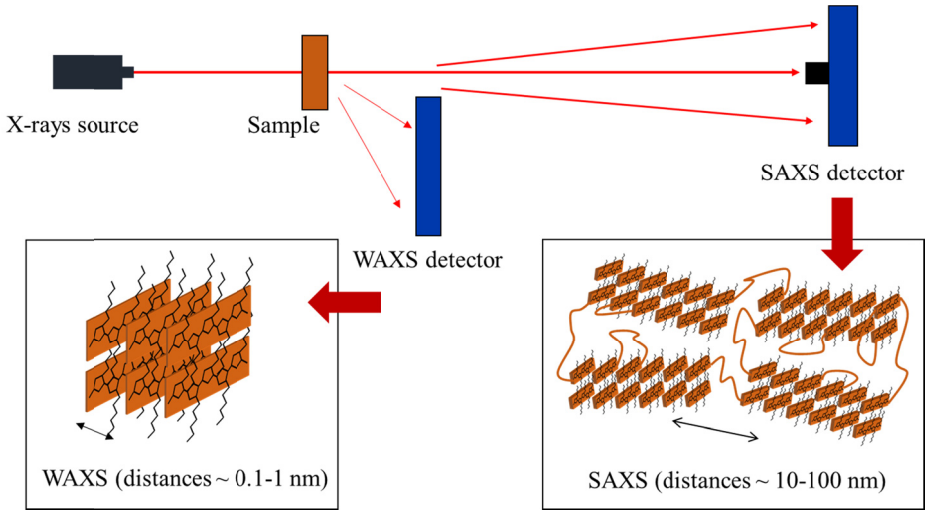

Figure 2.11. Typical set-up of a Small and Wide Angle X-ray Scattering experiment.[27] The cartoon illustrates characteristic length scales of polymers.

2.2.7.2. Source and characteristics of synchrotron radiation

Conventional X-rays sources can be used to generate monochromatic X-rays at given wavelengths. For instance, the Cu K-line generates X-rays with energy around 1 KeV. However, in a synchrotron source it is possible to generate X- rays in a broad region of the electromagnetic spectrum.[28] Considering the electromagnetic spectrum[26] (Figure 2.12), the X-rays range can be separated in two regions: the lowest energy region (200 eV < E < 3 keV) referred to as soft X-rays region and the highest energy region known as hard X-rays region (3 keV < E < 100 keV).

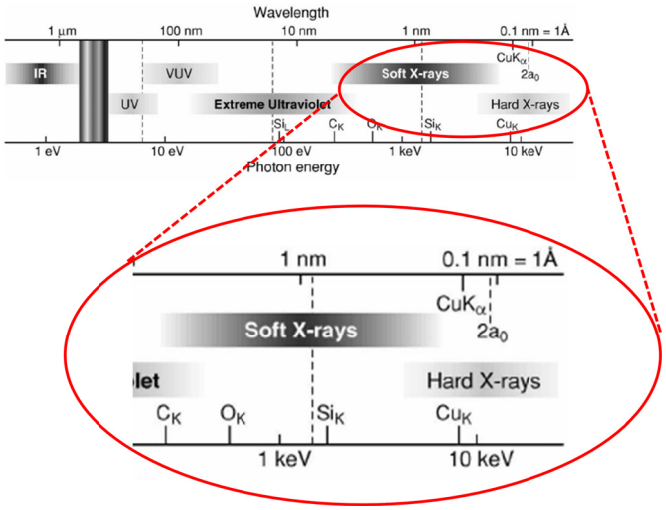

Figure 2.12. Electromagnetic spectral region covered by the synchrotron radiation.[26]

Nowadays, synchrotron radiation is produced in large facilities whose scheme is shown in Figure 2.13.[29-31] Electrons generated from an electron gun are accelerated in a linear accelerator (LINAC). When the accelerated electrons have enough energy they are moved into a circular ring called booster synchrotron. In this ring, the energy of electrons increases from about 250 MeV to several GeV depending on the critical energy of the synchrotron and the speed increases to almost the speed of light. Once the electrons reach the required energy, they are injected into the storage ring. In the storage ring electrons circulate for several hours and can deliver photons when the bending magnets change the direction of the electrons. Additionally, other insertion devices such as undulators and wigglers are used to produce a specific radiation that finally is guided into the corresponding beamlines.[32]

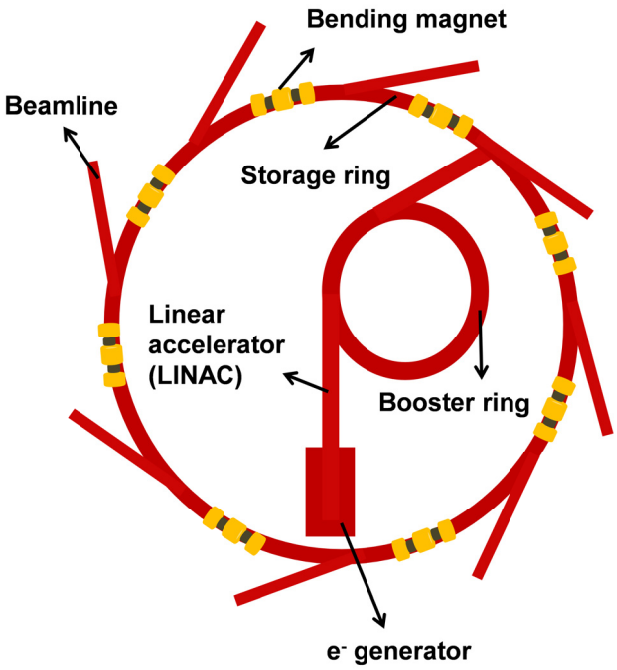

Figure 2.13. Scheme of a synchrotron radiation facility with its main components.

Some characteristics of the synchrotron light are:[28] (1) a very high brilliance, several orders of magnitude higher than those X-rays produced in conventional X-ray tubes, (2) a high level of polarization (linear, elliptical or circular), (3) high collimation (small angular divergence of the beam), (4) low emittance, i.e. the product of source cross section and solid angle of emission is small, (5) wide tunability in energy/wavelength by appropriate monochromatization.

2.2.7.3. Synchrotron techniques used in this thesis

(A) Near Edge X-ray Absorption Fine Structure

Near Edge X-ray Absorption Fine Structure (NEXAFS) is an X-ray absorption spectroscopy technique in which a core electron is excited into empty states near the photo-ionization threshold.[33] It is thus inherently element specific due to the specific elemental binding energies of core electrons. In addition, due to the close relationship between molecular bonding and the structure of the empty electronic states, NEXAFS is very sensitive to the detailed chemical structure of the sample. Polymers as organic components are widely studied in the carbon K-edge (280-320 eV). The energy levels implicated in a NEXAFS spectrum are associated to transitions from the core electrons of the carbon atom (1s) to non-bonding molecular levels (σ^*, π^*).[33] The chemical sensitivity is achieved due to the fact that different bonds have different energies and thus the transitions appear at different energies in the spectrum. It is worth noting that according to the molecular orbitals theory, in a molecule the inner orbitals do not contribute to the bond, so they may be considered as atomic orbitals. In the same way that other absorption spectroscopies such as UV-visible or IR spectroscopies, X- ray absorption spectroscopy can also give information about the chemical bonds and therefore to be chemically sensitive. Since the electronic structure and bonding of carbon are very diverse, the C 1s edge offers the best capability to spectrally differentiate chemical species. However, one should remember that there are NEXAFS spectra associated with the core edges of every element in a sample, and in many cases, other edges provide complementary information or even advantages over C 1s NEXAFS.

This NEXAFS technique can be used in different working modes[33] as described below and illustrated in Figure 2.14.

- **Transmission mode (**Figure 2.14.a): this is the conventional working mode for NEXAFS. The incident and transmitted intensity are measured. According to the Lambert-Beer law, the absorbance is directly proportional to the absorption coefficient and the thickness.

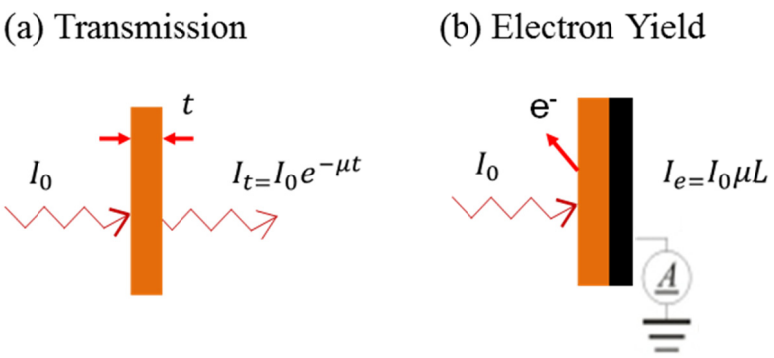

Figure 2.14. Working modes in Near Edge X-ray Absorption Fine Structure (NEXAFS) spectroscopy.[33] (a) Transmission and (b) electron yield modes.

- **Electron Yield mode (**Figure 2.14.b): in this case, the absorbed X-ray intensity is not measured directly, but instead the photoelectrons that are created by the absorbed X-rays. In general, X-rays are absorbed through excitations of core electrons to empty states above the vacuum or Fermi level. The created holes are then filled by Auger decay which consists in the electronic transition from a less bound shell to the created hole. The energy difference is transferred to other bound electrons which can then escape from the atom. These outgoing electrons are referred to as Auger electrons. The intensity of the emitted primary Auger electrons is a direct measurement of the X-ray absorption process and is used in the so-called Auger Electron Yield (AEY) measurements, which are highly surface sensitive.[33] As primary Auger electrons leave the sample, they create scattered secondary electrons which dominate the Total Electron Yield (TEY) intensity. Electrons created deeper in the sample lose too much energy to overcome the work function of the sample and therefore do not contribute to the TEY. The sampling depth in TEY measurements is typically a few nanometers, while it is often less than 1 nm for AEY measurements.

(B) Scanning Transmission X-ray Microscopy

Scanning Transmission X-ray Microscopy (STXM) is a powerful synchrotron-based technique that combines NEXAFS spectroscopy and microscopy, providing a high chemical sensitivity together with imaging capabilities at the nanoscale. In a scanning transmission X-ray microscope, images are obtained by mechanically raster scanning the sample through the focal point of a zone plate X-ray lens.[34, 35] STXM can quantitatively map the chemical composition of organic films with nanoscale resolution.

The STXM images can provide information on the domain sizes, shapes, and purities of thin film polymer blends with a spatial resolution of ~ 20 nm.[36]

In order to obtain quantitative chemical composition maps of a blend the Singular Value Decomposition (SVD) mathematical procedure has been used.[36] SVD requires previous knowledge of the mass absorption coefficients of the blend components. The transmitted X-ray intensity measured was converted to an X-ray optical density (OD) by means of Lambert Beer law:

$$OD = -\log\frac{I}{I_0} \tag{2.11}$$

where I is the transmitted X-ray intensity and I_0 is the incident X-ray intensity. Optical density (OD) is also related to the absorption coefficient as:

$$OD = \boldsymbol{\mu} t = \boldsymbol{\alpha}\rho t \tag{2.12}$$

where $\boldsymbol{\mu}$ is the linear absorption coefficient, and t the sample thickness. It is possible to determine the mass absorption coefficient, $\boldsymbol{\alpha}$, by normalizing the absorption by the mass density (ρ).

The SVD procedure also requires a series of images acquired at a number of energies that equal or exceed the number of compositional components. STXM images of the same area at selected energies can be transformed into thickness maps quantifying the composition of the sample in each pixel.[34, 37, 38]

$$\begin{pmatrix} OD^{E1} \\ OD^{E2} \\ OD^{E3} \\ OD^{E4} \end{pmatrix} = \begin{pmatrix} \boldsymbol{\alpha}_i^{E1} & \boldsymbol{\alpha}_j^{E1} \\ \boldsymbol{\alpha}_i^{E2} & \boldsymbol{\alpha}_j^{E2} \\ \boldsymbol{\alpha}_i^{E3} & \boldsymbol{\alpha}_j^{E3} \\ \boldsymbol{\alpha}_i^{E4} & \boldsymbol{\alpha}_j^{E4} \end{pmatrix} \begin{pmatrix} t_i \\ t_j \end{pmatrix} \tag{2.13}$$

In equation 2.13 the optical density at each energy (OD^{E1}) is obtained from a STXM image and the absorption coefficients of the individual components of the blend $\boldsymbol{\alpha}_i^{E1}$ and $\boldsymbol{\alpha}_j^{E1}$ are mandatory conditions to calculate the thicknesses map. Hence, the aim of the SVD procedure is to calculate the thicknesses, t_i and t_j, in each pixel in order to make the thicknesses map of each component. Finally, thickness compositional maps at

each pixel (X_i) can be obtained dividing the thickness of each component (t_i) by the total thickness (t_t).

$$X_i = \frac{t_i}{t_t} \tag{2.14}$$

(C) Grazing Incidence X-ray Scattering

Due to the nature of some samples investigated in this thesis, namely polymer thin films on silicon substrates, it was necessary to perform X-ray scattering experiments in grazing incidence geometry.[39-41]

In contrast to standard X-ray scattering experiments in transmission geometry, Grazing Incidence X-ray Scattering (GIXS) experiments are performed in reflection geometry. As X-rays laboratory sources are very limited in both brilliance and energy, the potential of GIXS is accomplished when using synchrotron radiation in combination with two-dimensional detectors.[39] Although similarities with transmission geometry are obvious, the presence of an incident angle introduces some geometrical modifications which are schematized in Figure 2.15.

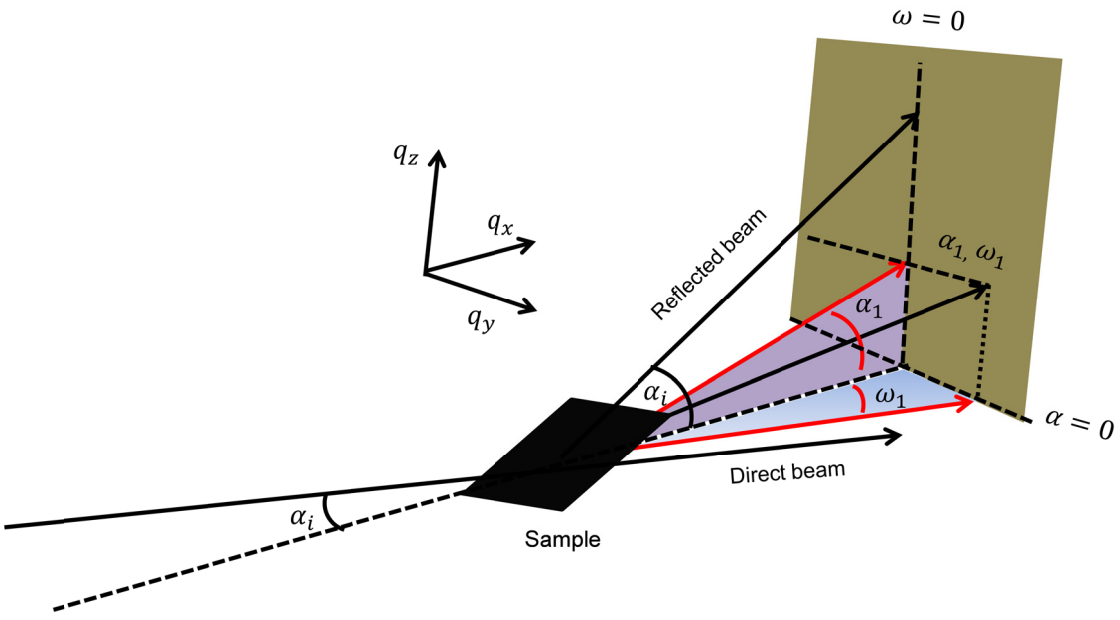

Figure 2.15. Scheme of a typical set-up for Grazing Incidence X-ray Scattering (GIXS) experiments.

When X-rays interact with a sample tilted with an incidence angle, α_i, X-rays can be transmitted, specularly reflected and scattered. With this geometry two exit angles (α, ω) are required to define the scattering vector. Correlations along the y-axis (at a constant angle α) give information about the lateral structures in the plane of the sample. On the contrary, correlations along the z-axis are related to structures along the depth of the sample.[39]

In this geometry, the scattering wave vector is defined by:

$$\vec{q} = (q_x, q_y, q_z) \tag{2.15}$$

With the components:

$$q_x = \frac{2\pi}{\lambda}[\cos(\omega)\cos(\alpha) - \cos(\alpha_i)] \tag{2.16.a}$$

$$q_y = \frac{2\pi}{\lambda}[\sin(\omega)\cos(\alpha)], \tag{2.16.b}$$

$$q_z = \frac{2\pi}{\lambda}[\sin(\alpha_i) + \sin(\alpha)] \tag{2.16.c}$$

In a GIXS experiment, the direct beam and specular reflected beam are often suppressed by beam stops to avoid the detector saturation as the intensity of the specular reflected beam is some orders of magnitude higher than sample scattering.

In the region of total external reflection ($\alpha_i > \alpha_{crit}$), the full depth of the sample is detected and the incident and exit angles are that small that it is sufficient a description based on one refractive index. The scattering between two media is originated basically from strong variations of the electronic density when interacting with X-rays.[39]

Thus, Grazing Incidence Small Angle X-ray Scattering (GISAXS) and Grazing Incidence Wide Angle X-ray Scattering (GIWAXS) provides structural information in the reciprocal space and can be used for the characterization of micro- and nanoscale correlations and the analysis of the crystalline phases respectively. GISAXS can be a useful complement to real space microscopy techniques such as AFM and TEM.

(D) Resonant Soft X-ray Scattering

Conventional SAXS measurements probe the scattering intensity variation at very small angles near the primary beam, as it was mentioned before. SAXS provides structural

information on the difference of the electron density at length scales from tens to hundreds of nanometers. This method yields not only information on sizes, shapes, and distributions of particles, but also on the structure of disordered and partially ordered systems. From the first Born approximation, the scattering intensity of SAXS is the modulus-squared Fourier transformation of the electron density of the sample in real space.[42] When the X-ray energy is high and far away from any absorption edges, the X-rays interact with the electrons as if they are free electrons. The scattering is essentially a sum of the scattering from all of the individual electrons. The contrast between the heterogeneities is determined by the difference in the electron density of each material. However, when the X-ray energy is tuned near the atomic absorption edge of constituent elements, for example the K absorption edge of carbon at 284 eV, the core electron is excited to an unoccupied molecular orbital, and strong resonance enhancement in the scattering intensity is observed, relative to energies far below or above this absorption edge.[43] In this case, X-rays are no longer interacting with 'free' electrons but with bound electrons. This resonance effect is analogous to the simple harmonic oscillator: the X-ray absorption and thus scattering reach the maximum when the incident X-ray energy matches the resonant frequency of the specific chemical bond. This process is elementally sensitive, as the core electron binding energy is elementally specific. Furthermore, this resonant process is also chemically sensitive, as the excited state that corresponds to an unoccupied molecular orbital is defined by the chemical bond environment. The anomalous scattering effect can be used to provide enhanced scattering intensity and chemical sensitivity of the scattering objects, thus resulting in an analytical capability of a tunable, chemically sensitive structure probe of nanoscale and mesoscale components in heterogeneous, complex materials, without the need for chemical modification.[26]

The physical basis of the contrast mechanism and the general advantages of Resonant Soft X-ray Scattering (RSoXS) have been demonstrated in the past few years.[44] The effects of the interaction of X-rays with matter are encoded in the complex refractive index, $n(\boldsymbol{E}) = 1 - \delta(\boldsymbol{E}) + i\beta(\boldsymbol{E})$, where $\boldsymbol{E}$ is the photon energy, δ is the dispersive component, and β is the absorptive component.[43, 45] Bond-specific contrast can be achieved in the same manner as done in NEXAFS spectroscopy, because δ and β change rapidly as a function of photon energy near absorption edges, and the quantity $\Delta\delta^2 + \Delta\beta^2$ determines the material contrast and scattering strength.[43]

However, the refractive indices of polymer semiconductor materials are usually unknown and must be determined whenever RSoXS experiments are performed. In the case of soft X-rays, organic materials present a strong absorption of X-rays in the region around 300 eV, providing that the absorptive component of the refractive index (β) cannot be neglected.

Typically, δ is not directly accessible. However, β can be easily determined by measuring the transmission or TEY NEXAFS spectra of the pure materials.[43, 45, 46] Thereby β is determined from the observed mass absorption coefficient $\boldsymbol{\alpha}(\boldsymbol{E})$ (Equation 2.17), where ρ denotes the mass density, h and c are Planck's constant and the speed of light, respectively:

$$\beta(\boldsymbol{E}) = \frac{\rho hc}{4\pi E}\boldsymbol{\alpha}(\boldsymbol{E}) \tag{2.17}$$

δ can be determined from β using the Kramers-Kronig relation:

$$\delta(\boldsymbol{E}) = -\frac{2}{\pi}P_C\int_0^{\infty}\frac{\beta(\boldsymbol{E'})\boldsymbol{E'}}{\boldsymbol{E'^2} - \boldsymbol{E^2}}d\boldsymbol{E'} \tag{2.18}$$

Because of the fact that samples are thin films deposited onto silicon substrates, and that some techniques used in this thesis require the use of soft X-rays, it has been necessary the use of synchrotron radiation sources. Specifically, part of this work has been performed in different beamlines located at different synchrotron radiation facilities: For hard X-rays scattering measurements, the BM26-B beamline was used (Dutch-Belgian beamline) which is a dedicated SAXS-WAXS station at the European Synchrotron Radiation Facility (ESRF). For STXM measurements, the PolLux beamline at the Swiss Light Source (SLS) was used. Lastly, RSoXS measurements were performed in the 11.0.1 beamline at the Advanced Light Source (ALS).

References

(1) Eggert Carlé, J.; Wenzel Andreasen, J.; Jørgensen, M.; Christian Krebs, F. *Solar Energy Materials and Solar Cells* **2010**, *94 (5)*, 774-780.

(2) Zhang, G.; Xu, H.; Liu, K.; Li, Y.; Yang, L.; Yang, M. *Synthetic Metals* **2010**, *160 (17–18)*, 1945-1952.

(3) Andersson, M.R.; Selse, D.; Berggren, M.; Jaervinen, H.; Hjertberg, T.; Inganaes, O.; Wennerstroem, O.; Oesterholm, J.E. *Macromolecules* **1994**, *27 (22)*, 6503-6506.

(4) Trinh Tung, N.; Duc Nghia, N.; Van Tuyen, N. *Advances in Natural Sciences: Nanoscience and Nanotechnology* **2012**, *3 (4)*, 045001.

(5) Hugger, S.; Thomann, R.; Heinzel, T.; Thurn-Albrecht, T. *Colloid and Polymer Science* **2004**, *282 (8)*, 932-938.

(6) Wu, Z.; Petzold, A.; Henze, T.; Thurn-Albrecht, T.; Lohwasser, R.H.; Sommer, M.; Thelakkat, M. *Macromolecules* **2010**, *43 (10)*, 4646-4653.

(7) Cho, S.; Seo, J.H.; Kim, G.-H.; Kim, J.Y.; Woo, H.Y. *Journal of Materials Chemistry* **2012**, *22 (39)*, 21238-21241.

(8) Beaupre, S.; Leclerc, M. *Journal of Materials Chemistry A* **2013**, *1 (37)*, 11097-11105.

(9) Blouin, N.; Michaud, A.; Gendron, D.; Wakim, S.; Blair, E.; Neagu-Plesu, R.; Belletête, M.; Durocher, G.; Tao, Y.; Leclerc, M. *Journal of the American Chemical Society* **2008**, *130 (2)*, 732-742.

(10) Lu, X.; Hlaing, H.; Germack, D.S.; Peet, J.; Jo, W.H.; Andrienko, D.; Kremer, K.; Ocko, B.M. *Nature Communications* **2012**, *3*, 795.

(11) Sun, K.; Zhang, S.; Li, P.; Xia, Y.; Zhang, X.; Du, D.; Isikgor, F.H.; Ouyang, J. *Journal of Materials Science: Materials in Electronics* **2015**, *26 (7)*, 4438-4462.

(12) Wakizaka, D.; Fushimi, T.; Ohkita, H.; Ito, S. *Polymer* **2004**, *45 (25)*, 8561-8565.

(13) Chen, D.; Nakahara, A.; Wei, D.; Nordlund, D.; Russell, T.P. *Nano Letters* **2011**, *11 (2)*, 561-567.

(14) Yin, W.; Dadmun, M. *ACS Nano* **2011**, *5 (6)*, 4756-4768.

(15) Chen, B.T. *Polymer Engineering & Science* **1983**, *23 (7)*, 399-403.

(16) Hall, D.B.; Underhill, P.; Torkelson, J.M. *Polymer Engineering & Science* **1998**, *38 (12)*, 2039-2045.

(17) Haugstad, G., Atomic Force Microscopy: Understanding Basic Modes and Advanced Applications, *John Wiley and Sons* (2012).

(18) Feynman, R.P. *Journal of Microelectromechanical Systems* **1992**, *1 (1)*, 60-66.

(19) Eftekhari, A., Nanostructured Conductive Polymers, *John Wiley & Sons, Ltd* (2010).

(20) Kelley, T.W.; Granstrom, E.; Frisbie, C.D. *Advanced Materials* **1999**, *11 (3)*, 261-264.

(21) Lanza, M., Conductive Atomic Force Microscope, *Wiley* (2017).

(22) Rebollar, E.; Perez, S.; Hernandez, M.; Domingo, C.; Martin, M.; Ezquerra, T.A.; Garcia-Ruiz, J.P.; Castillejo, M. *Physical Chemistry Chemical Physics* **2014**, *16 (33)*, 17551-17559.

(23) Perkampus, H.-H., UV-VIS Spectroscopy and Its Applications, *Springer-Verlag Berlin Heidelberg* (1992).

(24) Long, D.A., Raman Spectroscopy, *Mcgraw-Hill* (1977).

(25) Zink, J.I.; Shin, K.-S.K. Molecular Distortions in Excited Electronic States Determined from Electronic and Resonance Raman Spectroscopy In "Advances in Photochemistry"; *John Wiley & Sons, Inc.* (2007).

(26) Attwood, D.; Sakdinawat, A., Soft X-Rays and Extreme Ultraviolet Radiation: Principles and Applications, *Cambridge University Press* (2007).

(27) Rueda, D.R.; García-Gutiérrez, M.C.; Nogales, A.; Capitán, M.J.; Ezquerra, T.A.; Labrador, A.; Fraga, E.; Beltrán, D.; Juanhuix, J.; Herranz, J.F.; Bordas, J. *Review of Scientific Instruments* **2006**, *77 (3)*, 033904.

(28) García-Gutierrez, M.C.; Rueda, D.R. Bases of Synchrotron Radiation, Light Sources, and Features of X-Ray Scattering Beamlines In "Applications of Synchrotron Light to Scattering and Diffraction in Materials and Life Science"; T.A. Ezquerra; M.C. Garcia-Gutierrez; A. Nogales; M. Gomez (Eds.), *Springer-Verlag, Berlin Heidelberg* (2009).

(29) Willmott, P., An Introduction to Synchrotron Radiation: Techniques and Applications, *John Wiley & Sons, Ltd* (2011).

(30) Wiedemann, H., Synchrotron Radiation, *Springer-Verlag Berlin Heidelberg* (2003).

(31) Margaritondo, G., Introduction to Synchrotron Radiation, *Oxford University Press Inc* (1988).

(32) Synchrotron Light to Explore Matter, ISBN 3-540-14888-4 Copyright IMediaSoft (Bucharest and Meylan), *ESRF Grenoble and Springer-Verlag Berlin Heidelberg* (2001).

(33) Stöhr, J., NEXAFS Spectroscopy *New York: Springer-Verlag* (1992).

(34) Warwick, T.; Franck, K.; Kortright, J.B.; Meigs, G.; Moronne, M.; Myneni, S.; Rotenberg, E.; Seal, S.; Steele, W.F.; Ade, H.; Garcia, A.; Cerasari, S.; Denlinger, J.; Hayakawa, S.; Hitchcock, A.P.; Tyliszczak, T.; Kikuma, J.; Rightor, E.G.; Shin, H.-J.; Tonner, B.P. *Review of Scientific Instruments* **1998**, *69 (8)*, 2964-2973.

(35) Jacobsen, C.; Williams, S.; Anderson, E.; Browne, M.T.; Buckley, C.J.; Kern, D.; Kirz, J.; Rivers, M.; Zhang, X. *Optics Communications* **1991**, *86 (3)*, 351-364.

(36) Ade, H.; Stoll, H. *Nature Materials* **2009**, *8 (4)*, 281-290.

(37) Ade, H.; Zhang, X.; Cameron, S.; Costello, C.; Kirz, J.; Williams, S. *Science* **1992**, *258 (5084)*, 972-975.

(38) Ade, H.; Hitchcock, A.P. *Polymer* **2008**, *49 (3)*, 643-675.

(39) Müller-Buschbaum, P. A Basic Introduction to Grazing Incidence Small-Angle X-Ray Scattering In "Applications of Synchrotron Light to Scattering and Diffraction in Materials and

Life Science"; T.A. Ezquerra; M.C. Garcia-Gutierrez; A. Nogales; M. Gomez (Eds.), *Springer-Verlag, Berlin Heidelberg* (2009).

(40) Rueda, D.R.; Nogales, A.; Hernández, J.J.; García-Gutiérrez, M.-C.; Ezquerra, T.A.; Roth, S.V.; Zolotukhin, M.G.; Serna, R. *Langmuir* **2007**, *23 (25)*, 12677-12681.

(41) Toney, M.F.; Gordon, J.G.; Samant, M.G.; Borges, G.L.; Wiesler, D.G.; Yee, D.; Sorensen, L.B. *Langmuir* **1991**, *7 (4)*, 796-802.

(42) Wong, D.T.; Wang, C.; Pople, J.A.; Balsara, N.P. *Macromolecules* **2013**, *46 (11)*, 4411-4417.

(43) Liu, F.; Brady, M.A.; Wang, C. *European Polymer Journal* **2016**, *81*, 555-568.

(44) Wang, C.; Araki, T.; Watts, B.; Harton, S.; Koga, T.; Basu, S.; Ade, H. *Journal of Vacuum Science & Technology A: Vacuum, Surfaces, and Films* **2007**, *25 (3)*, 575-586.

(45) Swaraj, S.; Wang, C.; Yan, H.; Watts, B.; Lüning, J.; McNeill, C.R.; Ade, H. *Nano Letters* **2010**, *10 (8)*, 2863-2869.

(46) Schaffer, C.J.; Wang, C.; Hexemer, A.; Müller-Buschbaum, P. *Polymer* **2016**, *105*, 357-367.

Chapter 3. Phase separation and confinement effects in thin films of conjugated polymer blends

Organic Photovoltaics (OPVs) define a class of solar-energy conversion devices, offering the advantages of low cost, lightweight, solution-processability and mechanical flexibility over other existing photovoltaic technologies.[1-3] Organic Solar Cells (OSCs) are attractive due to a number of advantageous features,[2] including their thin-film architecture and low material consumption resulting from a high absorption coefficient, their use of organic solution processes and low manufacturing energy requirements. Efficient OSCs typically employ a Bulk Heterojunction (BHJ) photoactive layer, where an electron-donating (p-type) material and an electron-accepting (n-type) material form a nanosized phase-separated interpenetrating network, which can provide large enough heterointerface areas for efficient exciton dissociation and a continuous pathway for charge transport.[4] Fullerene derivatives are the most effective and commonly used acceptor materials. Polymer/fullerene BHJ solar cells have proven power conversion efficiencies of over 10% now reported.[5-7] All-Polymer Solar Cells (PSCs) have been also developed, where an n-type semiconducting polymer is used as the electron acceptor instead of a fullerene derivative blended with a p-type polymer. Although the efficiency of all-PSCs remains[8, 9] at ~ 4%, they offer some potential advantages including superior optical absorption and greater synthetic flexibility in tuning semiconducting properties such as the bandgap and energy levels.[10, 11] The bulk heterojunction concept relies on the high purity of donor and acceptor phases within the characteristic exciton diffusion length of ~ 10 nm, requiring percolating interconnected network morphology. The understanding of phase separation and morphology in all-polymer BHJ is crucial for the optimization of device performance.[11, 12] In general, a mixing of donor and acceptor on a length scale smaller than the exciton diffusion length optimizes charge generation, while coarser morphologies optimize the separation of charges away from the interface and their collection at the device electrodes. On the other hand, crystal morphology[13, 14] and structure confinement effects[15-17] such as crystallization inhibition in domains of tens of nanometers also play very important roles on charge transport and device performance.

In this chapter a study on the compatibility, phase separation and confinement in thin films of P3HT/PCDTBT blends with different thicknesses is presented. The influence of

morphology on nanoscale charge transport is also reported. Morphology and electrical properties have been investigated by AFM and C-AFM respectively. Finally, STXM measurements have been performed in order to obtain compositional maps of the polymer blends and GIWAXS to study the internal structure of components in the blend.

3.1. Sample preparation

Thin polymer films were prepared onto silicon substrates by spin-coating from different chlorobenzene solutions specified in Table 3.1. A rotation rate of 2400 rpm was kept during 120 s.

Table 3.1. Description of the samples including total concentration, thickness and zero-field mobility (μ_0) (see Section 3.6). P3HT/PCDTBT blends present two thicknesses corresponding to the different domains of the sample.

Sample	Concentration (g/L)	Thickness (nm)	μ_0 ($cm^2/V \cdot s$)
P3HT	24	145	2.3×10^{-2}
PCDTBT	24	190	-
P3HT/PCDTBT-1	12	40-75	1.2×10^{-5}
P3HT/PCDTBT-2	24	140-190	0.61
P3HT/PCDTBT-3	36	270-320	1.21

For STXM measurements thin films deposited onto silicon substrates were separated from the substrate by immersion in a dilute NaOH/water solution (0.25 wt %). By this procedure the thin polymer film separated from the substrate and floated on the liquid surface. Finally the floating film can be picked up using Transmission Electron Microscopy (TEM) grids. An example of the results of the described procedure is shown in Figure 3.1.

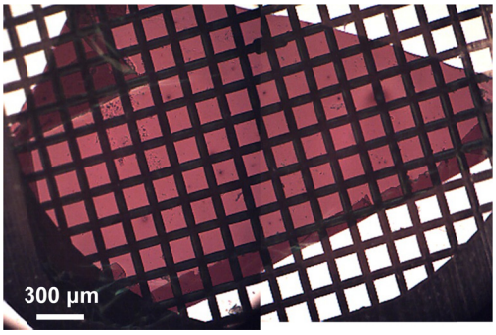

Figure 3.1. Optical microscopy image of a TEM grid with a sample of P3HT thin film.

3.2. Optical properties

As mentioned before, the absorption coefficient can be obtained by using the Lambert-Beer law (Equation 2.4). The variation of the absorption coefficient with the wavelength in the ultraviolet-visible (UV-vis) region for the pristine P3HT, PCDTBT and the blend P3HT/PCDTBT (1:1) spin-coated films from chlorobenzene are compared in Figure 3.2.

P3HT presents a main absorption band with the maximum at about 520 nm which is attributed to the electronic π-π* transition from the HOMO (π) to the LUMO (π*).[18] The position of the absorption maximum as well as the vibronic structure, which is detectable by a rough profile with different shoulders, depends on the conjugation length of the polymer chains. As expected, P3HT shows vibronic features over the investigated bandwidth suggesting that it presents structural order and a potential increment in light-harvesting ability.

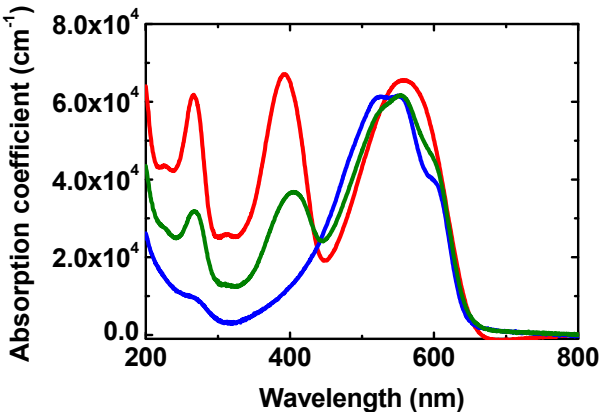

Figure 3.2. Linear absorption coefficient of P3HT (blue), PCDTBT (red) and P3HT/PCDTBT blend (1:1) (green) thin films.

PCDTBT exhibits three pronounced absorption bands: the PCDTBT band at approximately 385 nm is assigned to the π-π* transition of the conjugated main chain and the PCDTBT band at about 563 nm corresponds to the intramolecular charge transfer (ICT) interaction between carbazole and benzothiadiazole moieties.[19] These two bands are characteristic of donor-acceptor conjugated polymers. Moreover, the band at roughly 260 nm corresponds to low molecular weight species such as carbazole and benzothiadiazole monomers.

The spectrum of the P3HT/PCDTBT blend presents practically an arithmetic average of the individual components. In a first approach this suggests that P3HT and PCDTBT

components are phase separated and there are not new interactions which affect the absorption properties when P3HT and PCDTBT are blended.

3.3. Surface morphology

AFM in tapping mode was used to characterize both the surface topography at the nanoscale and the thickness of thin films prepared from different solution concentrations. The surface topography images of the P3HT and PCDTBT spin-coated films are shown in Figure 3.3.

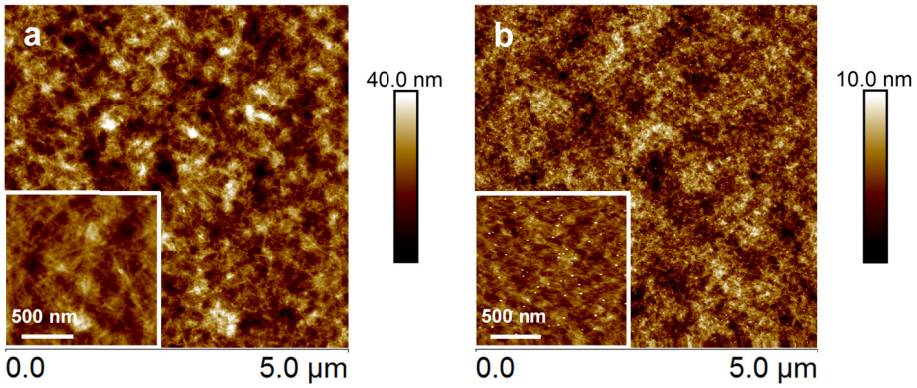

Figure 3.3. AFM topography images in tapping mode of: (a) P3HT and (b) PCDTBT spin-coated films. Insets show magnified images.

The topography of the P3HT (Figure 3.3.a) and PCDTBT (Figure 3.3.b) films is smooth with a roughness of $R_a \approx 9$ nm and $R_a \approx 1$ nm respectively. Small fiber-like crystallites can be observed for the P3HT (inset in Figure 3.3.a).

P3HT/PCDTBT (1:1) films (Figure 3.4) show the characteristic morphology of lateral phase separation, indicating immiscibility of the two polymers in agreement with previous reports.[20, 21] P3HT/PCDTBT-2 and P3HT/PCDTBT-3 thin films present a 50 nm difference in height between phases for an average film thickness of 165 and 295 nm respectively, the P3HT/PCDTBT-1 thin film shows 35 nm difference in height between phases for an average film thickness of 58 nm (see Table 3.1). These results indicate that domain size as well as film thickness increase with increasing polymer concentration. It is also interesting to point out the presence of a dense needle-like morphology in films with 165 and 295 nm average thicknesses (insets in Figures 3.4.b and 3.4.c) while no evidence of needle-like motifs appears in the thin film with 58 nm average thickness (inset in Figure 3.4.a). The samples were then annealed at 140ºC for

20 min (above the glass transition temperature of both polymers)[22] and cooled down to room temperature aiding the thermodynamic equilibration of the samples, but no change in morphology was observed.

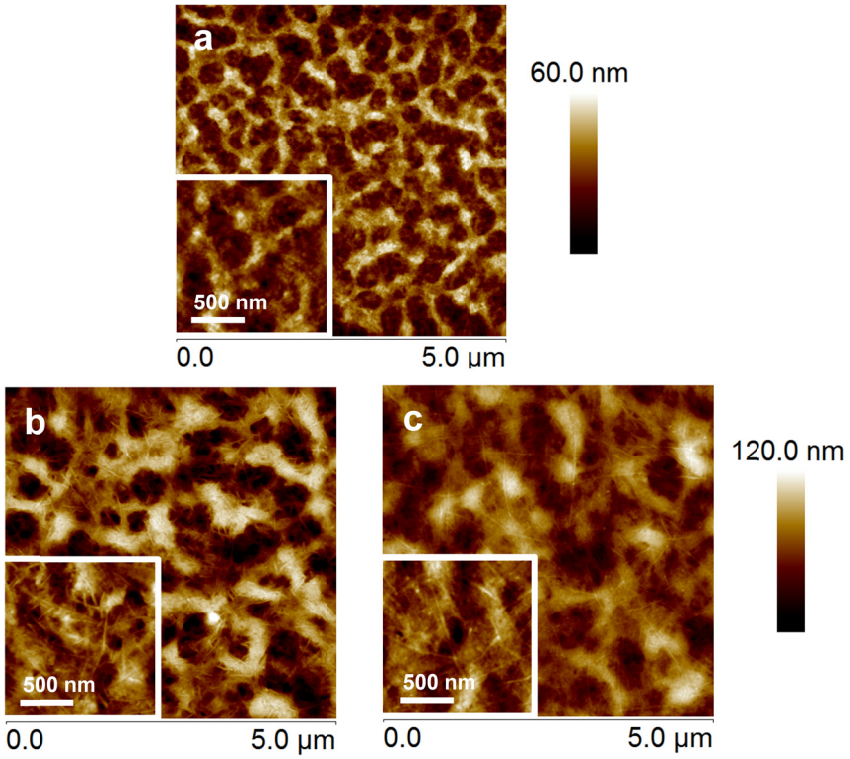

Figure 3.4. AFM topography images of polymer thin films: (a) P3HT/PCDTBT 1:1 (12 g/L), (b) P3HT/PCDTBT 1:1 (24 g/L) and (c) P3HT/PCDTBT 1:1 (36 g/L). Insets show magnified images.

3.4. Composition mapping

Since there is not a single technique capable to fully characterize the morphology of a thin-film polymer blend, the use of complementary techniques is required. Although AFM enables imaging of surface topography with high spatial resolution, to distinguish regions with different chemical composition can be cumbersome. STXM is a technique that provides an appropriate combination of spectroscopy and imaging capabilities at low radiation doses. As a powerful synchrotron-based technique, STXM can quantitatively map the chemical composition of organic films with nanoscale resolution.[23, 24] As explained in Section 2.2.7, the STXM images can provide information on the domain sizes, shapes, and purities of thin film polymer blends with a spatial resolution of ~ 20 nm.[25] In order to obtain quantitative chemical composition of the blend thin films we have used the Singular Value Decomposition (SVD)

mathematical procedure[23, 26] which requires previous knowledge of the mass absorption coefficients of the blend components. Figure 3.5 shows the mass absorption coefficients as a function of energy for P3HT and PCDTBT pristine films of known thickness (Table 3.1). The transmitted X-ray intensity measured was converted to an X-ray optical density collecting the I_0 and by using the equation 2.12, the mass absorption coefficient of each polymer can be obtained considering the values of thicknesses previously measured and density values of 1.13 and 1.33 g/cm^3 for P3HT and PCDTBT respectively.[27]

The SVD procedure also requires a series of images acquired at a number of energies that equal or exceed the number of compositional components. STXM images (Figure 3.5 top) of the same area of the P3HT/PCDTBT-2 thin film were taken at energies indicated by arrows in the NEXAFS spectra which correspond to 280 eV (pre-edge), 284.2 eV (PCDTBT resonance), 287.8 eV (P3HT resonance) and 320 eV (chemically insensitive). By using the *aXis2000* software package[28] where the SVD procedure is integrated, the information contained within the set of STXM images taken at the selected energies can be transformed into maps quantifying the composition and thickness of the sample in each pixel.[23, 26]

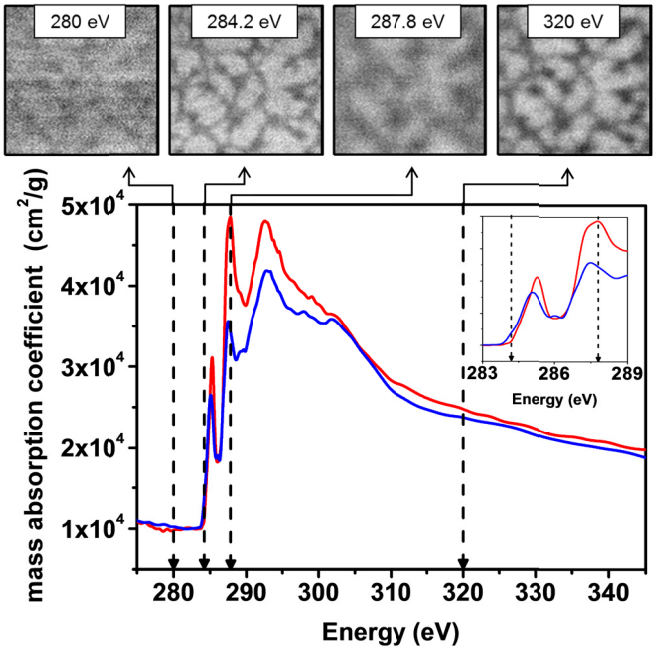

Figure 3.5. Reference NEXAFS spectra for pristine films of P3HT (red line) and PCDTBT (blue line). Vertical dashed arrows indicate the photon energies used to obtain the raw STXM. Images (6 µm × 6 µm) of the same sample area of a P3HT/PCDTBT-2 thin film, presented at the top. The inset highlights differences in the NEXAFS spectra of P3HT and PCDTBT.

The corresponding composition and thickness maps of the P3HT/PCDTBT-2 thin film are shown in Figure 3.6.a and b respectively. On the one hand, these images reveal the chemical nature of the different observed domains. On the other hand they reveal a structure of thinner P3HT-rich domains enclosed by a thicker PCDTBT-rich matrix. The thicknesses of domains are in agreement with the values measured by AFM.

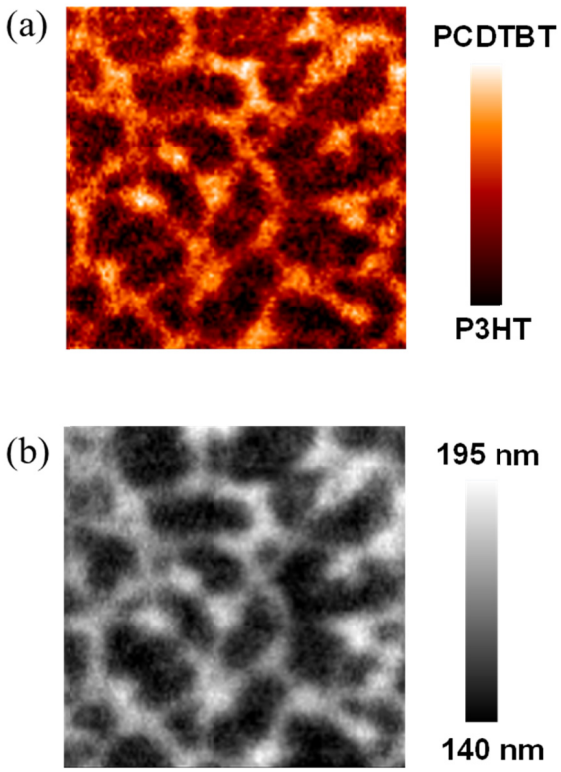

Figure 3.6. 6 µm × 6 µm images of: (a) quantitative composition and (b) thickness maps of the P3HT/PCDTBT-2 thin film, calculated from the set of raw images in Figure 3.5 top.

3.5. Internal structure

In order to complement the STXM studies, GIWAXS was used to probe changes in molecular and nanoscale structure in P3HT, PCDTBT and in the blend P3HT/PCDTBT-2 thin films, before and after annealing at 140ºC for 20 min. Figure 3.7.a shows the 2D scattering pattern for the P3HT as-cast film. Four main peaks can be seen, three out of plane reflections h00 having q-values of 3.8, 7.59 and 11.55 nm^{-1}, and one in plane reflection which is the superposition of the 020 and the weak 002 reflections,[29] with a q-value of 16.39 nm^{-1}. In agreement with previous reports,[29, 30] the pattern reveals the characteristic crystalline reflections corresponding to the crystal sheets formed by the π-π stacking of the thiophene rings. The h00 reflections

correspond to the intrachain distances and 0k0 to the π-π-stacking distances. In addition, the P3HT as-cast film is uniaxially oriented with mainly an edge-on configuration which corresponds to the usual conformation adopted by P3HT thin films, consisting of polymer chains parallel to the substrate.

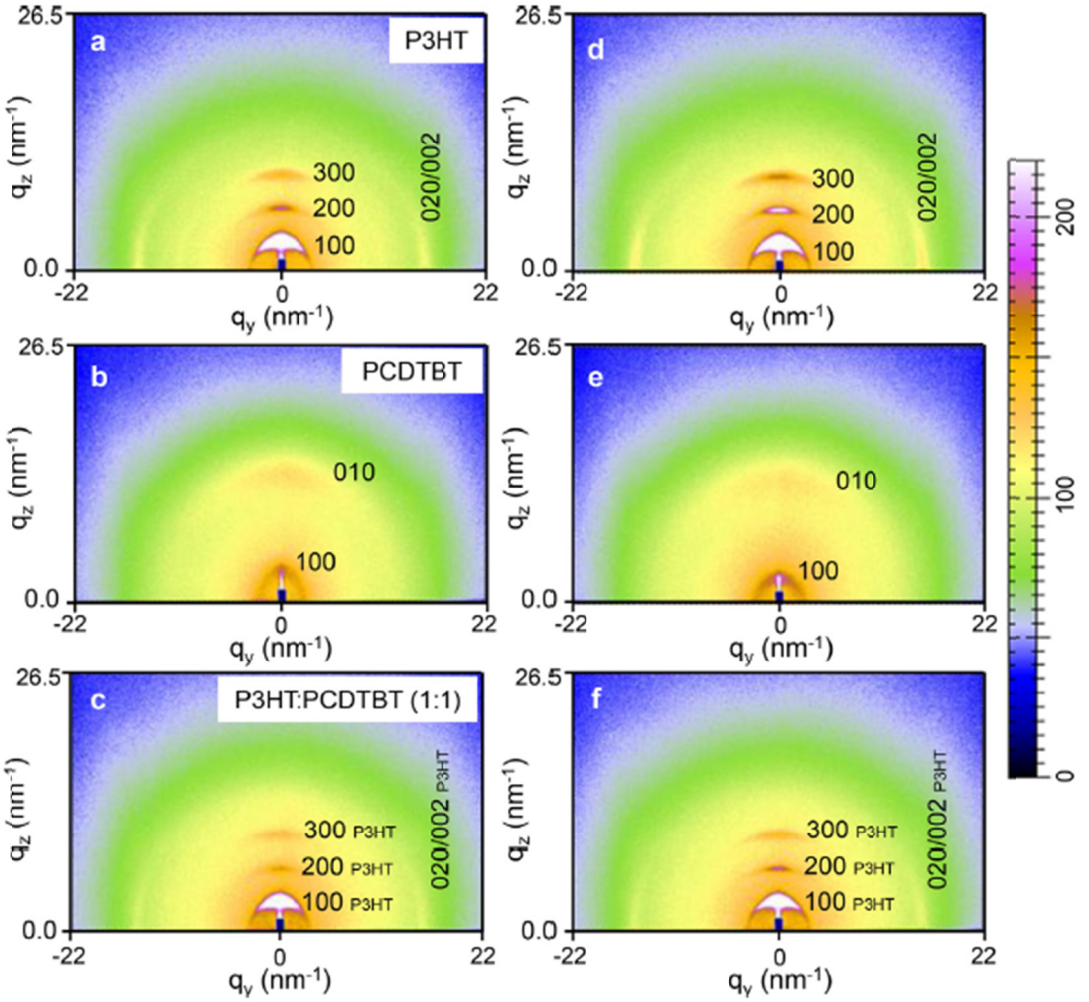

Figure 3.7. GIWAXS images of spin-coated thin films: (a) P3HT, (b) PCDTBT, (c) P3HT/PCDTBT-2. And after annealing at 140ºC for 20 min: (d) P3HT, (e) PCDTBT, (f) P3HT/PCDTBT-2.

The 2D scattering pattern of PCDTBT as-cast film, shown in Figure 3.7.b reveals a lower degree of crystallinity compared to P3HT. The broad peak at q ≈ 14.55 nm^{-1} in the out-of-plane direction, indexed as 010, corresponds to π-π stacking between PCDTBT back-bones while the diffraction peak at q ≈ 2.95 nm^{-1} also in the out of plane direction, indexed as 100, corresponds to the alkyl side-chain packing.[14, 27] The blend P3HT/PCDTBT-2 as-cast thin film presents a 2D scattering pattern (Figure 3.7.c) very similar to P3HT, where only the P3HT reflections are detected. These reflections appear

at similar q values as those of P3HT. No evidence of PCDTBT reflections is observed. These data reveal that P3HT and PCDTBT do not co-crystallize. After annealing the samples at 140ºC for 20 min, the P3HT thin film exhibits more intense reflections (Figure 3.7.d) suggesting an increase in crystallinity and a similar trend is observed for the blend (Figure 3.7.f). However, for PCDTBT Figure 3.7.e shows that while the 100 peak is better defined, the 010 loses intensity after annealing. This effect is even more evident for a thinner PCDTBT sample, as can be seen in Figure 3.8. The trend can be explained by considering that annealing improves side-chain order while reducing the π-π stacking, as has been previously proposed by Wang et al.[22] Figure 3.9 shows the scattering differences between P3HT/PCDTBT-1 and P3HT/PCDTBT-2 samples. As it is expected, thicker samples present higher scattering intensity.

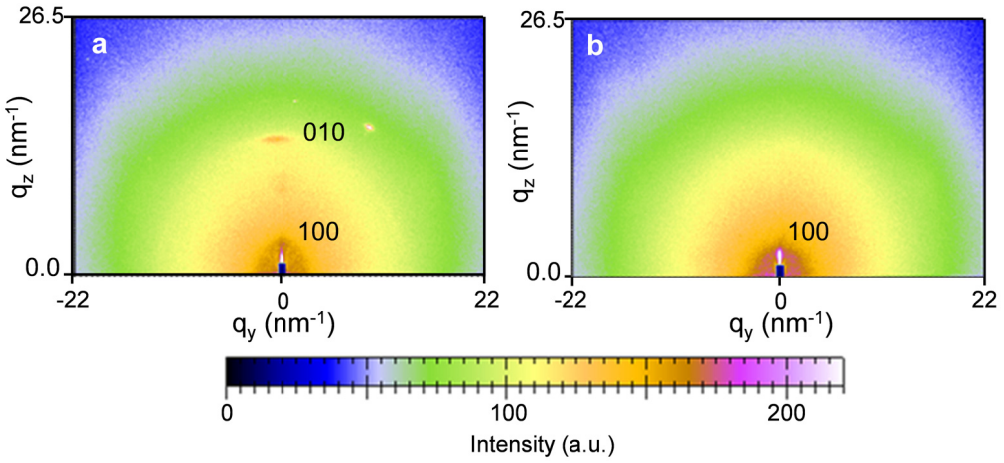

Figure 3.8. 2D GIWAXS patterns of PCDTBT thin films prepared from 12 g/L concentration solution: (a) spin-coated and (b) annealed at 140 ºC for 20 minutes.

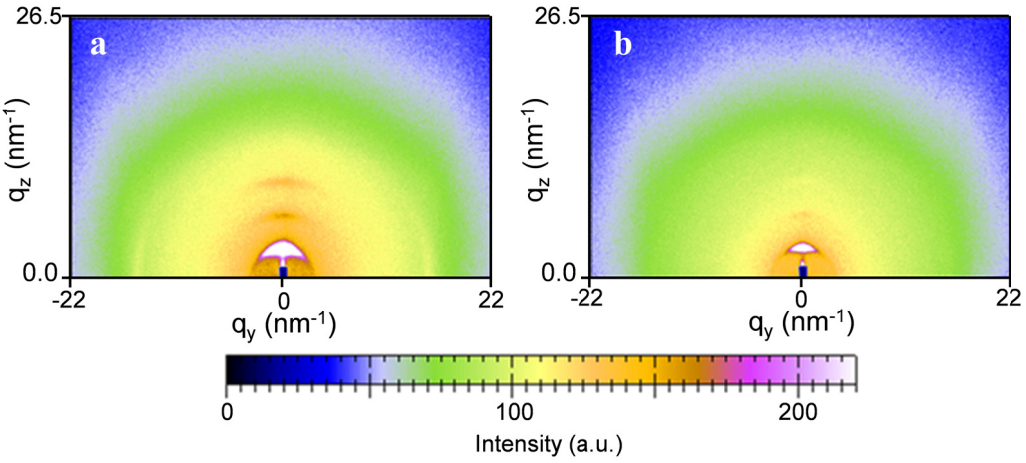

Figure 3.9. 2D GIWAXS of thin films: (a) P3HT/PCDTBT-2 and (b) P3HT/PCDTBT-1.

3.6. Nanoscale charge transport properties

Conductive-AFM (C-AFM) was used to characterize the electrical properties at the nanoscale of P3HT/PCDTBT (1:1) blend thin films with different thicknesses. Neat P3HT films were included in the study for the sake of comparison. Work functions of metal electrodes[31] are 4.8 eV for the n-type silicon anode and 5.6 eV for the Pt-Ir tip which works as cathode as it is shown in Figure 3.10. Since the difference between the HOMO level of polymer and the work function of both electrodes (Si substrates and Pt-Ir tip) is rather small, it is expected that ohmic contacts occur for a hole injection and strong energy barriers for electrons. As a consequence only holes can be injected to the electrodes.[32]

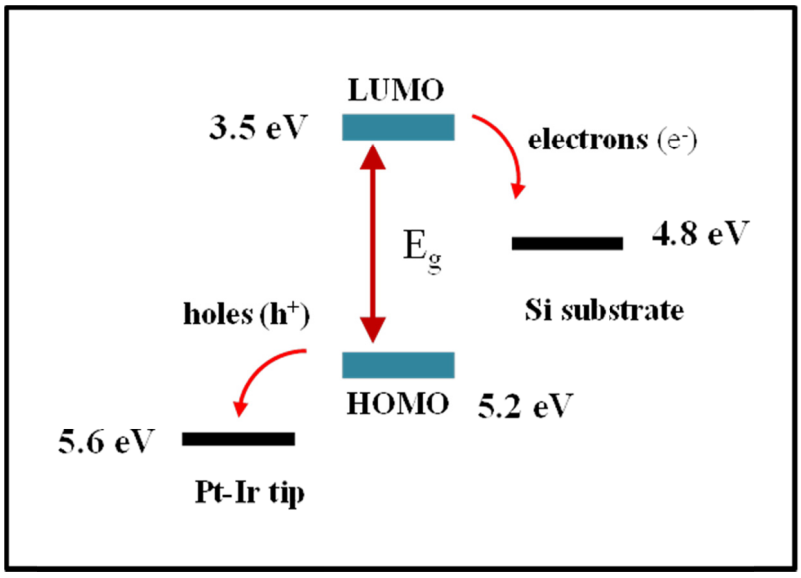

Figure 3.10. Energy level diagram for C-AFM setup. HOMO and LUMO energy level of the P3HT are represented as a model.

In this study hole current imaging was used to examine conductivity variations and to map the P3HT conducting network in the P3HT/PCDTBT (1:1) thin films. In these measurements, Pt-Ir coated silicon probes were used to ensure that holes are the major injected carriers.[33] Figure 3.11 shows contact mode AFM topography and current images of a P3HT thin film recorded simultaneously by applying a constant voltage of -5 V to the conducting substrate. The current image presented in Figure 3.11.b shows a homogeneous current variation throughout the film.

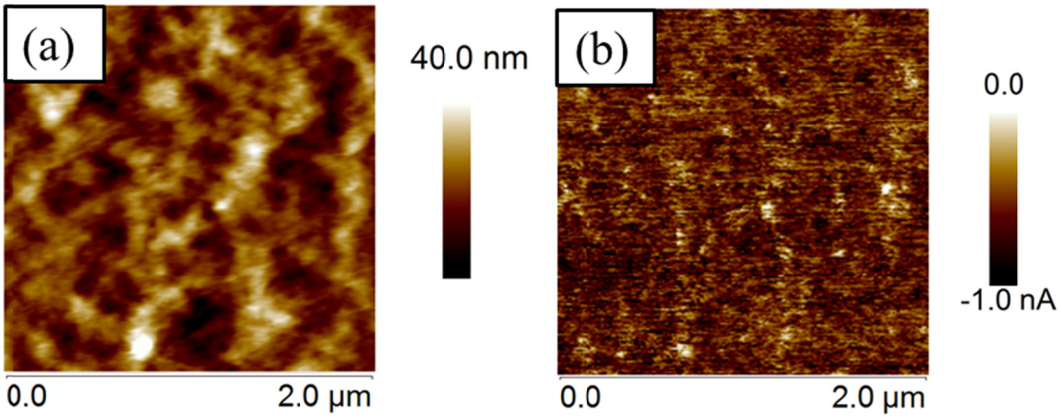

Figure 3.11. C-AFM measurements. (a) Topography and (b) current images of the P3HT thin film (24 g/L).

However, P3HT/PCDTBT (1:1) current images (Figure 3.12) present domains with high (dark region) and low (bright region) current. By comparing C-AFM images with the compositional maps shown in Figure 3.6, it is possible to assign the high current regions to the P3HT-rich domains and the low current ones to the PCDTBT phase. It is known that the thickness of thin films prepared by spin-coating is mainly related to the solution concentration. As previously commented, Table 3.1 shows the thicknesses of neat P3HT and PCDTBT thin films and the average thickness as well as the thicknesses of P3HT-rich and PCDTBT-rich domains of P3HT/PCDTBT (1:1) thin films prepared from solutions with different concentrations. It can be observed in Figure 3.12 that the electric current in the P3HT-rich domains increases dramatically with increasing thickness from hundreds of pA for the blend with a P3HT-rich domain thickness of 40 nm (Figure. 3.12.b) to several nA for blends with P3HT-rich domains thicker than 100 nm (Figures 3.12.d and 3.12.f).

Moreover it was pointed out previously the presence of a dense needle-like morphology in P3HT/PCDTBT-2 and P3HT/PCDTBT-3 films with 165 and 295 nm thicknesses respectively while no evidence of needle-like motifs appears in the 58 nm thick P3HT/PCDTBT-1 film. The current images of P3HT/PCDTBT-2 and P3HT/PCDTBT-3 films clearly show a fibrous network where the strongest current is measured. These results evidence that P3HT needle-like crystals grow from the P3HT-rich domains acting as bridges through the PCDTBT-rich domains. However, the current image of the P3HT/PCDTBT-1 thin film neither shows any fibrous network nor evidence of needle-

like motifs. This fact can be explained by confinement inhibiting crystallization due to the very thin domains of P3HT of only 40 nm as it is supported by GIWAXS measurements.

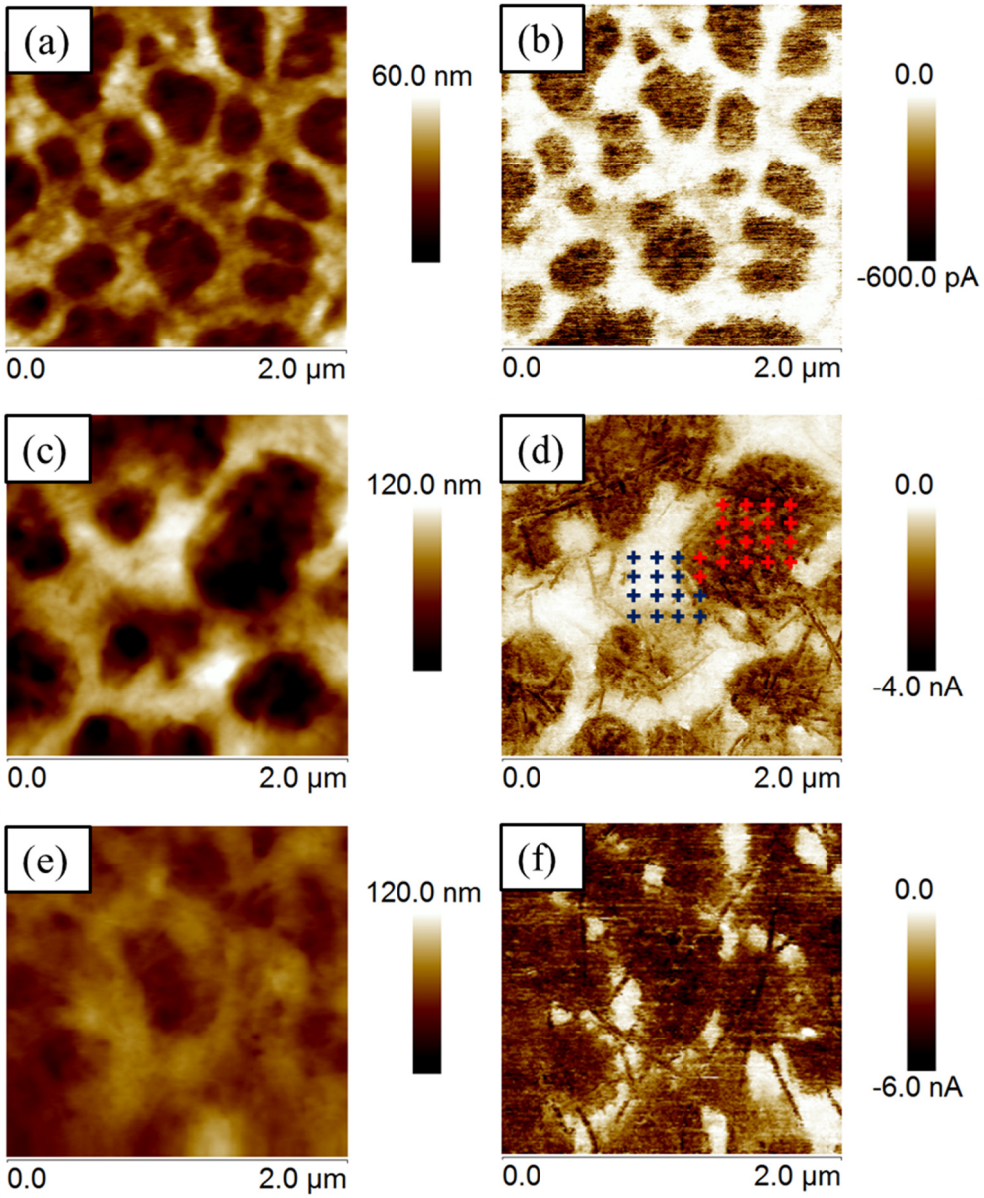

Figure 3.12. C-AFM measurements. (Left) Topography and (right) current images of: (a,b) P3HT/PCDTBT 1:1 (12 g/L), (c,d) P3HT/PCDTBT 1:1 (24 g/L), (e,f) P3HT/PCDTBT 1:1 (32 g/L). Red and blue crosses in Figure (d) correspond to different locations where I-V characteristics were measured.

In addition to current imaging with C-AFM, local I-V curves can also be collected. This technique of measuring I-V characteristics by C-AFM has the advantage that only a very small region of the film, comparable to the tip contact area, is probed.[33-35] Thus,

several areas can be examined aiming to provide information on the film electrical heterogeneity. I-V curves were collected from different locations within a P3HT-rich domain (red crosses in Figure 3.12.d) and from different locations within a PCDTBT-rich domain (blue crosses in Figure 3.12.d). I-V curves measured in both regions including the average curves (red and blue for the P3HT-rich domain and the PCDTBT-rich domain respectively) are shown in Figure 3.13.

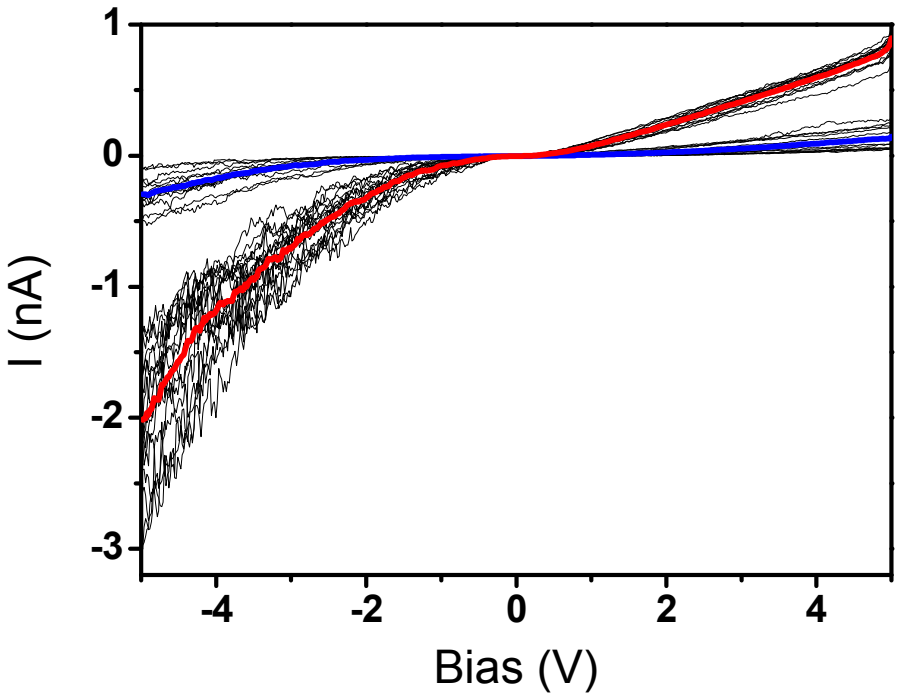

Figure 3.13. I-V curves measured in different locations into a P3HT-rich domain (red crosses in Figure 3.12.d) and in different locations into a PCDTBT-rich domain (blue crosses in Figure 3.12.d). Average I-V curves, red and blue for the P3HT-rich domain and the PCDTBT-rich domain are also included.

As one can see, while there is a negligible electrical current in the PCDTBT-rich domains, a significant electrical current is measured in the P3HT-rich domains. The same procedure was used for all the samples investigated. Average I-V curves for the neat P3HT, neat PCDTBT and P3HT-rich domains in P3HT/PCDTBT (1:1) films with different thicknesses are shown in Figure 3.14.a. The highest current for a similarly applied bias is measured for the P3HT/PCDTBT-2 thin film. Since the samples have different thicknesses, Figure 3.14.b presents the I-E curves where E=V/t is the electric field and t is the P3HT domain thickness.

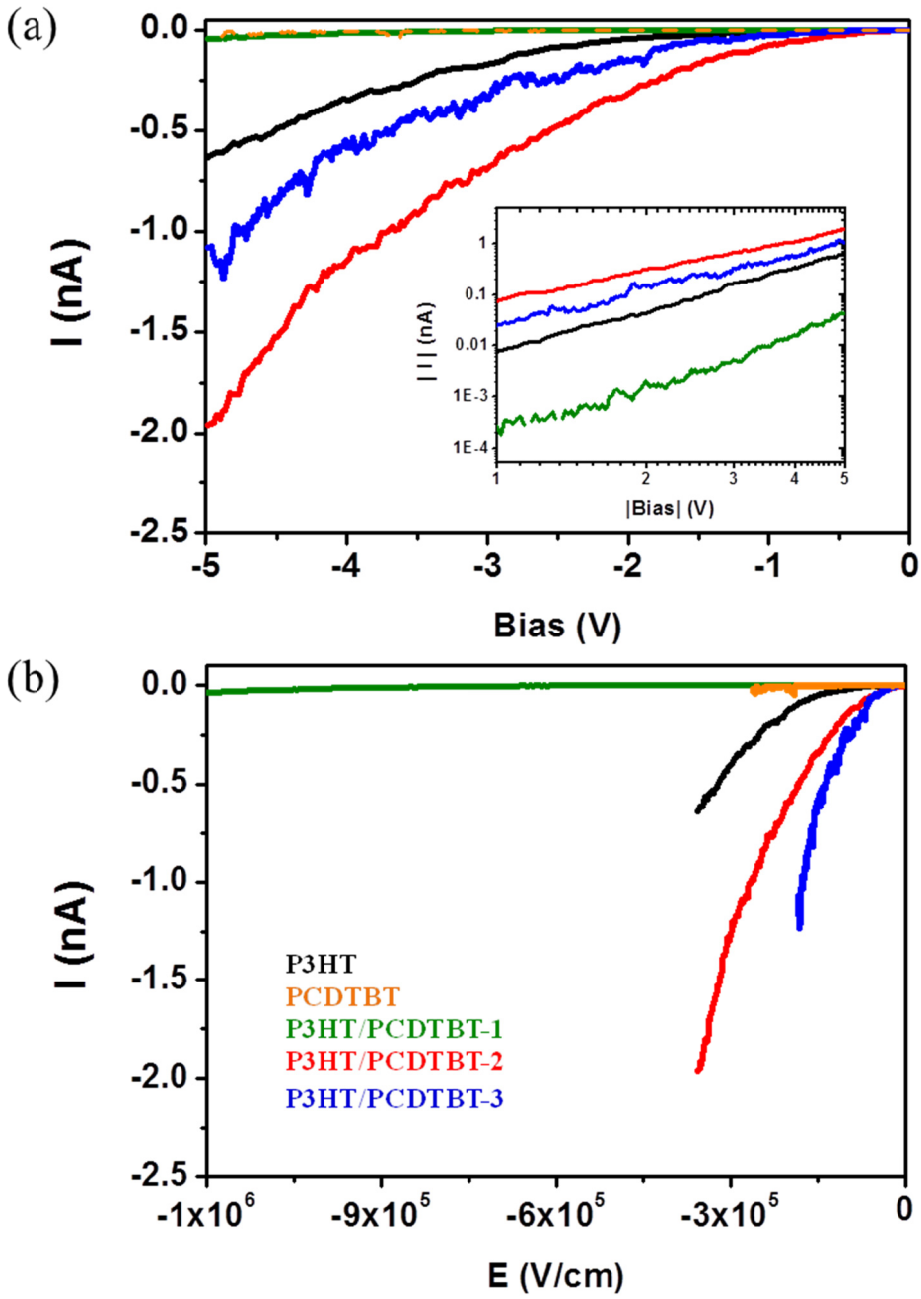

Figure 3.14. (a) Average I-V curves for pristine P3HT and PCDTBT thin films and P3HT-rich domains in P3HT/PCDTBT (1:1) thin films with different thicknesses. Inset shows the Space-Charge Limited Current (SCLC) region, (b) Average I-E curves for pristine P3HT and PCDTBT thin films and P3HT-rich domains in P3HT/PCDTBT (1:1) thin films with different thicknesses.

The log-log plot of the $|J| - |V|$ data, where J is the current density, is presented in Figure 3.15.

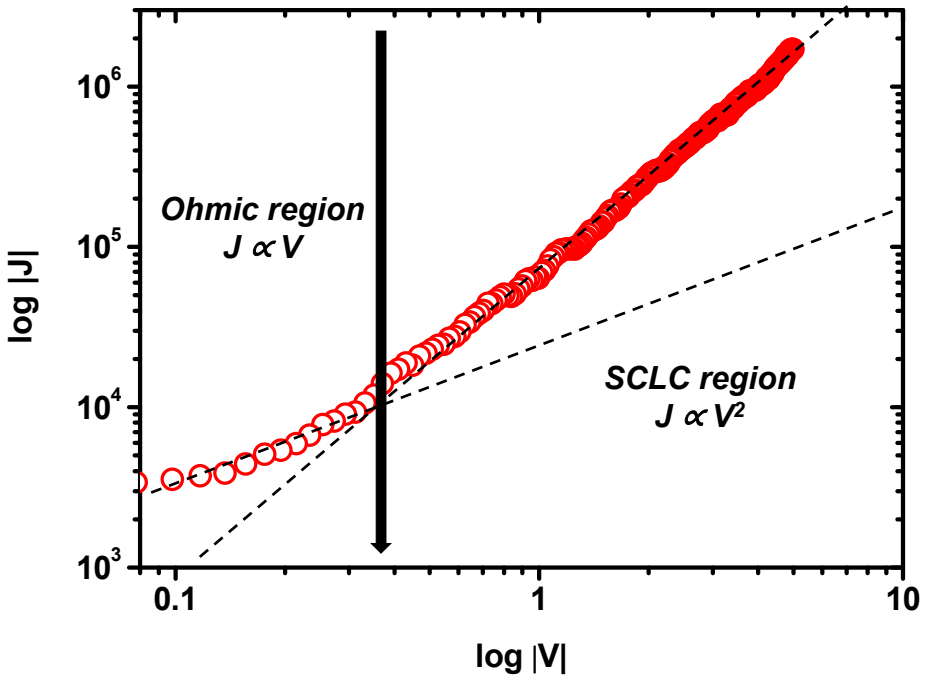

Figure 3.15. log-log plot of the J-V data where two different regimes of the electrical response can be observed.

It shows that for the investigated samples the electrical response exhibits two regimes: initially a short Ohmic range ($J \propto V$) and a more extended regime ($J \propto V^2$) denominated Space-Charge Limited Current (SCLC) regime. In the case of SCLC, the nanoscale charge mobility can be extracted by using the following expression:[36-38]

$$J = \frac{9}{8}\varepsilon_r \varepsilon_0 \mu \frac{V^2}{t^3} \tag{3.1}$$

where ε_r is the dielectric constant of the polymer for which we assumed a value of 3 as proposed in the literature,[39] ε_0 = 8.85 × 10^{12} F/m is the vacuum permittivity, μ is the charge mobility, V is the applied voltage, and t is the P3HT domain thickness. In order to verify whether the calculated carrier mobilities are field dependent we have used the approach for a field-dependent carrier mobility described by the Poole-Frenkel equation:[33]

$$\mu = \mu_0 e^{(E/E_0)^{1/2}} \tag{3.2}$$

where E is the electric field, μ_0 is the zero-field mobility, and E_0 is the field coefficient. The Poole-Frenkel plots ($\ln \mu$ vs $E^{1/2}$) are shown in Figure 3.16.

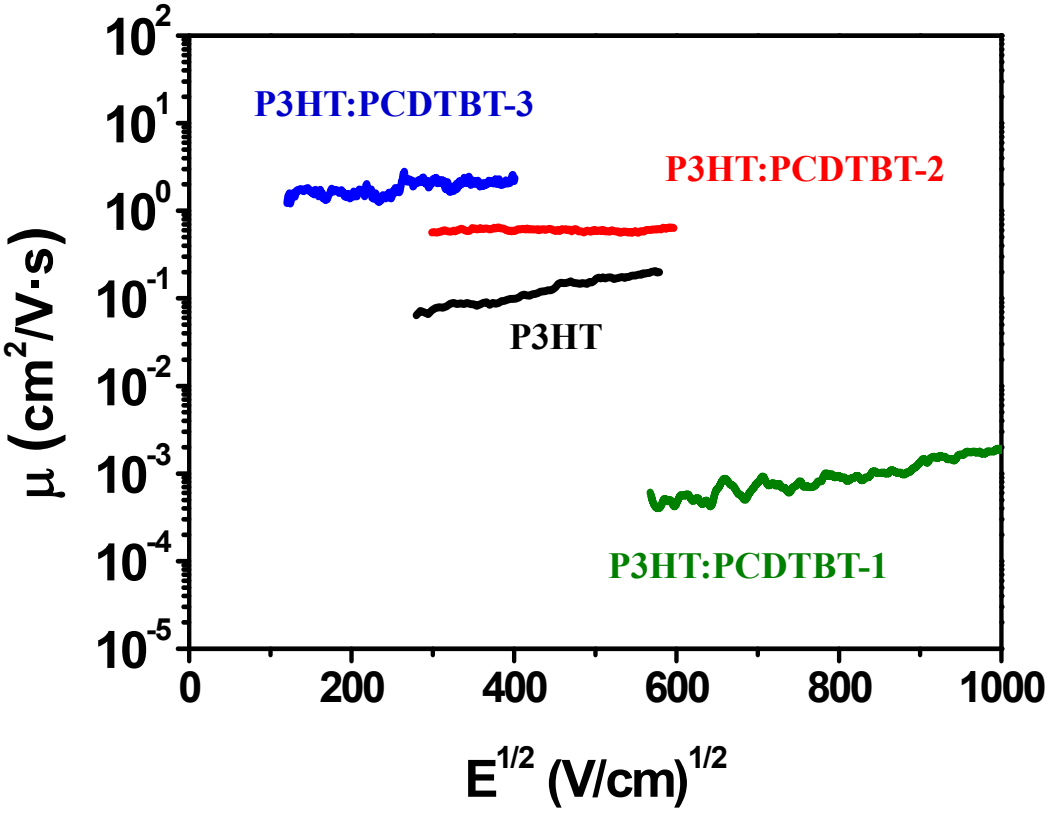

Figure 3.16. Hole mobilities for pristine P3HT (black) and P3HT-rich domains in P3HT/PCDTBT-1 (green), P3HT/PCDTBT-2 (red) and P3HT/PCDTBT-3 (blue).

All the samples exhibit similar behavior showing that the mobility depends weakly on the electric field. A significant zero-field hole mobility increase is observed for the P3HT/PCDTBT (1:1) films with increasing thickness (Table 3.1) from 1.2×10^{-5} $cm^2/V \cdot s$ for the P3HT/PCDTBT-1 thin film to 0.61 $cm^2/V \cdot s$ and 1.21 $cm^2/V \cdot s$ for the P3HT/PCDTBT-2 and P3HT/PCDTBT-3 thin films respectively. It is also interesting to note that a zero-field hole mobility increase of about two orders of magnitude is observed for the P3HT-rich domains in the P3HT/PCDTBT-2 thin film compared to the neat P3HT sample with similar thickness. It indicates a P3HT and PCDTBT synergy in the blend, probably related to the highly conductive needle like morphology induced in P3HT domains by the presence of the PCDTBT phase, as it is seen comparing the topography images for both samples (Figure 3.3.a and 3.4.b) and the current images (Figure 3.11.b and 3.12.d).

References

(1) Forrest, S.R. *Nature* **2004**, *428 (6986)*, 911-918.

(2) Dennler, G.; Scharber, M.C.; Brabec, C.J. *Advanced Materials* **2009**, *21 (13)*, 1323-1338.

(3) Tang, Y.; McNeill, C.R. *Journal of Polymer Science Part B: Polymer Physics* **2013**, *51 (6)*, 403-409.

(4) Yu, G.; Gao, J.; Hummelen, J.C.; Wudl, F.; Heeger, A.J. *Science* **1995**, *270 (5243)*, 1789-1791.

(5) He, Z.; Zhong, C.; Su, S.; Xu, M.; Wu, H.; Cao, Y. *Nature Photonics* **2012**, *6 (9)*, 591-595.

(6) Amb, C.M.; Chen, S.; Graham, K.R.; Subbiah, J.; Small, C.E.; So, F.; Reynolds, J.R. *Journal of the American Chemical Society* **2011**, *133 (26)*, 10062-10065.

(7) Small, C.E.; Chen, S.; Subbiah, J.; Amb, C.M.; Tsang, S.-W.; Lai, T.-H.; Reynolds, J.R.; So, F. *Nature Photonics* **2012**, *6 (2)*, 115-120.

(8) Zhou, E.; Cong, J.; Hashimoto, K.; Tajima, K. *Advanced Materials* **2013**, *25 (48)*, 6991-6996.

(9) Mori, D.; Benten, H.; Okada, I.; Ohkita, H.; Ito, S. *Advanced Energy Materials* **2014**, *4 (3)*, 1301006.

(10) McNeill, C.R.; Greenham, N.C. *Advanced Materials* **2009**, *21 (38-39)*, 3840-3850.

(11) Sepe, A.; Rong, Z.; Sommer, M.; Vaynzof, Y.; Sheng, X.; Muller-Buschbaum, P.; Smilgies, D.-M.; Tan, Z.-K.; Yang, L.; Friend, R.H.; Steiner, U.; Huttner, S. *Energy & Environmental Science* **2014**, *7 (5)*, 1725-1736.

(12) McNeill, C.R.; Abrusci, A.; Hwang, I.; Ruderer, M.A.; Müller-Buschbaum, P.; Greenham, N.C. *Advanced Functional Materials* **2009**, *19 (19)*, 3103-3111.

(13) Kim, F.S.; Ren, G.; Jenekhe, S.A. *Chemistry of Materials* **2011**, *23 (3)*, 682-732.

(14) Wang, H.-W.; Pentzer, E.; Emrick, T.; Russell, T.P. *ACS Macro Letters* **2014**, *3 (1)*, 30-34.

(15) Hernández, J.J.; Rueda, D.R.; García-Gutiérrez, M.C.; Nogales, A.; Ezquerra, T.A.; Soccio, M.; Lotti, N.; Munari, A. *Langmuir* **2010**, *26 (13)*, 10731-10737.

(16) Garcia-Gutierrez, M.-C.; Linares, A.; Martin-Fabiani, I.; Hernandez, J.J.; Soccio, M.; Rueda, D.R.; Ezquerra, T.A.; Reynolds, M. *Nanoscale* **2013**, *5 (13)*, 6006-6012.

(17) Pisula, W.; Kastler, M.; El Hamaoui, B.; García-Gutiérrez, M.-C.; Davies, R.J.; Riekel, C.; Müllen, K. *ChemPhysChem* **2007**, *8 (7)*, 1025-1028.

(18) Brown, P.J.; Thomas, D.S.; Köhler, A.; Wilson, J.S.; Kim, J.-S.; Ramsdale, C.M.; Sirringhaus, H.; Friend, R.H. *Physical Review B* **2003**, *67 (6)*, 064203.

(19) Duan, C.; Cai, W.; Hsu, B.B.Y.; Zhong, C.; Zhang, K.; Liu, C.; Hu, Z.; Huang, F.; Bazan, G.C.; Heeger, A.J.; Cao, Y. *Energy & Environmental Science* **2013**, *6 (10)*, 3022-3034.

(20) Boltau, M.; Walheim, S.; Mlynek, J.; Krausch, G.; Steiner, U. *Nature* **1998**, *391 (6670)*, 877-879.

(21) Heriot, S.Y.; Jones, R.A.L. *Nature Materials* **2005**, *4 (10)*, 782-786.

(22) Wang, T.; Pearson, A.J.; Dunbar, A.D.F.; Staniec, P.A.; Watters, D.C.; Yi, H.; Ryan, A.J.; Jones, R.A.L.; Iraqi, A.; Lidzey, D.G. *Advanced Functional Materials* **2012**, *22 (7)*, 1399-1408.

(23) Ade, H.; Hitchcock, A.P. *Polymer* **2008**, *49 (3)*, 643-675.

(24) Ade, H.; Stoll, H. *Nature Materials* **2009**, *8 (4)*, 281-290.

(25) Watts, B.; McNeill, C.R.; Raabe, J. *Synthetic Metals* **2012**, *161 (23–24)*, 2516-2520.

(26) Koprinarov, I.N.; Hitchcock, A.P.; McCrory, C.T.; Childs, R.F. *The Journal of Physical Chemistry B* **2002**, *106 (21)*, 5358-5364.

(27) Lu, X.; Hlaing, H.; Germack, D.S.; Peet, J.; Jo, W.H.; Andrienko, D.; Kremer, K.; Ocko, B.M. *Nature Communications* **2012**, *3*, 795.

(28) A.P. Hitchcock, a., analysis of X-ray Images and Spectra, 2000. http://unicorn.mcmaster.ca/aXis2000.html.

(29) Wu, Z.; Petzold, A.; Henze, T.; Thurn-Albrecht, T.; Lohwasser, R.H.; Sommer, M.; Thelakkat, M. *Macromolecules* **2010**, *43 (10)*, 4646-4653.

(30) Kohn, P.; Rong, Z.; Scherer, K.H.; Sepe, A.; Sommer, M.; Müller-Buschbaum, P.; Friend, R.H.; Steiner, U.; Hüttner, S. *Macromolecules* **2013**, *46 (10)*, 4002-4013.

(31) Lide, D.R., Handbook of Chemistry and Physics, *CRC Press* (2003).

(32) Alexeev, A.; Loos, J. *Organic Electronics* **2008**, *9 (1)*, 149-154.

(33) Dante, M.; Peet, J.; Nguyen, T.-Q. *The Journal of Physical Chemistry C* **2008**, *112 (18)*, 7241-7249.

(34) Kamkar, D.A.; Wang, M.; Wudl, F.; Nguyen, T.-Q. *ACS Nano* **2012**, *6 (2)*, 1149-1157.

(35) Mativetsky, J.M.; Loo, Y.-L.; Samori, P. *Journal of Materials Chemistry C* **2014**, *2 (17)*, 3118-3128.

(36) Bozano, L.; Carter, S.A.; Scott, J.C.; Malliaras, G.G.; Brock, P.J. *Applied Physics Letters* **1999**, *74 (8)*, 1132-1134.

(37) Goh, C.; Kline, R.J.; McGehee, M.D.; Kadnikova, E.N.; Fréchet, J.M.J. *Applied Physics Letters* **2005**, *86 (12)*, 122110.

(38) Blom, P.W.M.; de Jong, M.J.M.; van Munster, M.G. *Physical Review B* **1997**, *55 (2)*, R656-R659.

(39) Campbell, I.H.; Smith, D.L.; Neef, C.J.; Ferraris, J.P. *Applied Physics Letters* **1999**, *74 (19)*, 2809-2811.

Chapter 4. Laser-induced periodic surface structures on conjugated polymers

4.1. Laser-induced periodic surface structures on Poly(3-hexylthiophene-2,5-diyl)

The semiconducting semicrystalline polymer poly(3-hexylthiophene-2,5-diyl) (P3HT) has been widely studied as the active layer in organic field-effect transistors (OFET)[1-3] and organic solar cells.[4-7] In organic photovoltaics (OPVs), the dissociated free charges (electrons and holes) are generated at the interface between the donor (e− donor) and acceptor (e− acceptor) phases and then transported to their respective electrodes, forming the external circuit. Therefore, increasing the interfacial area between the e− donor and e− acceptor phases and limiting the morphology of the heterojunction to the nanoscale are critical for improving the device performance. Several attempts to produce nanostructures of semiconducting polymers have been carried out in order to improve the device efficiencies of P3HT-based polymer solar cells.[8, 9] Nanostructuring approaches such as those using either anodic aluminum oxide (AAO) membranes[10, 11] or nanoimprint lithography (NIL)[12, 13] have been successfully accomplished in P3HT. It is well-known that molecular order and crystallinity in semiconducting polymers have a significant impact on their physical properties.[14-16] In general, higher crystallinity levels increase the molecular order and enhance charge mobility along chains, leading to an improvement of the electrical transport properties of the material. Therefore, the knowledge about changes in the crystalline structure and molecular chain orientation of the polymer nanostructures is essential in order to correlate the structural parameters with the electrical properties.[17] P3HT consists of a relatively stiff main chain of thiophene rings with one hexyl group as side substituent to render the conjugated polymer more soluble in organic solvents. Typically, this polymer develops layered crystalline structures with separated main chain and hexyl groups. The π–π stacking of planar polymer backbones leads to delocalization of electronic states across different chains.[18] Regioregular P3HT (RR-P3HT) forms crystal sheets by π–π stacking of the thiophene rings in such a way that the alkyl side group can eventually crystallize. In addition, as typical semicrystalline polymers, P3HT forms ~10 nm wide crystalline regions separated by amorphous interlayers.[19-21] Variations in crystallinity and

orientation of P3HT under different conditions like thermal processing, doping with additives,[22] or by confinement[23, 24] have been detected by X-ray scattering techniques. In particular, confining P3HT within nanostructured grooves by NIL induces a 90° backbone reorientation near the grating sidewalls, which frustrates the strong tendency of P3HT molecules to orient edge-on relative to substrate and air interfaces in thin films.[25] A similar effect takes place for P3HT infiltrated into AAO membranes where it was found that the P3HT chains inside the nanorods are aligned in the direction normal to the AAO pore wall. Thus, chains in P3HT nanorods have a partial flat-on orientation with respect to the residual polymer film.[26] Besides common patterning methods, it is also possible to fabricate Laser-Induced Periodic Surface Structures (LIPSS) on polymer surfaces.[27, 28] This laser nanostructuring technique can be envisioned as a potential alternative to lithography processes, avoiding the necessity of using clean rooms, high vacuum systems, or mask fabrication among others.

4.1.1. Sample preparation

A solution of P3HT in chlorobenzene (24 g/L) was prepared and stirred at 30 °C for 1 h. Thin polymer films were prepared by spin-coating on the polished surface of silicon wafers (100) (ACM, France). The wafers were previously cleaned with acetone and isopropanol. A fixed amount of 0.2 mL of polymer solution was dropped by a pipette on a square silicon substrate placed in the center of a rotating metallic horizontal plate. A rotation rate of 2400 rpm was kept during 60 s. The thickness of the obtained thin films was 140 ± 20 nm with a roughness of a few nanometers, both measured by AFM. For NEXAFS measurements, polymer solutions were spin-coated on silicon substrates, and then floated off into a very dilute NaOH/water solution (0.25 wt %), and finally picked up with Transmission Electron Microscopy (TEM) grids.

Laser irradiation was carried out under ambient air conditions at normal incidence with a linearly polarized laser beam of a Q-switched Nd:YAG laser (pulse duration of 8 ns) at two different wavelengths, i.e., with the second, 532 nm, and fourth harmonic, 266 nm, at a repetition rate of 10 Hz. These wavelengths were selected for the experiments because P3HT absorbs efficiently with an absorption coefficient of $\approx 6.0 \times 10^4$ cm^{-1} at 532 nm and in the range of $\approx 1 \times 10^4$ cm^{-1} at 266 nm (see Figure 3.2).

4.1.2. Dependence of LIPSS on fluence and number of pulses at 532 nm

Typical nanostructures obtained irradiating with the laser at 532 nm with different fluences and number of pulses are shown in Figures 4.1 and 4.2, respectively. In both cases, by varying the laser conditions well-ordered ripples can be fabricated. From the AFM height profiles the sizes of the nanostructures can be analyzed.

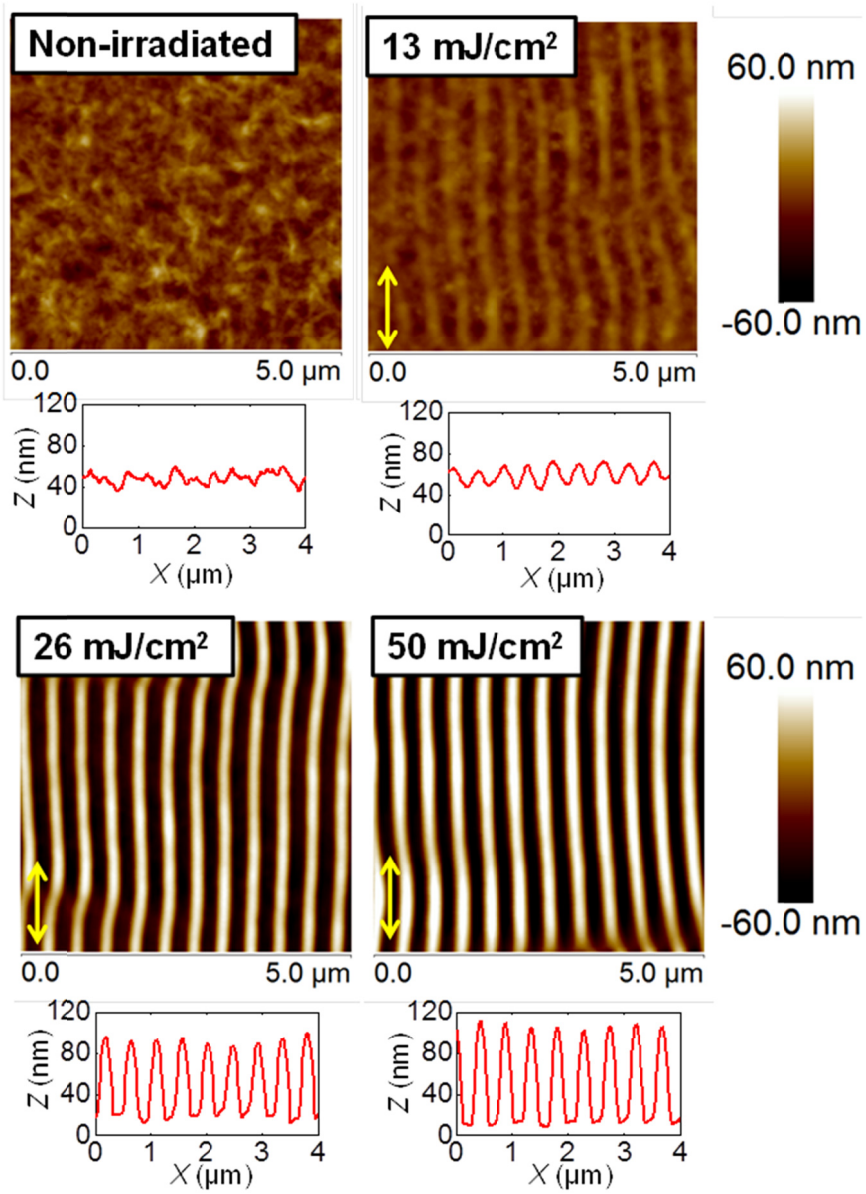

Figure 4.1. AFM height images of LIPSS on P3HT thin films at an irradiation wavelength of 532 nm upon irradiation with 3600 pulses varying the fluence. Height profiles over lengths of 4 µm are shown at the bottom of every image. The double arrow (↔) indicates the polarization vector of the laser beam.

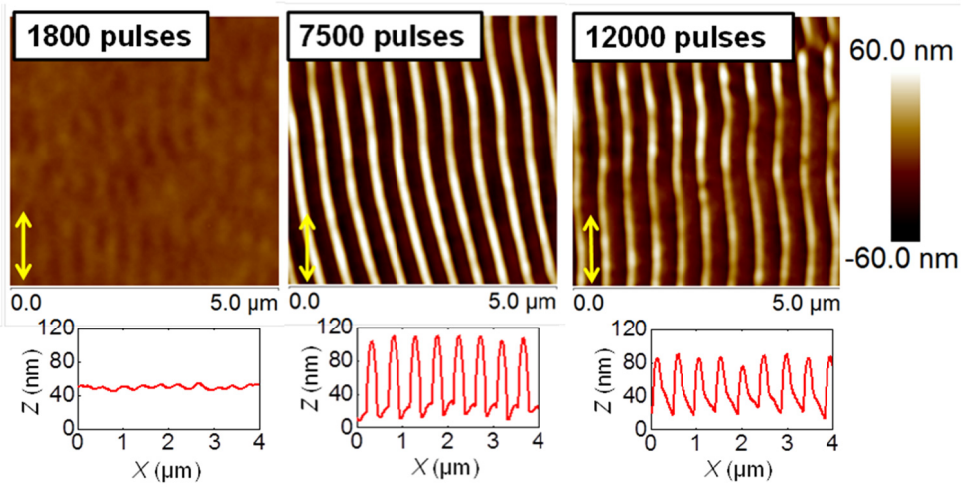

Figure 4.2. AFM height images of LIPSS on P3HT thin films at an irradiation wavelength of 532 nm and a fixed fluence of 26 mJ/cm^2 varying the number of pulses. Height profiles over lengths of 4 μm are shown at the bottom of every image. The double arrow (↔) indicates the polarization vector of the laser beam.

Ripple periods (L) and depths (Z) for samples irradiated at different fluences and number of pulses are represented in Figure 4.3 for the wavelength of 532 nm.

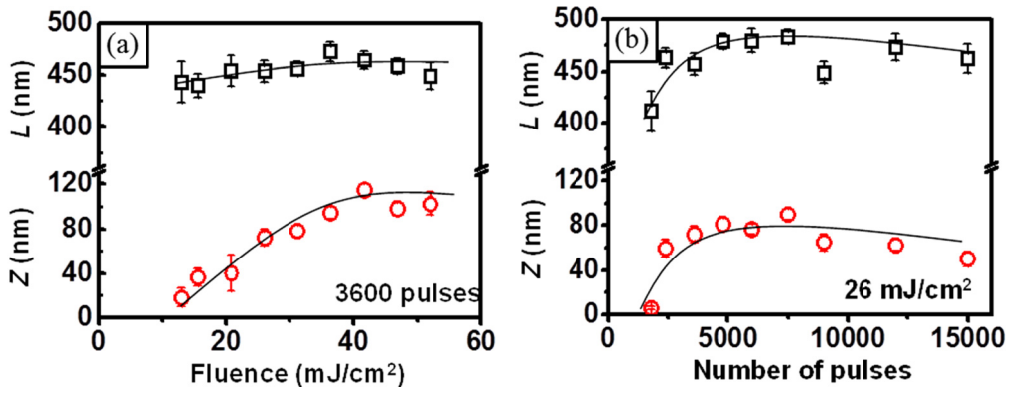

Figure 4.3. Variation of (□) periods (L) and (○) depths (Z) of LIPSS as a function of: (a) fluence and (b) number of pulses for the laser irradiation wavelength 532 nm. Lines are shown as visual guides.

The dependence of the period of LIPSS with the fluence at 3600 pulses is presented in Figure 4.3.a. This number of pulses was selected to ensure that LIPSS with good quality are obtained for several laser fluences. The figure shows that the period slightly increases up to a fluence of about 26 mJ/cm^2 and remains practically constant afterward. Above 50 mJ/cm^2, the ripples start to deteriorate. Regarding the depth of the ripples, it

increases up to 100 nm for 40 mJ/cm^2, reaching a plateau above this fluence value (Figure 4.3.a). At a constant fluence, the period increases up to ≈ 4500 pulses and reaches a plateau (Figure 4.3.b) with a value slightly smaller than the laser wavelength and decreases after about 10000 pulses. The depth of the ripples follows a similar tendency to what is observed in the dependence with the fluence, increasing up to 90 nm for ≈ 4500 pulses (Figure 4.3.a).

4.1.3. Dependence of LIPSS on the laser wavelength

Topography images of LIPSS obtained at 266 nm at a fixed number of pulses of 3600 and different fluences are shown in Figure 4.4. LIPSS present different periods and sizes. A similar behavior is observed in Figure 4.5 when fabricating LIPSS at a fluence of 13.4 mJ/cm^2 and different number of pulses.

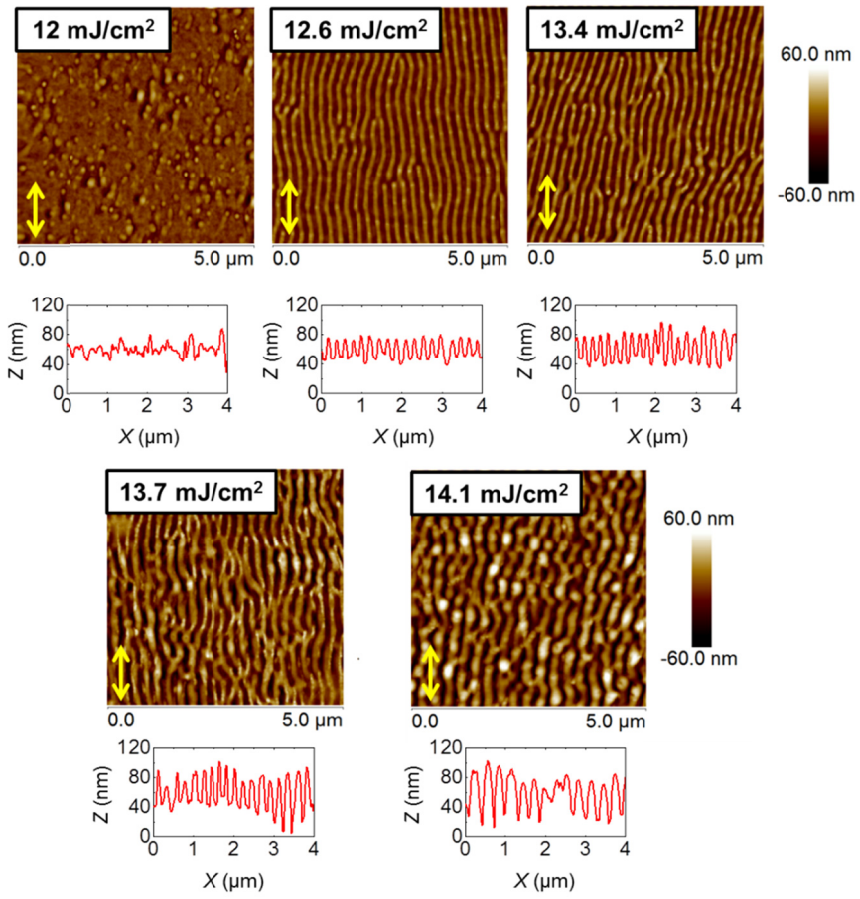

Figure 4.4. AFM height images of LIPSS on P3HT thin films at an irradiation wavelength of 266 nm and 3600 pulses varying the fluence. Height profiles over lengths of 4 µm are shown at the bottom of every image. The double arrow (↔) indicates the polarization vector of the laser beam.

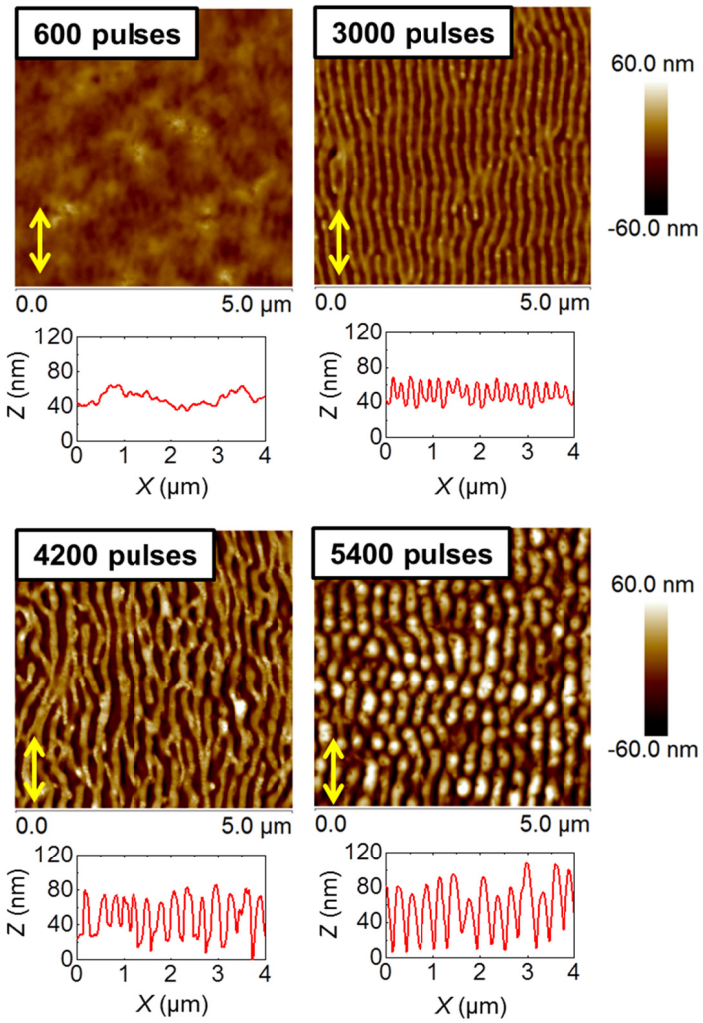

Figure 4.5. AFM height images of LIPSS on P3HT thin films at an irradiation wavelength of 266 nm and a fixed fluence of 13.4 mJ/cm^2 varying the number of pulses. Height profiles over lengths of 4 µm are shown at the bottom of every image. The double arrow (↔) indicates the polarization vector of the laser beam.

The dependence of the LIPSS period with the fluence at 3600 pulses is presented in Figure 4.6.a. The period increases up to a value of fluence of about 14 mJ/cm^2 and remains practically constant at a value close to the irradiation wavelength. Regarding the depth of ripples, it increases up to 85 nm for 14 mJ/cm^2, reaching a plateau at higher fluence values (Figure 4.6.a). Above 14.7 mJ/cm^2, the ripples start to deteriorate.

Figure 4.6.b shows the dependence of period and depth of ripples generated at 266 nm as a function of the number of pulses at a constant fluence of 13.4 mJ/cm^2. The period remains constant for about 2500 pulses and subsequently increases, reaching a plateau with a value close to the laser wavelength upon irradiation with 5500 pulses as shown in

Figure 4.6.b. The variation of LIPSS depth as a function of the number of pulses follows a similar behavior, increasing up to 5000 pulses and reaching a plateau of about 70 nm (Figure 4.6.b).

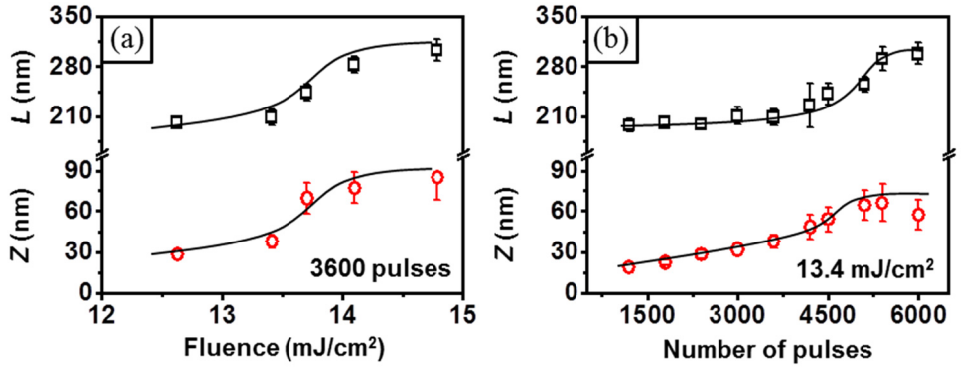

Figure 4.6. Variation of (□) periods (L) and (○) depths (Z) of LIPSS as a function of (a) fluence and (b) number of pulses for the laser irradiation wavelength of 266 nm. Lines are shown as visual guides.

Topography AFM images of the optimal P3HT LIPSS in terms of ripple depth and period for the two laser wavelengths used, 532 nm and 266 nm, are shown in Figure 4.7. In this case periods obtained were 450 nm and 250 nm for irradiation at 532 and 266 nm respectively.

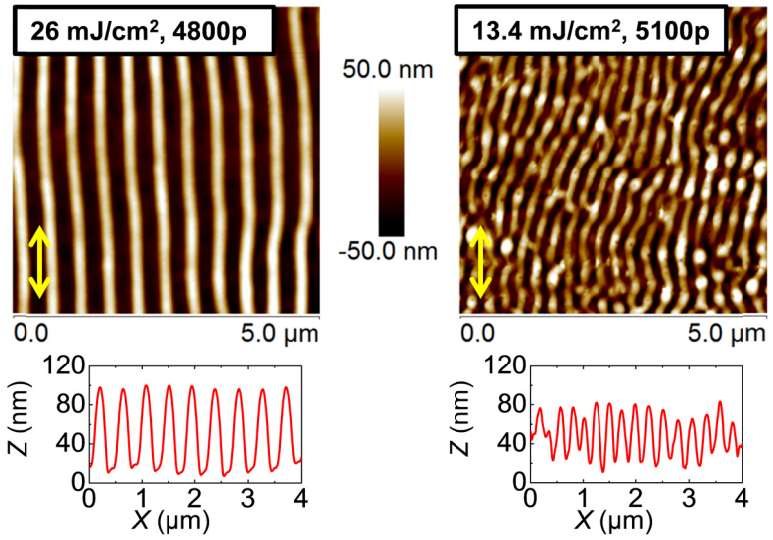

Figure 4.7. AFM height images of optimal LIPSS in terms of depth and period obtained on P3HT thin films: a) at 532 nm, fluence of 26 mJ/cm^2 and 4800 pulses and b) at 266 nm, fluence of 13.4 mJ/cm^2 and 5100 pulses. Height profiles over lengths of 4 µm are shown at the bottom of each image. The polarization vector of the laser beam is indicated by double arrows (↔).

In general, LIPSS fabricated at 266 nm present structures with a lower degree of order than those created with the irradiation wavelength of 532 nm. Differences in the quality of the structures in terms of regularity of lengths and size of the ripples are related to the absorption coefficient of the material at each wavelength. The higher absorption coefficient of P3HT at 532 nm in relation to that at 266 nm ($\boldsymbol{\mu}_{266} \approx 1 \times 10^4$ cm^{-1} vs $\boldsymbol{\mu}_{532} \approx 6 \times 10^4$ cm^{-1}), leads to the formation of better ordered ripples irradiating at 532 nm than those observed irradiating at 266 nm. However, formation of LIPSS has been reported for polymers with an absorption coefficient as low as 3000 cm^{-1}. This is the case of polystyrene[29] at 248 nm for which LIPSS have been reported upon irradiation at fluences in the range 7− 9 mJ/cm^2 after a few thousand pulses.[30] Therefore, there should be another reason accounting for LIPSS of less quality than those obtained at the visible wavelength. One possibility is the fact that hexylthiophenes with low molecular weight (oligomers) absorb efficiently in the region of 266 nm, whereas a higher degree of conjugation induces a shift in the absorption band toward larger wavelengths (around 500 nm). Therefore, in the UV−visible spectrum of P3HT (see Figure 3.2) the absorption at 266 nm is attributed to oligomers[31] and the LIPSS mechanism is less efficient.

It has been reported previously that in order to obtain LIPSS in amorphous polymers a minimum fluence value is necessary to ensure that the surface temperature overcomes the glass transition temperature (T_g), allowing the polymer chains to have enough segmental and chain dynamics to reorganize.[32] In the case of semicrystalline polymers, such as regioregular P3HT, the thermal properties are governed not only by the glass transition temperature but also by the melting temperature (T_m). It means that in the range of fluences for which LIPSS are obtained in this case the temperature reached at sample surface is expected to be higher than T_m and as a result of that superficial crystallites are expected to melt providing enough mobility to the polymer chains to reorganize spatially.

Due to the fact that LIPSS formed irradiating at 532 nm present more regular ripples, a more extensive characterization of the structures created in this case was accomplished.

4.1.4. Electrical characterization by conductive-AFM

C-AFM was used to characterize the electrical properties at the nanoscale of LIPSS produced by irradiating a P3HT thin film at 532 nm. Figure 4.8 shows the C-AFM current images (electric current map), acquired in contact mode, of a P3HT thin film sample before irradiation (Figure 4.8.a) and after irradiation with a fluence of 26 mJ/cm^2 and 4800 pulses (Figure 4.8.b) by applying a constant voltage of −5 V on the conducting substrate.

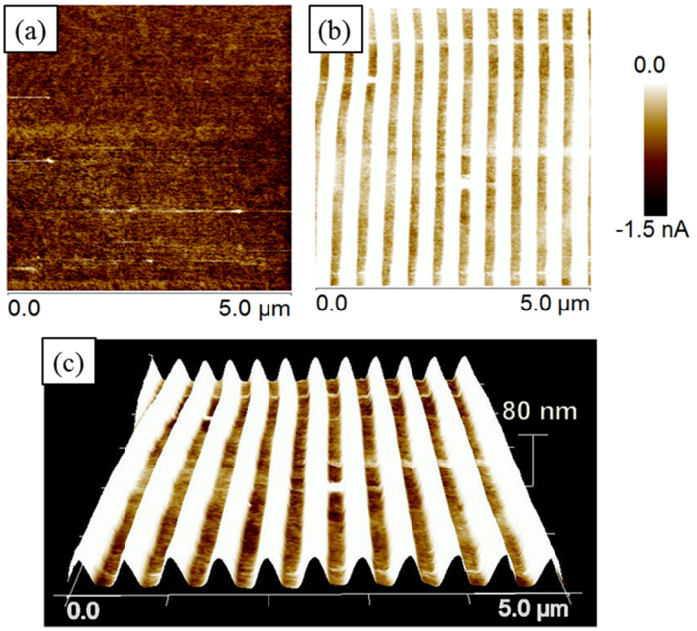

Figure 4.8. C-AFM current images of a P3HT thin film measured at a constant bias of -5 V. (a) Non-irradiated film, (b) film with LIPSS fabricated at 532 nm, 26 mJ/cm^2 and 4800 pulses. (c) Overlap of height and current images of P3HT with LIPSS. Height scale is 80 nm.

The current image of the sample before irradiation shows that the thin film is conductive in the whole area, whereas the image displaying the current map of the irradiated thin polymer film shows stripes with conductivity similar to that of the initial thin film separated by non-conductive ones. It is worth noting that C-AFM measurements performed in P3HT films with different thicknesses, ranging from 50 to 350 nm, revealed that all of them were conductive. Thus, it can be established that the observed effect in Figure 4.8.b is not caused by the thickness difference between trenches and ridges. To correlate conductive regions with either trenches (bottom) or ridges (top) observed in the height image, we have overlapped topography and current images (Figure 4.8.c). It is observed that conductive regions correspond to trenches and

non-conductive regions to ridges. This fact might be attributed in principle either to selective chemical damage because of laser irradiation or to reorganization of the polymer chains and therefore to possible structural changes like partial loss of crystallinity in the ridges. These two aspects will be addressed in the following sections.

4.1.5. Chemical stability and structural modification in nanostructured P3HT thin films

4.1.5.1. Near Edge X-ray Absorption Fine Structure

NEXAFS experiments were performed in order to gain further information about the chemical stability of the P3HT thin films after laser irradiation at 532 nm. The experiments were carried out at the PolLux beamline at the Swiss Light Source. A NEXAFS spectrum in the K-edge reveals the excitation of 1s electrons to unfilled molecular orbitals. The NEXAFS spectra in the carbon K-edge of pristine thin films and of those with LIPSS are presented in Figure 4.9. The shape of the spectra is as expected[33, 34] for P3HT. The sharp peak at 285 eV corresponding to the C1s → π* transitions is characteristic of the strong electronic delocalization along the conjugated backbone of thiophene rings and therefore very sensitive to differences in the polymer π backbone. Other characteristic peaks are assigned to C 1s → σ*(C−H) transitions at approximately 287−288 eV, corresponding to the hexyl group, and to a broad set of C 1s → σ* (C−C) transitions near 293 eV.[34] Overall, NEXAFS results suggest the absence of significant changes in the chemical structure of P3HT after LIPSS formation.

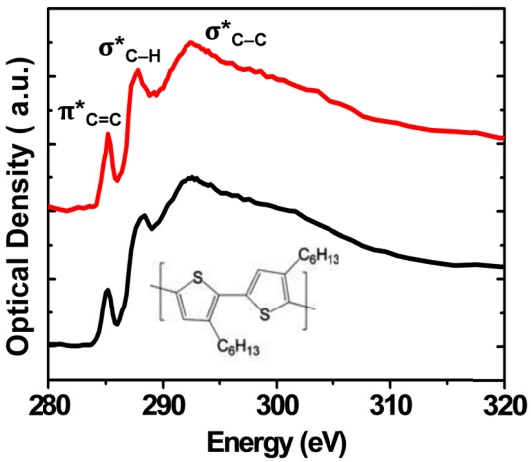

Figure 4.9. NEXAFS spectra in the carbon K-edge of P3HT (chemical structure shown) thin film (red line) and of P3HT film with LIPSS fabricated at 532 nm, 26 mJ/cm^2 and 4800 pulses (black line). The spectra have been vertically shifted for clarity.

4.1.5.2. Raman Spectroscopy

To elucidate the reason for the different electrical properties of ridges and trenches of P3HT films endowed with LIPSS at 532 nm, micro-Raman measurements were performed at different excitation conditions (λ_{exc} = 785, 532 and 442 nm). Figure 4.10 shows the Raman spectra of P3HT thin films (red) and P3HT with LIPSS fabricated at 532 nm, 26 mJ/cm^2 and 4800 pulses (black) at the different excitation wavelengths employed.

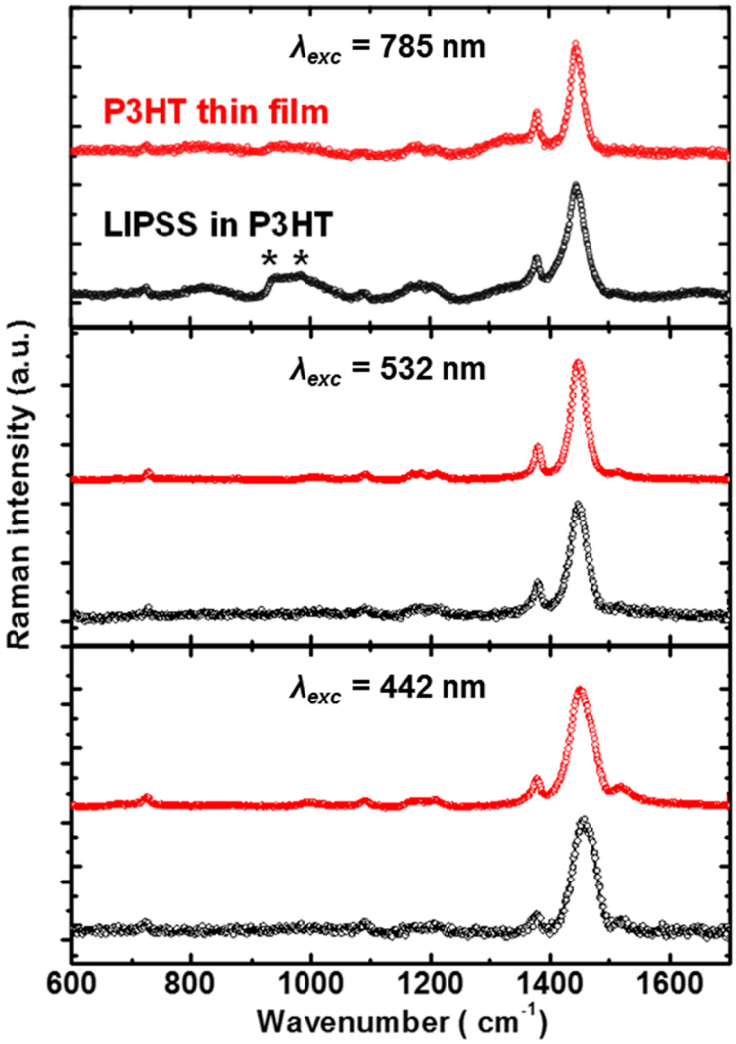

Figure 4.10. Raman spectra of non-irradiated P3HT thin films (red) and films with LIPSS fabricated at 532 nm, 26 mJ/cm^2 and 4800 pulses (black) under different excitation wavelengths. Star marks (**) in Figure (top) correspond to silicon bands.

The spectra present characteristic bands at 1445 and 1380 cm^{-1}, which can be assigned to the symmetric stretching mode of the C=C and C−C intra-rings bonds, respectively.[35]

In particular, one should focus on the 1350−1500 cm^{-1} spectral range which is shown enlarged in Figure 4.11. This region is known to be sensitive to the π-electron delocalization, i.e., related to the conjugation length and optical absorption, of the P3HT chains.[35, 36] It is well-known that regioregular P3HT (RR-P3HT) thin films present optical absorption between 400 and 600 nm.[6] This indicates that excitation at 785 nm occurs under non-resonance conditions, whereas excitation at 532 and 442 nm leads to measurements under resonance conditions. The spectra obtained under non-resonance conditions (λ_{exc} = 785 nm) exhibit similar positions for the ν(C=C) band (symmetric stretching mode) for both the non-irradiated films and those with LIPSS. There is no evidence of new bands, suggesting that the P3HT thin films are relatively stable under the irradiation conditions used for fabricating LIPSS at 532 nm. In addition, the peak intensity ratio between the two bands at 1380 and 1445 cm^{-1} is similar; therefore, no significant evidence of P3HT photo-degradation exists. The difference between non-irradiated and irradiated thin films (with LIPSS) is emphasized when focusing on the Raman spectra in the 1350− 1500 cm^{-1} spectral range shown in Figure 4.11 (top).

A detailed inspection reveals the appearance of a shoulder at 1420 cm^{-1} (marked by a continuous arrow) on the lower wavenumber region of the ν(C=C) band. This shoulder is assigned to the stretching of the C=C bond of the quinoid form of P3HT because of the oxidation of the aromatic backbone.[37-39] However, under resonance conditions the results are quite different. At this point, it is worth mentioning that the optical absorption of RR-P3HT in solution presents an absorption maximum near 400 nm, whereas RR-P3HT thin films present a redshift of absorption maximum up to 600 nm. This is due to the difference in conjugation length between RR-P3HT in solution where the polymer is disordered and RR-P3HT thin films where the polymer is semicrystalline and therefore partially ordered.[35] In principle, polymer segments in ordered regions should exhibit higher conjugation length than those located in the amorphous regions. Therefore, in RR-P3HT thin films, the absorption near 400 nm is associated with the disordered chains, whereas absorption near 600 nm is associated with ordered chains.[36, 40] Thus, in the Raman spectra under resonance conditions at λ_{exc} = 442 nm, corresponding to a region of high absorption for disordered P3HT chains, the ν(C=C) band shifts toward higher wavenumbers where it also presents a shoulder, marked by a dotted arrow in Figure 4.11 (bottom). It has been previously reported[16, 35, 41] that under resonance conditions, the intensity of Raman bands from disordered regions is

enhanced. Moreover, the Raman spectra collected at an excitation wavelength of 532 nm, for both the P3HT thin film and the P3HT with LIPSS, do not present noticeable variations in the position of the ν(C=C) band, similar to what is observed in the spectra collected at 785 nm. This effect may be related to the fact that under these resonance conditions (λ_{exc} = 532 nm), P3HT segments located in ordered regions absorb more strongly than those in the amorphous phase.[40]

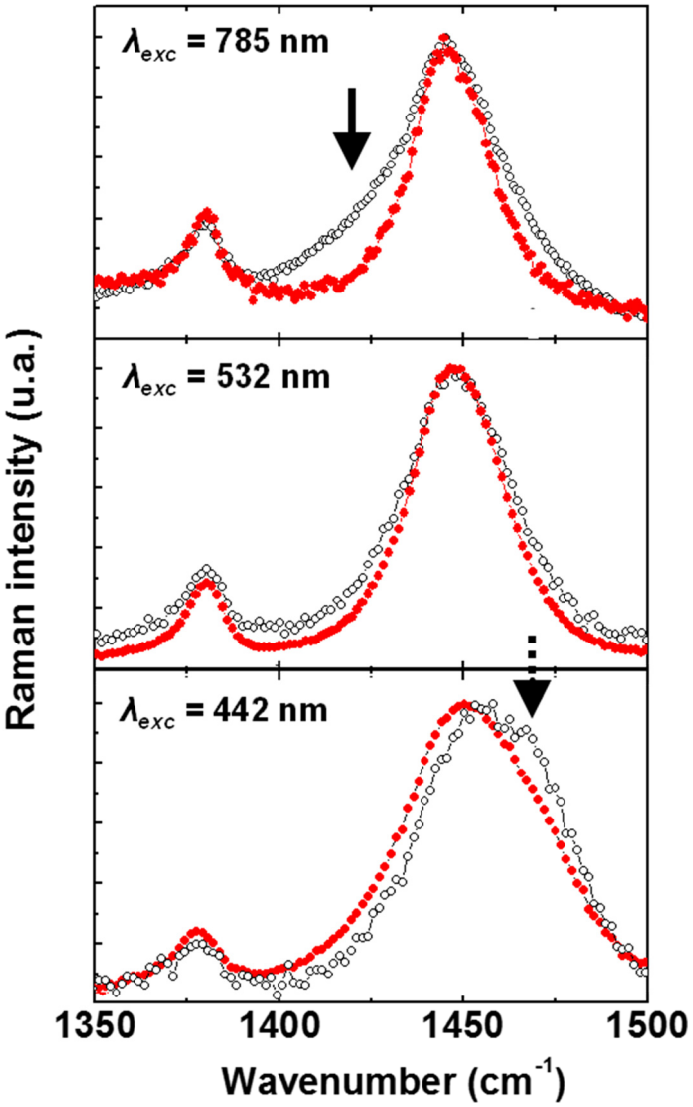

Figure 4.11. Comparison of the ν(C=C) band region before (red) and after laser irradiation (black). The continuous and dotted arrows indicate the ν(C=C) vibration of the quinoid form and amorphous phase respectively.

Because the Raman spectra obtained by excitation at λ_{exc} = 442 nm present variations, it is possible to deconvolute the Raman bands into their two contributions. The more intense contribution appearing at lower wavenumbers (~1445 cm^{-1}) corresponds to the crystalline phase with a higher conjugation length, whereas the less intense band (~1470 cm^{-1}) corresponds to the ν(C=C) bonds of the amorphous phase with lower conjugation length.[40] Figure 4.12 shows the deconvolution of the ν(C=C) band of non-irradiated P3HT thin film and P3HT thin film with LIPSS by simple Lorentzians, in accordance to previous works.[16, 41]

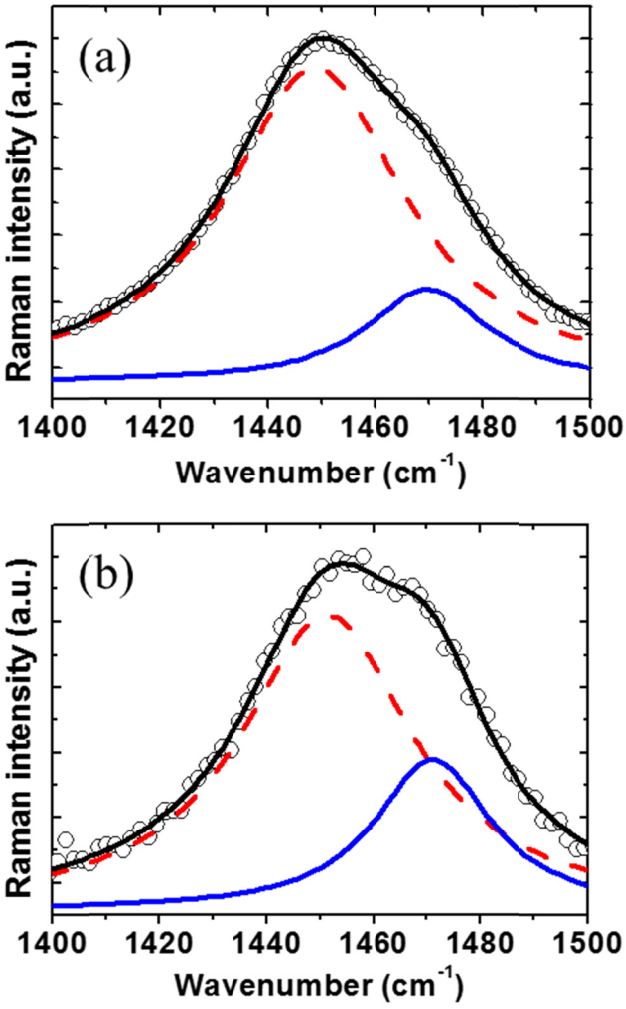

Figure 4.12. Deconvolution of the ν(C=C) band of the Raman spectra (circles) of a P3HT thin film collected at 442 nm laser excitation: (a) before and (b) after LIPSS formation by irradiation at 532 nm, 26 mJ/cm^2 and 4800 pulses. The red dashed line corresponds to the ordered phase and the blue continuous line to the disordered phase. The black continuous line is the fitting of the experimental data.

These results indicate a relative increase of the amorphous phase after laser irradiation. From Figure 4.12, we can estimate the relative fraction of crystalline phase (ϕ) of the P3HT thin film before and after LIPSS formation, by the relation $\phi = A_c/(A_c + A_a)$, where A_c is the area under the red dashed curve (ordered contribution) and A_a is the area under the blue continuous curve (disordered contribution) in Figure 4.12. We obtain values of $\phi_{P3HT} = 0.83$ and $\phi_{P3HT\text{-}LIPSS} = 0.71$. Because $\phi_{P3HT} > \phi_{P3HT\text{-}LIPSS}$, we can infer that the P3HT loses crystallinity during LIPSS formation. This result can be correlated with the overlapping image of height and current of the sample with LIPSS (Figure 4.8.c). Thus, we propose that the lower conductivity of the ridges can be attributed to an increase of the chain disorder after LIPSS formation. To further support this statement, GIWAXS experiments were performed and they will be discussed in the next section.

4.1.6. Structural modification of P3HT thin films during LIPSS formation as revealed by GIWAXS

The evolution of the structure of P3HT thin films during LIPSS formation has been investigated by *in situ* GIWAXS experiments using synchrotron radiation. The experiments were performed at BM26 beamline at the European Synchrotron (ESRF). The samples were irradiated at a repetition rate of 10 Hz by using the second harmonic of a Nd:YAG laser (532 nm) with pulses of 8 ns. GIWAXS patterns were acquired during repetitive laser pulse irradiation. The 2D X-ray scattering patterns presented in Figure 4.13 from the non-irradiated P3HT thin film (Figure 4.13.a) and for the film with LIPSS (Figure 4.13.b) show similar orientation and number of reflections. The three meridional reflections h00 are consecutive orders of the 100 reflection with a q-value of 3.8 nm^{-1}. The equatorial weak reflection with a reciprocal scattering vector q-value of 16.39 nm^{-1} is attributed to the superposition of the 020 and 002 reflections. In agreement with previous reports,[20, 21] crystal structure of P3HT consists of sheets formed by the π–π stacking of the thiophene rings. In addition, the meridional reflections reveal that the P3HT thin film is uniaxially oriented with mainly an edge-on configuration, which corresponds to the usual conformation adopted by P3HT thin films consisting of polymer chains parallel to the substrate. A similar orientation is observed for the film with LIPSS. Figure 4.14 presents the intensity profiles along the meridian (Figure 4.14.a) and along the equator (Figure 4.14.b), obtained by the radial integration of the 2D GIWAXS patterns as a function of number of pulses. The main result

obtained is that the crystalline structure is not significantly affected during LIPSS formation. This effect further supports the indication of chemical stability of P3HT during LIPSS formation, as observed by Raman spectroscopy and NEXAFS and previously discussed.

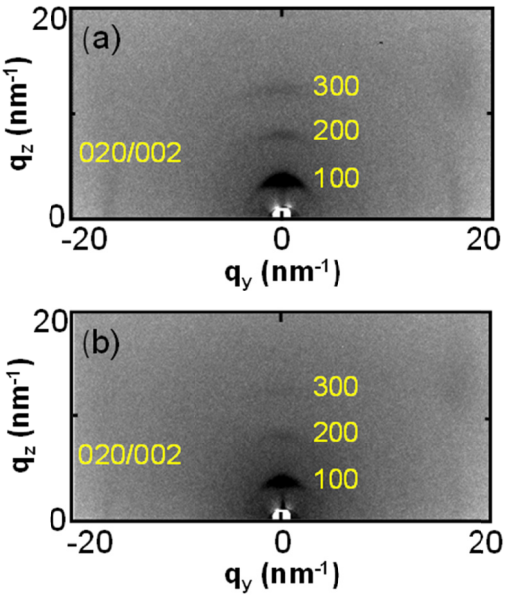

Figure 4.13. Two dimensional GIWAXS patterns for: (a) P3HT thin film and (b) P3HT with LIPSS after irradiation at a fluence of 26 mJ/cm^2 with 4800 pulses.

A close inspection of the diffraction patterns reveals that the intensity of both the 100 and the 020/002 peaks, in comparison with those of the pristine sample, decreases slightly after 50 pulses and remains essentially constant for the rest of the repetitive irradiation process. This agrees with previous reports suggesting that LIPSS formation in polymers proceeds by the heating of the outer polymer surface, enhancing polymer dynamics in a way that facilitates the reorganization of the material into the characteristic ripples.[32] Our GIWAXS results suggest that laser irradiation of P3HT induces melting of the polymer surface at the initial stages of laser irradiation. Moreover, comparison of initial and final GIWAXS patterns indicates a decrease in the crystallinity of LIPSS in relation to the initial thin film as revealed by the reduction of the intensity of the reflections. This explanation is in agreement with the increment of the amorphous phase observed by Raman spectroscopy. Additionally, by comparison with the C-AFM results (Figure 4.8), the GIWAXS experiments support the formation of ripples with molecular order lower than that of the original thin film. The ripples are over a continuous P3HT thin film whose initial orientation and crystallinity seems to be

unaffected. As a consequence, electrical conduction in the ripples is smaller than that in the trenches (Figure 4.8.c). This observation supports the superficial nature of the LIPSS formation process in which only the outer polymer surface is heated and rearranged.[32]

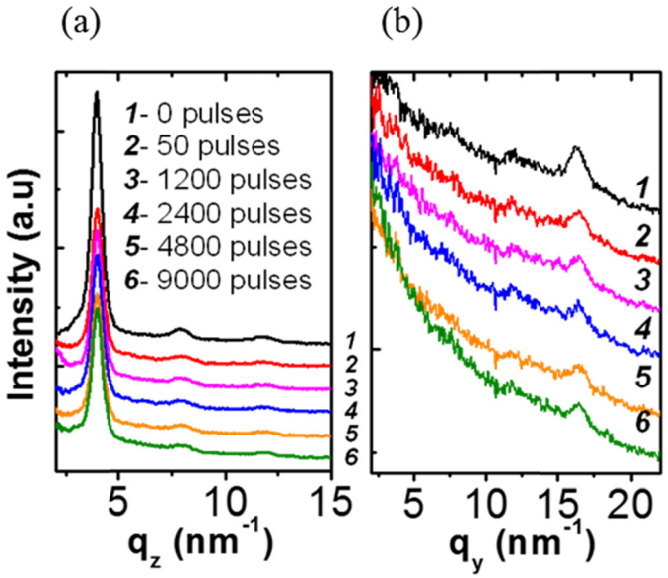

Figure 4.14. Intensity profiles derived for different number of pulses: (a) along the meridional direction and (b) along the equatorial direction.

4.2. Laser-induced periodic surface structures on Poly[N-90-heptadecanyl-2,7-carbazole-alt-5,5-(40,70-di-2-thienyl-20,10,30-benzothiadiazole) (PCDTBT)

4.2.1. Sample preparation

A solution of PCDTBT in chlorobenzene (24 g/L) was prepared and stirred during several hours until complete dissolution. Thin polymer films were prepared by spin-coating on arsenic n-doped silicon substrates (resistivity ≈ 0.001 Ω·cm, Wafer World). The wafers were previously cleaned with acetone and isopropanol. A fixed amount of 0.2 mL of polymer solution was dropped by a pipette on a square silicon substrate placed in the center of a rotating metallic horizontal plate. A rotation rate of 2400 rpm was kept during 60 s for obtaining films of about 190 nm.

For NEXAFS measurements, polymer solutions were spin-coated on silicon substrates, and then floated off into a very dilute NaOH/water solution (0.25 wt %), and finally picked up with Transmission Electron Microscopy (TEM) grids.

Laser irradiation was carried out under ambient air conditions at normal incidence with a linearly polarized laser beam of a Q-switched Nd:YAG laser (pulse duration of 8 ns) at two different wavelengths, i.e., with the second, 532 nm, and fourth harmonic, 266 nm, at a repetition rate of 10 Hz. These wavelengths were selected for the experiments because PCDTBT absorbs efficiently as it is shown in Figure 3.2.

4.2.2. Dependence of LIPSS on fluence and number of pulses at 266 and 532 nm

AFM image shown in Figure 4.15.a reveals that as-cast films of PCDTBT present rather smooth surfaces with a mean surface roughness R_a = 1.2 nm and thus without morphological indications of crystallization. After laser irradiation, under certain fluence conditions well below the ablation threshold, ripples parallel to the polarization vector of the laser are observed. As an example, Figures 4.15.a and 4.15.b show, together with the AFM image of the initial non-irradiated sample, selected height images of PCDTBT films irradiated at 532 nm with different fluences and number of pulses respectively.

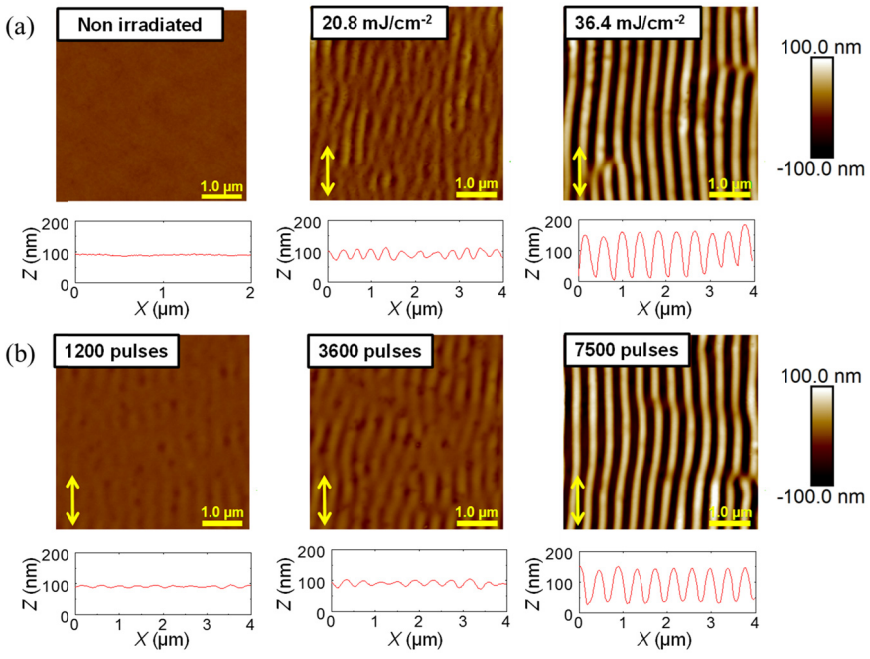

Figure 4.15. AFM height images (5 × 5 µm^2) of PCDTBT: (a) non-irradiated and irradiated at 532 nm with 3600 pulses at different fluences labeled in the upper left corner. (b) Irradiated at 532 nm with a fluence of 26 mJ/cm^2 as a function of number of pulses labeled in the upper left corner. The height profile along a 4 µm line perpendicular to the ripples is shown below every image. The arrows indicate the polarization vector of the laser (↔).

The dependence of the period and depth of LIPSS with the fluence, at 532 nm and 3600 pulses as derived from AFM analysis, is represented in Figure 4.16.a. As observed, the period increases up to a fluence of ≈ 31.2 mJ/cm^2 and remains practically constant afterward with a value slightly smaller than the irradiation wavelength. The depth of ripples follows a similar tendency as the period, increasing up to 120 nm for ≈ 36.4 mJ/cm^2 and reaching a plateau. The dependence of period (L) and depth (Z) of LIPSS at a constant fluence of 26 mJ/cm^2 with the number of pulses is represented in Figure 4.16.b. It shows that the period increases slightly up to ≈ 3600 pulses and reaches a steady level for higher number of pulses. The depth of the ripples increases up to ≈ 6000 pulses reaching a plateau of about 150 nm.

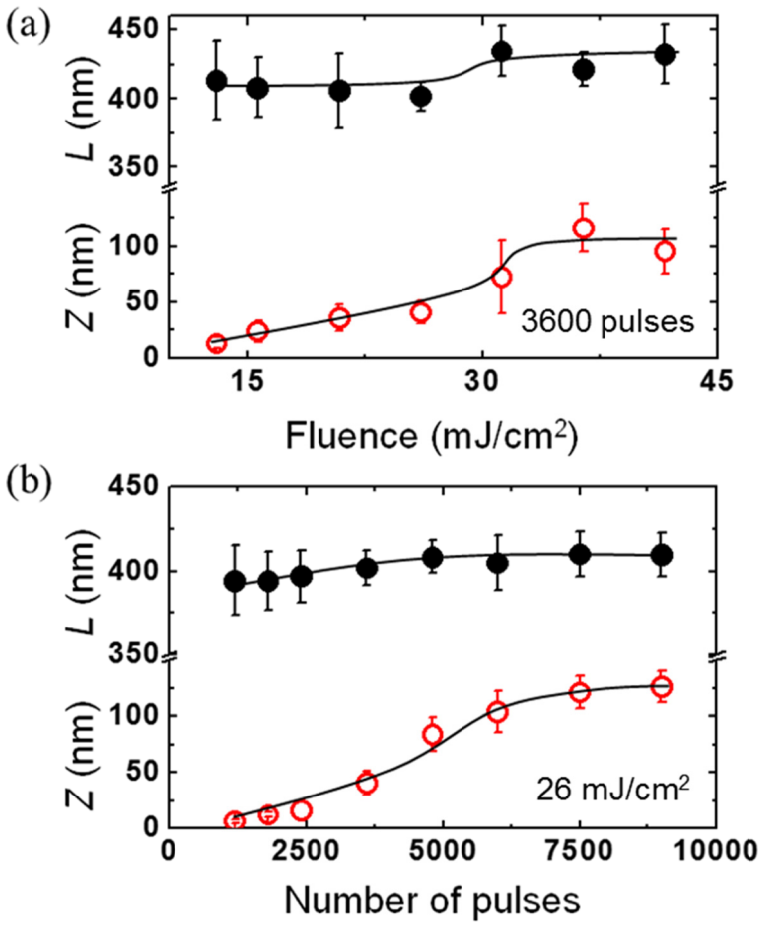

Figure 4.16. Variation of periods (L, filled circles) and depths (Z, empty circles) of LIPSS as a function of: (a) fluence and (b) number of pulses for the laser irradiation wavelength 532 nm. Lines are shown as visual guides.

LIPSS of smaller dimensions are obtained by irradiating the PCDTBT thin films at 266 nm. Selected height AFM images of PCDTBT films irradiated with different fluences and number of pulses are shown in Figure 4.17.

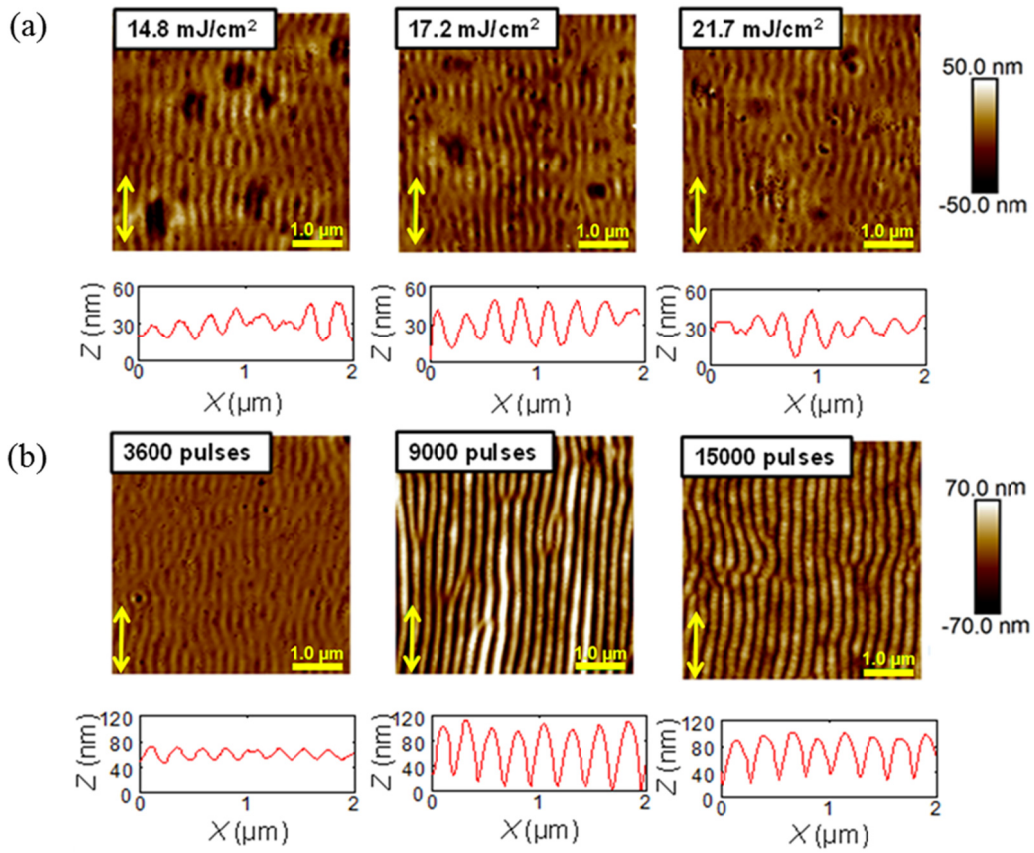

Figure 4.17. AFM height images (5 × 5 µm^2) of PCDTBT: (a) Irradiated at 266 nm with 3600 pulses at different fluences labeled in the upper left corner. (b) Irradiated at 266 nm with a fluence of 13.4 mJ/cm^2 as a function of number of pulses as labeled in the upper left corner. The height profile along a 2 µm line perpendicular to the ripples is shown below every image. The arrows indicate the polarization vector of the laser (↔).

The dependence of the period and depth of LIPSS with the fluence, at 266 nm and 3600 pulses is represented in Figure 4.18.a. It is shown that the period remains practically constant with a value of about 250 nm in the investigated fluence range of 13.4 - 21.7 mJ/cm^2. The depth of ripples follows a similar tendency as the period, remaining almost constant at 30 nm in the investigated fluence range. The dependence of period and depth of LIPSS at a constant fluence of 13.4 mJ/cm^2 with the number of pulses is shown in Figure 4.18.b. It shows that the period increases slightly up to ≈ 3600 pulses and reaches a steady level for higher number of pulses. The depth of the

ripples increases up to 100 nm for ≈ 9000 pulses reaching a plateau and decreases above ≈ 15000 pulses when the ripples start to deteriorate.

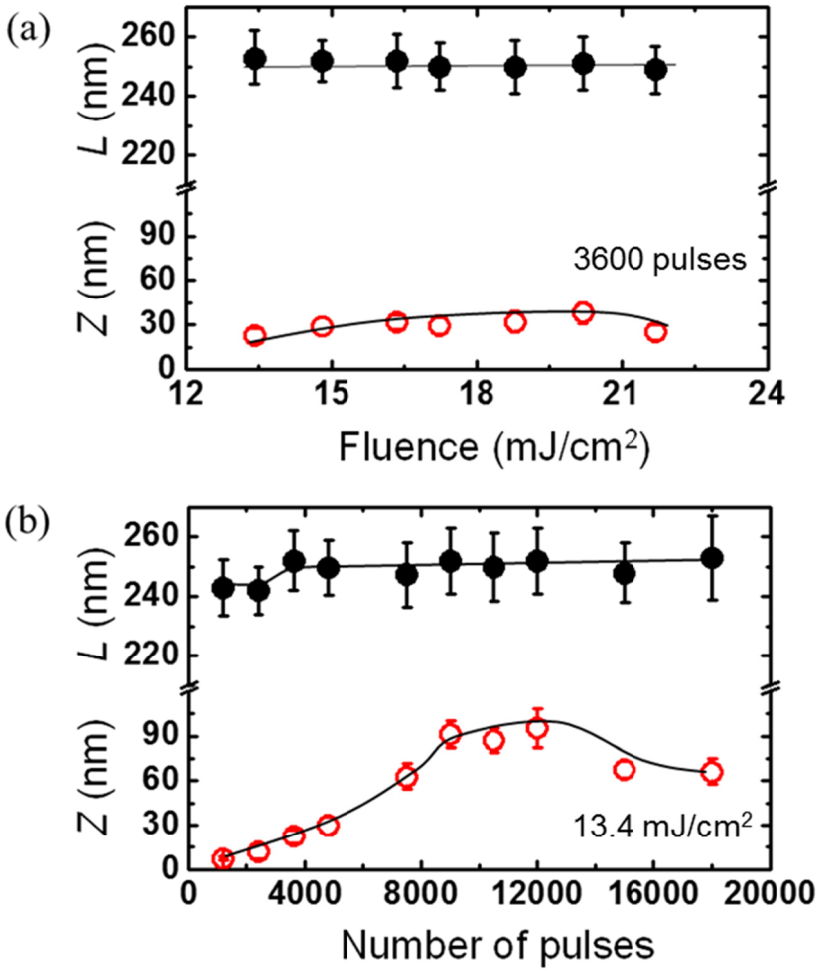

Figure 4.18. Variation of periods (*L*, filled circles) and depths (*Z*, empty circles) of LIPSS as a function of (a) fluence and (b) number of pulses for the laser irradiation wavelength 266 nm. Lines are shown as visual guides.

4.2.3. Chemical stability and structural modification in nanostructured PCDTBT thin films

4.2.3.1. Near Edge X-ray Absorption Fine Structure

NEXAFS experiments were performed in order to gain further information about the chemical stability of the PCDTBT thin films after laser irradiation at 532 nm. The experiments were carried out at the PolLux beamline at the Swiss Light Source. A

NEXAFS spectrum in the K-edge reveals the excitation of 1s electrons to unfilled molecular orbitals. The NEXAFS spectra in the carbon K-edge of pristine thin films and of those with LIPSS are presented in Figure 4.19. The π* (C=C) bands in both cases are similar suggesting that the π-backbone is not affected by laser irradiation. The main difference is found in the band σ* (C-H) with the appearance of a new band near 288 eV, probably related to a weak modification of the polymer lateral chains. Overall, NEXAFS results suggest the absence of significant changes in the chemical structure of PCDTBT after LIPSS formation similarly as previously discussed for LIPSS in P3HT.

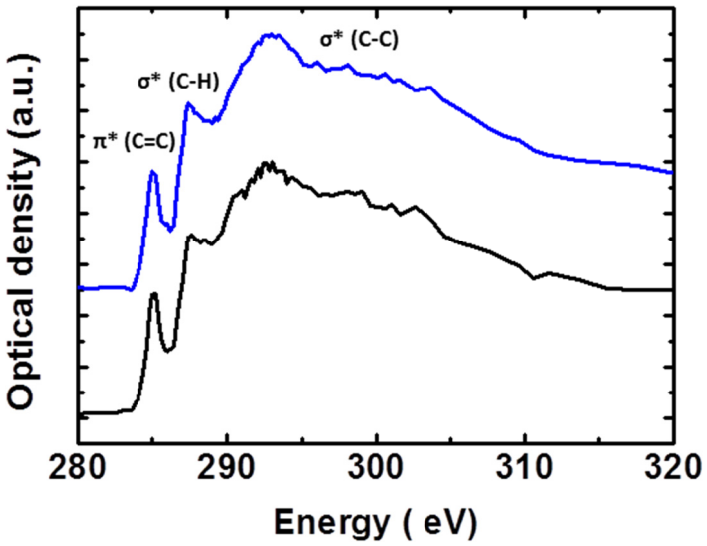

Figure 4.19. NEXAFS spectra in the carbon K-edge of PCDTBT thin film (blue) and of PCDTBT film with LIPSS fabricated at 532 nm, 26 mJ/cm^2, and 9000 pulses (black). The spectra have been vertically shifted for clarity.

4.2.3.2. Raman Spectroscopy

Figure 4.20 shows the Raman spectra of PCDTBT thin films (blue) and PCDTBT with LIPSS fabricated at 532 nm, 26 mJ/cm^2 and 7500 pulses (black) at the different excitation wavelengths used (λ_{exc} = 785, 532 and 442 nm). As it is shown in Figure 3.2 and in agreement with previous reports,[42, 43] PCDTBT thin films present optical absorption between 250 and 600 nm. This indicates that excitation at 785 nm occurs under non-resonance conditions, whereas excitation at 532 and 442 nm leads to measurements under resonance conditions. The UV-Vis absorption band at 395 nm is

attributed to π–π* transition, whereas the absorption band at 570 nm is known to be due to a charge transfer from donor carbazole unit to acceptor DTBT unit.[42]

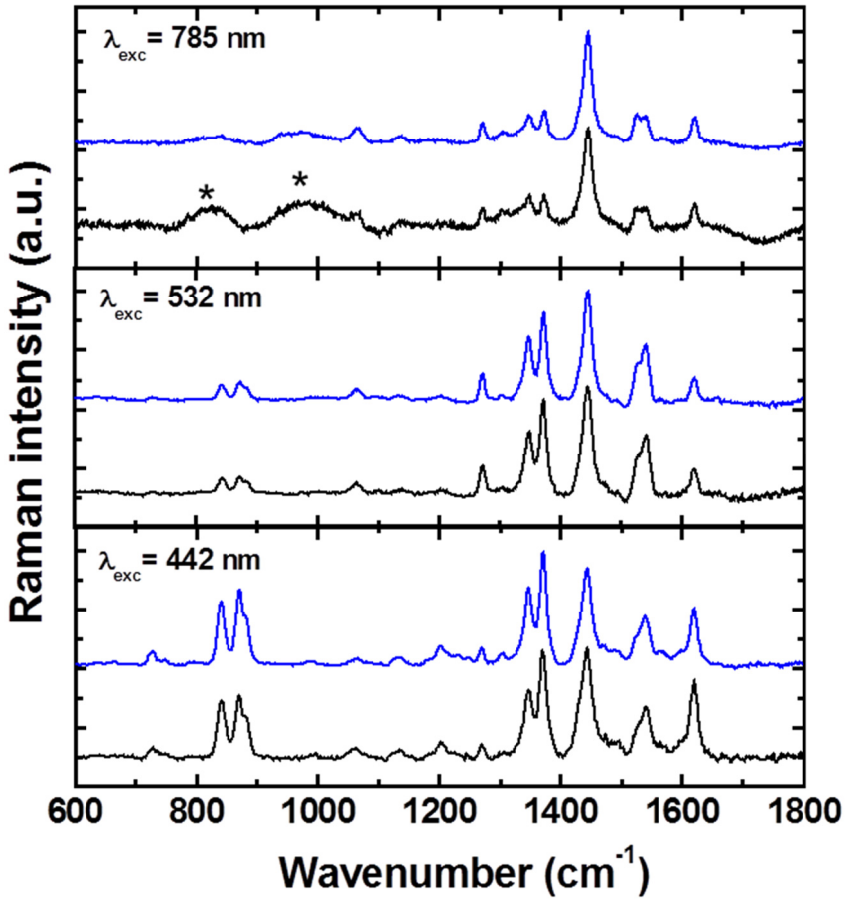

Figure 4.20. Raman spectra of PCDTBT thin films (blue) and LIPSS in PCDTBT (black) at different excitation wavelengths, λ_{exc} labelled in the upper left corners. Star marks (**) in Figure (top) correspond to silicon bands.

The PCDTBT Raman spectra show several characteristic bands. The one present with high intensity at every excitation wavelength and located at 1444 cm^{-1} is a mode assigned to a broad ring stretch focused on the DTBT acceptor unit that is delocalized across the benzothiadiazole and the two thiophenes.[43] The 1541 cm^{-1} mode corresponds to the benzothiadiazole ring stretching mode, and the band at 1623 cm^{-1} is associated with the ring stretching mode of the carbazole. Peaks at 1349 and 1373 cm^{-1} are attributed to the C–C stretching mode of the carbazole and DTBT unit, respectively.[42, 44, 45] The modes for lower frequency Raman bands at 844 and 874 cm^{-1}, present under resonance conditions but almost completely absent under non-resonance

conditions, are difficult to assign unambiguously but are tentatively assigned as in-plane bending modes of the DTBT group.[42]

No significant changes are observed in PCDTBT spectra, at the different excitation wavelengths used, for both the non-irradiated films and those with LIPSS (Figure 4.20). There is no evidence of new bands, however some slight changes of the intensity ratio between bands can be detected. These differences are difficult to interpret but the main bands are maintained suggesting that the PCDTBT thin films evidence a weak impact on its chemical structure under the irradiation conditions used for fabricating LIPSS.

4.2.4. Electrical properties of nanostructured PCDTBT thin films

C-AFM was used to characterize the electrical properties at the nanoscale of LIPSS produced by irradiating a PCDTBT thin film at 532 nm. Figure 4.21 shows the C-AFM current images which can be considered as electric current maps, acquired in contact mode of a PCDTBT thin film sample before irradiation (Figure 4.21.a) and after irradiation with a fluence of 26 mJ/cm^2 and 9000 pulses (Figure 4.21.b) by applying a constant voltage of -5 V on the conducting substrate. The current image of the sample before irradiation shows a little current variation throughout the film, whereas the image displaying the current map of the irradiated thin polymer film shows stripes with conductivity similar to that of the initial thin film separated by non-conductive ones. Comparing the topography and current images measured simultaneously, we can conclude that conductive regions correspond to trenches and nonconductive regions to ridges.

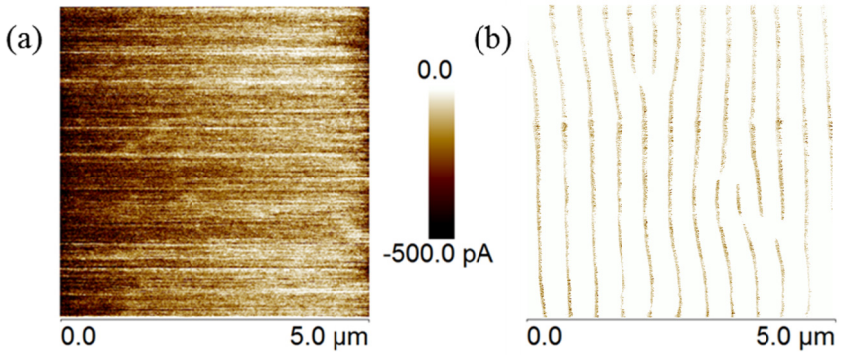

Figure 4.21. C-AFM current images of a PCDTBT film measured at a constant bias of -5 V. (a) Non-irradiated thin film, (b) film with LIPSS fabricated at 532 nm, 26 mJ/cm^2 and 9000 pulses.

A similar behavior explained previously in this chapter for the electrical properties related to LIPSS formation in P3HT has been also observed for the PCDTBT samples. Although the as-cast PCDTBT thin film presents a very low crystallinity (Figure 3.7.b) and no differences between the Raman spectra of non-irradiated films and those with LIPSS are observed (Figure 4.20), it is known that the annealing of PCDTBT thin films at temperatures close to its melting point improves side-chain order while the π-π stacking is reduced (Figure 3.7.e).[46, 47] Accordingly, the results suggest that the temperature reached during LIPSS formation could has a similar effect in the surface of PCDTBT thin films. Thus, due to the distortion of π-π stacking the conductivity of the ridges in the nanostructured sample is expected to be reduced.

4.3. Laser-induced periodic surface structures on the P3HT/PCDTBT blend

4.3.1. Sample preparation

Separated solutions of P3HT and PCDTBT in chlorobenzene (24 g/L) were prepared and stirred during several hours until complete dissolution. Afterwards, a volume of 1 mL of each solution is mixed to obtain a total concentration of 24 g/L. Thin polymer films were prepared by spin-coating on arsenic n-doped silicon substrates (resistivity ≈ 0.001 Ω·cm, Wafer World). The wafers were previously cleaned with acetone and isopropanol. A fixed amount of 0.2 mL of polymer solution was dropped by a pipette on a square silicon substrate placed in the center of a rotating metallic horizontal plate. A rotation rate of 2400 rpm was kept during 60 s for obtaining films with an averaged thickness of 165 nm for the P3HT/PCDTBT blend. For NEXAFS measurements, polymer solutions were spin-coated on silicon substrates, and then floated off into a very dilute NaOH/water solution (0.25 wt %), and finally picked up with TEM grids.

Laser irradiation was carried out under ambient air conditions at normal incidence with a linearly polarized laser beam of a Q-switched Nd:YAG laser (pulse duration of 8 ns) at two different wavelengths, i.e., with the second, 532 nm, and fourth harmonic, 266 nm, at a repetition rate of 10 Hz.

4.3.2. Dependence of LIPSS on fluence and number of pulses at 266 and 532 nm

After proving the formation of LIPSS in semiconducting homopolymers like P3HT and PCDTBT in previous sections, the feasibility of fabricating LIPSS in the P3HT/PCDTBT (1:1) blend has been investigated. This blend has been used as bulk-heterojunction acting as the active layer in organic solar cells.[48] As-cast films of P3HT/PCDTBT (1:1) present the characteristic morphology of lateral phase separation (Figure 4.22.a), indicating immiscibility of the two polymers as it has been discussed in Chapter 3. The blend thin films present about 50 nm difference in height between P3HT and PCDTBT domains for an average film thickness of 165 nm. Figures 4.22.a and 4.22.b show, together with the AFM image of the initial non-irradiated sample, selected height images of P3HT/PCDTBT (1:1) films irradiated at 532 nm with different fluences and number of pulses respectively. Both, P3HT and PCDTBT domains present well defined LIPSS.

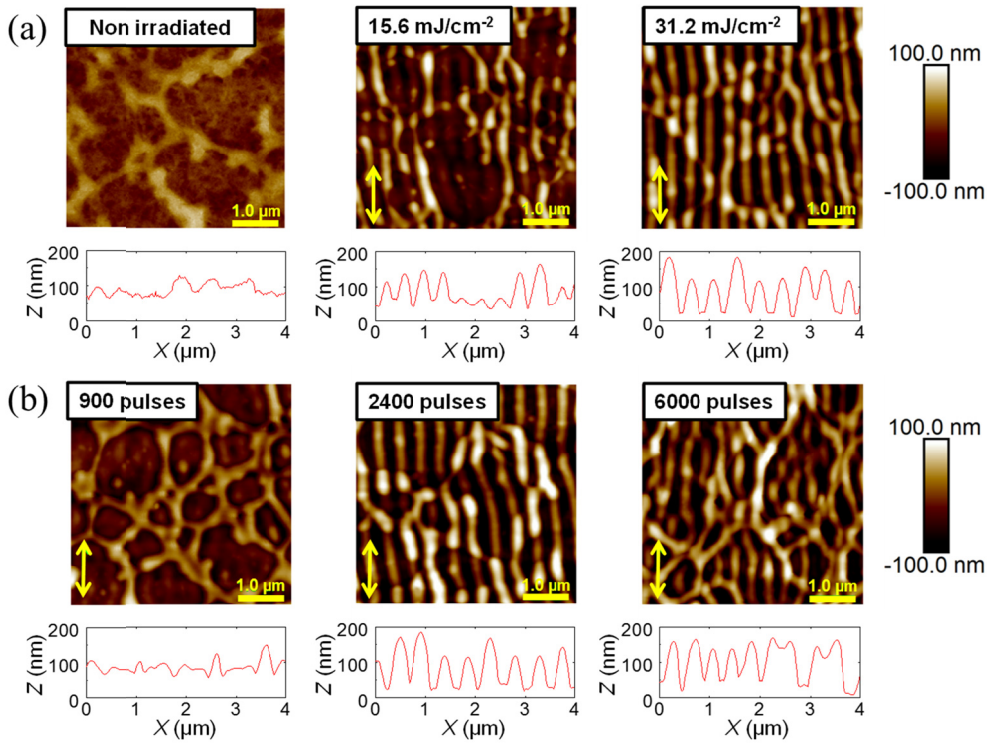

Figure 4.22. AFM height images (5 × 5 µm^2) of P3HT/PCDTBT: (a) Non-irradiated and irradiated at 532 nm with 3600 pulses at different fluences labeled in the upper left corner. (b) Irradiated at 532 nm with a fluence of 26 mJ/cm^2 as a function of number of pulses as labeled in the upper left corner. The height profile along a 4 µm line perpendicular to the ripples is shown below every image. The arrows indicate the polarization vector of the laser (↔).

The dependence of the period (L) and depth (Z) of LIPSS with the fluence, at 532 nm and 3600 pulses, is represented in Figure 4.23.a. It is observed that the period increases up to a fluence of ≈ 16 mJ/cm^2 and reaches a plateau with a value slightly smaller than the irradiation wavelength. While the measured period is similar for both phases, the depth of ripples follows a similar tendency as the period but they appear for PCDTBT at lower fluence than for P3HT and the depth of ripples is higher for PCDTBT in the range of fluences studied. The dependence of period and depth of LIPSS at a constant fluence of 26 mJ/cm^2 with the number of pulses is represented in Figure 4.23.b. It shows that the period increases slightly up to ≈ 900 pulses and reaches a steady level for higher number of pulses. The depth of the ripples increases with the number of pulses up to ≈ 2400 pulses reaching a value of about 150 nm for PCDTBT and about 90 nm for P3HT, for higher number of pulses up to 6000 the depth of the ripples for PCDTBT decreases matching the depth of P3HT ripples.

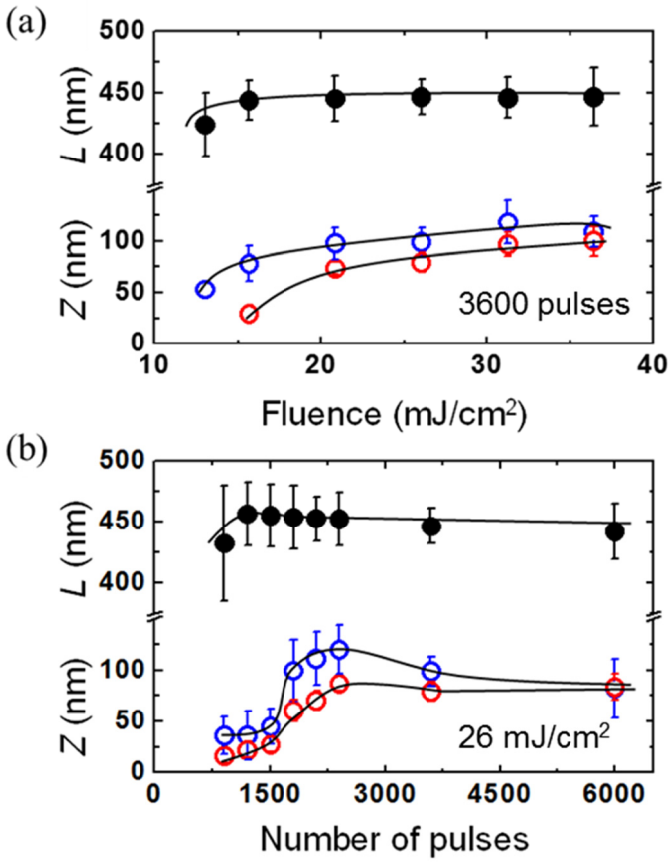

Figure 4.23. Variation of periods (L, black filled circles) and depths (Z, P3HT red empty circles and PCDTBT blue empty circles) of LIPSS as a function of (a) fluence and (b) number of pulses for the laser irradiation wavelength 532 nm. Lines are shown as visual guides.

LIPSS in the blend were also fabricated by irradiating at 266 nm. Selected height AFM images of P3HT/PCDTBT (1:1) films irradiated with different fluences and number of pulses are shown in Figure 4.24.

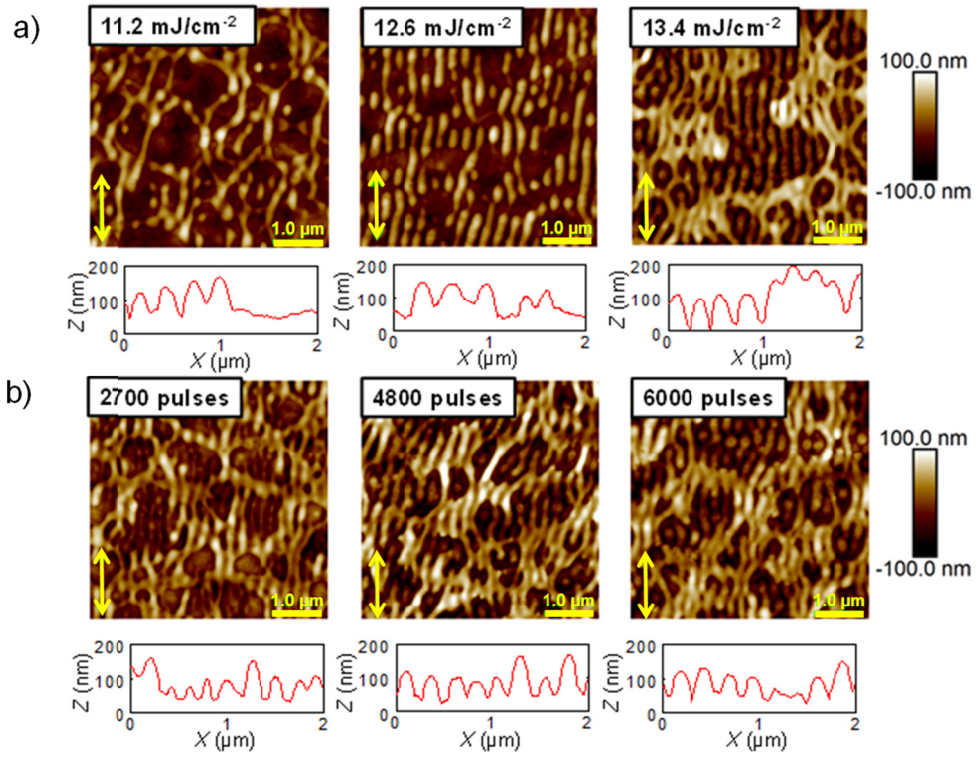

Figure 4.24. AFM height images (5 × 5 µm^2) of P3HT/PCDTBT: (a) Irradiated at 266 nm with 3600 pulses at different fluences labeled in the upper left corner. (b) Irradiated at 266 nm with a fluence of 26 mJ/cm^2 as a function of number of pulses as labeled in the upper left corner. The height profile along a 2 µm line perpendicular to the ripples is shown below every image. The arrows indicate the polarization vector of the laser (↔).

The dependence of the period and depth of LIPSS with the fluence, at 266 nm and 3600 pulses is represented in Figure 4.25.a. It is shown that the period remains essentially constant with a value of about 250 nm in the investigated fluence range. The ripples appear for PCDTBT at lower fluence than for P3HT and the depth of ripples is higher for PCDTBT in the range of fluences studied. In addition the depth of the ripples increases up to ≈ 13 mJ/cm^2 reaching a value of about 100 nm for PCDTBT and about 90 nm for P3HT, for higher fluences the depth of the ripples for P3HT decreases slightly while for PCDTBT decreases abruptly. The dependence of period and depth of LIPSS at a constant fluence of 13.4 mJ/cm^2 with the number of pulses is represented in Figure 4.25.b. It shows that the period increases up to ≈ 3600 pulses and reaches a plateau for higher number of pulses. The depth of the ripples also increases up to ≈ 3600

pulses reaching a similar value of about 90 nm for both P3HT and PCDTBT, for higher number of pulses up to 6000 the depth of the ripples decreases faster for PCDTBT than for P3HT.

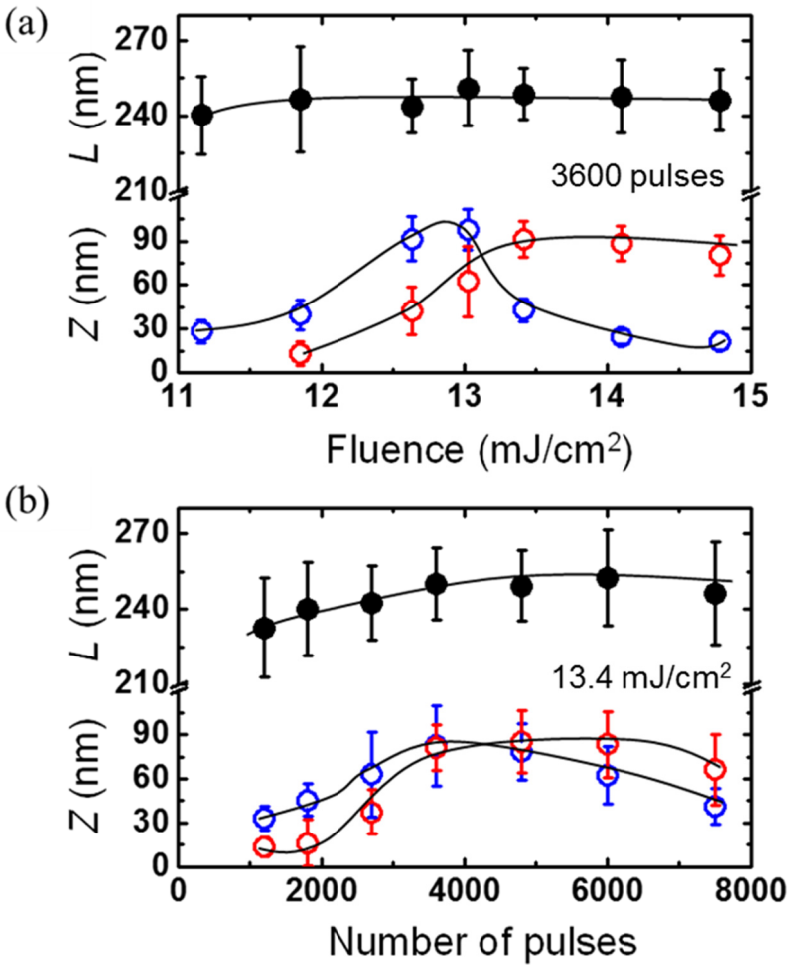

Figure 4.25. Variation of periods (*L* ,filled circles) and depths (*Z*, P3HT red empty circles and PCDTBT blue empty circles) of LIPSS as a function of (a) fluence and (b) number of pulses for the laser irradiation wavelength 266 nm. Lines are shown as visual guides.

It is interesting to point out the synergy found for both components in the P3HT/PCDTBT blend when irradiating at wavelengths of 532 nm and 266 nm. P3HT and PCDTBT in the blend need, at a constant number of pulses, less fluence than in the case of irradiating the homopolymers in order to optimize LIPSS morphology. The same behavior is found when irradiating the blend at a constant fluence, P3HT and PCDTBT components need less number of pulses in order to optimize LIPSS morphology than in the case of irradiating the homopolymers.

4.3.3. Composition mapping

As mentioned before, STXM is a technique that provides an appropriate combination of spectroscopy and imaging capabilities at low radiation doses.[49, 50] The STXM images can provide information on the domain sizes, shapes, and purities of thin film polymer blends with a spatial resolution of ~ 20 nm.[51]

In Chapter 3 the STXM technique has been used in order to investigate the composition and phase separation in P3HT/PCDTBT (1:1) blends as a function of thickness. The STXM technique has been also used to investigate whether the LIPSS formation may induce either a further phase segregation or a mixture of the components. The experiments were performed at the PolLux beamline at the Swiss Light Source. In order to obtain quantitative chemical composition of the blend thin film irradiated at 532 nm the SVD mathematical procedure[49, 52] has been used. Figure 4.26 shows the mass absorption coefficients as a function of energy for P3HT and PCDTBT films irradiated at 532 nm of known thickness measured before irradiation. STXM images (Figure 4.26 top) of the same area of the P3HT/PCDTBT (1:1) thin film irradiated at 532 nm were taken at energies indicated by arrows in the NEXAFS spectra which correspond to 280 eV (pre-edge), 284.2 eV (PCDTBT resonance), 287.8 eV (P3HT resonance) and 320 eV (chemically insensitive). By using the aXis2000 software package[53] where the SVD procedure is integrated, the information contained within the set of STXM images taken at the selected energies can be transformed into maps quantifying the composition and thickness of the sample in each pixel.[49, 52]

The corresponding composition and thickness maps of the P3HT/PCDTBT (1:1) irradiated at 532 nm are shown in Figure 4.27. These images reveal the chemical nature of the different observed domains and the morphology of thinner P3HT-rich domains enclosed by a thicker PCDTBT-rich matrix. The thicknesses of domains and the height of ridges and trenches are in agreement with the values measured by AFM, considering that the STXM takes into account the complete sample thickness and the AFM is only able to obtain surface information. In addition it seems that LIPSS formation does not induce a further phase segregation or a mixture of the components.

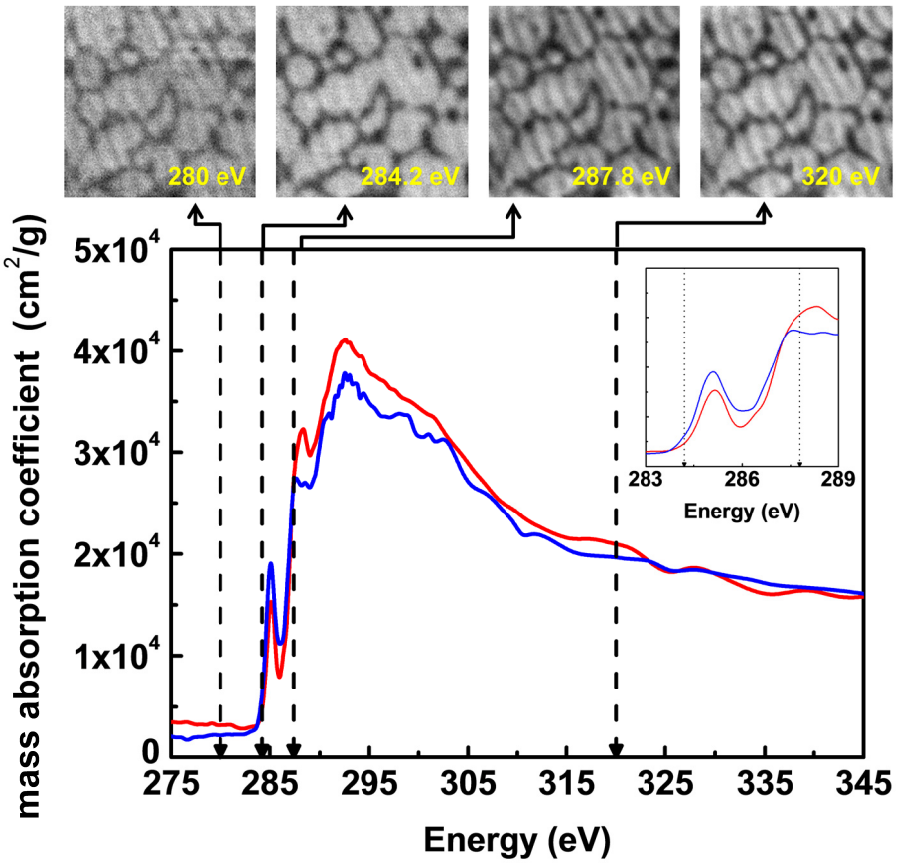

Figure 4.26. Reference NEXAFS spectra for films of P3HT (red line) and PCDTBT (blue line) irradiated at 532 nm with a fluence of 26 mJ/cm^2, 3600 and 9000 pulses respectively. Vertical arrows indicate the photon energies used to obtain the raw STXM images (5 µm x 5 µm) of the same sample area of a P3HT/PCDTBT (1:1) thin film irradiated at 532 nm with a fluence of 26 mJ/cm^2 and 3600 pulses, presented at the top. The inset highlights differences in the NEXAFS spectra of P3HT and PCDTBT in the C-1s / π* region.

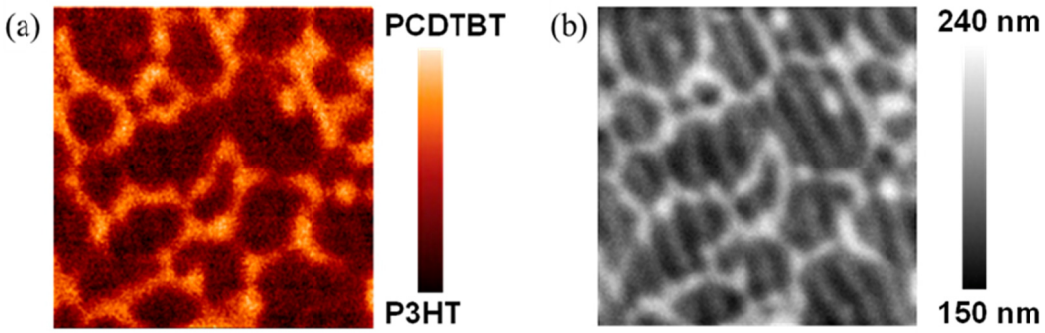

Figure 4.27. 5 µm x 5 µm images of: (a) polymer composition and (b) thickness maps of the P3HT/PCDTBT (1:1) blend irradiated at 532 nm, calculated from the set of raw images in Figure 4.26 (top).

4.3.4. Chemical stability and structural modification in nanostructured P3HT/PCDTBT (1:1) thin films

Figure 4.28 shows the Raman spectra of P3HT/PCDTBT (1:1) blend thin films (green) and P3HT/PCDTBT (1:1) blend with LIPSS fabricated at 532 nm, 26 mJ/cm^2 and 2400 pulses (black) at the different excitation wavelengths employed. The Raman spectra for the P3HT/PCDTBT (1:1) blend is the sum of the Raman spectra for the net components. No new bands are observed. We focus on the 1400−1500 cm^{-1} spectral range (enlarged in Figure 4.28.b) where the band centered at 1445 cm^{-1} is the composition of the PCDTBT band located at 1444 cm^{-1} and the P3HT band located at 1445 cm^{-1}. As we have pointed out no evidence of new bands neither change of peak intensity ratio between bands is observed for PCDTBT non-irradiated films and those with LIPSS (Figure 4.20), hence the changes observed in Figure 4.28.b between the spectra of P3HT/PCDTBT (1:1) non-irradiated films and those with LIPSS could be attributed to the P3HT component.

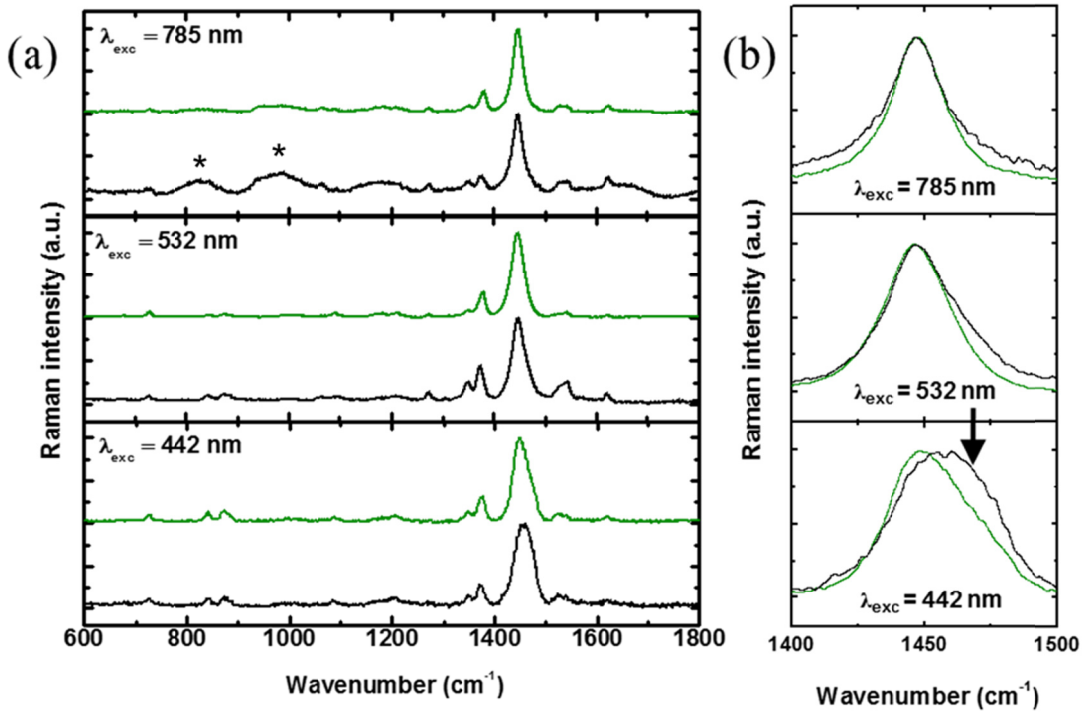

Figure 4.28. (a) Raman spectra of non-irradiated P3HT/PCDTBT thin films (green) and films with LIPSS fabricated at 532 nm, 26 mJ/cm^2 and 2400 pulses (black) under different excitation wavelengths. (b) Comparison of the ν(C=C) band region before (green) and after laser irradiation (black). Star marks (**) in Figure (top) correspond to silicon bands.

It seems that in the blend the P3HT behaves in a similar way as it does as a neat homopolymer. In section 4.2.3.2 it has been mentioned[54] that in the Raman spectrum of pure P3HT with LIPSS under resonance conditions (λ_{exc} = 442 nm) the ν(C=C) band shifts toward higher wavenumbers where it presents a shoulder, marked by an arrow in Figure 4.28.b (bottom). This shoulder can be assigned to a relative increase of the amorphous phase after laser irradiation.[41, 54] The Raman spectra collected at an excitation wavelength of 532 nm, for the P3HT with LIPSS, also presents the mentioned shoulder but in less extension. This effect may be related to the fact that under these resonance conditions (λ_{exc} = 532 nm), P3HT segments located in ordered regions absorb more strongly than those in the amorphous phase.[55] Under non-resonance conditions (λ_{exc} = 785 nm) for both the P3HT thin film and the P3HT with LIPSS, the Raman spectra do not present noticeable variations, only a small increase of the width of the ν(C=C) band located at 1445 cm^{-1} is appreciated. However, it was pointed out that the pure P3HT with LIPSS presents a shoulder at 1420 cm^{-1} on the lower wavenumber region of the ν(C=C) band located at 1445 cm^{-1}. This shoulder is assigned to the stretching of the C=C bond of the quinoid form of P3HT because of the oxidation of the aromatic backbone.[39, 56] The absence of the mentioned shoulder in the blend could be explained either by the absence of oxidation of the P3HT aromatic backbone due to the presence of high stable PCDTBT, or by the limit of detection of Raman taking into account that in the blend there is 50% of P3HT.

4.3.5. Electrical properties of nanostructured P3HT/PCDTBT (1:1) thin films

Current imaging by C-AFM was used to examine conductivity variations in the P3HT/PCDTBT (1:1) thin films structured by LIPSS. Figure 4.29 shows the C-AFM current images, acquired in contact mode, of a P3HT/PCDTBT thin film blend before irradiation (Figure 4.29.a) and after irradiation with a fluence of 26 mJ/cm^2 and 3600 pulses (Figure 4.29.b) by applying a constant voltage of -5 V on the conducting substrate. The P3HT/PCDTBT (1:1) thin film shows domains with high (dark region) and low (bright region) current. By comparison with the compositional maps extracted from STXM experiments, we can assign the high current regions to the P3HT-rich domains and the low current ones to PCDTBT.[46] On the other hand, the image displaying the current map of the irradiated thin film polymer blend shows a similar

trend to the one followed by the irradiated homopolymer thin films, consisting in trenches with conductivity values close to those of the initial thin film separated by non-conductive ridges.

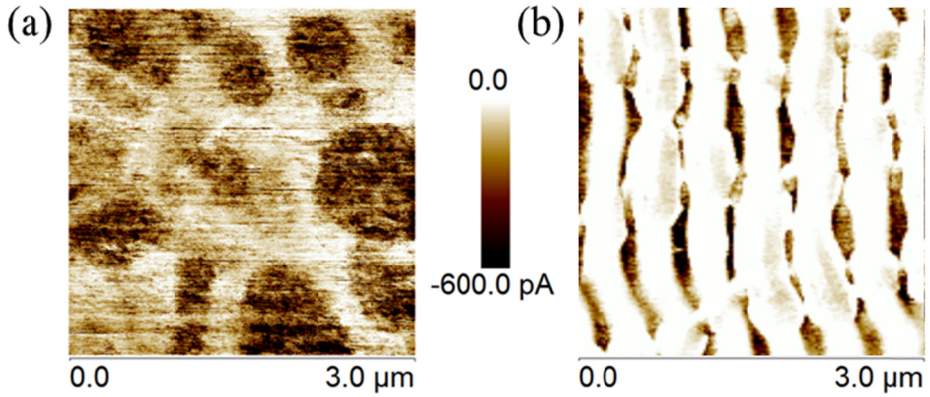

Figure 4.29. C-AFM current images of a P3HT/PCDTBT thin film measured applying a constant bias of -5 V. (a) Non-irradiated film, (b) film with LIPSS fabricated at 532 nm with a fluence of 26 mJ/cm^2 and 3600 pulses.

The C-AFM results obtained for the irradiated P3HT/PCDTBT (1:1) thin film can be explained by the same bases considered for the irradiated homopolymer thin films. During irradiation melting of the blend surface takes place leading to ripple morphology into the P3HT and PCDTBT domains, which leads to the existence of low crystallinity and non-conducting ridges over a continuous and more-conducting either P3HT or PCDTBT residual domain layer whose initial crystallinity in the case of P3HT and order of π-π stacking in the case of PCDTBT seems to be unaffected in comparison to that of the non-irradiated P3HT/PCDTBT (1:1) thin film.

4.4. Laser-induced periodic surface structures on the P3HT/$PC_{71}BM$ blend

Polymer blends of P3HT with fullerene materials including C60, [6,6]-phenyl C61-butyric acid methyl ester ($PC_{61}BM$) or [6,6]-phenyl C71-butyric acid methyl ester ($PC_{71}BM$) have shown to be attractive functional materials for their application in organic photovoltaics (OPV).[57, 58] In this case the interfacial area between the donor material, P3HT, and the acceptor one, PCBM, which forms the heterojunction is a critical factor for the performance of the OPV device.[59-61]

In recent years, grazing incidence small-angle X-ray and neutron scattering have been employed to probe the evolution of the phase separation in P3HT/PCBM blends during a thermal annealing process.[62-66] However, discrepancies both in terms of phase separation mechanism and data interpretation have been reported.[5] On the one hand, when annealing a P3HT/PCBM blend, some works reached the conclusion that phase separation competes with crystallization since the time of phase separation is faster than crystallization,[67, 68] however other works found that polymer crystallization is the driving force of phase separation.[69] This is in agreement with other reports in which the crystallization of the polymer is thermodynamically hindered giving rise to films constituted by droplets of the fullerene within a polymer layer.[70] In this case liquid-liquid demixing will occur before polymer crystallization.[71, 72] On the other hand, the data interpretations of the origins of scattering intensities differ. The aggregation of PCBM molecules[63, 68] and the distance between P3HT nanocrystals[65, 73] have been interpreted as the cause of the scattering at large length scale. Anyway, since pure P3HT crystals embedded in a mixed phase would have similar scattering contrast and cause similar scattering patterns as PCBM agglomerates in a mixed phase, the assignment of the scattering feature to a specific particular material and morphology is difficult.[5]

Additionally, scattering techniques have contributed to the knowledge about the effect of film morphology and crystalline structure on the performance in P3HT/PCBM devices. In particular, annealing has been demonstrated to have a positive effect on the polymer/fullerene solar cells provoked by the growing of pure P3HT crystallites and the increase of the phase separation exhibiting even larger average distance between domains.[64]

In the Section 4.1, LIPSS have been used in order to create sub-micron gratings on P3HT. On the basis of wide angle X-ray scattering experiments, a reduction of the crystallinity of the hills was proposed as the cause of this effect. Among the scattering techniques for investigating larger length scales, resonant soft X-ray scattering technique is a potential candidate for investigating multicomponent systems like organic blends since it brings together the possibility of performing scattering experiments with enhanced intensity and chemical sensitivity. In this section the viability of fabricating LIPSS in a P3HT/$PC_{71}BM$ blend, the surface chemical characterization and the analysis of the phase separation in the blends are discussed.

4.4.1. Sample preparation

Solutions of P3HT and $PC_{71}BM$ in chlorobenzene (24 g/L) were prepared and stirred during several hours until complete dissolution. Afterwards solutions were blended with a weight ratio of 1:1. A fixed amount of 0.2 mL of polymer/fullerene solution was dropped onto a substrate placed in the center of a rotating metallic horizontal plate. A rotation rate of 2400 rpm was kept during 60 s for obtaining thin films of about 120 nm, as revealed by AFM. For AFM and C-AFM measurements, polymer/fullerene solutions were spin-coated on silicon substrates. For NEXAFS and RSoXS measurements films were deposited by spin-coating on silicon substrates with a previous spin-coated layer of PEDOT:PSS. Since PEDOT:PSS is soluble in water, polymer/fullerene films were separated from the substrate by immersing them in water. Finally the floating films were picked up with silicon nitride membranes. For UV-visible spectroscopy measurements, quartz substrates were used. UV-visible spectrum of the P3HT and $PC_{71}BM$ is presented in Figure 4.30.

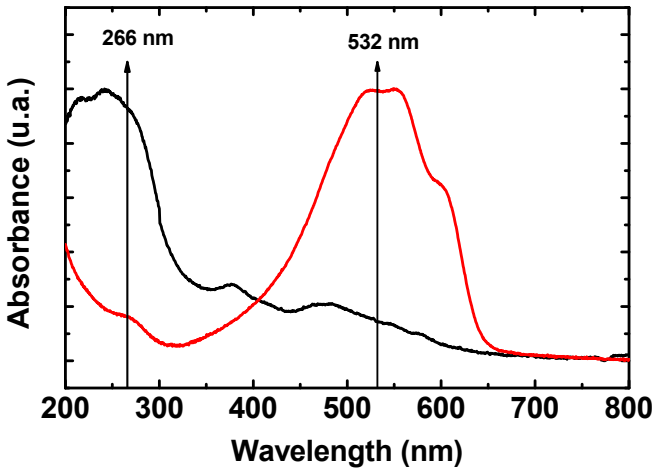

Figure 4.30. UV-visible spectra of P3HT (red) and $PC_{71}BM$ (black) thin films on quartz substrates.

In this case, laser irradiation of P3HT/$PC_{71}BM$ thin films was carried out both under ambient air conditions and under vacuum at normal incidence with a linearly polarized laser beam of a Q-switched Nd:YAG laser (pulse duration of 8 ns) at two different wavelengths, i.e., with the second, 532 nm, and fourth harmonic, 266 nm, at a repetition

rate of 10 Hz. These wavelengths were selected for the experiments because P3HT and $PC_{71}BM$ absorb efficiently as it is shown in Figure 4.30.

4.4.2. LIPSS morphology as revealed by AFM

Topography AFM images of LIPSS obtained at 266 nm with a fluence of 13.5 mJ/cm^2 and 3600 pulses and at 532 nm with a fluence of 26 mJ/cm^2 and 3600 pulses are shown in Figure 4.31. This laser conditions were selected according to the previous work on P3HT described in Section 4.1. It is observed that regular LIPSS are obtained at both wavelengths. Dimensions obtained from the AFM analysis correspond to periods of 225 ± 9 nm for irradiation at 266 nm and 350 ± 8 nm for irradiation at 532 nm and corresponding depths of 61 ± 8 nm and 111 ± 9 nm, respectively.

It is worth mentioning that parallel and well-ordered LIPSS are formed in P3HT/$PC_{71}BM$ upon irradiation at 266 nm by using the same laser conditions than in the case of P3HT homopolymer led to distorted LIPSS (Figure 4.5). This effect can be explained in terms of material absorption since the $PC_{71}BM$ component absorbs much more than P3HT at 266 nm (Figure 4.30), and thus it contributes to a more effective LIPSS formation.

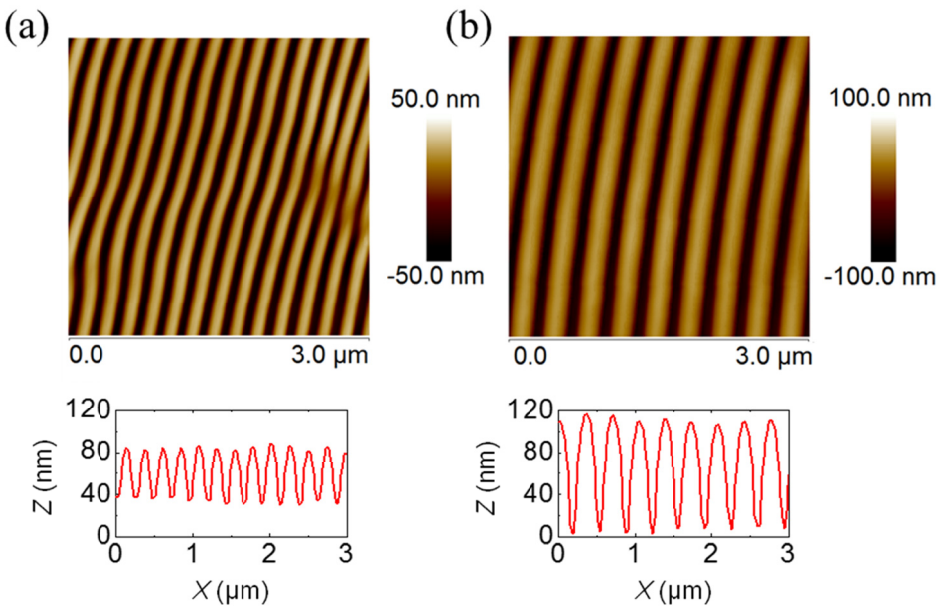

Figure 4.31. Topography AFM images of LIPSS fabricated on P3HT/$PC_{71}BM$ under air conditions at (a) 266 nm with a fluence of 13.5 mJ/cm^2 and 3600 pulses and (b) 532 nm with a fluence of 26 mJ/cm^2 and 3600 pulses. The height profile along a 3 µm line perpendicular to the ripples is shown below both images.

Figure 4.32 shows the LIPSS morphology after irradiation in vacuum at 266 nm. Main differences are related to the shape and size of the structures obtained. The AFM topography image of the nanostructures fabricated under vacuum is presented in Figure 4.32.a. LIPSS have an average period of 235 ± 6 nm and a depth of 18 ± 4 nm. The topography of LIPSS after annealing for 4 minutes at 140 ºC is shown in Figure 4.32.b. In this case, the average period and depth are 230 ± 5 nm and 8 ± 2 nm respectively.

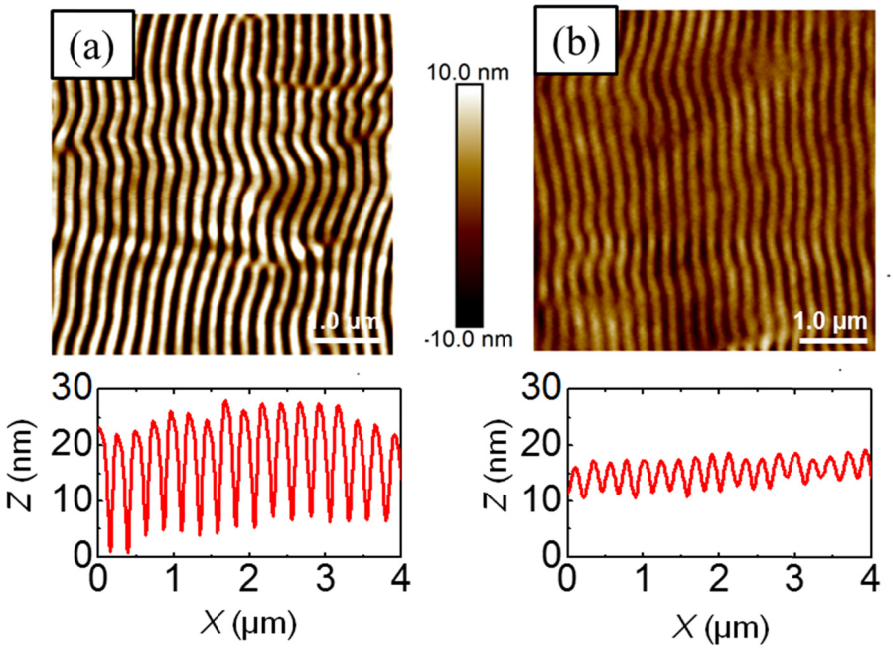

Figure 4.32. Topography AFM images of LIPSS fabricated at 266 nm in vacuum with a fluence of 13.5 mJ/cm^2 and 3600 pulses on P3HT/$PC_{71}BM$, (a) before and (b) after an annealing step for 4 minutes at 140ºC.

4.4.3. Chemical characterization by NEXAFS spectroscopy

NEXAFS experiments were performed in order to gain information about the chemical stability of the P3HT/$PC_{71}BM$ thin films after laser irradiation at 266 nm. The experiments were performed at Beamline 11.0.1.2 at the Advanced Light Source at Lawrence Berkeley National Laboratory (LBNL). Both transmission and Total Electron Yield (TEY) NEXAFS of the P3HT/PCBM blends are shown in Figures 4.33 and 4.34 respectively. Figure 4.33 shows the transmission NEXAFS spectra of the spin-coated P3HT/$PC_{71}BM$ thin film (blue), LIPSS obtained under air conditions (green) and LIPSS obtained under vacuum conditions (orange) and also includes the P3HT (red) and $PC_{71}BM$ (black) spectra for comparison.

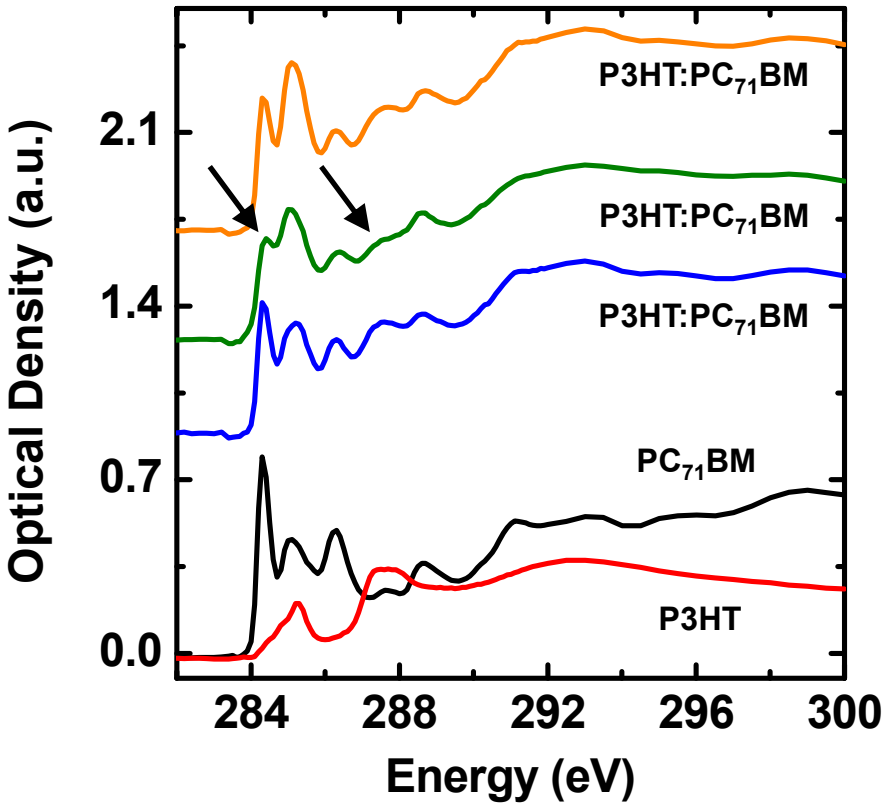

Figure 4.33. Transmission NEXAFS spectra of P3HT/$PC_{71}BM$ films: spin-coated (blue line), with LIPSS formed upon irradiation in air (green line) at 266 nm and with LIPSS formed upon irradiation in vacuum (orange line) at 266 nm. P3HT and $PC_{71}BM$ thin films are shown as reference (red and black line, respectively). The black arrows indicate the bands which present a decreased intensity after irradiation.

The NEXAFS spectrum of the P3HT/$PC_{71}BM$ sample with LIPSS obtained in air shows a decrease of intensity in two bands in comparison with the non-irradiated one as marked by arrows in Figure 4.33: $PC_{71}BM$ π-band at about 284 eV as well as the band roughly at 287.5 eV. These results can be interpreted as a possible photo-oxidation of the polymer/fullerene blend after laser irradiation in air. On the other hand P3HT/$PC_{71}BM$ samples with LIPSS obtained in vacuum show a profile very similar compared with the unstructured P3HT/$PC_{71}BM$ with the exception of the band at 285 eV which exhibits an increased intensity. In previous works[34, 74, 75] this band has been assigned to the sum of the P3HT π-band and the $PC_{71}BM$ π-band of the phenyl groups. Additionally, the intensity of this band is sensitive to the orientation due to the planarity of the π-bonds. Further work should be done to elucidate the meaning of these changes in the intensity.

A detailed study of the surface can be performed with TEY NEXAFS. Figure 4.34 shows the spectra of the different P3HT/$PC_{71}BM$ samples. As reference, P3HT and $PC_{71}BM$ thin films spectra are presented in the graph (red and black line).

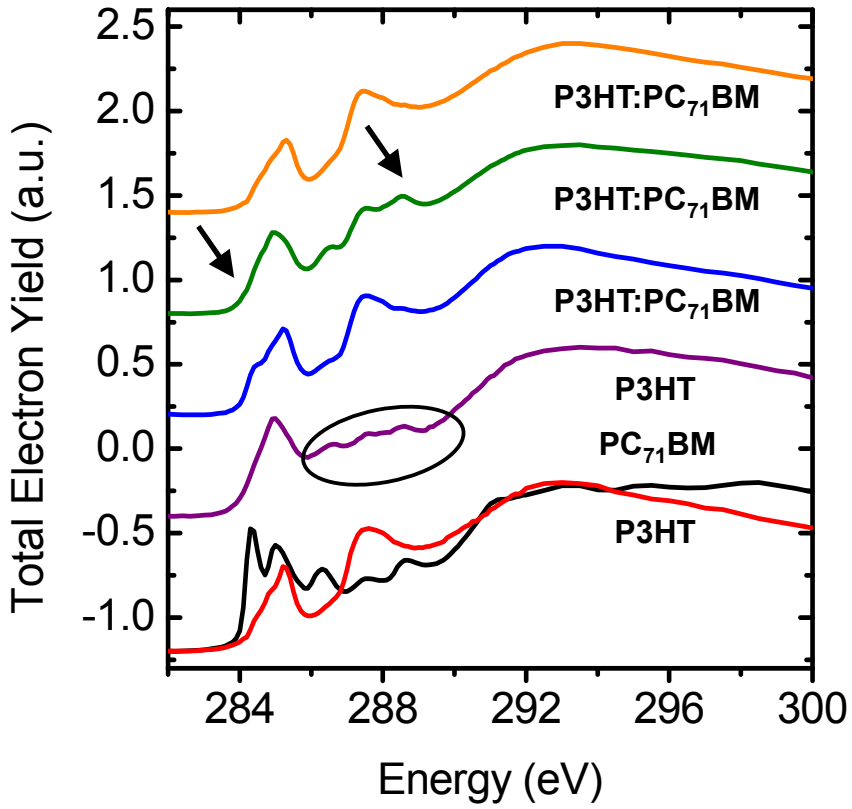

Figure 4.34. TEY NEXAFS spectra collected in transmission of different P3HT/$PC_{71}BM$ films: spin-coated (blue line), with LIPSS formed upon irradiation in air (green line) at 266 nm and with LIPSS formed upon irradiation in vacuum (orange line) at 266 nm. P3HT and $PC_{71}BM$ thin films are shown as reference (red and black lines respectively). P3HT film with LIPSS formed at 266 nm is also included for comparison (purple line). The black arrows indicate the bands which present changes in the intensity after irradiation.

A first view suggests that surface is richer in P3HT since TEY-NEXAFS spectra of P3HT/$PC_{71}BM$ films results to be similar to the P3HT homopolymer film as some works have already reported.[76-78] Compositional analysis of the spectra was carried out in a similar way that those performed for the analysis of the composition in P3HT/PCDTBT blends detailed in Chapter 2.2. Fits presented in Figure 4.35 were performed assuming the absence of new bands due to the interaction between P3HT and $PC_{71}BM$. The results indicate that P3HT/$PC_{71}BM$ thin films exhibit only 20 % of $PC_{71}BM$ in the surface (Figure 4.35.a).

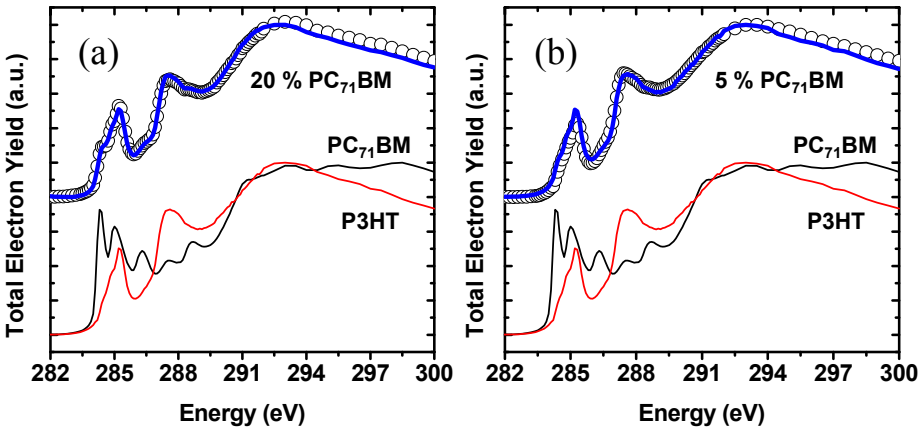

Figure 4.35. Compositional decomposition of TEY NEXAFS spectra. (a) Unstructured P3HT/$PC_{71}BM$ thin film and (b) P3HT/$PC_{71}BM$ with LIPSS obtained in vacuum at 266 nm. Red and black lines correspond to the reference P3HT and $PC_{71}BM$ thin films spectra respectively and blue lines are the fitted curves assuming the labelled amount of $PC_{71}BM$ on the surface.

Regarding the TEY-NEXAFS of the sample with LIPSS, some differences can be appreciated (Figure 4.34). Starting with the sample irradiated in air, a new band appears at 289 eV, which in principle could be due either to a $PC_{71}BM$ surface enrichment or to the photo-oxidation of the polymer chains. However the spectrum cannot be successfully fitted with the individual components since the LIPSS spectrum (green line in Figure 4.34) does not show the band at 284 eV associated to the $PC_{71}BM$. In addition the TEY-NEXAFS spectrum (purple line) of a sample with LIPSS on P3HT homopolymer obtained upon irradiation in air is presented in Figure 4.34. This spectrum presents similar bands to the P3HT/$PC_{71}BM$ irradiated in air suggesting that the new bands are not related to the $PC_{71}BM$ phase. On the other hand, with respect to the sample irradiated in vacuum, differences are less obvious and just a detailed inspection of the zone at 284-285 eV can detect them. In particular, a decrease of the small shoulder at 284 eV which corresponds to the $PC_{71}BM$ can be appreciated. The fit of this spectrum is presented in Figure 4.35.b, confirming that an increase of the P3HT phase at the surface of the sample occurs after irradiation in vacuum.

From these results one can conclude that P3HT/$PC_{71}BM$ films irradiated with an ultraviolet laser at 266 nm may present some chemical modifications of the polymer-fullerene structure when the laser irradiation is performed in air and the chemical modification is enhanced in the surface. In contrast, the chemical modification is almost negligible when the irradiation is performed under vacuum conditions.

4.4.4. Evolution of the phase separation as revealed by Resonant Soft X-ray Scattering

4.4.4.1. Phase separation in unstructured P3HT/$PC_{71}BM$ as revealed by Resonant Soft X-ray Scattering

As commented in Chapter 1, P3HT/$PC_{71}BM$ is one of the most studied active layers for organic solar cells. In order to improve the efficiency of such solar cell, the knowledge of the phase separation between the donor and acceptor phases is essential. In this context RSoXS is a potential technique since it allows obtaining an enhanced scattering by varying the X-ray energy in the C absorption edges (270-320 eV). The scattered intensity is related to the scattering contrast between both phases. Therefore, to obtain the scattering contrast and perform RSoXS experiments the following steps have been carried out. In order to exploit RSoXS it is necessary to calculate the imaginary and real parts of refraction index of individual components. The imaginary part, β, is related to the NEXAFS spectra by means of Equation 2.2. Through the Kramers-Kronig relations (Equation 2.3) the real part of the refraction index can be estimated. These calculations were performed with the *KKcalc* program developed by B.Watts.[79]

The imaginary and real parts of the refraction index of the P3HT and $PC_{71}BM$ are shown in Figure 4.36 estimated from the respective NEXAFS spectrum.

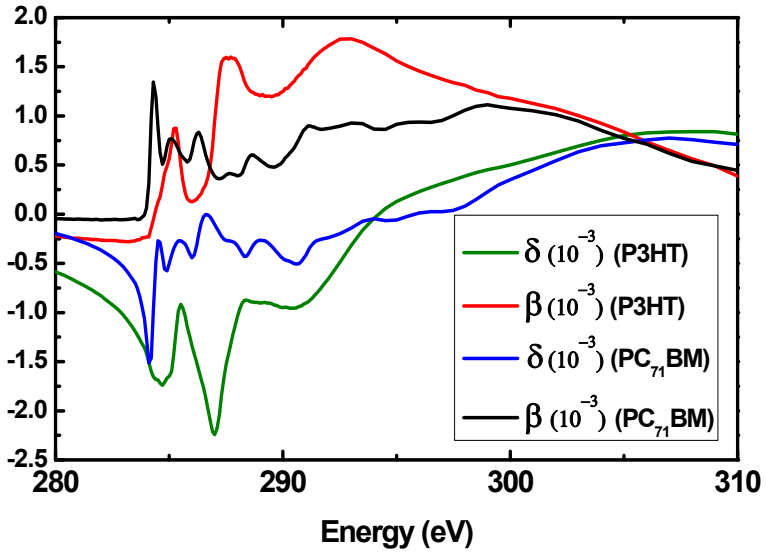

Figure 4.36. Real (δ) and imaginary (β) parts of the refraction index for P3HT and $PC_{71}BM$ as labeled.

The second necessary step is to estimate the scattering contrast between components which is given by the quantity $\Delta\delta^2 + \Delta\beta^2$ which determines the material contrast and

scattering strength. The material scattering contrast calculated for the P3HT and the $PC_{71}BM$ is shown in Figure 4.37.

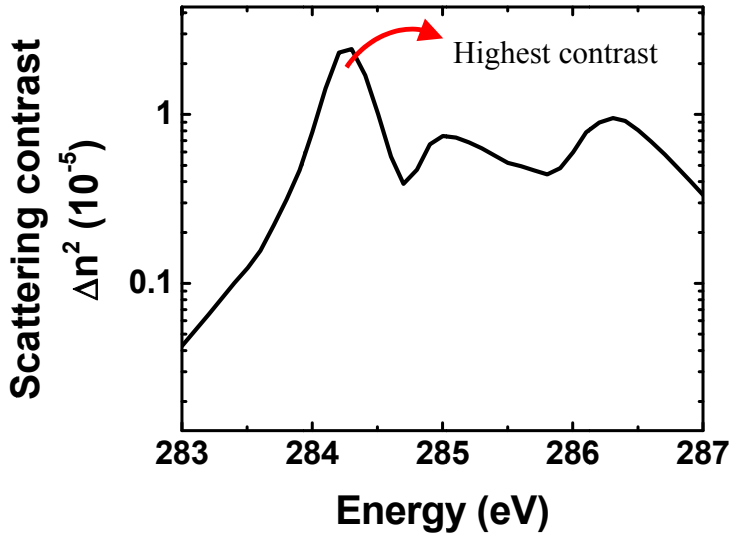

Figure 4.37. Materials scattering contrast between P3HT and $PC_{71}BM$ at the carbon K-edge.

The third necessary step is to select energies with the highest scattering contrast. Once the material contrast is known it is possible to select the energies with higher contrast between P3HT and $PC_{71}BM$. In this case, the highest contrast is obtained at energies around 284 eV. In Figure 4.38 one example is presented where the scattering pattern collected at one energy with high contrast between the components, namely 284.2 eV is compared with the one collected at another energy with low contrast, 285 eV.

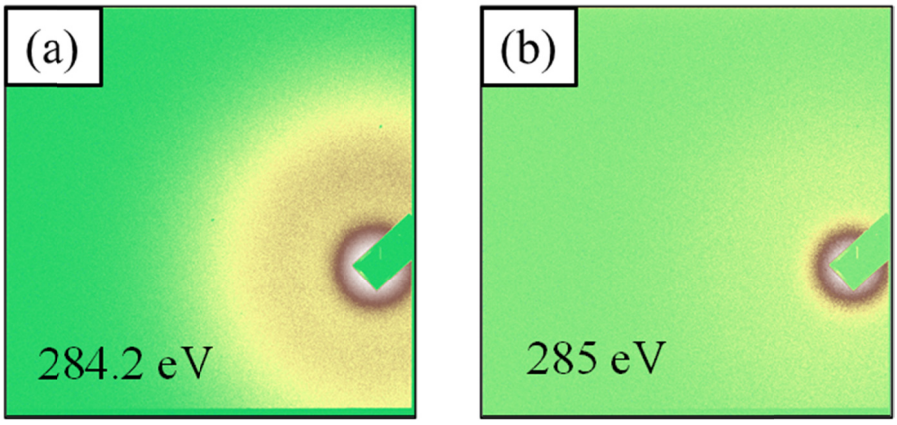

Figure 4.38. 2D RSoXS patterns taken at energies with (a) high and (b) low scattering contrast between P3HT and $PC_{71}BM$.

2D RSoXS patterns of a P3HT/$PC_{71}BM$ thin film at selected energies are presented in Figure 4.39. A weak scattering reflection q_1 = 0.389 nm, highlighted by a red arrow, appears at each energy, being enhanced at energies near 284 eV. In the literature this reflection has been assigned to either $PC_{71}BM$ clusters distances or to P3HT nanocrystal- nanocrystal distances.[63, 65, 68, 73]

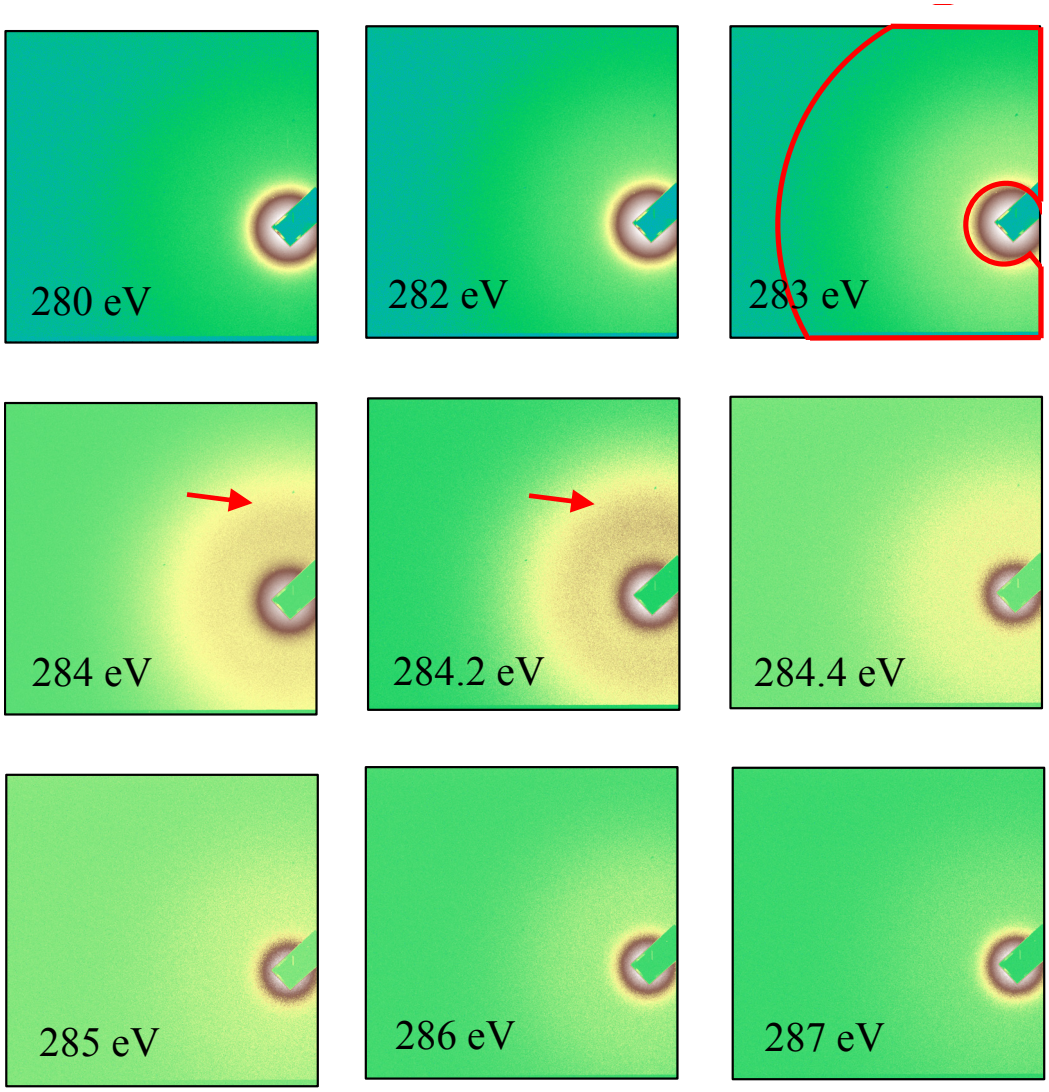

Figure 4.39. 2D RSoXS patterns at different carbon K-edge energies of the P3HT/$PC_{71}BM$ film. Circular sector labeled in red in the upper right pattern corresponds to the area used for the integration of the scattered intensity in the profiles shown in Figure 4.40. Red arrows indicate the scattering reflection enhanced at 284.2 eV.

Typically, the P3HT/$PC_{71}BM$ blend is described as a complex system formed by neat P3HT crystals, neat $PC_{71}BM$ clusters and an amorphous phase being a mixture of P3HT and $PC_{71}BM$.[80] One interpretation of the patterns shown in Figure 4.39 might be that $PC_{71}BM$ clusters are located between P3HT crystals surrounded by the amorphous

P3HT/$PC_{71}BM$ phase. In this way, the average distance between $PC_{71}BM$ clusters can be considered to be governed by the average distance between P3HT nanocrystals. According to this model the scattering maximum observed in the P3HT/$PC_{71}BM$ thin film would provide this characteristic length, i.e. the average distance between clusters, being this a possible way to evaluate the degree of phase separation between P3HT and $PC_{71}BM$.

Fig. 4.40 shows the intensity profiles at different carbon K-edge energies as labeled of the P3HT/$PC_{71}BM$ thin film obtained by integration of the scattering intensity over an area included in the circular sector described in Figure 4.39.

Accordingly, as the highest contrast is obtained at resonance energies characteristics of $PC_{71}BM$ (284.2 eV) as it is shown by the highest intensity of the shoulder of the red curve in Figure 4.40, it is reasonable to assume that the distance associated to this reflection in the reciprocal space is related to distances between $PC_{71}BM$ domains.

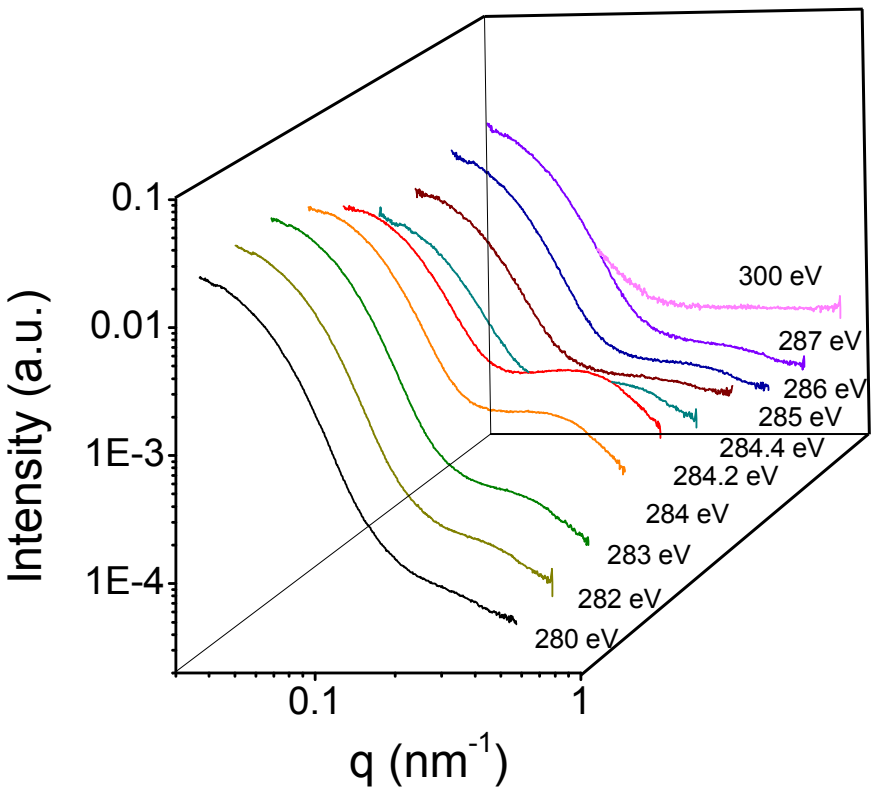

Figure 4.40. 1D intensity profiles at different carbon K-edge energies, as labeled, of the P3HT/$PC_{71}BM$ thin film obtained by integration of the scattering intensity over an area included in the circular sector described in Figure 4.39.

Figure 4.41 shows the intensity profiles at different energies for the P3HT/$PC_{71}BM$ sample thin film after annealing at 140 ºC for 4 minutes. The maximum associated to phase separation increases the intensity and is slightly shifted towards low q-values (Table 4.1). This behavior has been observed by hard X-ray and neutron experiments.[63, 65, 68] After annealing, both P3HT crystallization and $PC_{71}BM$ agglomeration are expected to happen. Both processes lead to an enrichment of the phases and hence to an enhancement of the scattering contrast between them. In addition, the P3HT crystallization explains the intensity increase and the $PC_{71}BM$ agglomeration explains the shift of the intensity maximum to lower q-values due to a larger distance between phases.

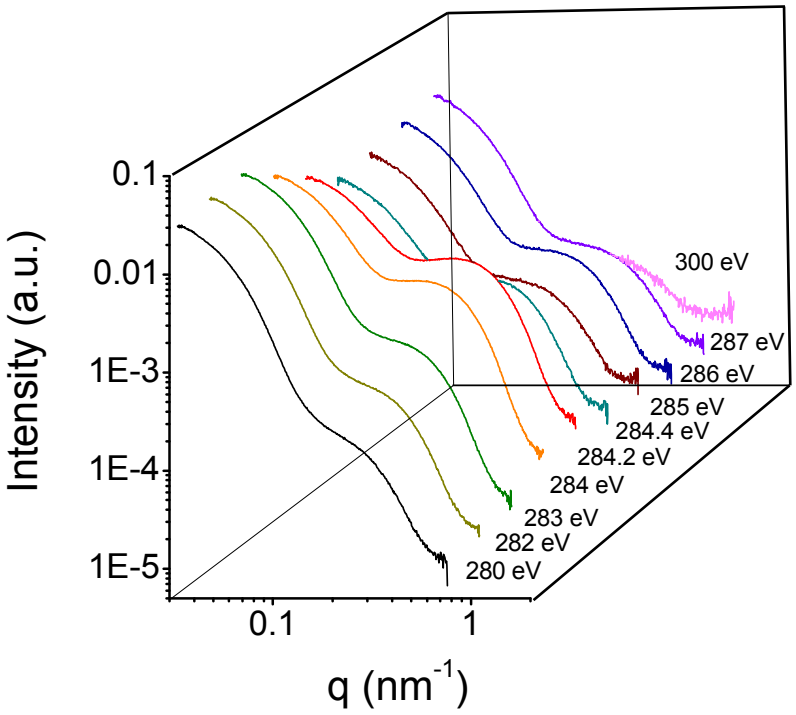

Figure 4.41. 1D intensity profiles at different carbon K-edge energies, as labeled, of the annealed P3HT/$PC_{71}BM$ thin film obtained by integration of the scattering intensity over a circular sector.

4.4.4.2. Phase separation in LIPSS on P3HT/$PC_{71}BM$ irradiated in air

Regarding the samples with LIPSS, the thin film irradiated at 266 nm under air conditions shows a grating-type pattern (Figure 4.42) in which the periodicity of the laser-induced structures may be estimated from the q-value of the first order peak in the

1D intensity profiles shown in Figure 4.42.b. Additionally, a ring appears at low q-values with an isotropic shape (Figure 4.42.a and 4.42.c). This scattering located at $q = 0.023$ nm^{-1} and indicated by an arrow in Figure 4.42.a arises from large length correlations with an average distance of 270 nm. Since LIPSS samples are anisotropic they exhibit oriented patterns. Thus, a main direction across the scattering maxima of the LIPSS can be defined as S and another perpendicular as P.

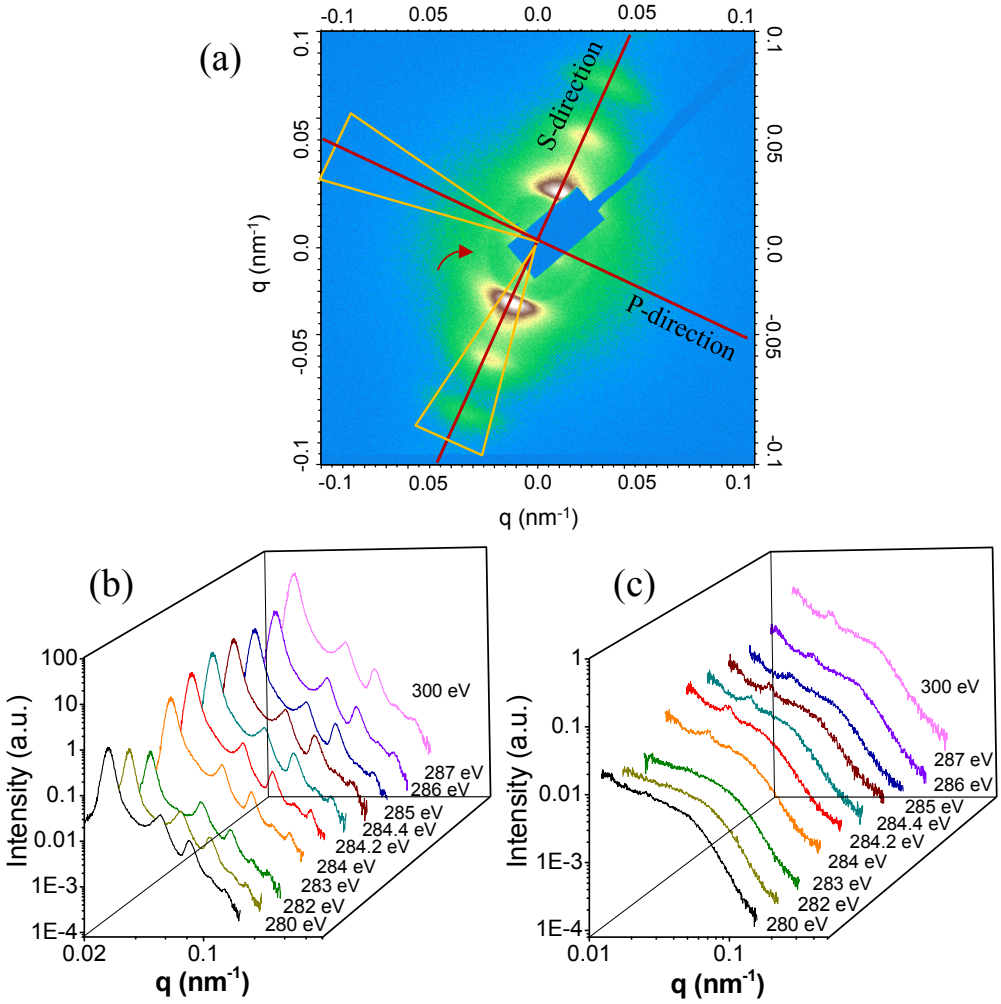

Figure 4.42. (a) 2D RSoXS pattern of the P3HT/$PC_{71}BM$ thin film with LIPSS obtained upon irradiation at 266 nm in air collected at a sample-detector distance of 150 nm with an energy of 284.2 eV. (b) 1D intensity profiles at different carbon K-edge energies, as labeled, obtained by integration of the scattering intensity in the S-direction along the scattering maxima over the area included in Figure 4.42.a. (c) 1D intensity profiles at different carbon K-edge energies, as labeled, obtained by integration of the scattering intensity in the P-direction over the area included in Figure 4.42.a. Red arrow corresponds to the scattering with a ring shape at $q = 0.023$ nm^{-1}.

In order to access to a larger q-values range, the scattered intensity was collected at a shorter sample-detector-distance. Figure 4.43 shows a scattering pattern similar to that shown in Figure 4.42 in a larger q-range for the P3HT/$PC_{71}BM$ thin film. In this case, an additional scattering maximum at larger q-values ($q_2 = 0.235$ nm^{-1}), indicated by an arrow in Figure 4.43.a, is enhanced at 284.2 eV and could be related to the phase separation as observed in the non-irradiated sample with a q-value of 0.389 nm^{-1}. This maximum indicates the existence of a characteristic correlation length orthogonal to the ripple direction of the LIPSS periodicity. Figure 4.43.b shows the scattered intensity integrated in an angular sector orthogonal to the ripples as depicted in Figure 4.43.a. The maximum scattered intensity appears at 284.2 eV which should be related with the distances between $PC_{71}BM$ domains.

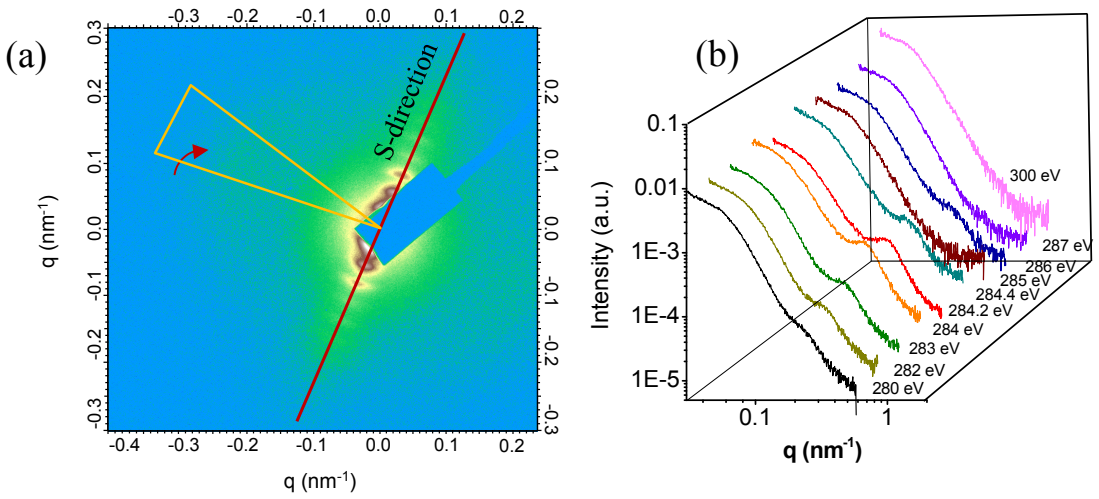

Figure 4.43. (a) 2D RSoXS pattern of the P3HT/$PC_{71}BM$ thin film with LIPSS obtained upon irradiation at 266 nm in air collected at a sample-detector distance of 50 nm with an energy of 284.2 eV. (b) 1D intensity profiles at different carbon K-edge energies, as labeled, obtained by integration of the scattering intensity in the P-direction over the area included in Figure 4.43.a. Red arrow corresponds to the scattering related to the phase separation average distance at $q_2 = 0.235$ nm^{-1}.

4.4.4.3. Phase separation in LIPSS on P3HT/$PC_{71}BM$ irradiated in vacuum

The P3HT/$PC_{71}BM$ LIPSS formed by laser illumination under vacuum conditions (Figure 4.44.a) also show a gratings-type pattern. The scattering maximum at $q_2 = 0.157$ nm^{-1}, indicated by an arrow, is here enhanced in comparison with the

previous case (Figure 4.43) and indicates the existence of a characteristic correlation length which is perpendicular to the LIPSS. This maximum can be associated to the correlation distances between $PC_{71}BM$ clusters and hence associated to the degree of phase separation between P3HT and $PC_{71}BM$ as it was commented before.

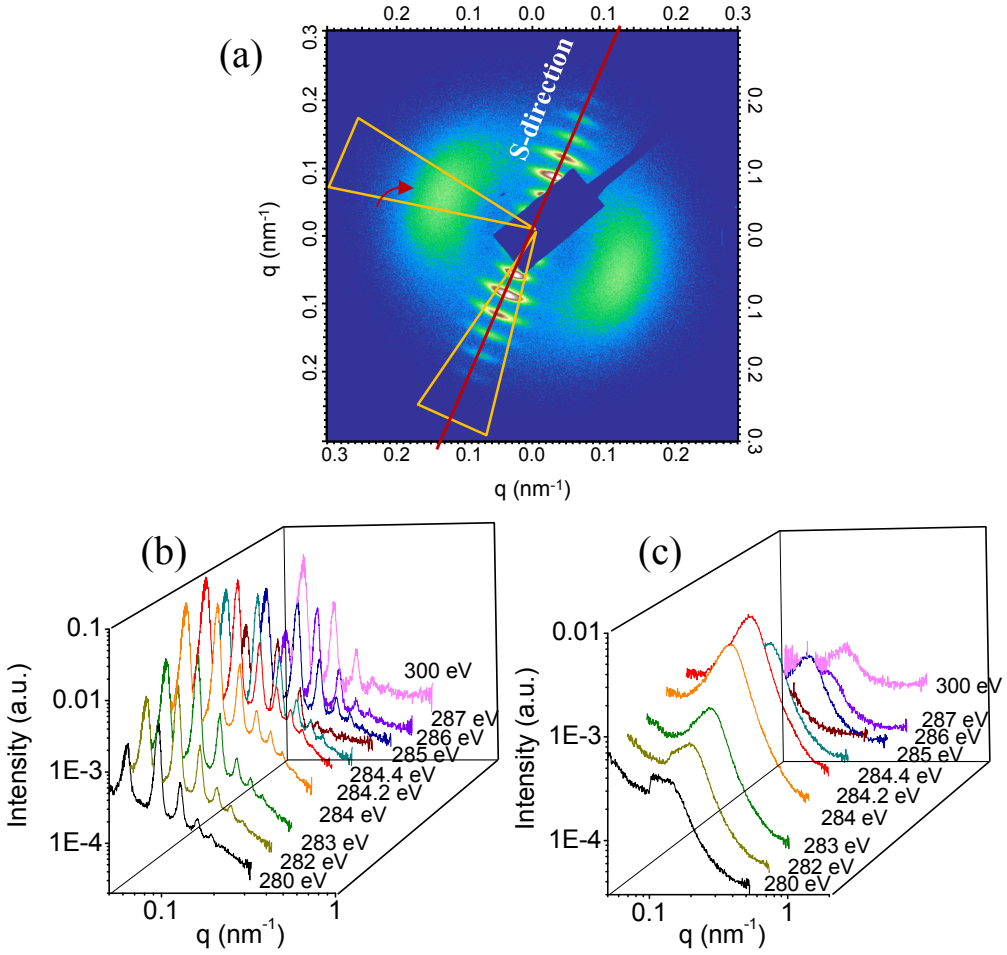

Figure 4.44. (a) 2D RSoXS pattern of the P3HT/$PC_{71}BM$ thin film with LIPSS obtained upon irradiation at 266 nm in vacuum collected at a sample-detector distance of 50 nm with an energy of 284.2 eV. (b) 1D intensity profiles at different carbon K-edge energies, as labeled, obtained by integration of the scattering intensity in the S-direction along the scattering maxima over the area included in Figure 4.44.a. (c) 1D intensity profiles at different carbon K-edge energies, as labeled, obtained by integration of the scattering intensity in the P-direction over the area included in Figure 4.44.a. Red arrow indicates the scattering maxima related to the phase separation at $q_2 = 0.157$ nm^{-1}.

Figure 4.44.b shows the 1D intensity profiles at different energies for the P3HT/$PC_{71}BM$ sample with LIPSS irradiated in vacuum, obtained from the integration

of 2D patterns using the cakes drawn in Figure 4.44.a along the S- and P-directions. Comparing these intensity profiles to those from the P3HT/$PC_{71}BM$ sample with LIPSS obtained in air (Figure 4.42.b and 4.43.b), it is seen that the maximum related to the phase separation is both more intense and better defined. This result suggests that P3HT and $PC_{71}BM$ phases are separated along the ripples. According to the mechanism of LIPSS formation, when irradiating a polymer material the surface reaches a temperature above the T_m in the case of a semicrystalline polymer and thus during the reorganization process a liquid-liquid demixing mechanism might be the driving mechanism of such phase separation.

A schematic model of this interpretation is shown in Figure 4.45 showing the two characteristic correlation lengths of the LIPSS, d_1 being the average distance between ripples and d_2 being the average distance between $PC_{71}BM$ clusters within the ripple. The average distances that can be obtained from the scattering pattern are $d_1 \approx 209$ nm and $d_2 \approx 40$ nm for the LIPSS obtained upon irradiation in vacuum. The scattered intensity at low q-values is almost vanished for the sample irradiated in vacuum, suggesting that oxidation or carbon formation does not take place during LIPSS formation in vacuum.

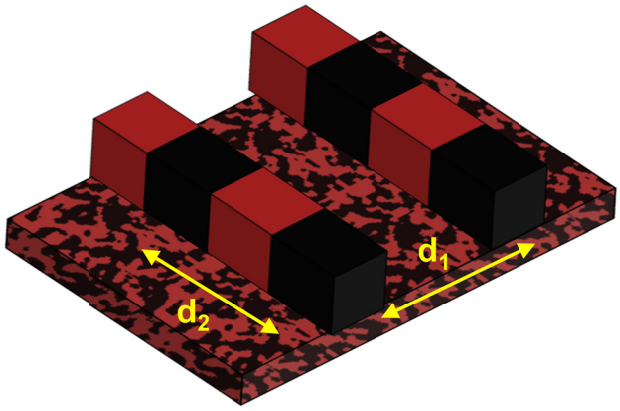

Figure 4.45. Proposed model for P3HT/$PC_{71}BM$ sample with LIPSS.

The presence and high intensity of the reflection at $q_2 = 0.157$ nm^{-1}, confirm the presence of a phase separation between the P3HT and the $PC_{71}BM$. In principle this is not expectable since laser provokes the reduction of the polymer and $PC_{71}BM$ crystallinity and as a consequence the diffusion of the fullerene molecules into amorphous P3HT phase.[81] However the hindered crystallization produced during the laser illumination

could give rise to a liquid-liquid demixing during the reorganization process and as a consequence a large phase separation between both components.

4.4.4.4. Effect of annealing on the phase separation of P3HT/$PC_{71}BM$

Figure 4.46.a shows that after annealing for 4 min at 140 ºC the LIPSS sample fabricated in air at 266 nm, no scattering signal related to phase separation is detected in the q-range investigated (Figure 4.46.c). However the scattering from the LIPSS is maintained indicating that LIPSS remains after thermal annealing.

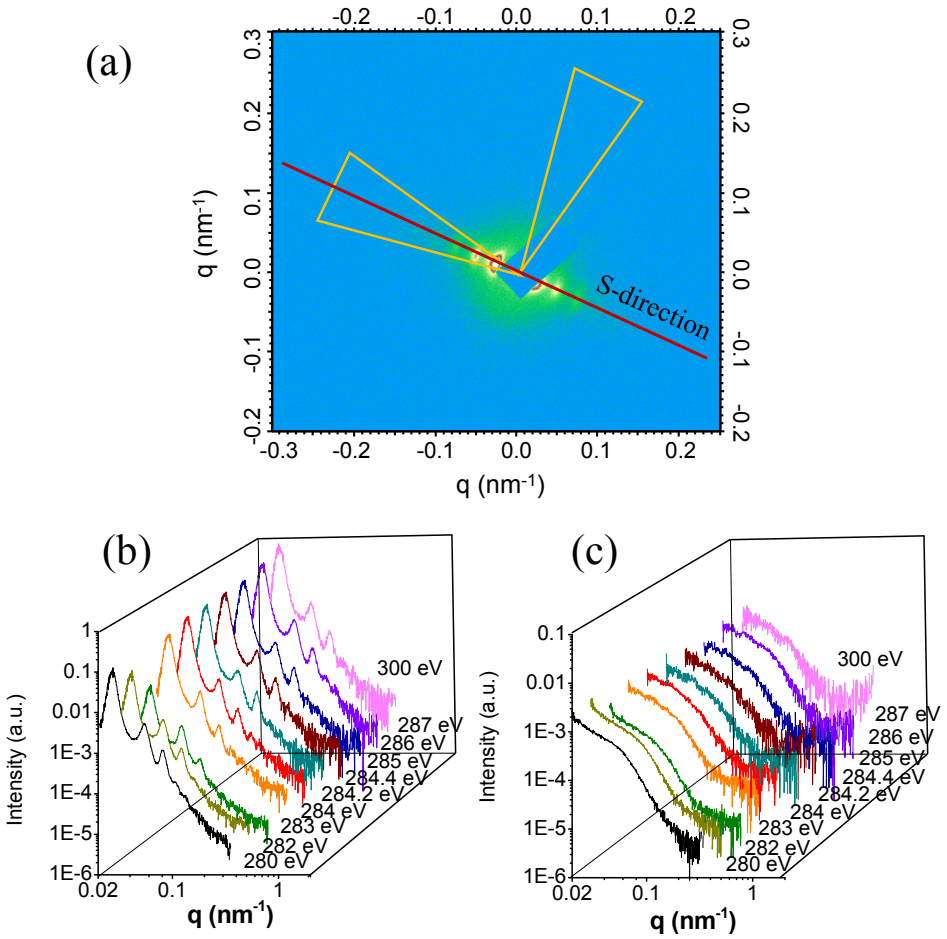

Figure 4.46. (a) 2D RSoXS of the P3HT/$PC_{71}BM$ thin film with LIPSS obtained upon irradiation at 266 nm in air after annealing for 4 min at 140 ºC, collected at a sample-detector distance of 70 nm with an energy of 284.2 eV. (b) 1D intensity profiles at different carbon K-edge energies, as labeled, obtained by integration of the scattering intensity in the S-direction along the scattering maxima over the area included in Figure 4.46.a. (c) 1D intensity profiles at different carbon K-edge energies, as labeled, obtained by integration of the scattering intensity in the P-direction over the area included in Figure 4.46.a.

Nevertheless, after annealing the LIPSS sample fabricated in vacuum at 266 nm, the scattering from the LIPSS periodicity is maintained and the reflection related to phase separation of the components is also present but it loses the orientation as it is shown in Figure 4.47.a. The 1D orthogonal intensity profiles at different energies are presented in Figures 4.47.b and 4.47.c. In the case of the reflection related to the phase separation a shift of the intensity maximum to higher q-values is observed in comparison with the intensity profiles from the same sample without annealing (Table 4.1).

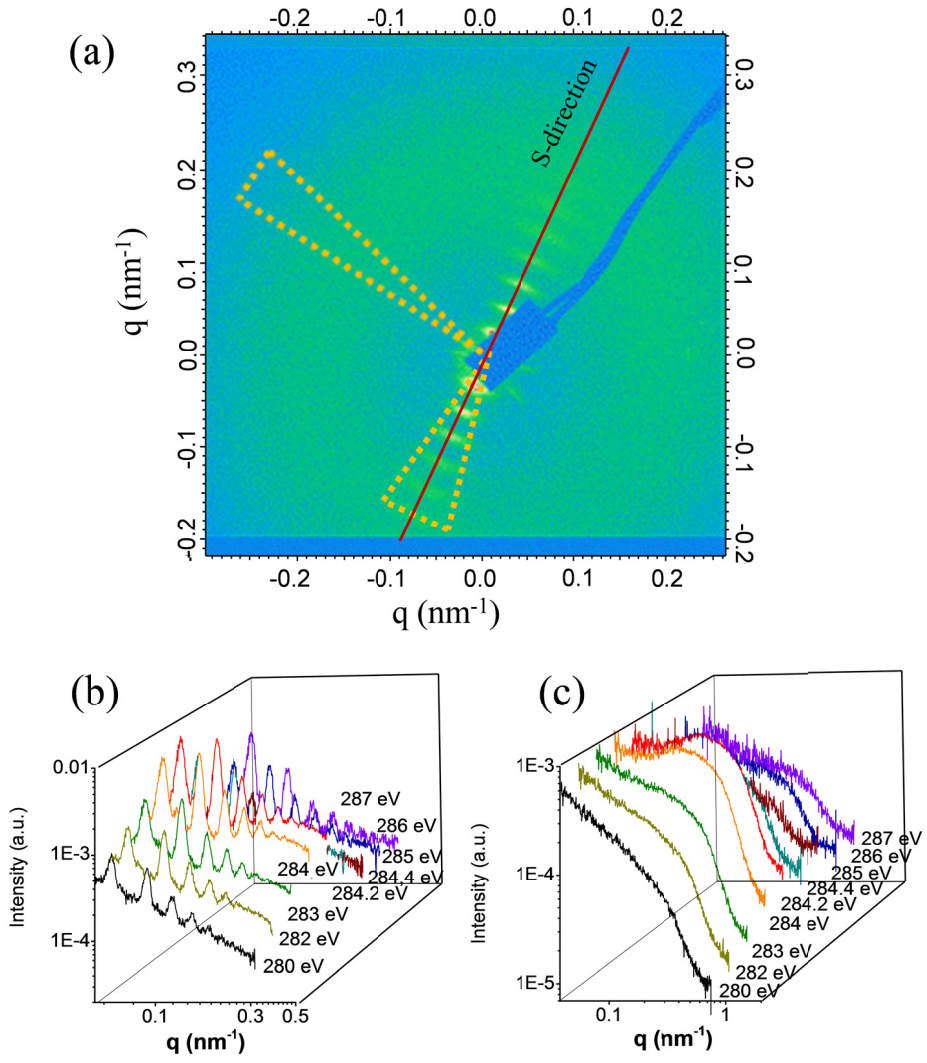

Figure 4.47. (a) 2D RSoXS pattern of the P3HT/$PC_{71}BM$ thin film with LIPSS obtained upon irradiation at 266 nm in vacuum after annealing for 4 min at 140 ºC, collected at a sample-detector distance of 70 nm with an energy of 284.2 eV. (b) 1D intensity profiles at different carbon K-edge energies, as labeled, obtained by integration of the scattering intensity in the S-direction along the scattering maxima over the area included in Figure 4.47.a. (c) 1D intensity profiles at different carbon K-edge energies, as labeled, obtained by integration of the scattering intensity in the P-direction over the area included in Figure 4.46.a.

To discuss further the results, the scattering related to the phase separation has been analyzed. In Figure 4.48.a the 1D intensity profiles at 284.2 eV of the P3HT/$PC_{71}BM$ thin film before and after annealing are presented. As mentioned before the scattering intensity is shifted to lower q-values. The 1D profiles in the P-direction at 284.2 eV of the LIPSS in P3HT/$PC_{71}BM$ thin films obtained upon irradiation at 266 nm in air (green), in vacuum (orange) and in vacuum after annealing (purple) are presented in Figure 4.48.b. Distances obtained from both, the maximum of intensity related to the LIPSS periodicity (q_1) and the maximum related to phase separation distance (q_2) are presented in Table 4.1 for the samples investigated. Results show that annealing the thin film produces a shift of the maximum related to the phase separation to lower q-values (blue to black line). However, after annealing the sample irradiated in vacuum the maximum shifts to a higher q-value that coincides with the q-value of the annealed thin film.

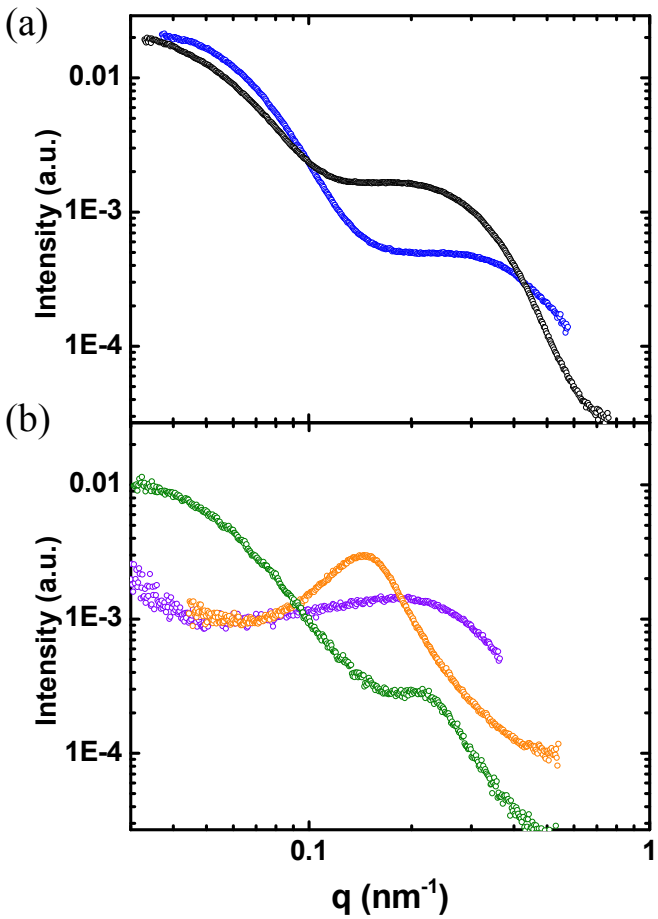

Figure 4.48. (a) Comparison of the 1D intensity profiles at 284.2 eV of the P3HT/$PC_{71}BM$ thin film before (blue) and after (black) annealing. (b) 1D profiles in the P-direction at 284.2 eV of the LIPSS in P3HT/$PC_{71}BM$ thin films obtained upon irradiation at 266 nm in air (green), in vacuum (orange) and in vacuum after annealing (purple).

Table 4.1. Characteristic lengths d_1 and d_2 of the model illustrated in Figure 4.45 obtained from the scattering of the maxima at the corresponding q-values for P3HT/$PC_{71}BM$ samples.

Sample	Annealing	LIPSS	q_1 (nm^{-1})	q_2 (nm^{-1})	d_1 (nm)	d_2(nm)
P3HT:$PC_{71}BM$	NO	NO	--	0.389	--	16
P3HT:$PC_{71}BM$	YES	NO	--	0.291	--	22
P3HT:$PC_{71}BM$	NO	air	0.0273	0.235	232	27
P3HT:$PC_{71}BM$	YES	air	0.0282	--	224	--
P3HT:$PC_{71}BM$	NO	vacuum	0.0301	0.157	209	40
P3HT:$PC_{71}BM$	YES	vacuum	0.0292	0.29	216	22

In summary, according to RSoXS results (Table 4.1) the characteristic phase separation distance increases from 16 to 22 nm when annealing the P3HT/$PC_{71}BM$ thin film, due mainly to the growth of $PC_{71}BM$ aggregates with temperature. For LIPSS samples obtained under vacuum, the characteristic phase separation distance decreases from 40 to 22 nm when annealing. The final value coincides with the phase separation distance of the annealed thin film. It can be explained considering that the AFM images of LIPSS after annealing shows an enormous decrease of the LIPSS depth compared with the initial LIPSS (Figure 4.32). Taking this into account, it can be suggested that after annealing the main contribution to the RSoXS pattern is the non-structured thin film under a structured surface of only 8 nm thickness.

4.4.5. Electrical properties of nanostructured P3HT/$PC_{71}BM$ thin films

Electrical properties at the nanoscale have been analyzed by C-AFM. P3HT/$PC_{71}BM$ thin films nanostructured by LIPSS in vacuum and with post annealing at 140 ºC for 4 minutes are shown in Figure 4.49. Before annealing the current image exhibits the characteristic heterogeneous conductivity observed in samples with LIPSS. As discussed in Section 4.2, the loss of the P3HT crystallinity could be the cause of the low conductivity observed in the ripples. After annealing the sample present an increase of conductivity. These results confirm that P3HT crystallizes after annealing and also that it is possible to fabricate active layers with LIPSS without disrupting the phase separation morphology and its electrical properties.

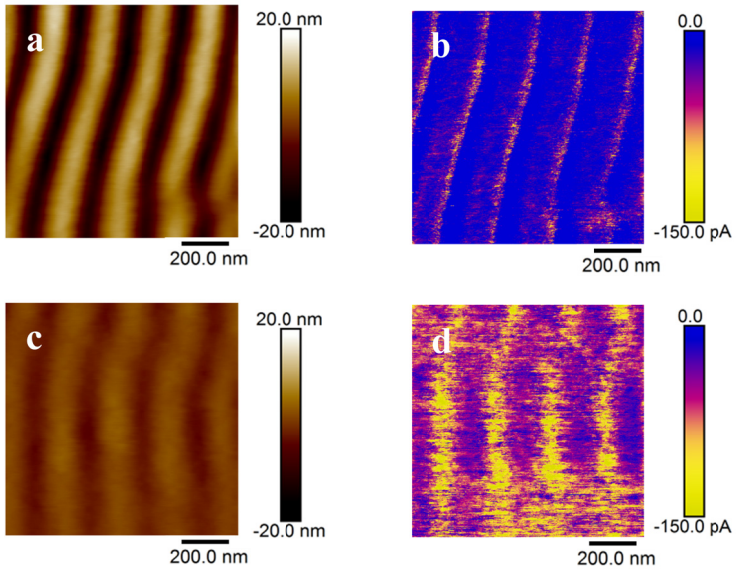

Figure 4.49. C-AFM topography and current images of LIPSS on P3HT/P_{71}CBM fabricated at 266 nm in vacuum. (a,b) before and (c,d) after annealing.

4.5. *In situ* LIPSS formation on conjugated polymers monitored by Grazing Incidence Small Angle X-ray Scattering (GISAXS)

In this section the LIPSS formation on the surface of different polymer films by using GISAXS with synchrotron radiation will be described. The polymers investigated have been PCDTBT and the P3HT/PCDTBT 1:1 blend.

4.5.1. Simultaneous GISAXS-LIPSS experimental set up

In previous sections, the structural characterization of LIPSS has been undertaken by AFM. However, microscopy becomes cumbersome or even not possible upon dealing with evaluation of fast processes in real time. For this reason the use of X-ray scattering techniques with synchrotron radiation can be very useful since they allow obtaining reciprocal space time resolved structural information with a time resolution in the range of milliseconds.[82] To perform X-ray diffraction on surface nanostructures it is very convenient to work under total X-ray reflection conditions.[83-85] The diffraction pattern provides statistical information integrated over a large sample area covered by the footprint of the incident beam on the material surface. Therefore, the scattering pattern can deliver structural information averaged over an area of several tens of microns. Previous studies on P3HT LIPSS formation have been done "ex-situ".[27, 28] However, this procedure limits the amount of samples and rules out real time analysis and the investigation of irradiation by a high repetition rate.

For LIPSS formation on the polymer spin-coated films, the 2nd harmonic of a Nd:YAG laser (Lotis TII LS-2131M, λ = 532 nm) and pulses of 8 ns were used. The monitoring of LIPSS formation *in situ* was accomplished by using synchrotron radiation at the DUBBLE beamline of the European Synchrotron (ESRF), Grenoble, France. GISAXS patterns were acquired while simultaneous laser irradiation on the sample was taking place. A scheme of the simultaneous experiment is shown in Figure 4.50.

The laser beam (red dashed line) is directed by a collection of three mirrors to the sample surface. The laser beam size is controlled by an iris and its intensity by a variable attenuator. The X-ray beam reaches the sample which is positioned in grazing incidence conditions.[27, 28] The scattering plane, containing both the direct and the specular beams intersects the detector along the meridian of the GISAXS pattern. The horizon is the intersection between the sample plane and the plane of the detector. The study has been performed at the laser wavelength 532 nm for three different laser pulse repetition rates: 2, 5 and 10 Hz.

In this set-up, the sample must be placed horizontal and parallel to the X-ray beam in a grazing incidence geometry. A precise alignment of the laser beam is required in order to reach the sample surface perpendicularly. Furthermore, the laser polarization vector must be parallel to the X-ray beam direction.

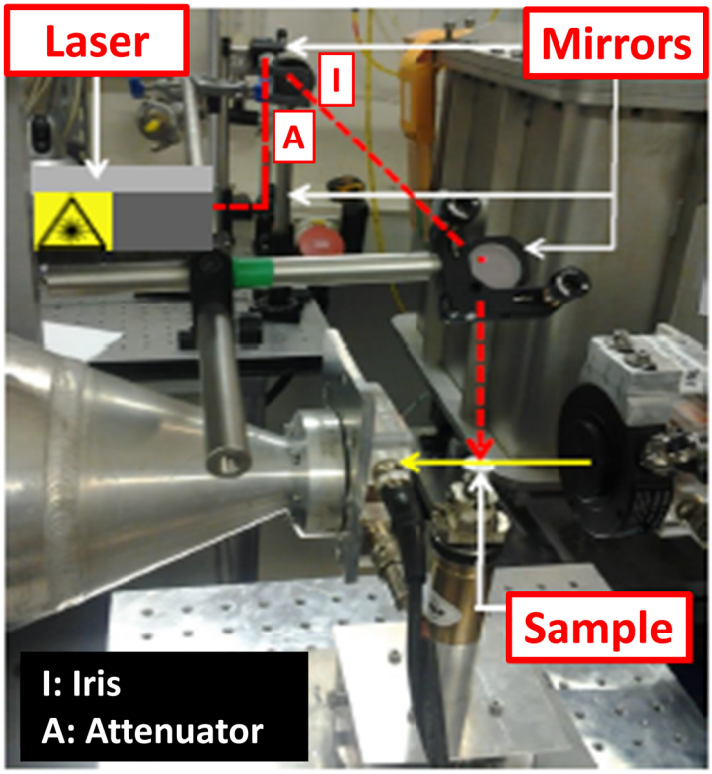

Figure 4.50. Set-up of the simultaneous GISAXS- LIPSS experiment. Laser beam is marked by a red dashed line and the X-ray beam is marked by the yellow arrow.

On the basis of previous studies a laser fluence of 26 mJ/cm^2 was used for all the experiments which were carried out at different repetition rates of 2, 5, and 10 Hz. For the sake of comparison all the samples were irradiated with 9000 pulses. A laser irradiated area of 5 mm diameter was selected by using an iris. For the GISAXS measurements a wavelength, $\lambda = 0.124$ nm and a beam size (H×V) of 1.1 × 0.5 mm^2 were used. The GISAXS patterns were recorded by a Pilatus detector of 981 × 1043 pixels, 172.0 µm × 172.0 µm pixel size, which was located at 7 m from the sample position. The sample was aligned with its surface horizontal and parallel to the X-ray beam and at a height which intercepted half of the beam intensity. Then, for the GISAXS experiments, the sample is rotated in order to reach an incidence angle between sample surface and the beam, α_i, of 0.4º. The experimental set-up for a GISAXS experiment has been described in Section 2.2.7.3. In order to follow *in situ* the LIPSS formation both laser irradiation and GISAXS acquisition were simultaneously activated. Acquisition time for the GISAXS patterns for the laser irradiation at 2 Hz was 100 s while for the irradiations at 5 and 10 Hz two acquisition times were selected: 5 s

for the first 3000 pulses and 20 s for the rest of the experiment. GISAXS patterns were analyzed by the Fit2D software.[86] After GISAXS experiments the samples were examined by AFM in tapping mode.

4.5.2. *In situ* LIPSS formation in PCDTBT as revealed by GISAXS

The Figure 4.51 shows a sequence of GISAXS patterns during irradiation of a PCDTBT film as a function of both the number of pulses and the corresponding real experimental time. This *in situ* experiment makes possible the study of the scattering evolution during the LIPSS formation exploiting the potential of the synchrotron techniques to investigate processes in real time.

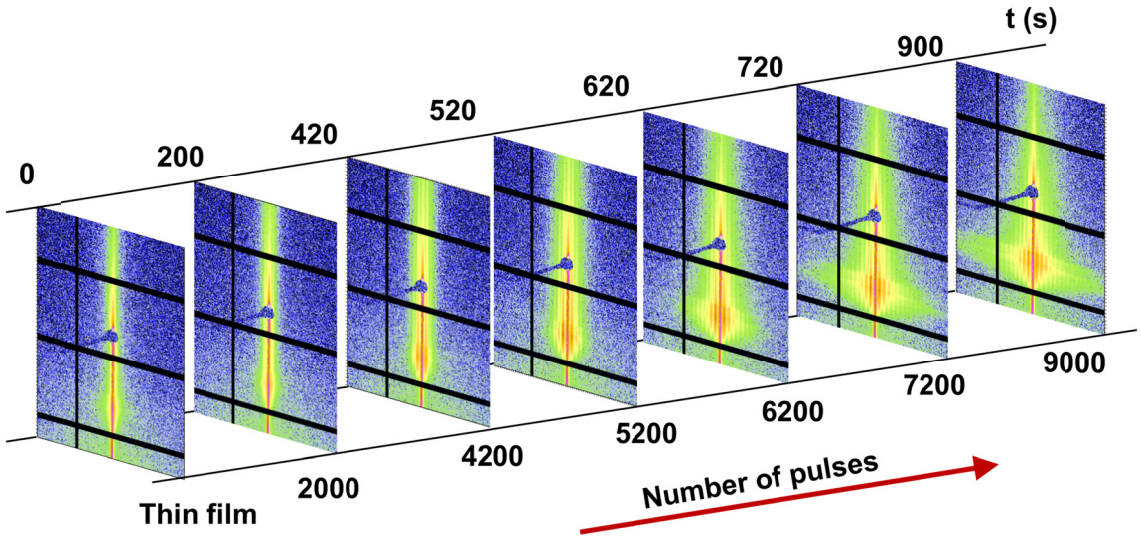

Figure 4.51. Real time LIPSS formation on PCDTBT upon irradiation at 532 nm at 10 Hz as revealed by GISAXS.

Some selected GISAXS patterns of LIPSS evolution in PCDTBT during laser irradiation are presented in Figure 4.52 for the repetition rate of 10 Hz. The first pattern in Figure 4.52 corresponds to the spin-coated PCDTBT thin film. This pattern is the characteristic one for a spin-coated film in absence of relevant structure in the angular range investigated.[87] After laser irradiation with 1000 pulses (100 s) the GISAXS pattern starts exhibiting an increase of the intensity around the region referred to as Yoneda peak[88] which appears at around half of the reflection angle α_i and it is related to the critical angle of polymers for the X-rays. The intensity increases with the number of pulses and develops a clear vertical reflection with a rod shape. For higher number of

pulses the GISAXS pattern is characterized by an increasing number of the vertical rods.

From the GISAXS patterns horizontal intensity profiles along ω for constant α values have been extracted (see Figure 2.15). These were obtained by vertical integration of a horizontal strip (15 pixel wide) as the one shown in Figure 4.52 around the maximum of intensity of the vertical diffraction maxima (α ≈ 0.15º). As it was commented above, this angular region corresponds to the Yoneda peak.[88]

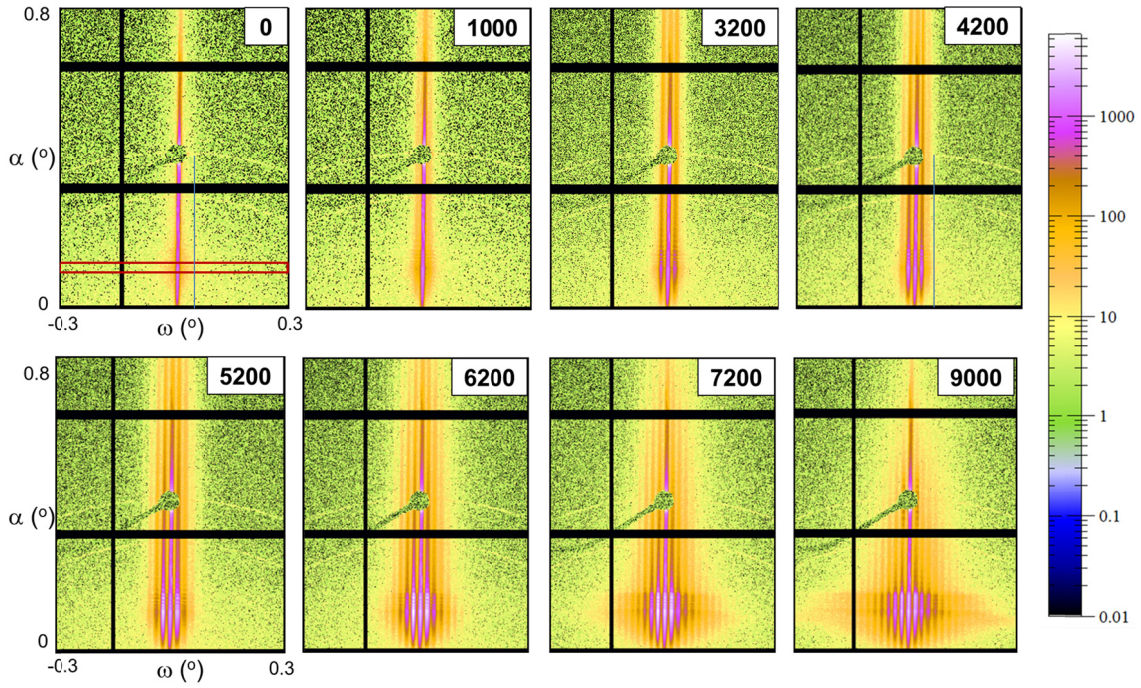

Figure 4.52. Evolution of GISAXS patterns as a function of the number of pulses during the *in situ* LIPSS formation in PCDTBT thin films at 532 nm for the repetition rate of 10 Hz. The number of pulses is labelled on every pattern in the upper right corner.

The corresponding intensity profiles for the GISAXS patterns as a function of the number of pulses are plotted in Figure 4.53 for different repetition rates. The period (L) of the LIPSS can be derived from the lateral position of the first maxima, that is the nearest one to ω = 0º (q_y = 0 nm^{-1}). The ω angle and the q_y component of the scattering vector ($\vec{q}$) are related by the Equation 2.16.b and therefore, L can be obtained using the expression: ($L = 2\pi/q_{ymax}$). The outer maxima are consecutive orders of the first one.[27] A clear evolution of the intensity and the number of reflections is observed.

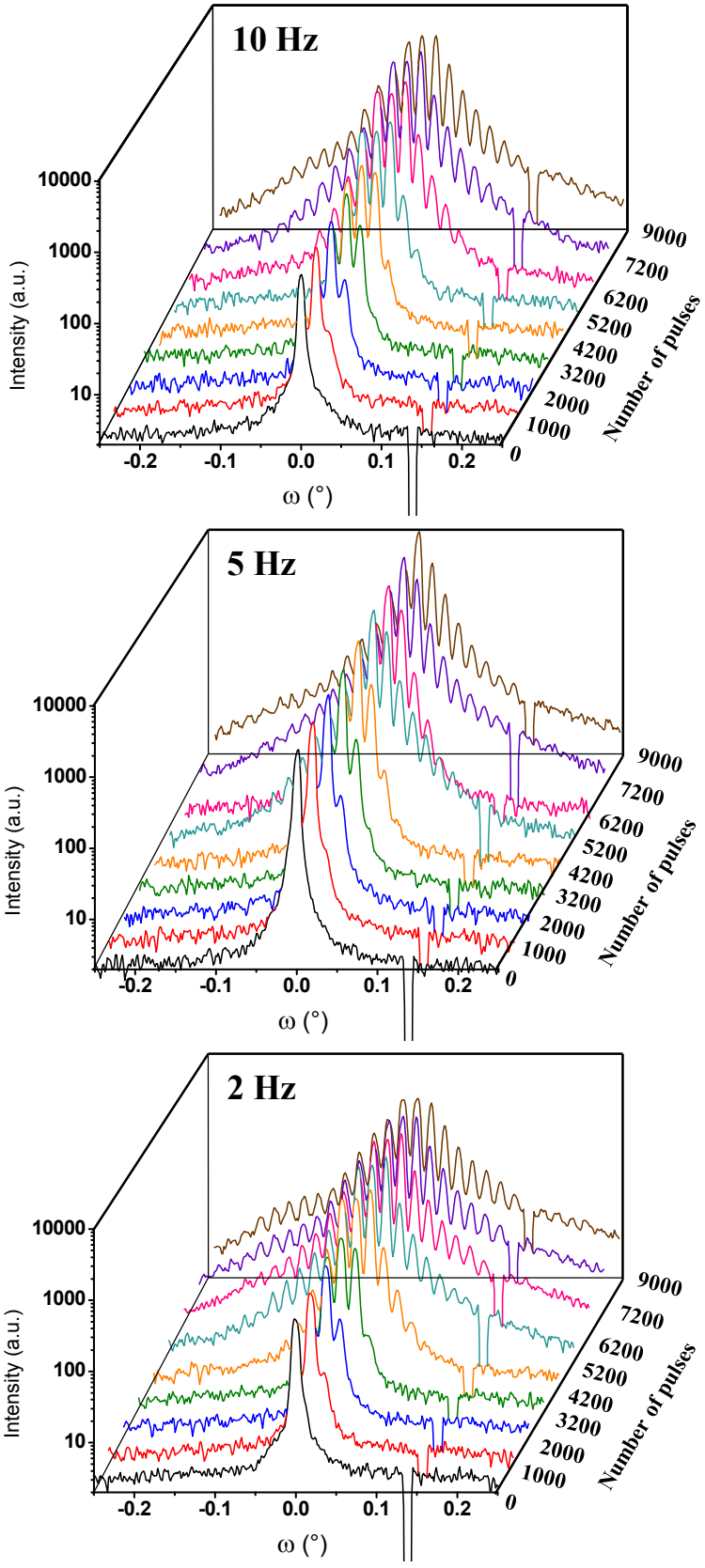

Figure 4.53. Intensity profiles, in a logarithmic scale, as a function of ω and the number of pulses obtained from the GISAXS patterns at a constant α = 0.15º for different repetition rates, as labeled.

The evolution of the LIPSS period extracted from the GISAXS analysis with the number of pulses for the different laser repetition rates is presented in Figure 4.54.

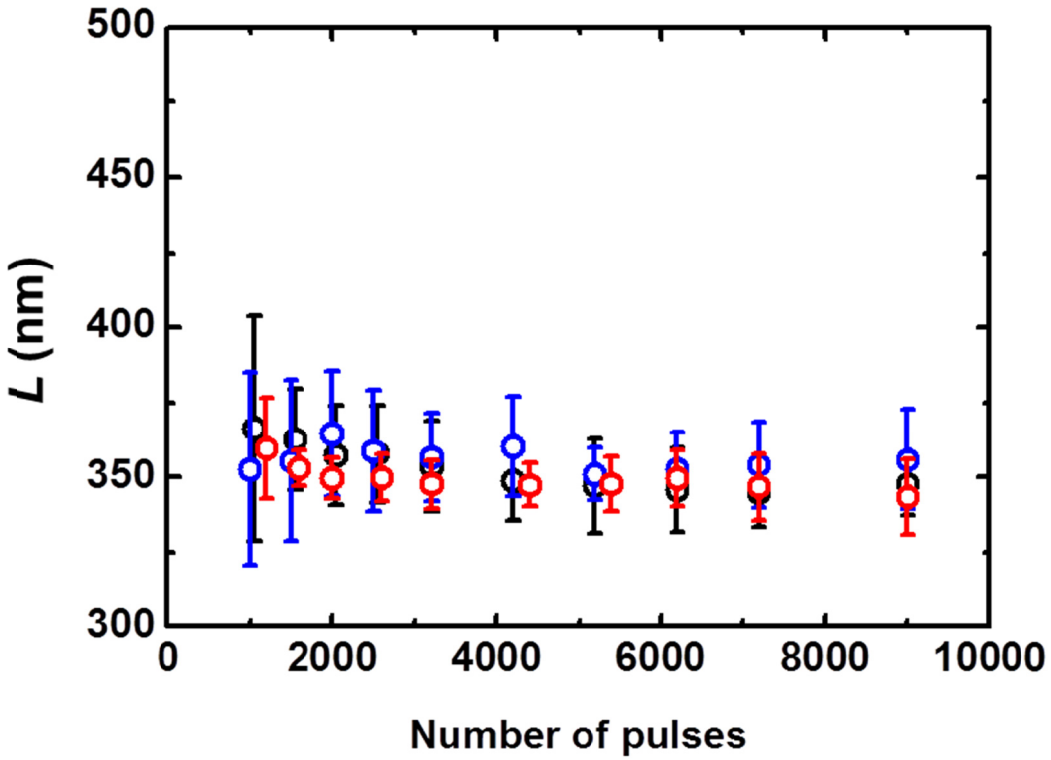

Figure 4.54. Variation of the periods (L) with the number of pulses at different repetition rates: 10 Hz (black circles), 5 Hz (blue circles) and 2 Hz (red circles).

The results indicate that the LIPSS period remains practically constant with a value of 350 nm in the whole range of pulses employed. Moreover, results are qualitatively similar for the three laser repetition rates used.

In order to compare the evolution with time of LIPSS formation for the different repetition rates, in Figure 4.55 the total integrated intensity of the 1D profiles, which is the sum of the total intensity of the horizontal strip represented in the Figure 4.52 (0 pulses), has been represented as a function of the number of pulses. For the sake of comparison we have subtracted the integrated intensity of the intensity profile corresponding to the first GISAXS pattern for each experiment. Figure 4.55 shows that for all the investigated repetition rates the integrated intensity follows three regimes as a function of number of pulses: the first regime of incubation where the integrated intensity increases slowly with number of pulses, a second regime where the integrated

intensity increases rapidly with increasing number of pulses and a third regime where the integrated intensity reaches a plateau. The complete process seems to be faster for a lower repetition rate.

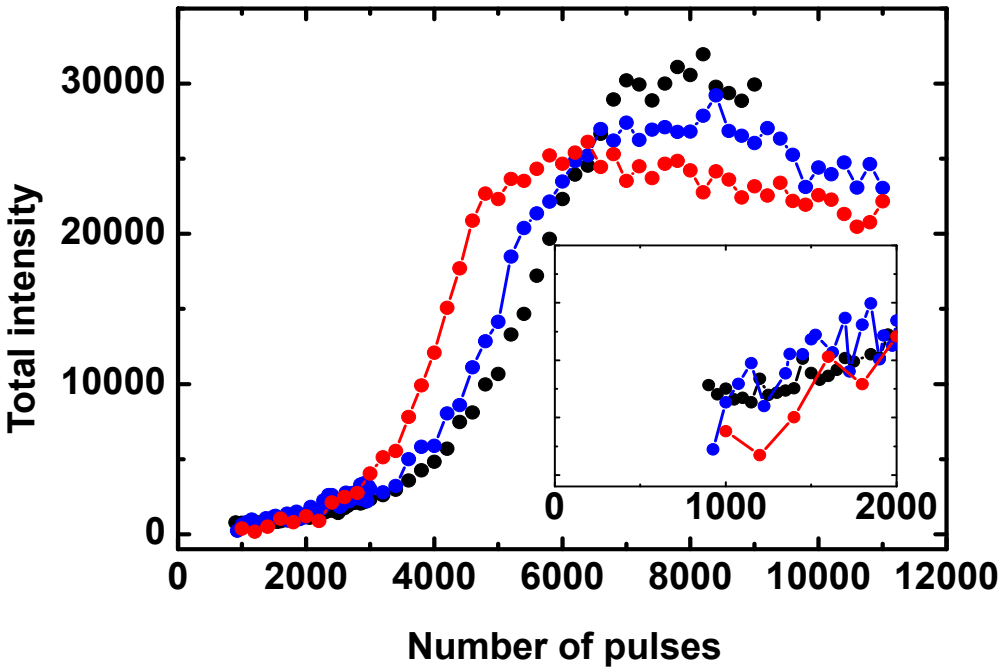

Figure 4.55. Total integrated intensity obtained from the GISAXS pattern at $\alpha = 0.15^{o}$ as a function of the number of pulses at different repetition rates: 10 Hz (black circles), 5 Hz (blue circles) and 2 Hz (red circles). The inset is a zoom of the total integrated intensity of the first stages of the LIPSS formation.

The influence of the laser repetition rate on LIPSS formation is illustrated in Figures 4.56, 4.57 and 4.58 for selected GISAXS patterns corresponding to different stages of the LIPSS formation.

Samples irradiated with 2000 pulses for the three repetition rates are shown in Figure 4.56. Apparently, similar patterns in intensity and number of reflections are reached at the three repetition rates. In addition, GISAXS patterns at 4200 pulses are presented in Figure 4.57 for the three repetition rates. In contrast to the patterns obtained at 2000 pulses (in the initial regime), after 4200 pulses differences in the GISAXS pattern are considerable. Finally, after 9000 pulses GISAXS patterns (Figure 4.58) present a large number of reflections which is characteristic of well-ordered LIPSS as it was observed in a previous work in which the number of reflections was related with a disorder paracrystalline parameter.[27]

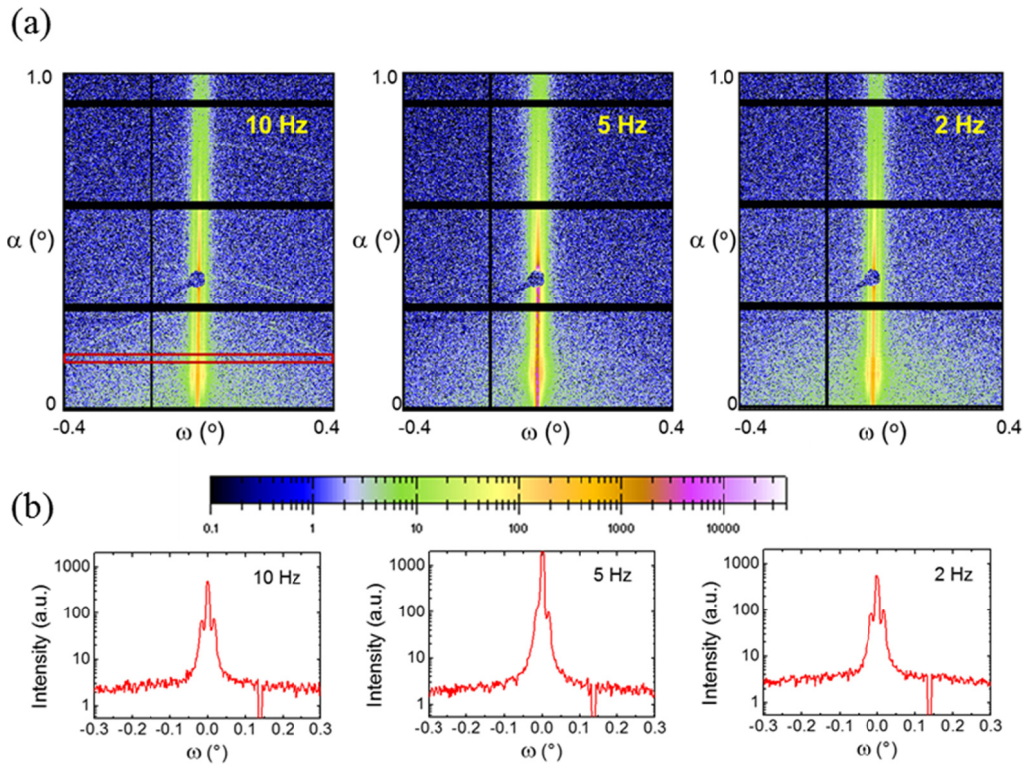

Figure 4.56. (a) GISAXS patterns during LIPSS formation irradiated with 2000 pulses and different laser repetition rate. (b) Intensity profiles taken at α = 0.15º.

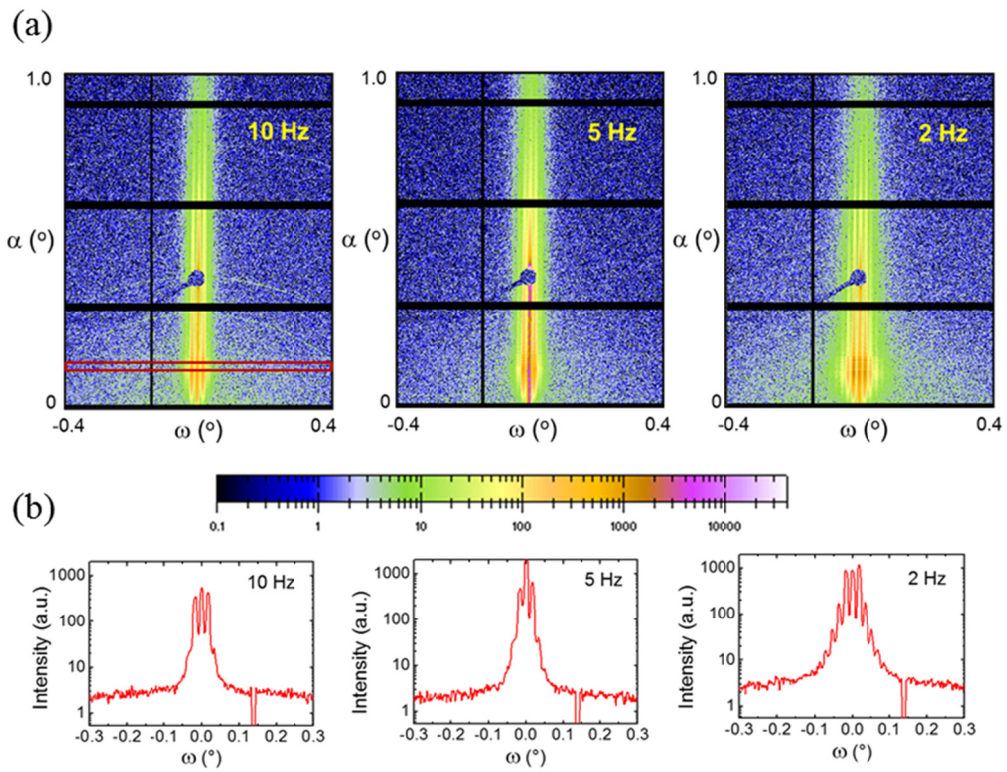

Figure 4.57. (a) GISAXS patterns during LIPSS formation irradiated with 4200 pulses and different laser repetition rate. (b) Intensity profiles taken at α = 0.15º.

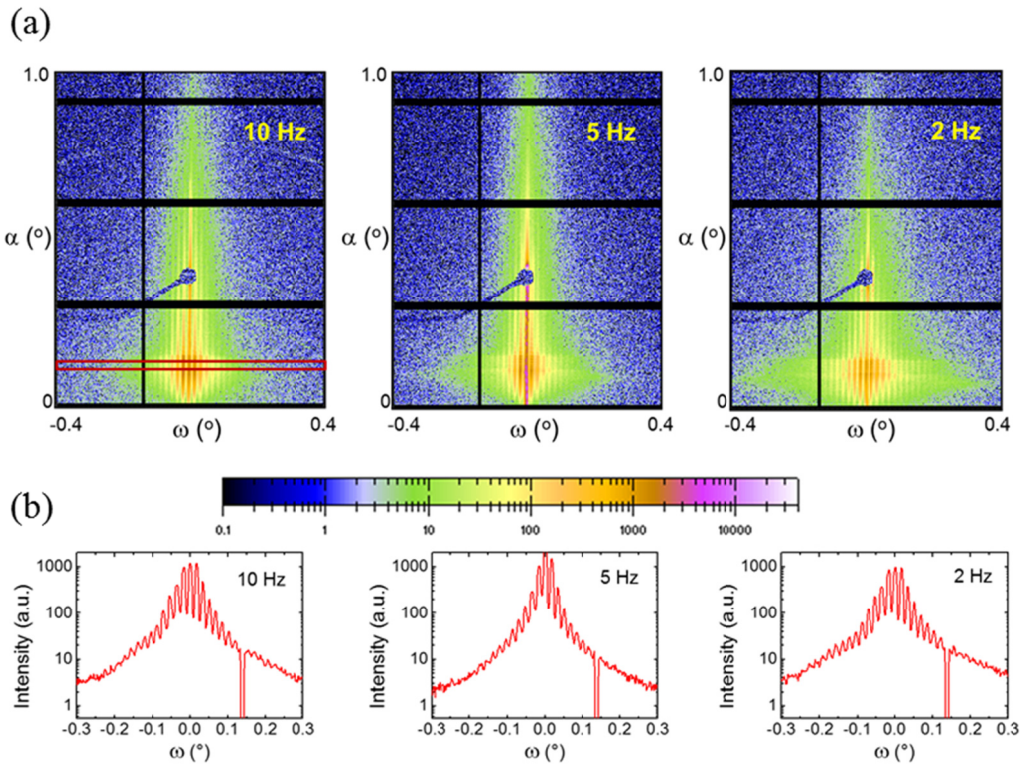

Figure 4.58. (a) GISAXS patterns during LIPSS formation irradiated with 9000 pulses and different laser repetition rate. (b) Intensity profiles taken at $\alpha = 0.15^{\circ}$.

These results reveal that LIPSS formation is faster when irradiating at lower repetition rates. After several cycles of laser pulses, polymer surface is melted and cooled down quickly. The time between consecutive pulses is longer for lower repetition rates (0.1 versus 0.2 and 0.5 s respectively). Therefore, when irradiating at 10 Hz, pulses reach the sample faster than at 5 and 2 Hz and when each pulse reaches the surface it is further heated up with shorter time for cooling down than at lower repetition rates. This fact indicates that in this polymer the higher temperature reached at the fastest repetition rate (10 Hz) hinders the LIPSS structuring. In general, a more effective mechanism for LIPSS formation in polymers has been observed when using conditions which promote higher temperatures.[32, 45] This observation has been explained in terms of their thermal properties since polymers need to reach a temperature above their T_g in the case of amorphous polymers or above their T_m for semicrystalline ones.

However, in this case, PCDTBT reaches an adequate temperature to organize in LIPSS at the three repetition rates used and differences observed in the kinetics of LIPSS formation can be attributed to the particular thermal properties of the PCDTBT such as the phase transition at high temperatures to a crystal liquid phase.[89]

4.5.2.1. LIPSS morphology in PCDTBT as revealed by AFM

10 µm x 10 µm AFM topography images of the samples irradiated during the *in situ* experiments are presented in Figure 4.59 for the three repetition rates used. Apparently, the LIPSS in the three samples are very similar as can be confirmed with the height profiles obtained from the AFM images. Periods of the structures fabricated are 361 ± 11 nm, 348 ± 10 nm and 354 ± 8 nm for the 10, 5 and 2 Hz repetition rate respectively.

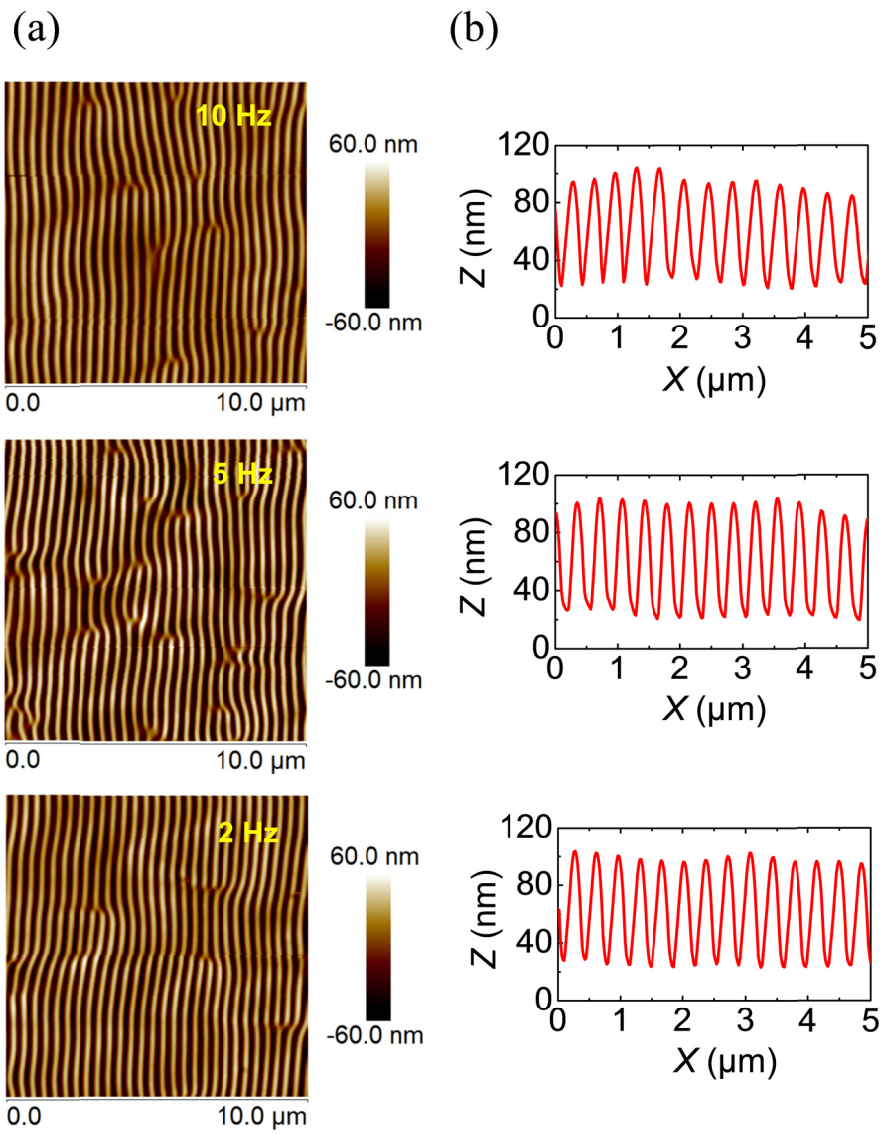

Figure 4.59. (a) Topography AFM images of LIPSS fabricated *in situ* at 26 mJ/cm^2 and 9000 pulses for the three different repetition rates: 10, 5 and 2 Hz. (b) Height profiles obtained along 10 µm perpendicularly to the LIPSS.

4.5.3. *In situ* LIPSS formation in P3HT/PCDTBT blends as revealed by GISAXS

Selected GISAXS patterns of LIPSS evolution during irradiation of a P3HT/PCDTBT blend thin film are presented in Figure 4.60 for the repetition rate of 10 Hz.

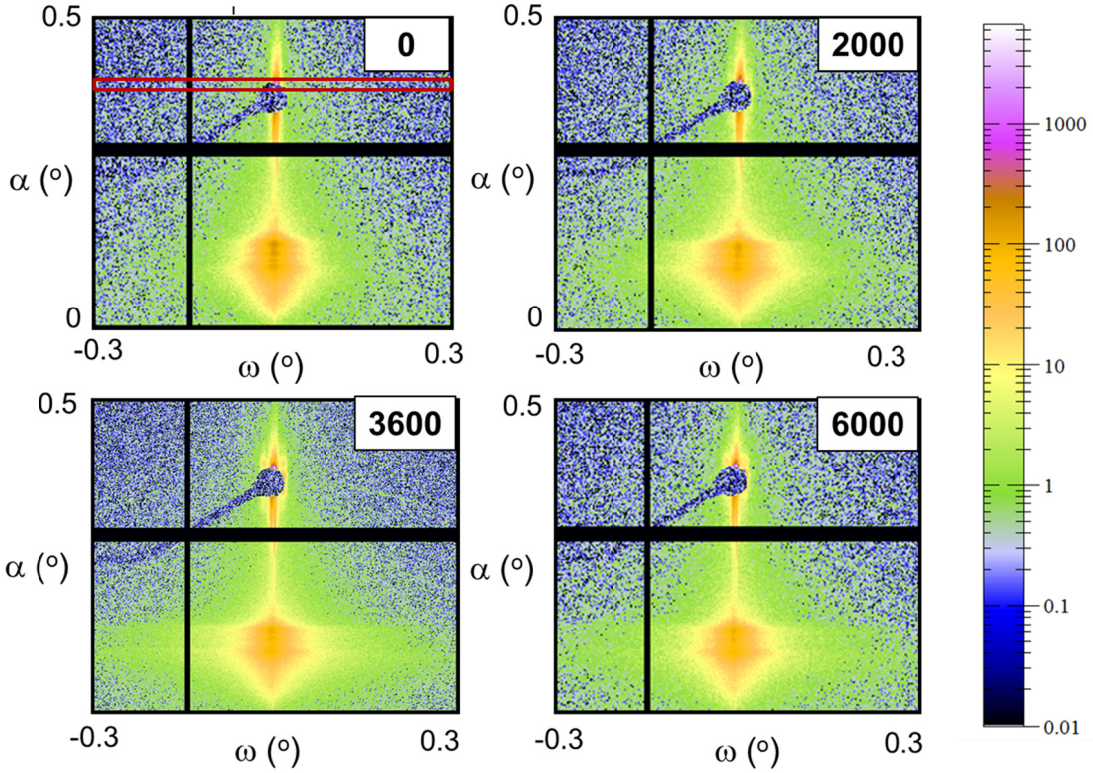

Figure 4.60. Evolution of GISAXS patterns as function of the number of pulses during the *in situ* LIPSS formation in P3HT/PCDTBT thin films upon irradiation at 532 nm and a repetition rate of 10 Hz.

The first pattern in Figure 4.60 corresponds to the spin-coated P3HT/PCDTBT thin film. After laser irradiation with 2000 pulses (200 s) the GISAXS pattern starts exhibiting small increase of the intensity around the Yoneda peak. In this case the pattern does not exhibit vertical rods around the Yoneda Peak. However a weak reflection appears around the reflected beam during the laser irradiation. According to the AFM images performed in the *ex situ* experiments (Section 4.3.2), the structures in this blend have very short correlation lengths distributed at different heights. This fact leads to the absence of the vertical rods observed in a characteristic LIPSS pattern.

From the GISAXS patterns horizontal intensity profiles along ω for a constant α have been extracted. These profiles were obtained by vertical integration of a horizontal strip (15 pixel wide) as the one shown in Figure 4.63 around the reflected beam (α ≈ 0.4º).

The obtained intensity profiles are represented in Figure 4.61 in order to compare the GISAXS evolution during LIPSS formation. In this case, period of the LIPSS also remains practically constant with a value around 360 nm in the whole range of pulses employed. Moreover, results are qualitatively similar for the three laser repetition rates used.

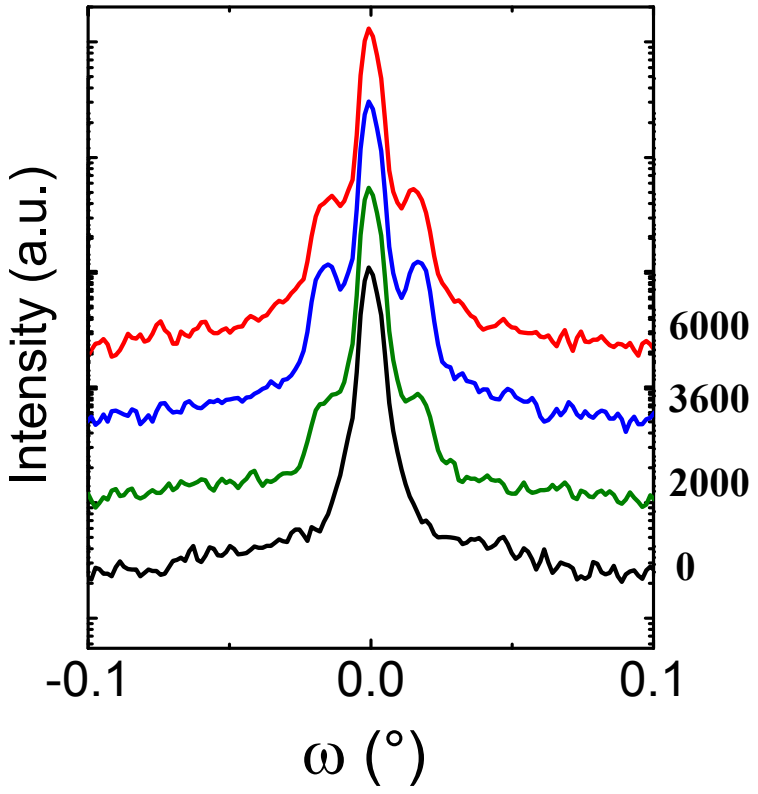

Figure 4.61. Intensity profiles as a function of ω obtained from the 2D GISAXS patterns at a constant α = 0.4º for different number of pulses (labeled in the right) during the LIPSS formation in P3HT/PCDTBT at 10 Hz.

In order to compare the evolution with time of LIPSS formation in the P3HT/PCDTBT blend for the different repetition rates, in Figure 4.62 the total integrated intensity, which is the sum of the total intensity of the horizontal strip shown in Figure 4.60, has been extracted from the intensity profiles and has been represented, as a function of the number of pulses. For the sake of comparison we have subtracted the integrated

intensity of the intensity profile corresponding to the first GISAXS pattern for each experiment. Figure 4.62 shows that for all the investigated repetition rates the integrated intensity follows two regimes as a function of number of pulses: the first regime where the integrated intensity increases rapidly with increasing number of pulses reaching a maximum and a second regime where the integrated intensity decreases with increasing number of pulses. It is interesting to point out that the complete process of LIPSS formation is faster for the blend than for the PCDTBT. This observation is in agreement with the *ex situ* experiments included in the Section 4.3.2. In this case the LIPSS formation seems to be also faster for lower repetition rates as it was observed for PCDTBT.

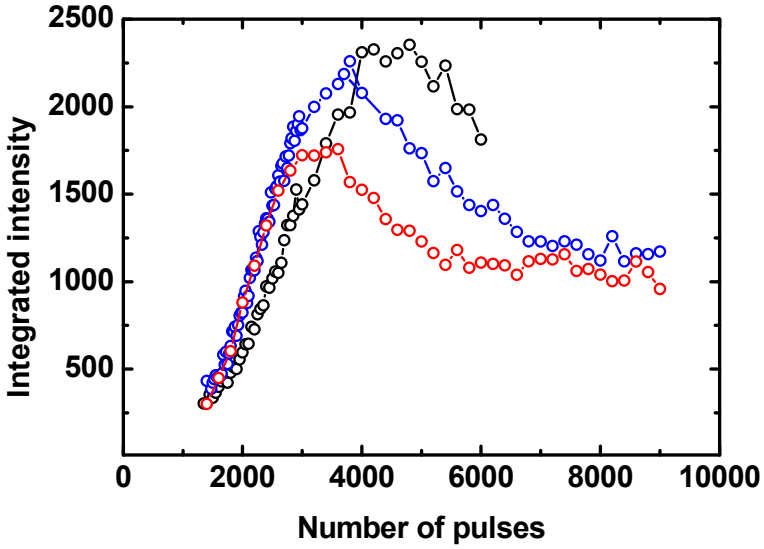

Figure 4.62. Total integrated intensity obtained from the GISAXS pattern at α=0.4 º as a function of the number of pulses at different repetition rates: 10 Hz (black circles), 5 Hz (blue circles) and 2 Hz (red circles).

References

(1) Bao, Z.; Dodabalapur, A.; Lovinger, A.J. *Applied Physics Letters* **1996**, *69 (26)*, 4108-4110.

(2) Kim, D.H.; Park, Y.D.; Jang, Y.; Yang, H.; Kim, Y.H.; Han, J.I.; Moon, D.G.; Park, S.; Chang, T.; Chang, C.; Joo, M.; Ryu, C.Y.; Cho, K. *Advanced Functional Materials* **2005**, *15 (1)*, 77-82.

(3) Zhang, R.; Li, B.; Iovu, M.C.; Jeffries-El, M.; Sauve, G.; Cooper, J.; Jia, S.; Tristram-Nagle, S.; Smilgies, D.M.; Lambeth, D.N.; McCullough, R.D.; Kowalewski, T. *Journal of American Chemical Society* **2006**, *128 (11)*, 3480-3481.

(4) Campoy-Quiles, M.; Ferenczi, T.; Agostinelli, T.; Etchegoin, P.G.; Kim, Y.; Anthopoulos, T.D.; Stavrinou, P.N.; Bradley, D.D.C.; Nelson, J. *Nature Materials* **2008**, *7 (2)*, 158-164.

(5) Collins, B.A.; Tumbleston, J.R.; Ade, H. *The Journal of Physical Chemistry Letters* **2011**, *2 (24)*, 3135-3145.

(6) Li, G.; Shrotriya, V.; Huang, J.; Yao, Y.; Moriarty, T.; Emery, K.; Yang, Y. *Nature Materials* **2005**, *4 (11)*, 864-868.

(7) Sirringhaus, H.; Brown, P.J.; Friend, R.H.; Nielsen, M.M.; Bechgaard, K.; Langeveld-Voss, B.M.W.; Spiering, A.J.H.; Janssen, R.A.J.; Meijer, E.W.; Herwig, P.; de Leeuw, D.M. *Nature* **1999**, *401 (6754)*, 685-688.

(8) Na, S.-I.; Kim, S.-S.; Jo, J.; Oh, S.-H.; Kim, J.; Kim, D.-Y. *Advanced Functional Materials* **2008**, *18 (24)*, 3956-3963.

(9) Yang, Y.; Mielczarek, K.; Aryal, M.; Zakhidov, A.; Hu, W. *Nanoscale* **2014**, *6 (13)*, 7576-7584.

(10) Chen, D.; Zhao, W.; Russell, T.P. *ACS Nano* **2012**, *6 (2)*, 1479-1485.

(11) Vohra, V.; Campoy-Quiles, M.; Garriga, M.; Murata, H. *Journal of Materials Chemistry* **2012**, *22 (37)*, 20017-20025.

(12) Aryal, M.; Trivedi, K.; Hu, W.W. *ACS Nano* **2009**, *3 (10)*, 3085-3090.

(13) Yang, Y.; Mielczarek, K.; Aryal, M.; Zakhidov, A.; Hu, W. *ACS Nano* **2012**, *6 (4)*, 2877–2892.

(14) Shen, X.; Duzhko, V.V.; Russell, T.P. *Advanced Energy Materials* **2013**, *3 (2)*, 263-270.

(15) Singh, C.R.; Gupta, G.; Lohwasser, R.; Engmann, S.; Balko, J.; Thelakkat, M.; Thurn-Albrecht, T.; Hoppe, H. *Journal of Polymer Science Part B: Polymer Physics* **2013**, *51 (12)*, 943-951.

(16) Wood, S.; Kim, J.S.; James, D.T.; Tsoi, W.C.; Murphy, C.E.; Kim, J.-S. *The Journal of Chemical Physics* **2013**, *139 (6)*, 064901.

(17) Xin, H.; Reid, O.G.; Ren, G.; Kim, F.S.; Ginger, D.S.; Jenekhe, S.A. *ACS Nano* **2010**, *4 (4)*, 1861-1872.

(18) Jiang, X.M.; Österbacka, R.; Korovyanko, O.; An, C.P.; Horovitz, B.; Janssen, R.A.J.; Vardeny, Z.V. *Advanced Functional Materials* **2002**, *12 (9)*, 587-597.

(19) Hugger, S.; Thomann, R.; Heinzel, T.; Thurn-Albrecht, T. *Colloid and Polymer Science* **2004**, *282 (8)*, 932-938.

(20) Kohn, P.; Rong, Z.; Scherer, K.H.; Sepe, A.; Sommer, M.; Müller-Buschbaum, P.; Friend, R.H.; Steiner, U.; Hüttner, S. *Macromolecules* **2013**, *46 (10)*, 4002-4013.

(21) Wu, Z.; Petzold, A.; Henze, T.; Thurn-Albrecht, T.; Lohwasser, R.H.; Sommer, M.; Thelakkat, M. *Macromolecules* **2010**, *43 (10)*, 4646-4653.

(22) Treat, N.D.; Shuttle, C.G.; Toney, M.F.; Hawker, C.J.; Chabinyc, M.L. *Journal of Materials Chemistry* **2011**, *21 (39)*, 15224-15231.

(23) Hlaing, H.; Lu, X.; Hofmann, T.; Yager, K.G.; Black, C.T.; Ocko, B.M. *ACS Nano* **2011**, *5 (9)*, 7532-7538.

(24) Martin, J.; Campoy-Quiles, M.; Nogales, A.; Garriga, M.; Alonso, M.I.; Goni, A.R.; Martin-Gonzalez, M. *Soft Matter* **2014**, *10 (18)*, 3335-3346.

(25) Johnston, D.E.; Yager, K.G.; Hlaing, H.; Lu, X.; Ocko, B.M.; Black, C.T. *ACS Nano* **2013**, *8 (1)*, 243-249.

(26) Kim, Y.; Cook, S.; Tuladhar, S.M.; Choulis, S.A.; Nelson, J.; Durrant, J.R.; Bradley, D.D.C.; Giles, M.; McCulloch, I.; Ha, C.-S.; Ree, M. *Nature Materials* **2006**, *5 (3)*, 197-203.

(27) Martin-Fabiani, I.; Rebollar, E.; Perez, S.; Rueda, D.R.; Garcia-Gutierrez, M.C.; Szymczyk, A.; Roslaniec, Z.; Castillejo, M.; Ezquerra, T.A. *Langmuir* **2012**, *28 (20)*, 7938-7945.

(28) Rebollar, E.; Perez, S.; Hernandez, J.J.; Martin-Fabiani, I.; Rueda, D.R.; Ezquerra, T.A.; Castillejo, M. *Langmuir* **2011**, *27 (9)*, 5596-5606.

(29) Rebollar, E.; Gaspard, S.; Oujja, M.; Villavieja, M.M.; Corrales, T.; Bosch, P.; Georgiou, S.; Castillejo, M. *Applied Physics A* **2006**, *84 (1)*, 171-180.

(30) Rebollar, E.; Frischauf, I.; Olbrich, M.; Peterbauer, T.; Hering, S.; Preiner, J.; Hinterdorfer, P.; Romanin, C.; Heitz, J. *Biomaterials* **2008**, *29 (12)*, 1796-1806.

(31) Izumi, T.; Kobashi, S.; Takimiya, K.; Aso, Y.; Otsubo, T. *Journal of the American Chemical Society* **2003**, *125 (18)*, 5286-5287.

(32) Rebollar, E.; Pérez, S.; Hernández, J.J.; Martín-Fabiani, I.; Rueda, D.R.; Ezquerra, T.A.; Castillejo, M. *Langmuir* **2011**, *27 (9)*, 5596-5606.

(33) Kanai, K.; Miyazaki, T.; Suzuki, H.; Inaba, M.; Ouchi, Y.; Seki, K. *Physical Chemistry Chemical Physics* **2010**, *12 (1)*, 273-282.

(34) Watts, B.; Swaraj, S.; Nordlund, D.; Lüning, J.; Ade, H. *The Journal of Chemical Physics* **2011**, *134 (2)*, 024702.

(35) Tsoi, W.C.; James, D.T.; Kim, J.S.; Nicholson, P.G.; Murphy, C.E.; Bradley, D.D.C.; Nelson, J.; Kim, J.-S. *Journal of the American Chemical Society* **2011**, *133 (25)*, 9834-9843.

(36) Brown, P.J.; Thomas, D.S.; Köhler, A.; Wilson, J.S.; Kim, J.-S.; Ramsdale, C.M.; Sirringhaus, H.; Friend, R.H. *Physical Review B* **2003**, *67 (6)*, 064203.

(37) Furukawa, Y. *The Journal of Physical Chemistry* **1996**, *100 (39)*, 15644-15653.

(38) Louarn, G.; Trznadel, M.; Buisson, J.P.; Laska, J.; Pron, A.; Lapkowski, M.; Lefrant, S. *The Journal of Physical Chemistry* **1996**, *100 (30)*, 12532-12539.

(39) Shi, G.; Xu, J.; Fu, M. *The Journal of Physical Chemistry B* **2002**, *106 (2)*, 288-292.

(40) Clark, J.; Silva, C.; Friend, R.H.; Spano, F.C. *Physical Review Letters* **2007**, *98 (20)*, 206406.

(41) Gao, Y.; Grey, J.K. *Journal of the American Chemical Society* **2009**, *131 (28)*, 9654-9662.

(42) Reish, M.E.; Nam, S.; Lee, W.; Woo, H.Y.; Gordon, K.C. *The Journal of Physical Chemistry C* **2012**, *116 (40)*, 21255-21266.

(43) Jha, P.; Koiry, S.P.; Saxena, V.; Veerender, P.; Gusain, A.; Chauhan, A.K.; Debnath, A.K.; Aswal, D.K.; Gupta, S.K. *Organic Electronics* **2013**, *14 (10)*, 2635-2644.

(44) Provencher, F.; Bérubé, N.; Parker, A.W.; Greetham, G.M.; Towrie, M.; Hellmann, C.; Côté, M.; Stingelin, N.; Silva, C.; Hayes, S.C. *Nature Communications* **2014**, *5*, 4288.

(45) Rebollar, E.; Rueda, D.R.; Martín-Fabiani, I.; Rodríguez-Rodríguez, Á.; García-Gutiérrez, M.-C.; Portale, G.; Castillejo, M.; Ezquerra, T.A. *Langmuir* **2015**, *31 (13)*, 3973-3981.

(46) Rodríguez-Rodríguez, Á.; Soccio, M.; Martínez-Tong, D.E.; Ezquerra, T.A.; Watts, B.; García-Gutiérrez, M.-C. *Polymer* **2015**, *77*, 70-78.

(47) Wang, T.; Pearson, A.J.; Dunbar, A.D.F.; Staniec, P.A.; Watters, D.C.; Yi, H.; Ryan, A.J.; Jones, R.A.L.; Iraqi, A.; Lidzey, D.G. *Advanced Functional Materials* **2012**, *22 (7)*, 1399-1408.

(48) Liu, X.; Huettner, S.; Rong, Z.; Sommer, M.; Friend, R.H. *Advanced Materials* **2012**, *24 (5)*, 669-674.

(49) Ade, H.; Hitchcock, A.P. *Polymer* **2008**, *49 (3)*, 643-675.

(50) Ade, H.; Stoll, H. *Nature Materials* **2009**, *8 (4)*, 281-290.

(51) Watts, B.; McNeill, C.R.; Raabe, J. *Synthetic Metals* **2012**, *161 (23–24)*, 2516-2520.

(52) Koprinarov, I.N.; Hitchcock, A.P.; McCrory, C.T.; Childs, R.F. *The Journal of Physical Chemistry B* **2002**, *106 (21)*, 5358-5364.

(53) Hitchcock, A.P. *aXis 2000*. http://unicorn.mcmaster.ca/aXis2000.html.

(54) Rodríguez-Rodríguez, Á.; Rebollar, E.; Soccio, M.; Ezquerra, T.A.; Rueda, D.R.; Garcia-Ramos, J.V.; Castillejo, M.; Garcia-Gutierrez, M.-C. *Macromolecules* **2015**, *48 (12)*, 4024-4031.

(55) Shrotriya, V.; Ouyang, J.; Tseng, R.J.; Li, G.; Yang, Y. *Chemical Physics Letters* **2005**, *411 (1–3)*, 138-143.

(56) Yu, W.; Zhou, J.; Bragg, A.E. *The Journal of Physical Chemistry Letters* **2012**, *3 (10)*, 1321-1328.

(57) Günes, S.; Neugebauer, H.; Sariciftci, N.S. *Chemical Reviews* **2007**, *107 (4)*, 1324-1338.

(58) Hoppe, H.; Sariciftci, N.S. *Journal of Materials Research* **2004**, *19 (7)*, 1924-1945.

(59) Mayer, A.C.; Scully, S.R.; Hardin, B.E.; Rowell, M.W.; McGehee, M.D. *Materials Today* **2007**, *10 (11)*, 28-33.

(60) Ruderer, M.A.; Guo, S.; Meier, R.; Chiang, H.-Y.; Körstgens, V.; Wiedersich, J.; Perlich, J.; Roth, S.V.; Müller-Buschbaum, P. *Advanced Functional Materials* **2011**, *21 (17)*, 3382-3391.

(61) He, Z.; Zhong, C.; Su, S.; Xu, M.; Wu, H.; Cao, Y. *Nature Photonics* **2012**, *6 (9)*, 591-595.

(62) Chiu, M.-Y.; Jeng, U.S.; Su, C.-H.; Liang, K.S.; Wei, K.-H. *Advanced Materials* **2008**, *20 (13)*, 2573-2578.

(63) Kiel, J.W.; Eberle, A.P.R.; Mackay, M.E. *Physical Review Letters* **2010**, *105 (16)*, 168701.

(64) Liao, H.-C.; Tsao, C.-S.; Lin, T.-H.; Chuang, C.-M.; Chen, C.-Y.; Jeng, U.S.; Su, C.-H.; Chen, Y.-F.; Su, W.-F. *Journal of the American Chemical Society* **2011**, *133 (33)*, 13064-13073.

(65) Yin, W.; Dadmun, M. *ACS Nano* **2011**, *5 (6)*, 4756-4768.

(66) Ruderer, M.A.; Meier, R.; Porcar, L.; Cubitt, R.; Müller-Buschbaum, P. *The Journal of Physical Chemistry Letters* **2012**, *3 (6)*, 683-688.

(67) Agostinelli, T.; Lilliu, S.; Labram, J.G.; Campoy-Quiles, M.; Hampton, M.; Pires, E.; Rawle, J.; Bikondoa, O.; Bradley, D.D.C.; Anthopoulos, T.D.; Nelson, J.; Macdonald, J.E. *Advanced Functional Materials* **2011**, *21 (9)*, 1701-1708.

(68) Wu, W.-R.; Jeng, U.S.; Su, C.-J.; Wei, K.-H.; Su, M.-S.; Chiu, M.-Y.; Chen, C.-Y.; Su, W.-B.; Su, C.-H.; Su, A.-C. *ACS Nano* **2011**, *5 (8)*, 6233-6243.

(69) Kozub, D.R.; Vakhshouri, K.; Orme, L.M.; Wang, C.; Hexemer, A.; Gomez, E.D. *Macromolecules* **2011**, *44 (14)*, 5722-5726.

(70) Treat, N.D.; Chabinyc, M.L. *Annual Review of Physical Chemistry* **2014**, *65 (1)*, 59-81.

(71) Hellmann, C.; Treat, N.D.; Scaccabarozzi, A.D.; Razzell Hollis, J.; Fleischli, F.D.; Bannock, J.H.; de Mello, J.; Michels, J.J.; Kim, J.-S.; Stingelin, N. *Journal of Polymer Science Part B: Polymer Physics* **2015**, *53 (4)*, 304-310.

(72) Kouijzer, S.; Michels, J.J.; van den Berg, M.; Gevaerts, V.S.; Turbiez, M.; Wienk, M.M.; Janssen, R.A.J. *Journal of the American Chemical Society* **2013**, *135 (32)*, 12057-12067.

(73) Gu, Y.; Wang, C.; Liu, F.; Chen, J.; Dyck, O.E.; Duscher, G.; Russell, T.P. *Energy & Environmental Science* **2014**, *7 (11)*, 3782-3790.

(74) Germack, D.S.; Chan, C.K.; Hamadani, B.H.; Richter, L.J.; Fischer, D.A.; Gundlach, D.J.; DeLongchamp, D.M. *Applied Physics Letters* **2009**, *94 (23)*, 233303.

(75) Bazylewski, P.F.; Kim, K.H.; Forrest, J.L.; Tada, H.; Choi, D.H.; Chang, G.S. *Chemical Physics Letters* **2011**, *508 (1–3)*, 90-94.

(76) Chen, D.; Nakahara, A.; Wei, D.; Nordlund, D.; Russell, T.P. *Nano Letters* **2011**, *11 (2)*, 561-567.

(77) Chen, D.; Liu, F.; Wang, C.; Nakahara, A.; Russell, T.P. *Nano Letters* **2011**, *11 (5)*, 2071-2078.

(78) Chintala, R.; Tait, J.G.; Eyben, P.; Voroshazi, E.; Surana, S.; Fleischmann, C.; Conard, T.; Vandervorst, W. *Nanoscale* **2016**, *8 (6)*, 3629-3637.

(79) Watts, B. *https://bitbucket.org/benajamin/kkcalc*.

(80) Collins, B.A.; Gann, E.; Guignard, L.; He, X.; McNeill, C.R.; Ade, H. *The Journal of Physical Chemistry Letters* **2010**, *1 (21)*, 3160-3166.

(81) Treat, N.D.; Brady, M.A.; Smith, G.; Toney, M.F.; Kramer, E.J.; Hawker, C.J.; Chabinyc, M.L. *Advanced Energy Materials* **2011**, *1 (1)*, 82-89.

(82) Portale, G.; Cavallo, D.; Alfonso, G.C.; Hermida-Merino, D.; van Drongelen, M.; Balzano, L.; Peters, G.W.M.; Goossens, J.G.P.; Bras, W. *Journal of Applied Crystallography* **2013**, *46 (6)*, 1681-1689.

(83) Müller-Buschbaum, P. *Advanced Materials* **2014**, *26 (46)*, 7692-7709.

(84) Narayanan, S.; Lee, D.R.; Hagman, A.; Li, X.; Wang, J. *Physical Review Letters* **2007**, *98 (18)*, 185506.

(85) Renaud, G.; Lazzari, R.; Leroy, F. *Surface Science Reports* **2009**, *64 (8)*, 255-380.

(86) *Hammersley, A. FIT2D Website. http://www.esrf.eu/computing/scientific/FIT2D*.

(87) Hernández, J.J.; Rueda, D.R.; García-Gutiérrez, M.C.; Nogales, A.; Ezquerra, T.A.; Soccio, M.; Lotti, N.; Munari, A. *Langmuir* **2010**, *26 (13)*, 10731-10737.

(88) Yoneda, Y. *Physical Review* **1963**, *131 (5)*, 2010-2013.

(89) Blouin, N.; Michaud, A.; Gendron, D.; Wakim, S.; Blair, E.; Neagu-Plesu, R.; Belletête, M.; Durocher, G.; Tao, Y.; Leclerc, M. *Journal of the American Chemical Society* **2008**, *130 (2)*, 732-742.

Chapter 5. Laser-Induced Periodic Surface Structures applied to organic photovoltaics

Polymer blends of poly(3-hexylthiophene-2,5-diyl) (P3HT) with fullerene materials including C60, [6,6]-phenyl C61-butyric acid methyl ester ($PC_{61}BM$) or [6,6]-phenyl C71-butyric acid methyl ester ($PC_{71}BM$) have shown to be attractive functional materials for their application in organic photovoltaics (OPV).[1-3] In this case the interfacial area between the donor material, P3HT, and the acceptor one, PCBM, which forms the heterojunction is a critical factor for the performance of the OPV device.[1, 4] Several approaches have been followed in order to fabricate controlled micro- and nanostructures on P3HT for OPV applications including soft lithography,[5] nanoimprint lithography[6, 7] and templating by Anodic Aluminium Oxide (AAO) membranes[8] among others**.**

In Section 4.1 LIPSS have been used in order to create sub-micron gratings on P3HT. It was shown that, in spite of the well-known photo degradability of P3HT and of the high power of laser pulses, LIPSS on P3HT at 532 nm are produced with a weak impact on its chemical structure. However the electrical conductivity of the P3HT ripples exhibits a heterogeneous nature consisting of an alternation of conducting valleys and non-conducting hills.[9] On the basis of Raman spectroscopy and of X-ray scattering experiments, a reduction of the crystallinity of the hills was proposed as the cause of the loss of conductivity in the hills. From the perspective of OPV, several questions arise about the potential integration of P3HT LIPSS structures in solar cell architecture.[10, 11] These include: (1) The possibility of creating LIPSS on an active layer comprising P3HT and $PC_{71}BM$. (2) The feasibility of intercalation of the LIPSS active layer between a bottom indium tin oxide (ITO) electrode coated with a thin layer of poly(3,4-ethylenedioxythiophene):poly(styrenesulfonate) (PEDOT:PSS) and a metallic top electrode. (3) The role of chemical degradation of the P3HT/$PC_{71}BM$ by laser illumination which may compromise, or even destroy, the performance of the device. (4) The impact of the heterogeneous electrical conductivity of the P3HT LIPSS surface on the OPV device properties. In this chapter, some answers to the above mentioned questions will be discussed.

5.1. Preparation and characterization of P3HT/$PC_{71}BM$ solar cells

Organic solar cells were prepared on 3 x 3 mm^2 ITO-covered glass substrates (Solems S.A, France). ITO acts as a transparent electrode and because of the geometry of the I-V measurements, a small area of the ITO coating needs to be patterned. The complete preparation process is presented in Figure 5.1:

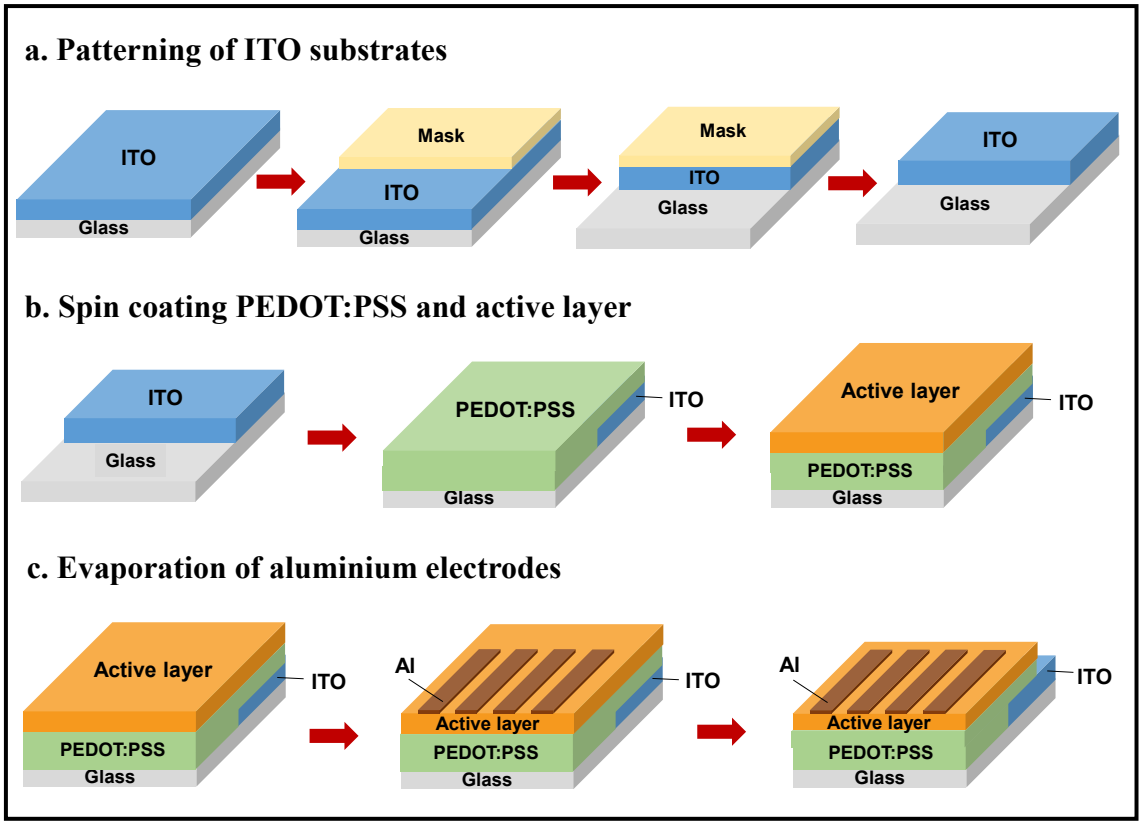

Figure 5.1. Scheme of the solar cells preparation used in this thesis.

a. Patterning of ITO substrates:

ITO substrates need to be etched in order to avoid a short circuit when we connect the electrodes. For this purpose the first step is to mask the area of the ITO substrate which will remain after etching by covering around the half of a substrate with some tape. Afterwards the clear ITO area is covered with zinc powder. After applying a water solution of HCl with a concentration of 50:50 in volume onto the zinc covered area, the ITO is selectively etched. This reaction involves the reduction of the ITO ions to a

metallic state. Zinc generates H_2 when contacting with HCl and this H_2 is the reducing agent of the ITO.

b. Deposition of the PEDOT:PSS film and the active layer by spin-coating:

A thin layer of PEDOT:PSS was deposited by spin-coating at 5000 rpm on top of a patterned ITO-covered glass substrate. For preparation of the active layers, P3HT and $PC_{71}BM$ were solved in chlorobenzene (24 g/L). Two different P3HT/$PC_{71}BM$ active layers were prepared in order to fabricate two different architectures for the solar cells.
(a) A bilayer was fabricated by depositing a P3HT layer spin-coated at 2400 rpm for 120 s on the underlying PEDOT:PSS layer and subsequently covered by another $PC_{71}BM$ layer spin-coated at 4000 rpm for 10 s from a 5 g/L dichloromethane solution. This solvent was used because P3HT is insoluble avoiding the deterioration of the bottom layer when $PC_{71}BM$ is spin-coated.[12]

(b) A bulk heterojunction active layer was fabricated by spin-coating the P3HT/$PC_{71}BM$ blend (weight ratio of 1:1) over the PEDOT:PSS film at 2400 rpm for 120 s.

c. Evaporation of the aluminum electrodes:

After depositing the active layer, aluminum top electrodes were deposited by thermal evaporation in vacuum. In this case, a mask with four pixels (see the architecture in Figure 5.2) was used due to the geometry of the measurements and to obtain statistics of the experiments. Finally, a thermal annealing step of 4 min at 140 °C was performed in a glovebox under N_2 atmosphere to ensure a good contact with the active layer. The final scheme of a typical solar cell used in this study is shown in Figure 5.2.

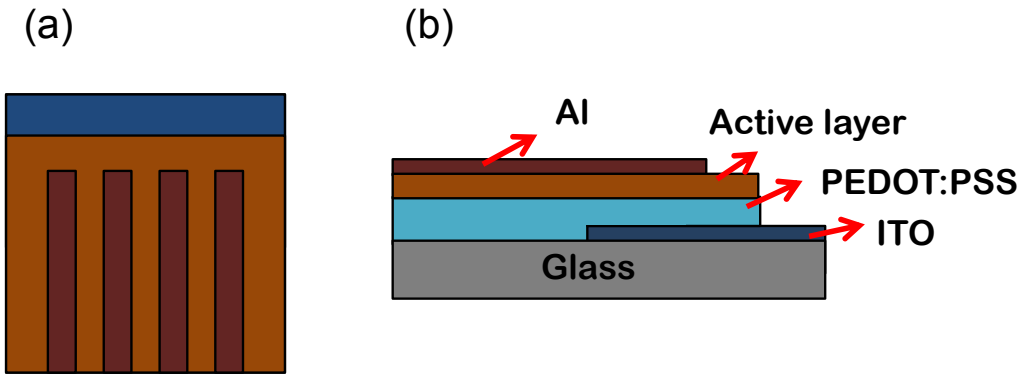

Figure 5.2. Architecture of a solar cell: (a) top view, (b) lateral view.

The photovoltaic devices were characterized under ambient conditions with the AM 1.5 global reference spectrum and 100 mW/cm^2 irradiance. The current density – voltage (J–V) measurements were recorded using a source meter (Keithley 2400).

5.2. Laser irradiation

Laser irradiation was accomplished at atmospheric conditions under normal incidence by using a linearly polarized laser beam of a Q-switched Nd:YAG laser (Lotis TII LS-2131M, pulse duration of 8 ns). The second harmonic (λ=532 nm) was used for the LIPSS fabrication, since previous studies showed that P3HT form well-ordered ripples at this wavelength.[13, 14] The irradiation fluences were determined by measuring the laser energy in front of the sample with a Joulemeter (Gentec-E, QE25SP-H-MB-D0) and by calculating the area of the irradiated spots, considering a diameter of 5 mm. According to the optimal laser conditions for LIPSS fabrication in P3HT (Section 4.1), the irradiation of P3HT/$PC_{71}BM$ films were performed with 3600 pulses at a fluence of 26 mJ/cm^2, the constant repetition rate is 10 Hz for all samples. In Section 4.4 it has been demonstrated that using these conditions well-ordered LIPSS are obtained in P3HT/$PC_{71}BM$ films.

5.3. LIPSS in P3HT and $PC_{71}BM$ bilayer for photovoltaics

As mentioned before, for photovoltaics characterization both bilayer and standard bulk heterojunction solar cells[15] were prepared. In both cases the thickness of the active layer is about 110 ± 10 nm as measured by AFM. Figure 5.3 shows a scheme of the bilayer device architecture approach. After spin-coating the P3HT on a patterned ITO substrate, it is possible to irradiate the sample using the same conditions described in Section 4.1.

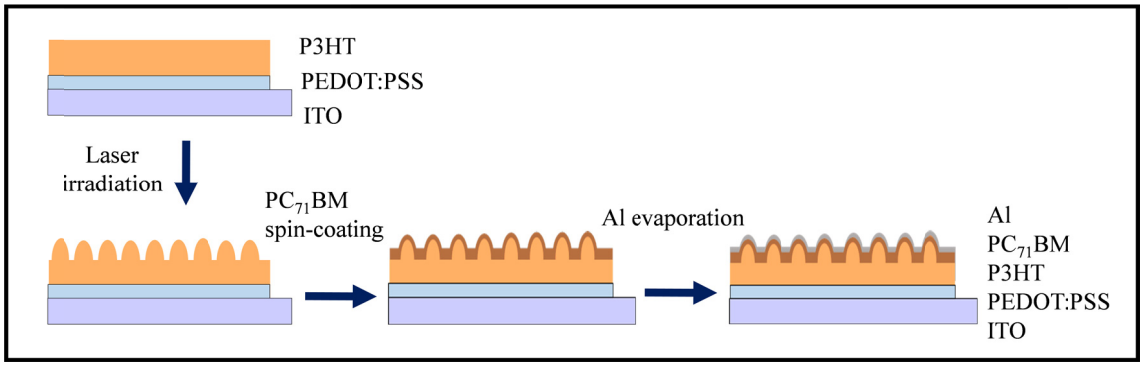

Figure 5.3. Scheme of the bilayer device architecture tested for photovoltaic characterization of P3HT and $PC_{71}BM$ systems with LIPSS.

LIPSS appear on P3HT after appropriate laser irradiation conditions as shown in Figure 5.4.a. Afterwards, a $PC_{71}BM$ thin film is spin-coated over the P3HT film with LIPSS. The upper surface of this bilayer is shown in Figure 5.4.b, where the LIPSS imposed on P3HT are maintained. The final deposition of aluminum top contacts by thermal evaporation keep as well the LIPSS relief essentially unchanged (Figure 5.4.c) with only a slight modification of the depth profile.

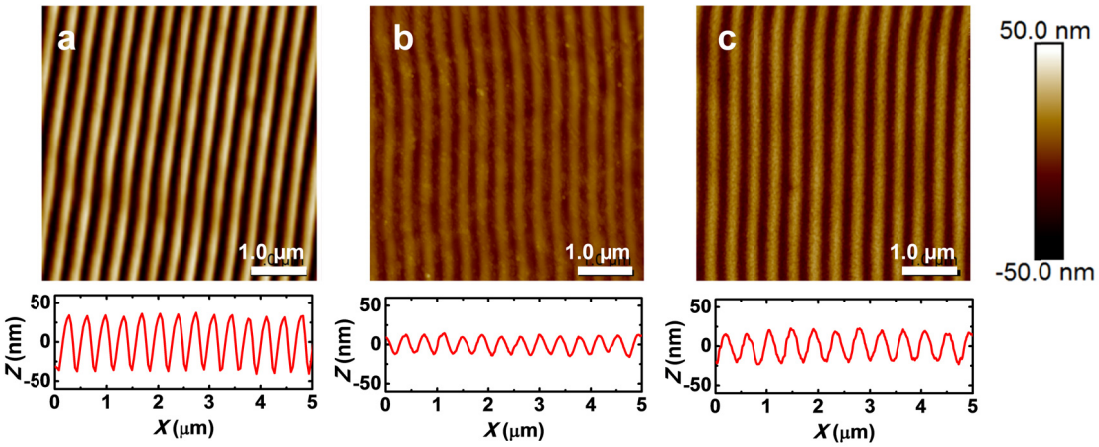

Figure 5.4. 5 ×5 µm^2 AFM images of bilayer solar cell: (a) P3HT surface after laser irradiation and (b) $PC_{71}BM$ film surface deposited on top of P3HT film with LIPSS by spin-coating. (c) Surface after deposition of the aluminum top electrode and after a thermal annealing at 140 °C for 4 min. Height profiles are provided at the bottom of the images.

A real bilayer solar cell is presented in Figure 5.5. It can be observed that the LIPSS area presents different color since the structures are acting as a diffraction grating.

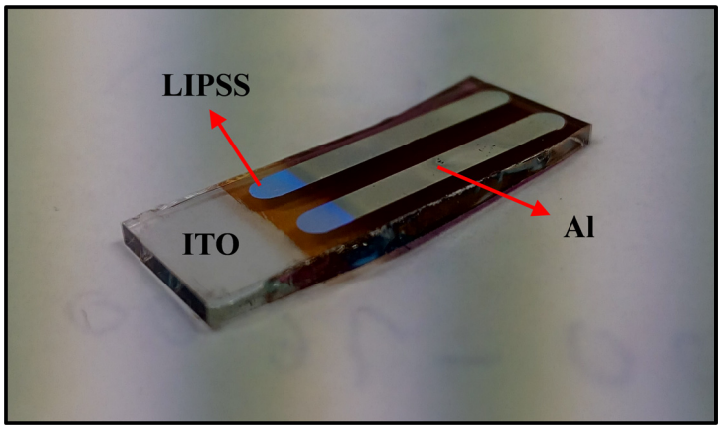

Figure 5.5. A real bilayer solar cell device photo. The blue color corresponds to the iridescence of the LIPSS area acting as a diffraction grating.

An example of the J−V characteristics of the LIPSS solar cell in the dark and under illumination is shown in Figure 5.6. Although the overall device performance can be optimized, the J−V characteristic of the LIPSS bilayer proves that photocurrent is generated by light illumination. Since also the reference P3HT/$PC_{71}BM$ solar cells without LIPSS show very limited performance, it is obvious that the bilayer device geometry is not optimized. Moreover, polymer/fullerene solar cells in bilayer configuration tend to yield rather poor efficiency values due to the small interface between donor and acceptor phases.[16, 17]

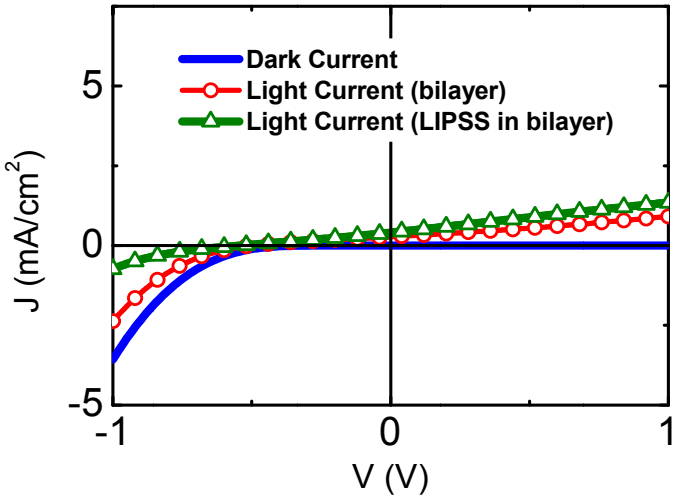

Figure 5.6. J−V characteristics of the LIPSS solar cell in the dark and under illumination. For the sake of comparison, data for the unstructured bilayer solar cell are also included).

5.4. LIPSS in P3HT/$PC_{71}BM$ blend for photovoltaics

A scheme of the bulk heterojunction architecture is shown in Figure 5.7.

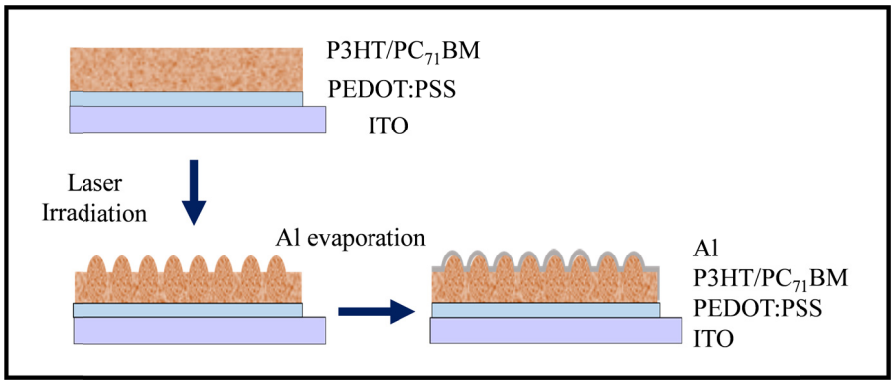

Figure 5.7. Scheme of the bulk heterojunction architecture tested for photovoltaic characterization of P3HT/$PC_{71}BM$ systems with LIPSS.

The corresponding results for the bulk heterojunction solar cells are illustrated in Figure 5.8. The upper surface of the initial spin-coated P3HT/$PC_{71}BM$ film is shown before (Figure 5.8.a) and after laser irradiation (Figure 5.8.b). It is important to point out that even after thermal annealing LIPSS keep their structure unchanged, at least under the aluminum electrode (see Figure 5.8.c). As one can see, similarly as for P3HT, rather ordered LIPSS are formed

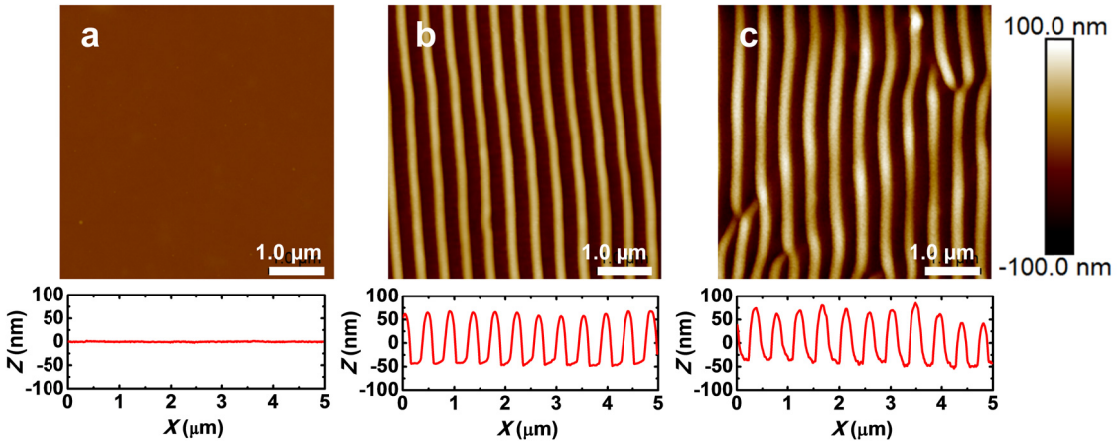

Figure 5.8. 5 ×5 μm^2 AFM images of the surface of the active layer on a BHJ solar cell: (a) before, (b) after laser irradiation, and (c) after deposition of the aluminum top electrode and after a thermal annealing at 140 °C for 4 min. Height profiles are provided at the bottom of the images.

An example of solar cells fabricated with the active layer structured by LIPSS is shown in Figure 5.9. A strong iridescence can be observed due to LIPSS area acting as a diffraction grating even when aluminum electrode is deposited.

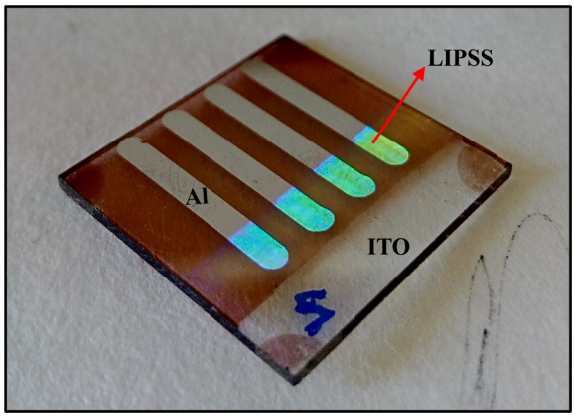

Figure 5.9. A real LIPSS bulk heterojunction solar cell device photo. The green-blue color corresponds to the iridescence of the LIPSS area acting as a diffraction grating.

Representative J−V characteristic of the BHJ LIPSS solar cell in the dark and under illumination is shown in Figure 5.10. The J−V characteristic of the LIPSS heterojunction also proves that photocurrent is generated by light illumination although a lower photocurrent is generated in comparison with the unstructured control bulk heterojunction solar cell.

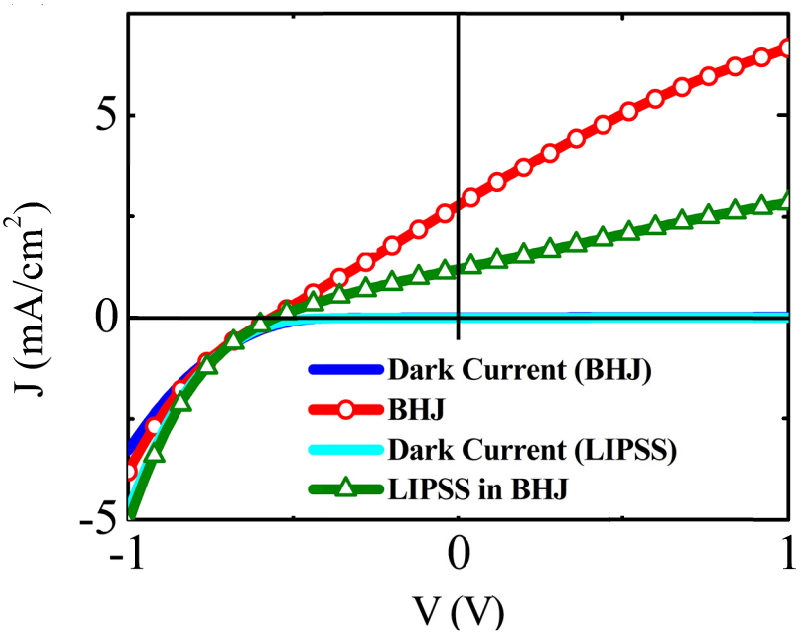

Figure 5.10. J−V characteristic of the LIPSS solar cell in the dark and under illumination. For the sake of comparison, data for the unstructured BHJ solar cell are also included.

To obtain device statistics about the performance of the LIPSS solar cells, measurements for both device architectures were performed for eight different structured solar cells and for four reference solar cells. The results are shown in Figure 5.11 in terms of power conversion efficiency (PCE), fill factor (FF), short-circuit current density (J_{sc}), and open-circuit voltages (V_{oc}).

The performance of the solar cells with LIPSS in comparison with that of the unstructured ones is lower for the bulk heterojunction and similar for the bilayer architectures. One possible reason for that is related to the need of optimization for the presented photovoltaic systems. For the current device arrangement, according to the AFM depth profiles (Figures 5.4 and 5.8), the top-to-valley distance is comparable to the thickness of the unstructured films. Thus, after LIPSS formation, it is expected a

depletion of the active layer between the PEDOT:PSS and the aluminum electrode in the valley. This effect could explain the lower performance of the LIPSS devices.

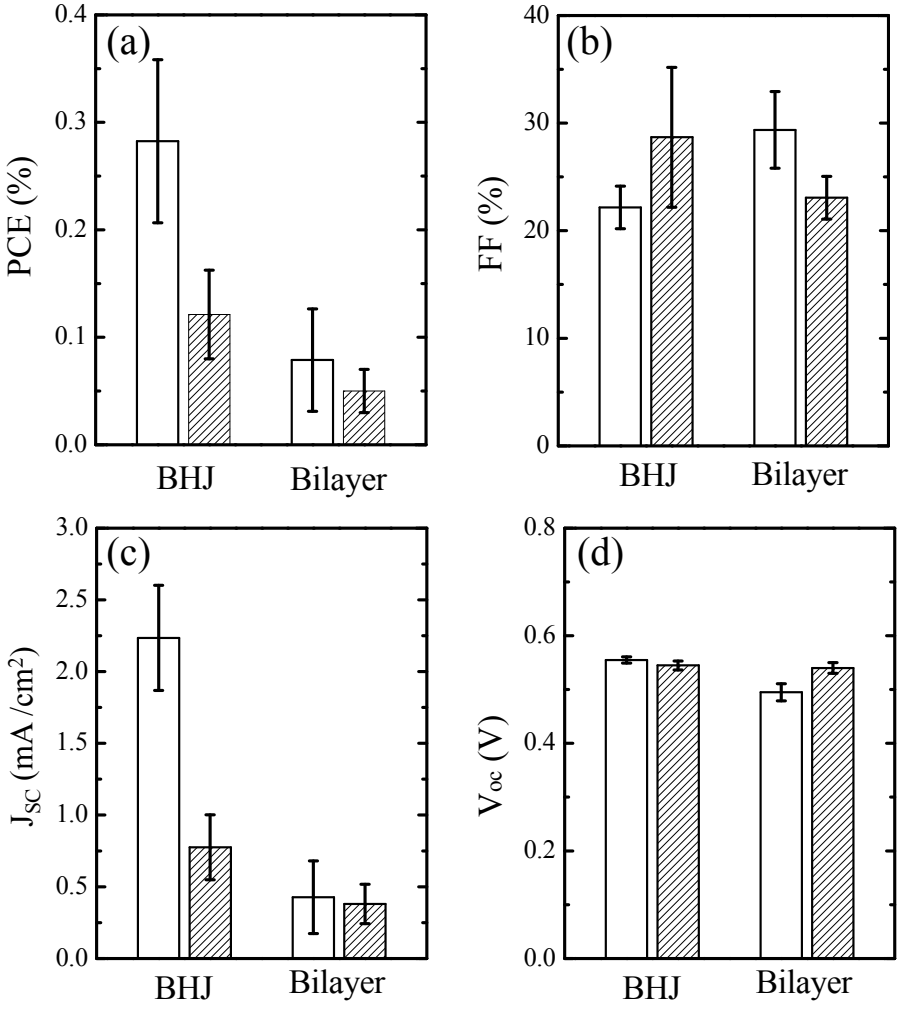

Figure 5.11. (a) Power conversion efficiency (PCE), (b) fill factor (FF), (c) short-circuit current density (J_{sc}), and (d) open-circuit voltages (V_{oc}) for the unstructured (non-textured bars) bilayer and bulk heterojunction (BHJ) solar cell architectures and for the corresponding ones with LIPSS (textured bars).

Another important feature to note is that the solar cells that underwent a LIPSS structuring process have been previously laser irradiated prior to the photovoltaic characterization. Previous Raman spectroscopy results have shown that laser irradiation of P3HT provokes a decrease of the ordered phase rather than a significant chemical degradation.[9] This effect could lead to a decrease of the electrical conductivity responsible for the decreased short-circuit current density upon LIPSS structuring. In spite of that, it is important to remark that LIPSS devices are operational as solar cells. The FF values suggest that solar cell geometry can be optimized, although comparable

values are obtained for LIPSS devices and the reference unstructured ones. As expected, the photogenerated short-circuit current of bilayer solar cells is lower than that of BHJ mainly due to the smaller donor/ acceptor interface. The V_{oc} values are similar for both LIPSS and unstructured devices. This indicates a sound preservation of the device layout and the structural integrity of the materials composing the whole layer stack. Moreover, we can see how for bilayer solar cells the V_{oc} increases by about 10%. Taking into account that the vertical profile of the imprinted structure has a height comparable to the original film thickness, it becomes remarkable that the LIPSS process means a dramatic gain in donor−acceptor interface for bilayer devices. This enlarged interface is expected to significantly decrease the non-geminate recombination, feature which is in good agreement with the improved V_{oc}.[18, 19] In spite of the quantitative results, our data proves that both the LIPSS P3HT/PC_{71}BM bilayer system and the LIPSS P3HT/PC_{71}BM blend system, preserve their photovoltaic properties for photocurrent generation. Moreover, LIPSS show the path for device improvement upon structuring and yields improvements in FF and V_{oc} that could potentially lead to improved solar devices after optimization. This demonstrates that LIPSS can be, in principle, incorporated into organic photovoltaics technology although additional effort is necessary to improve the performance of the LIPSS devices. It is clear that it will be necessary to further advance in the knowledge of physicochemical and morphological changes occurring during light exposure to characterize the reorganization processes that take place during irradiation. In particular, to optimize the active layer in the valleys of LIPSS devices a first approach would consist in considering thicker films with different levels of LIPSS order. In addition by using different irradiation conditions like fluence, number of pulses, laser beam polarization or combining successive irradiations with different polarization orientation[20] could be explored to improve performance of LIPSS solar cells. In fact, wrinkles and folds resulting from linear and non-linear elastic instabilities have been reported to guide and retain light within the photoactive regions of photovoltaics.[21]

References

(1) Li, Z.; Wong, H.C.; Huang, Z.; Zhong, H.; Tan, C.H.; Tsoi, W.C.; Kim, J.S.; Durrant, J.R.; Cabral, J.T. *Nature Communications* **2013**, *4*, 2227.

(2) Liu, Y.; Chen, C.-C.; Hong, Z.; Gao, J.; Yang, Y.; Zhou, H.; Dou, L.; Li, G.; Yang, Y. *Scientific Reports* **2013**, *3*, 3356.

(3) Ruderer, M.A.; Guo, S.; Meier, R.; Chiang, H.-Y.; Körstgens, V.; Wiedersich, J.; Perlich, J.; Roth, S.V.; Müller-Buschbaum, P. *Advanced Functional Materials* **2011**, *21 (17)*, 3382-3391.

(4) Liu, Y.; Zhao, J.; Li, Z.; Mu, C.; Ma, W.; Hu, H.; Jiang, K.; Lin, H.; Ade, H.; Yan, H. *Nature Communications* **2014**, *5*, 5293.

(5) Na, S.-I.; Kim, S.-S.; Jo, J.; Oh, S.-H.; Kim, J.; Kim, D.-Y. *Advanced Functional Materials* **2008**, *18 (24)*, 3956-3963.

(6) Aryal, M.; Trivedi, K.; Hu, W. *ACS Nano* **2009**, *3 (10)*, 3085-3090.

(7) Pfadler, T.; Coric, M.; Palumbiny, C.M.; Jakowetz, A.C.; Strunk, K.-P.; Dorman, J.A.; Ehrenreich, P.; Wang, C.; Hexemer, A.; Png, R.-Q.; Ho, P.K.H.; Müller-Buschbaum, P.; Weickert, J.; Schmidt-Mende, L. *ACS Nano* **2014**, *8 (12)*, 12397-12409.

(8) Chen, D.; Zhao, W.; Russell, T.P. *ACS Nano* **2012**, *6 (2)*, 1479-1485.

(9) Rodríguez-Rodríguez, Á.; Rebollar, E.; Soccio, M.; Ezquerra, T.A.; Rueda, D.R.; Garcia-Ramos, J.V.; Castillejo, M.; Garcia-Gutierrez, M.-C. *Macromolecules* **2015**, *48 (12)*, 4024-4031.

(10) García-Valverde, R.; Cherni, J.A.; Urbina, A. *Progress in Photovoltaics: Research and Applications* **2010**, *18 (7)*, 535-558.

(11) Zhou, H.; Yang, L.; You, W. *Macromolecules* **2012**, *45 (2)*, 607-632.

(12) Vohra, V.; Campoy-Quiles, M.; Garriga, M.; Murata, H. *Journal of Materials Chemistry* **2012**, *22 (37)*, 20017-20025.

(13) Mihailetchi, V.D.; Xie, H.X.; de Boer, B.; Koster, L.J.A.; Blom, P.W.M. *Advanced Functional Materials* **2006**, *16 (5)*, 699-708.

(14) Shrotriya, V.; Ouyang, J.; Tseng, R.J.; Li, G.; Yang, Y. *Chemical Physics Letters* **2005**, *411 (1–3)*, 138-143.

(15) Lu, L.; Zheng, T.; Wu, Q.; Schneider, A.M.; Zhao, D.; Yu, L. *Chemical Reviews* **2015**, *115 (23)*, 12666-12731.

(16) Chen, D.; Liu, F.; Wang, C.; Nakahara, A.; Russell, T.P. *Nano Letters* **2011**, *11 (5)*, 2071-2078.

(17) Gevaerts, V.S.; Koster, L.J.A.; Wienk, M.M.; Janssen, R.A.J. *ACS Applied Materials & Interfaces* **2011**, *3 (9)*, 3252-3255.

(18) Brabec, C.J.; Cravino, A.; Meissner, D.; Sariciftci, N.S.; Fromherz, T.; Rispens, M.T.; Sanchez, L.; Hummelen, J.C. *Advanced Functional Materials* **2001**, *11 (5)*, 374-380.

(19) Foertig, A.; Wagenpfahl, A.; Gerbich, T.; Cheyns, D.; Dyakonov, V.; Deibel, C. *Advanced Energy Materials* **2012**, *2 (12)*, 1483-1489.
(20) Rebollar, E.; Castillejo, M.; Ezquerra, T.A. *European Polymer Journal* **2015**, *73*, 162-174.
(21) Kim, J.B.; Kim, P.; Pegard, N.C.; Oh, S.J.; Kagan, C.R.; Fleischer, J.W.; Stone, H.A.; Loo, Y.-L. *Nature Photonics* **2012**, *6 (5)*, 327-332.

Chapter 6. Conclusions

The main conclusions of this thesis are summarized below:

- P3HT/PCDTBT blends with different concentrations are prepared giving rise to thin films with different thicknesses with lateral phase separation when spin-coated. The domain sizes of both components decrease as film thickness decreases. Conductive-AFM results show that the thicker blend films (165 and 295 nm thick), present a fibrous network where the strongest current is measured. These results evidence that P3HT needle-like crystals grow from the P3HT-rich domains, acting as bridges through the PCDTBT-rich domains. A strong impact of the crystal morphology on hole mobility is evidenced. In particular, a significant zero-field hole mobility increase is observed for the P3HT/PCDTBT thin films with increasing thickness.

- Laser-induced periodic surface structures on poly(3-hexylthiophene-2,5-diyl) thin films can be prepared with periods close to the irradiation wavelengths of 532 and 266 nm, and by selecting different laser parameters such as fluence and the number of pulses, it is possible to obtain LIPSS with different depths, periodicities, and degree of order. NEXAFS and Raman spectroscopy measurements reveal a good chemical stability of P3HT thin films under the laser irradiation conditions used for LIPSS formation. Conductive atomic force microscopy shows that in the nanostructures the trenches present a higher conductivity than the ridges. The structural characterization suggests that during irradiation melting of the surface takes place leading to a ripple morphology characterized by the existence of low crystallinity and non-conducting ridges over a continuous and more-conducting P3HT residual layer whose initial crystallinity seems to be unaffected in comparison to that of the pristine P3HT thin film. In addition, a zero field hole mobility increase of about two orders of magnitude is observed for P3HT domains in the 165 nm blend films compared to a neat P3HT film with similar thickness, probably related to the highly conductive needle-like network induced in P3HT by the presence of the PCDTBT phase.

- Laser-induced periodic surface structures are formed on PCDTBT thin films both at 532 and 266 nm. NEXAFS and Raman spectroscopy measurements reveal good chemical stability of nanostructured PCDTBT thin films under the laser irradiation conditions used for LIPSS formation. Conductive atomic force microscopy shows that in the nanostructures the trenches present a higher conductivity than the ridges as in the case of P3HT films.

- Laser-induced periodic surface structures are also prepared on P3HT/PCDTBT blends thin films both at 532 and 266 nm. As obtained from STXM analysis, LIPSS formation do not induce a further phase segregation neither a mixture of the components and NEXAFS and Raman spectroscopy measurements reveal good chemical stability of the polymer components. Conductive atomic force microscopy shows that in the nanostructures the trenches present a higher conductivity than the ridges as in the case of the homopolymer films.

- LIPSS can also be fabricated on P3HT/$PC_{71}BM$. In this case the effect of the irradiation in air or in vacuum is analyzed and the results show that while films irradiated in air present some chemical modifications of the polymer-fullerene structure, especially at the surface, the chemical modification is negligible when the irradiation is performed under vacuum conditions. It is also shown that P3HT and $PC_{71}BM$ phases are separated along the ripples.

- The investigation of LIPSS in P3HT/$PC_{71}BM$ blends by resonant soft X-ray scattering has proven that during LIPSS formation in vacuum, segregated domains are oriented along the ripples.

- LIPSS formation can be monitored by *in situ* GISAXS measurements during laser irradiation of the spin-coated polymer films and the results obtained indicate that there is a dependence on the laser repetition rate of the kinetics of LIPSS formation.

- LIPSS have been successfully incorporated in active layers of organic solar cells which suggest that LIPSS could be a compatible technology with organic photovoltaic devices. In particular, LIPSS have been formed on P3HT:$PC_{71}BM$

blend on both bilayer and bulk heterogeneous solar cell architecture. For the bilayer architecture an increase of about 10% is observed in the V_{oc} for the LIPSS cell.

List of scientific publications:

(1) E. Rebollar, D. R. Rueda, I .Martín-Fabiani, A. Rodríguez-Rodríguez, M.C. García-Gutiérrez, G. Portale, M. Castillejo, T.A. Ezquerra.
"In situ monitoring of Laser Induced Periodic Surface Structures formation on polymer films by Grazing Incidence Small Angle X-ray Scattering"
Langmuir, 2015, 31 (13), 3973

(2) A. Rodríguez-Rodríguez, E. Rebollar, M.Soccio, T.A. Ezquerra, D. R. Rueda, J.V. García-Ramos, M. Castillejo, M.C. García-Gutiérrez.
"Laser induced periodic surface structures on conjugated polymers: Poly(3-hexylthiophene)"
Macromolecules, 2015, 48 (12), 4024

(3) A. Rodríguez-Rodríguez, M. Soccio, D.E. Martínez-Tong, T.A. Ezquerra, B. Watts, M.C. García-Gutiérrez.
"Competition between phase separation and structure confinement in P3HT/PCDTBT heterojunctions: Influence on nanoscale charge transport"
Polymer, 2015, 77, 70

(4) D. E. Martínez-Tong, A. Rodríguez-Rodríguez, A. Nogales, M.C. García-Gutiérrez, T.A. Ezquerra, E. Rebollar.
"Laser fabrication of polymer ferroelectric nanostructures for non-volatile organic memory devices"
ACS Applied Materials and Interfaces, 2015, 7 (35), 19611

(5) J. Cui, A. Rodríguez-Rodríguez, M. Hernández, M.C. García-Gutiérrez, A.Nogales, M. Castillejo, D. Moseguí González, P. Müller-Buschbaum, T.A. Ezquerra, E. Rebollar
"Laser induced periodic surface structures on P3HT and on its photovoltaic blend with $PC_{71}BM$"
ACS Applied Materials and Interfaces, 2016, 8 (46), 31894

(6) A. Rodríguez-Rodríguez, E. Gutiérrez; M. Hernández, M.C. García-Gutiérrez, A. Nogales, J.V. García-Ramos, R. Serna, T.A. Ezquerra, E. Rebollar.
"Functional nanostructured surfaces induced by laser on fullerene materials"
In progress

(7) A. Rodriguez-Rodriguez, E. Rebollar, T.A. Ezquerra, J.V. García-Ramos, M. Castillejo, M.C. García-Gutiérrez.
"Laser-Induced Periodic Surface Structures on Conjugated Polymers: PCDTBT and the Heterojunction P3HT/PCDTBT"
In progress